U.PORTO

FEUP FACULDADE DE ENGENHARIA
UNIVERSIDADE DO PORTO

Master Thesis in Mechanical Engineering

Joining magnesium and aluminum alloy sheets by a novel hole hemming process

Author:

José António da Cruz Pereira

Supervisor:

Mohammad Mehdi Kasaei

Co-Supervisor:

Lucas Filipe Martins da Silva

Ricardo João Camilo Carbas

Master in Mechanical Engineering

September, 2022

Resumo

O design com multimateriais é um conceito usado por fabricantes de carro modernos para produzir estruturas automóveis de baixo peso com materiais dissimilares. As ligas de magnésio são uma nova tendência na indústria automóvel para fabricar estruturas de veículos de alta performance, sendo notáveis por terem a menor densidade de entre todos os metais estruturais, terem uma resistência similar a ferro fundido e muitas ligas de alumínio convencionais usadas na indústria automóvel e terem uma rigidez específica maior que muitos materiais poliméricos e compósitos. As ligas de alumínio têm sido extensivamente usadas na indústria automóvel devido às suas propriedades atrativas tais como baixa densidade, resistência e ductilidade moderadamente alta, boa resistência à corrosão e relativamente baixo custo. É dos materiais mais fáceis de conformar, reciclar e maquinar. Estes materiais caem dentro do conceito de design de baixo peso e, por isso, há uma crescente necessidade de juntar e combinar as suas propriedades desejáveis. Só as tecnologias de ligação podem fornecer a oportunidade de empregar as vantagens de ambos os materiais simultaneamente.

No entanto, as ligas de magnésio debatem-se para ser empregadas em aplicações automóveis devido à sua reduzida ductilidade à temperatura ambiente associada à sua estrutura cristalina hexagonal compacta, criando dificuldades associadas ao processo de fabricação, processamento, montagem, performance e custo. Tecnologias de ligação por conformação são baseadas em deformação plástica dos materiais para produzir ligações mecânicas e, por isso, a fiabilidade destes processos depende da ductilidade dos materiais a ser juntados, sendo então difíceis de aplicar em ligas de magnésio. Friction Stir Welding (FSW) é amplamente usado na indústria automóvel por ter um grande potencial para juntar materiais dissimilares eficientemente devido à baixa geração de temperaturas. Contudo, limitações na solubilidade entre fases sólidas de magnésio e alumínio ainda provocam a formação de fases intermetálicas frágeis que têm um impacto negativo na performance das juntas.

Recentemente, uma nova tecnologia de ligação por conformação denominada “Hole Hemming” foi desenvolvida e proposta para juntar materiais com propriedades mecânicas muito diferentes. O presente trabalho tem como objetivo desenvolver experimentalmente este processo para juntar ligas de alumínio e magnésio.

As propriedades mecânicas dos materiais foram caracterizadas pela realização de testes de tração uniaxial, enquanto que os limites à fratura dos materiais foram definidos pela realização de testes de formabilidade e usando um critério de fratura dúctil adequado para prever fratura nos modelos de elementos finitos. No fim, foi comprovado a baixa ductilidade das ligas de magnésio quando comparadas com as ligas de alumínio.

A influência dos parâmetros e a fiabilidade do processo para juntar estes dois materiais foram estudados ao efetuar simulações de elementos finitos e estabelecendo uma janela de processamento.

Os ensaios experimentais do processo foram realizados e os resultados mostram que o processo “Hole hemming” pode ligar apropriadamente as chapas de magnésio e alumínio sem a ocorrência de fraturas. Para além disso, as juntas resistiram uma carga máxima de 2.9 kN através do mecanismo de falha gradual de cedência de furo.

Abstract

Multi-material design is a concept used by modern car manufactures to produce lightweight automotive bodies with dissimilar materials. Magnesium alloys are a new trend in the automotive industry to manufacture high performance vehicle structures being noteworthy for having the lowest density among all structural metals, a specific strength similar to cast iron and many traditional automotive aluminum alloys, and a higher specific stiffness than many polymeric materials and composites. Aluminum alloys have been widely used in the automotive industry due to its attractive properties such as low density, fairly high strength and high ductility, good corrosion resistance and relatively low cost. It is one of the easiest metals to form, recycle and machine. These materials fit perfectly in the lightweight design concept and thus there is a growing need to join and combine their desirable properties. It is the joining technologies that can provide the opportunity to employ the advantages of both metals simultaneously.

Nonetheless, magnesium alloys struggle to be employed in automotive applications due the reduced ductility at room temperature associated to its hexagonal close packed crystal structure, creating challenges associated with manufacturing, processing, assembly, in-service performance and cost. Joining by forming processes are based on plastic deformation of the materials to produce a mechanical interlock and so the feasibility of these processes depends on the ductility of the materials, and so difficult to apply to magnesium alloys. Friction Stir Welding (FSW) is widely used in the automotive industry as it has the potential to join dissimilar materials efficiently due to low temperature generation. Nonetheless, solubility limitations between magnesium and aluminum in solid-solid phase still provokes the formation of brittle intermetallic phases that negatively impact the performance of the joint.

Recently, a novel joining by forming process denominated “Hole Hemming” was developed and proposed to join materials with very different mechanical properties. The present work has the objective to experimentally develop this process to join a magnesium and aluminum alloy.

The mechanical properties of the materials were characterized by performing uniaxial tension tests, while the fracture limits of the materials were defined by performing formability tests and using a proper ductile fracture criterion to predict fracture in the finite element model. In the end, it was shown the poor ductility of the magnesium alloy compared with the aluminum alloy.

The influence of the process parameters and the feasibility of the hole hemming process to join these two alloys was studied by conducting finite element simulations and establishing a process window.

The experimental tests of the process were then carried out and results show that the hole hemming process can appropriately join the magnesium and aluminum alloy sheets without the occurrence of fracture. Furthermore, the hole-hemmed joints resisted a maximum load of 2.9 kN with a gradual failure mechanism of hole bearing.

Ackowledgements

First, I would like to thank to my supervisor Dr. Mehdi Kasei for all the support in the multiple stages of the work and for the precious knowledge and data provided during the thesis.

I want to thank to Prof. Lucas da Silva for the questions and suggestions in the weekly meetings. To Dr. Eduardo Marques I thank for the information provided about different subjects. A special thanks to Dr. Ricardo Carbas for the invaluable help in the cutting and machining of the materials.

To Adriano Conceição I want to thank the excellent tool design that made it possible to put in practice the hole hemming process.

To all the master´s and doctoral students of the AJPU group, I would like to thank the warm welcome and availability to help, with a special thanks to Diogo Santos which helped me multiple times to find my way in the lab and assisted, among other things, in the assembly of the hole hemming tool.

I would also like to express my gratitude to Prof. Carlos Silva for the help in the assembling of the hole hemming tool. To Mr. Domingos for the fast and precise machining of the formability specimens. For Dr. Alireza Safar I would like to thank the assistance and knowledge to operate the software of the servo hydraulic machine.

To my longtime friends and to the friends who shared with me this long 5 years journey, I would like to express my deeply gratitude for all the priceless moments, stories and adventures we spent together, it would be impossible to complete this journey without your support and my life without you would be empty. I´m very keen on continuing to cultivate and grow this friendship for many years to come.

Finally, but most important, to my parents, the ones that unconditionally loved and supported me since the very beginning and provided the means for a good education, both social and scholar. To my sister, for all the love, companionship, mentorship and protection. I will forever love you.

Contents

1 Introduction 1
1.1 Background and motivation 1
1.2 Objectives 1
1.3 Methodology 2
1.4 Dissertation outline 2

2 Literature review 3
2.1 Lightweight materials in the automotive industry 3
2.1.1 Magnesium 3
2.1.2 Aluminum 4
2.2 Joining by forming processes 5
2.3 Joining magnesium and aluminum alloys 10
2.4 Ductile fracture 13
2.4.1 Damage evolution 13
2.4.2 Ductile fracture modeling and prediction 14
2.4.3 Modified Mohr Coulomb fracture criterion 15
2.5 Hole hemming process 17
2.6 Design of the process 19

3 Experiments 20
3.1 Material characterization 20
3.1.1 Mechanical properties 23
3.1.2 Anisotropy 27
3.1.3 Yield criterion 28
3.1.4 Hardening law 30
3.2 Formability tests 32
3.3 Hole hemming experiments 36
3.4 Single lap shear test 40
3.5 Work plan 41

4 Finite element modeling 42
4.1 Calibration tests 42
4.2 Hole hemming 44
5.2.1 Destructive tests 45
4.3 Work plan 46

5 Fracture modeling 48
5.1 Ductile fracture criterion 48
5.2 Calibration method 48
5.3 Fracture envelopes 54
5.3.1 Evaluation of the fracture criterion 56

6 Results and discussion 57
6.1 Deformation mechanics 57
6.2 Influence of the process parameters 58
6.3 Process window 65
6.4 Hole design 68
6.5 Experimental hole hemmed joints 70
6.6 Destructive tests 75
6.6.1. Comparison of the hole-hemmed joints with other joints 79

7 Conclusion 81

8 Future works 82

References 83

Appendix A Paper 89

List of Acronyms

AHSS	**A**dvanced **H**igh **S**trength **S**teel
CFRP	**C**arbon **F**iber **R**einforced **P**olymer
CNC	**C**omputer **N**umerical **C**ontrol
DFC	**D**uctile **F**racture **C**riterion
DIC	**D**igital **I**mage **C**orrelation
DSSPR	**D**ouble-**S**ided **S**elf **P**ierce **R**iveting
FE	**F**inite **E**lement
FEM	**F**inite **E**lement **M**odel
FFLD	**F**racture **F**orming **L**imit **D**iagram
FSBR	**F**riction **S**tir **B**lind **R**iveting
FSW	**F**riction **S**tir **W**elding
HCP	**H**exagonal **C**lose **P**acked
IMC	**I**nter**M**etallic **C**ompounds
J-C	**J**ohnson-**C**ook
MMC	**M**odified **M**ohr **C**oulomb
MVC	**M**icro**V**oid **C**oalescence
NT	**N**otched **T**ension
PS	**P**lane **S**train
PVC	**P**oly**V**inyl **C**hloride
SFR	**S**elf **P**ierce **R**iveting
ST	**S**hear **T**ension
UFSW	**U**nderwater **F**riction **S**tir **W**elding
UT	**U**niaxial **T**ension

List of figures

Figure 1 – Comparison of mass savings in automotive applications for advanced materials vs mild steel in structural panels for equivalent bending stiffness and bending strength. Adapted from [5]. 3

Figure 2 - Mach-II body-in-white design by Ford heavy on magnesium. Adapted from [5]. ... 4

Figure 3 - Hexagonal close packed (HCP) crystal structure. 4

Figure 4 - Most common types of hems. Adapted from [17]. 6

Figure 5 – Schematic representation of the hemming process. Adapted from [20]. 6

Figure 6 – Defects of the hemming process. Adapted from [18]. 7

Figure 7 – Wrinkling and splitting defects in the hemming process. Adapted from [17]. 7

Figure 8 - Conventional clinching process using a fixed die. Adapted from [23]. 7

Figure 9 - Schematic illustration of the shear clinching process: 1 - Fixation and preloading, 2 – Drawing and shear-cutting, 3 – Compression and extrusion, 4 – Back stroke and eject. Adapted from [2]. 8

Figure 10 – Self-pierce riveting process illustration. (a) Clamping; (b) Piercing; (c) Flaring; (d) Releasing. Adapted from [28]. 9

Figure 11 - Schematic illustration of the DSSPR process: (a) before joining and (b) after joining. Adapted from [31]. 10

Figure 12 - Friction stir welding schematic illustration. Adapted from [35]. 11

Figure 13 – Schematic illustration of the Friction Stir Blind Riveting (FSBR) process: (a) Plunging, (b) Stirring, (c) Upsetting and (d) Joint. Adapted from [43]. 12

Figure 14 – Schematic illustration of dieless rivet clinching. Adapted from [48]. 12

Figure 15 – Void nucleation. (a) Initial material; (b) Nucleation of the voids after application of a tensile load. (1) Initial porosity and (2) Inclusions. 13

Figure 16 – Void growth and coalescence due to the further increase of the plastic deformation. 14

Figure 17 - The correlation between the stress triaxiality and the normalized Lode angle parameter under plane stress condition. 16

Figure 18 - Schematic ilustration of the Hole Hemming process: (a) Flanging stage and (b) Hemming stage. 18

Figure 19 - Schematic illustration of the Hole Hemming process and process parameters. 19

Figure 20 - Dimensions of the uniaxial tension specimens for (a) AA6082-T4 and (b) AZ31. (c) AA6082-T4 and AZ31 uniaxial tension specimens. Dimensions in mm. 20

Figure 21 – AZ31 specimen during the uniaxial tension test in the INSTROM 3367 machine equipped with a digital camera for measuring strain and displacement. 21

Figure 22 – AZ31 uniaxial tension specimens painted with a stochastic pattern. 21

Figure 23 - A fractured AA6082-T4 uniaxial tension specimen after being tested. 22

Figure 24 – Method of obtaining data in the GOM correlate DIC software: (a) displacement of the gauge section and (b) major and minor strains at a point of the fracture zone. 23

Figure 25 – Load-displacement curves for the AA6082-T4 uniaxial tension specimens in the (a) 0° (b) 45° and (c) 90° directions. 24

Figure 26 – Load-displacement curves for the AZ31 uniaxial tension specimens in the (a) 0° (b) 45° and (c) 90° directions. 24

Figure 27 – Stress-strain curves for the AA6082-T4 uniaxial tension specimens in the (a) 0° (b) 45° and (c) 90° directions. 25

Figure 28 – Stress-strain curves for the AZ31 uniaxial tension specimens in the (a) 0° (b) 45° and (c) 90° directions. 26

Figure 29 – Yield locus defined by the Hill 1948 criterion. 30

Figure 30 - Comparison of the experimental and numerical load-displacement curves using the Hollomon hardening law: (a) AA6082-T4 and (b) AZ31. 31

Figure 31 - Comparison of the experimental and numerical load/displacements curves using the combination of the Swift and Voce hardening law for the AA6082-T4 32

Figure 32 - Experimental formability test specimens: PS - Plane Strain tension specimen, ST - Shear Tension specimen and NT - Notched Tension specimen. 33

Figure 33 - Dimensions of the formability test specimens: (a) Notched Tension specimen, (b) Plane Strain tension specimen and (c) Shear Tension specimen. Dimensions in mm. 33

Figure 34 - AA6082-T4 calibration test specimens painted with a stochastic pattern. 34

Figure 35 - Load/displacement curves of the AA6082-T4 calibration tests: (a) Notched Tension specimens, (b) Plane Strain tension specimens and (c) Shear Tension specimens. 35

Figure 36 - Load/displacement curves of the AZ31 calibration tests: (a) Notched Tension specimens, (b) Plane Strain tension specimens and (c) Shear Tension specimens. 35

Figure 37 - Illustration of the hole hemming tool: 1 - Flanging punch, 2 - Bottom die, 3 - Upper die, 4 - Blank holder, 5 - Hemming punch. 36

Figure 38 – Experimental equipment of the hole hemming process. 37

Figure 39 - Experimental hole hemming specimens: (a) On the left, AA6082-T4 joint characterization specimen, on the right, single lap shear test specimen and (b) on the left, AZ31 joint characterization specimen, on the right, single lap shear test specimen. 37

Figure 40 – Flanging stage components and positioning of the outer sheet: (a) 1 – Flanging punch and 2 – bottom die, (b) 3 – upper die and (c) positioning of the outer sheet in the top of the bottom die by means of alignment pins. 38

Figure 41 - Formed specimen after the flanging stage. 38

Figure 42 - Hemming stage components and positioning of the sheets: (a) 1 – Hemming punch and 2 – blank holder, (b) 3 – bottom die, (c) 4 – inner sheet and 5 – outer sheet and (d) positioning of the sheets in the top of the blank holder by means of alignment pins. 39

Figure 43 – Final joint: (a) top view, (b) bottom view and (c) lateral view. 39

Figure 44 - Single lap shear test specimen. 40

Figure 45 – Single lap shear test specimen fixed to the testing machine. 40

Figure 46 - FE models of the calibration tests with mesh details and boundary conditions: (a) Shear tension test, (b) Notched tension test, (c) Plane strain test, (d) Uniaxial tension test. ... 42

Figure 47 - Stress state and Equivalent plastic strain in a AA6082-T4 uniaxial tension FEM specimen before fracture: (a) Stress triaxiality, (b) Normalized Lode angle parameter and (c) Equivalent plastic strain. 43

Figure 48 - AA6082-T4 uniaxial tension FEM specimen after fracture. 43

Figure 49 – Hole hemming FE model mesh details of a AA6082-T4 sheet. 44

Figure 50 - FE modeling apparatus of the hole hemming process. 45

Figure 51 – Geometry and boundary conditions of the destructive test specimens FE models: (a) single lap shear test and (b) peel test. 46

Figure 52 - Typical MMC fracture envelope expressed in a 2D space of Equivalent Plastic Strain and Stress Triaxiality. 48

Figure 53 – Major strain of a AZ31 notched tension test specimen before fracture. 49

Figure 54 - Comparison between the strain contour of the FE model and the experimental test of a AA6082-T4 notched tension test: (a) FE model equivalent plastic strain countor and (b) DIC major strain countor. 49

Figure 55 – Load-displacement curves comparison between the experimental and numerical results: (a) AA6082-T4 and (b) AZ31. 50

Figure 56 – Evolution of the Stress triaxiality (left) and Normalized Lode angle parameter (right) for the AA6082-T4. 50

Figure 57 - Evolution of the stress triaxiality (left) and Normalized Lode angle parameter (right) for the AZ31. 51

Figure 58 - Calibration points for both materials obtained by FEM and DIC: (a) AA6082-T4 and (b) AZ31. 52

Figure 59 - Plane stress condition verification: (a) AA6082-T4 and (b) AZ31. 53

Figure 60 – 3D MMC fracture envelopes: (a) AA6082-T4 and (b) AZ31. The red line present in the surface shows the fracture strain for plane stress state. 54

Figure 61 – MMC fracture envelopes with the respective calibration points: (a) AA6082-T4 and (b) AZ31. 55

Figure 62 - Comparison of the AA6082-T4 and AZ31 fracture envelopes. 55

Figure 63 – Contour values of equivalent plastic strain and damage indicator in the outer sheet during the hole hemming process: (a) equivalent plastic strain at the end of the flanging stage, (b) damage value of the outer sheet at the end of the flanging stage, (c) equivalent plastic strain at the end of the hemming stage, (b) damage value of the outer sheet at the end of the hemming stage. 57

Figure 64 – Loading path of the critical regions on the outer sheet along the hole hemming process. 58

Figure 65 - Damage distribution in the outer sheet in the end of the flanging stage for different values of fillet radius of the upper die: (a) fr_d = 3 mm and (b) fr_d = 4 mm. 58

Figure 66 - Damage evolution in the critical zones during the flanging stage for different fr_d: (a) Bend zone and (b) edge zone. 59

Figure 67 - Damage distribution in the outer sheet in the end of the flanging stage for different values of flange lengths: (a) F = 3 mm, (b) F = 3.25 mm, (c) F = 3.5 mm, (d) F = 3.75 mm and (e) F = 4 mm. 59

Figure 68 - Damage evolution in the edge zone during the flanging stage for different flange lengths (F). 60

Figure 69 - Damage distribution in the outer sheet during the hemming stage for different values of flange lengths (F): (a) F = 3 mm, (b) F = 3.25 mm, (c) F = 3.5 mm, (d) F = 3.75 mm and (e) F = 4 mm. 60

Figure 70 - Effect of the flange length on the required force in the flanging punch during the flanging stage. 61

Figure 71 – Damage distribution in the outer sheet and contact length between the outer and inner during the hemming stage for different values of hemming punch fillet radius: (a) R = 4 mm, (b) R = 6 mm, (c) R = 8 mm and (d) R = 10 mm. 61

Figure 72 - Damage evolution in the bend zone during the hemming stage for different hemming punch fillet radius (R). 62

Figure 73 - Effect of the fillet radius of the hemming punch (R) on the required force in the hemming punch during the hemming stage. 62

Figure 74 - Damage distribution in the outer sheet during the hole hemming process for different values of R_o. (a) and (b) damage distribution in the end of the flanging stage for R_o = 7 mm and R_o = 9 mm, respectively, (c) and (d) damage distribution in the middle of the hemming stage for R_o = 7 mm and R_o = 9 mm, respectively. 63

Figure 75 - Damage evolution in the edge zone during the hole hemming process for different outer sheet hole radius (R_o). 63

Figure 76 - Damage evolution in the bend zone during the hole hemming process for different outer sheet hole radius (R_o). 64

Figure 77 - Damage distribution in the inner sheet in the end of the hemming stage (a) using 5 elements through thickness and a time period of 0.0005, (b) using 10 elements through thickness and a time period of 0.0005 and (c) using 10 elements through thickness and a time period of 0.0015. 65

Figure 78 – Finite element process window for different values of flange length (F). 65

Figure 79 - Process window for different values of hemming punch filler radius (R). 66

Figure 80 - Damage distribution in the outer sheet during the hemming stage for the experimental cases: (a) F = 3.5 mm, (b) F = 4 mm and (c) F = 4.5 mm. 67

Figure 81 – Process window for the experimental cases. 67

Figure 82 - New outer sheet hole design consisting in four branches. 68

Figure 83 - Damage distribution in the outer sheet during the hole hemming process using hole branch design (C = 6 mm and L = 2.5 mm). 68

Figure 84 – Damage evolution in the edge zone during the hole hemming process for different hole designs. 69

Figure 85 - Loading path of the branch zone critical region along the hole hemming process. 69

Figure 86 - Hole hemming specimens after the flanging stage: (a) F = 3.5 mm (Ro = 9 mm), (b) F = 4 mm (Ro = 8.5 mm) and (c) F = 4.5 mm (Ro = 8 mm) 70

Figure 87 – Flanging stage load-displacement curves comparison between the experimental and numerical results. 70

Figure 88 – Hole hemmed joints for the F = 4.5 mm case. 71

Figure 89 - Hemming stage load-displacement curves comparison between the experimental and numerical results for F = 4.5 mm. 71

Figure 90 - Hole hemmed joints for the F = 4 mm case: Experimental (a) joint without cracks and (b) joint with cracks, and FE (c) joint without cracks and (d) joint with cracks. 72

Figure 91 - Hemming stage load-displacement curves comparison between the experimental and numerical results for F = 4 mm. 73

Figure 92 – First attempts for the F = 3.5 mm case: (a) failed joint and (b) compressed flange after the hemming stage. 74

Figure 93 - Hole hemmed joints for the F = 3.5 mm case after applying lubricant: (a) lower displacement (b) higher displacement. 74

Figure 94 - Hemming stage load-displacement curves comparison between the experimental and numerical results for F = 3.5 mm. 75

Figure 95 - Joints for the single lap shear tests: (a) joint no.1, (b) joint no.2, (c) joint no.3 and (d) joint no.4. 75

Figure 96 - Load-displacement curves of the experimental and numerical single lap shear tests for the F = 4 mm case and numerical load-displacement curve for the peel test. 76

Figure 97 - Front view of the joint aspect during the single lap shear test: (a) end of stage 1, (b) end of stage 2, (c) during stage 3 and (d) end of the test. 77

Figure 98 – Side view of the joint aspect during the single lap shear test: (a) end of stage 1, (b) end of stage 2, (c) during stage 3 and (d) end of the test. 77

Figure 99 – Failure mode of the FEM peel test. 78

Figure 100 - Joint 4 after the performance of the single lap shear test. 78

Figure 101 – Aspect of a hole hemmed joint and sheets after the single lap shear test: (a) front view and (b) side view of the hole hemmed joint, (c) magnesium sheet and (d) aluminum sheet. 79

List of tables

Table 1 - Advantages and disadvantages of the clinching process [24]. 8

Table 2 - Advantages and disadvantages of the self-pierce riveting process. [28] 9

Table 3 - Dimensions of the thickness and width in the AA6082-T4 uniaxial tension specimens. t - average thickness (mm) measured in three different points; w – average width (mm); A – cross section area (mm^2). 22

Table 4 – Dimensions of the thickness and width in the AZ31 uniaxial tension specimens. t - average thickness (mm) measured in three different points; w – average width (mm); A – cross section area (mm^2). 22

Table 5 - Mechanical properties of the AA6082-T4. 26

Table 6 - Mechanical properties of the AZ31. 26

Table 7 – Lankford coefficients and normal and planar anisotropy parameters of the AA6082-T4. 28

Table 8 - Lankford coefficients and normal and planar anisotropy parameters of the AZ31. 28

Table 9 - Hill 1948 anisotropic yield stress ratios. 30

Table 10 - Hill 1948 material constants. 30

Table 11 - Coefficients of the Hollomon hardening law for both materials. 31

Table 12 – Parameters of the combination of the Swift and Voce Hardening law for the AA6082-T4. 32

Table 13 - Thickness of the calibration tests for both materials. Dimensions in mm. 34

Table 14 - Hole hemming experimental work plan. Dimensions in mm. 41

Table 15 - Work plan used to study the hole hemming process parameters. 47

Table 16 - Calibration points for the AA6082-T4. 53

Table 17 - Calibration points for the AZ31. 53

Table 18 - MMC material constants. 54

Table 19 – Fracture displacement error prediction using the calibrated MMC for the AA6082-T4. 56

Table 20 - Fracture displacement error prediction using the calibrated MMC for the AZ31. 56

Table 21 – Optimal process parameters for the hole hemming process. 66

Table 22 – FE model fracture prediction error. 73

Table 23 – Hole hemming process compared with other joining by forming processes. 79

1 Introduction

1.1 Background and motivation

Nowadays, there is an urge in the automotive industry to lighten the weight of the automobiles in order to improve both the performance and fuel efficiency for environmental and economic reasons [1]. Nonetheless, the comfort and safety of the passengers are also important consideration, which increases the weight of the car construction [2]. Modern car manufacturers produce lightweight automotive bodies using dissimilar materials to meet these requirements. This process is known as “multi-material design” [3] and involves using various lightweight materials including advanced high-strength steel (AHSS), aluminum alloys, composites and magnesium alloys [4].

Magnesium alloys are a new trend in the automotive industry to create high performance vehicle structures [5]. Magnesium alloys are noteworthy for having the lowest density among all structural materials, as well as a specific strength comparable to cast iron and similar or higher than many conventional automotive aluminum alloys. However, the limited formability of magnesium alloys at room temperature prevents the joining operations using plastic deformation. In fact, due to difficulties with manufacturing, processing, assembly, in-service performance and cost, magnesium alloys only make up a small portion of the overall weight in automobiles [1].

Due to the characteristics of the base materials, there is a growing need for joining magnesium to aluminum alloys. Individually, aluminum alloys are widely utilized in the automotive and aerospace industries due to various advantages, including light weight, high specific strength and recyclability. As previously said, some specific advantages may favor magnesium alloys, while others aluminum alloys. The ability to use the benefits of both materials at once can only be achieved through joining technologies [6].

Dissimilar welding of magnesium and aluminum from conventional processes is difficult or impossible to the formation of brittle intermetallic phases that impacts severely the mechanical properties of the joint [6]. Friction stir welding (FSW), which is widely used to join dissimilar materials due to the low temperature generation, also faces limitations while joining magnesium and aluminum alloys [7]. Joining processes by plastic deformation, which are processes that use plastic deformation of the parts to be joined to create a mechanical interlock between them, such as clinching and self-pierce riveting are also difficult to apply because of the low ductility at room temperature of magnesium alloys [8].

Thus, the success of magnesium alloys trend in the automotive industry depends on the development of novel joining processes that should be capable of joining the magnesium alloys to other structural materials, such as the aluminum alloys.

1.2 Objectives

The present work has two main objectives. The first is to continue the development of the hole hemming process to form hole-hemmed joints without fracture, which is accomplished by the development of a numerical hole hemming model and the performance of experimental hole hemming joints. The second is to prove the capacity of the hole hemming process to join dissimilar materials with very different strengths and/or formability.

1.3 Methodology

Initially it was undergone a literature review about the state of art of the joining methods used in the automotive industry, focusing in the joining by plastic deformation of dissimilar materials, and the study of ductile fracture.

Then, the materials were characterized with the performance of experimental uniaxial tension tests and using GOM correlate Digital Image Correlation (DIC) software and the fracture limits of the materials were defined using the Modified Mohr Coulomb fracture criterion with the performance of both numerical and experimental formability tests.

Knowing the materials properties and fracture limits, a numerical model of the hole hemming process was developed and it was studied the process window as well as the critical regions of the process and respective loading paths. The performed joints were also tested under different loading conditions.

The numerical results were then evaluated by conducting experimental hole-hemmed joints and the performance of the joints were compared against that obtained with other joining methodologies.

1.4 Dissertation outline

This dissertation is organized in seven chapters. The present introductory chapter contains a brief introduction to the project, describes the methodology used and exposes the aimed main objectives.

The second chapter covers a brief literature review about the magnesium and aluminum alloys used in the automotive industry, joining by forming processes, ductile fracture and a introduction to the hole hemming process.

The third chapter addresses all the experimental work done along the dissertation, including the characterization of the materials, the work plan for the hole hemming tests and respective specimens and the performance of destructive tests to characterize the joint strength.

The fourth chapter exposes the finite element models made to assist the experimental work and the work plan to study the hole hemming process parameters.

In the fifth chapter, the fracture limits of the materials under different loading conditions are studied in order to accurately design and predict fracture during the simulations of the hole hemming process.

In the sixth chapter, both numerical and experimental hole hemming results are presented, compared and discussed.

In the seventh chapter, the main conclusion that resulted from the dissertation development are presented. Finally, in the eighth chapter some suggestions are proposed for future work, not only to improve the results obtained but also to unlock new boundaries in the applicability of the hole hemming process.

2 Literature review

2.1 Lightweight materials in the automotive industry

Nowadays the automotive industry is under pressure to reduce the carbon emissions of the automobiles as a result of the growing social environmental awareness while facing other challenges such as the improvement of vehicle performance. To accomplish this, the automotive industry is focusing on the design of lightweight vehicles [1] by utilizing advanced materials, which outperform conventional materials with superior properties such as stiffness and strength (figure 1), hardness, elasticity, durability and toughness [9]. In fact, lightweight design confers up to 7% improvement in fuel efficiency for each 10% reduction in vehicle weight when combines with an appropriately sized powertrain. Furthermore, a decrease in the weight also improves vehicle performance attributes such as acceleration, braking and handling [1].

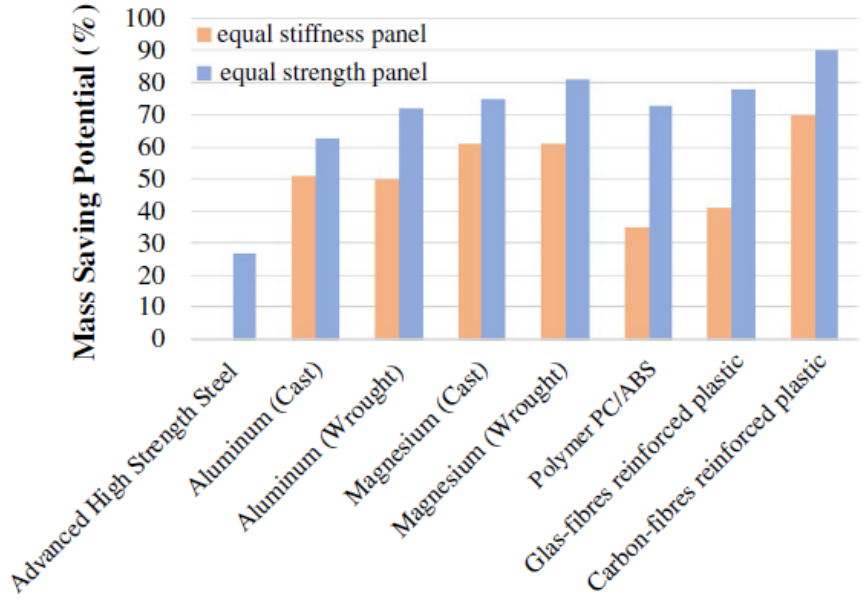

Figure 1 – Comparison of mass savings in automotive applications for advanced materials vs mild steel in structural panels for equivalent bending stiffness and bending strength. Adapted from [5].

2.1.1 Magnesium

With a density of 1.74 $g.cm^{-3}$, magnesium is the lightest of all the structural metals, being 35% lighter than aluminium (2.7 $g.cm^{-3}$) and about four times lighter than steel (7.86 $g.cm^{-3}$). It has better noise and vibration characteristics than aluminium and great formability at high temperatures [10]. Magnesium has a specific strength similar to cast iron and similar or higher than many traditional automotive aluminum alloys and thus it can enhance more mass reduction relatively to aluminium alloys. Moreover, it has a higher specific stiffness than many polymeric materials and composites, leading to an improved mass reduction [11].

Magnesium has been used in a wide variety of automotive applications including body-in-white (figure 2), chassis and interior components, such as instrument panels, steering wheels, engine cradles, seats, transfer cases and many different housings [1].

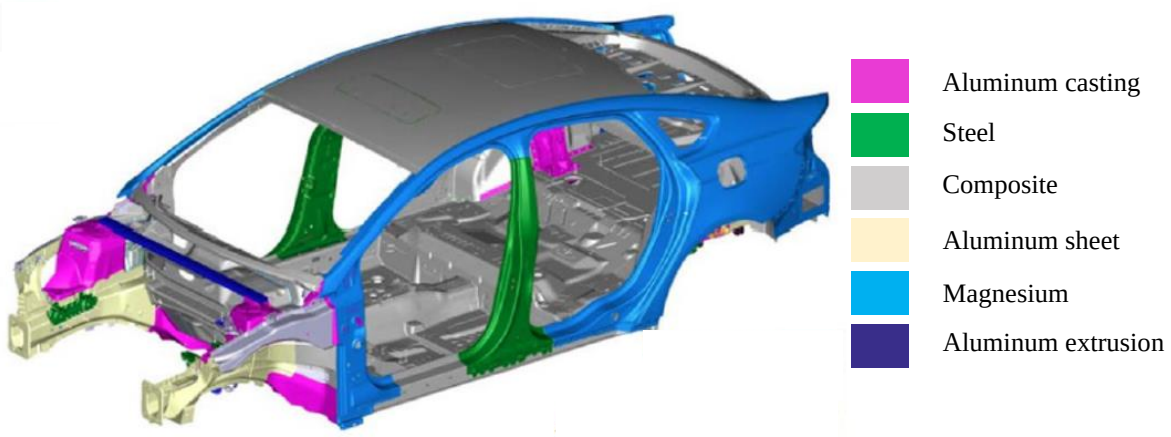

Figure 2 - Mach-II body-in-white design by Ford heavy on magnesium. Adapted from [5].

However, the weight of magnesium alloys constitutes only a small percentage of the total weight of a vehicle due to challenges associated with manufacturing, processing, assembly, in-service performance and cost [1]. In fact, the majority of the manufacturing processes for converting metal sheets into automobile parts occur at room temperature, including stamping, bending, hemming, flanging and trimming. The poor ductility of the magnesium is related to the hexagonal close packed crystal structure (figure 3), which has fewer slip systems compared with other structural metals such as iron and aluminum (which have a cubic crystal structure), making the deformation at room temperature difficult [11, 12] and limiting the application of magnesium alloys in the automotive industry.

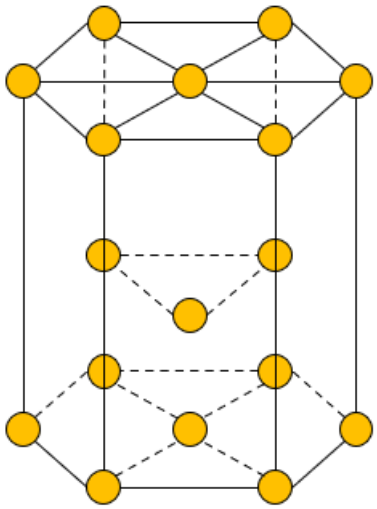

Figure 3 - Hexagonal close packed (HCP) crystal structure.

2.1.2 Aluminum

About 25% of the production of Aluminum alloys is used in the transportation industry due to its attractive properties such as low density, fairly high strength and high ductility, good corrosion resistance and relatively low cost. It is one of the easiest metals to form, recycle and machine. The precipitation hardened alloys can be formed in a specially soft state and then heat treated to substantially increase the strength [13]. Furthermore, the forming, joining and painting of aluminum alloys can be accomplished by similar production paths of conventional steel body construction [14]. These aspects makes the aluminum alloys good candidates in

overthrowing the steel dominance and leading the light weighting efforts in the automotive industry [13, 14].

Nonetheless, aluminum alloys do not display a true endurance limit, which can lead to the failure of parts exposed to fatigue even if under relatively low stresses. Furthermore, the melting point and hardness of aluminum alloys is considerably lower than steel and so it can´t be used in parts exposed to high temperature and wear environments [13].

The aluminum alloys can be classified as casting or wrought alloys. The wrought alloys are shaped by plastic deformation and the most commonly used alloys in sheet metal forming are from the 5xxx series (AA5022, AA5182, AA5052, among others) and the 6xxx series (AA6061, AA6022, AA6016, among others) [15, 16]. The 6xxx series alloys have good formability as well as high strength and excellent surface finish, making them a good choice for internal structural parts and exterior body panels. On the other side, 5xxx series alloys are used in nonvisible automotive inner body panels (in contrast to the 6xxx series it is prone to develop Lüder lines) where deep drawing is required [16].

In the future the development of new heat treatments and alloying have a high potential to achieve higher strength and ductility of the aluminum alloys. Furthermore, the development of new processes such as hot stamping and warm forming can be employed to form higher strength parts of 7xxx series alloys (which have limited room temperature formability). These high temperature processes can be applied to form aluminum alloys in the fully hardened state, dispensing a heat treatment after the forming process, though it is still a challenge to warm forming without altering the mechanical properties due to the exposure to high temperatures [16].

2.2 Joining by forming processes

Nowadays the production of automotive bodies faces several challenges. In fact, on the one hand, there is an urge in the automotive industry to reduce the weight of the automobiles in order to improve both the performance and fuel efficiency for environmental and economic reasons [1]. On the other hand, concerns related to comfort and safety of the passengers is also a priority which leads to an increase in the weight of the automotive structure [2]. To accomplish these requirements, modern car manufactures produce lightweight automotive bodies with dissimilar materials in a design concept known as “multi-material design” [3], which consists in using different lightweight materials such as advanced high-strength steel (AHSS), aluminum alloys, composites and magnesium alloys [4]. However, the accomplishment of the multi-material design depends on the feasibility of the processes used to join such dissimilar materials [3].

Joining by forming processes are based on mechanical deformation of the sheets to produce a mechanical interlock and so the feasibility of the process depends on the ductility of the materials [8]. In this chapter the most common joining by forming processes in the automotive industry are briefly reviewed.

The hemming process is the base for the hole hemming process, which is studied in this project. In the hemming process a sheet edge is bent by 180° or even more. Hemming can be performed either with a single sheet to increase the stiffness, improve appearance and eliminate acute edges or with two sheets to join parts [17].

There are different types of hems depending on the material and purpose, as shown in figure 4. Open, teardrop and flattened hems are employed to improve the appearance and edge finish of a single sheet while the rope, modified rope, radius flat and modified flat hems are used to join two sheet metal parts. The rope hems are commonly used for brittle materials and the modified flat hem has a better shape fixation and fitting behavior comparing with the radius hem [17].

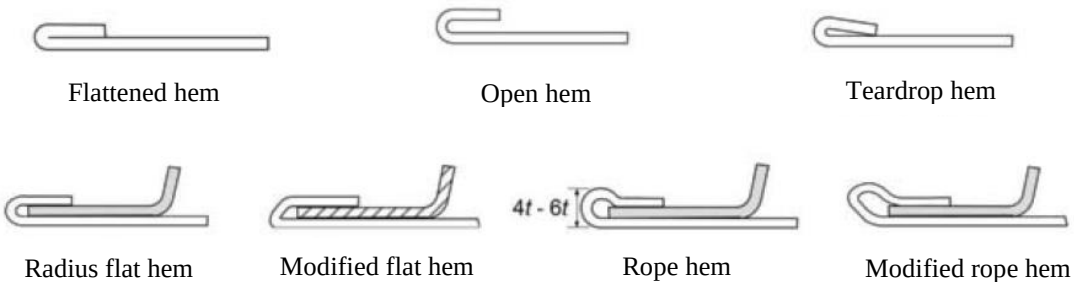

Figure 4 - Most common types of hems. Adapted from [17].

The hemming process can be divided in two main categories, the conventional hemming and the roller hemming process. The conventional hemming process is usually performed in three different stages. In the first stage, the bending or flanging stage, the outer sheet is bent in a 90° degree angle. In the second stage, the pre-hemming stage, the inner sheet is placed over the outer sheet and the outer sheet is further bent to 135° and in the final stage, the hemming stage, the outer sheet is bent up to 180° to form the hem, as shown in figure 5 [18]. It is the most suitable method in the case of mass production [4]. The roll hemming process differs from the conventional hemming process as it utilizes a robot guided roller to bend the sheet [18] and it possesses an higher flexibility for more complex parts [4]. Nevertheless, hemming produces joints with lower strengths than the ones produced by welding and so adhesives can be used along with hemming to increase the strength and tightness of the joint [19].

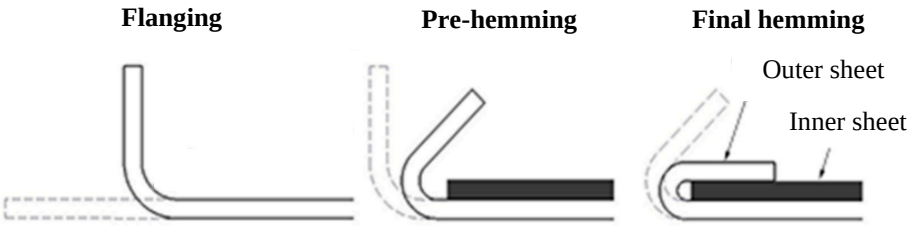

Figure 5 – Schematic representation of the hemming process. Adapted from [20].

The hemming process is mainly applied in the automotive industry to manufacture parts such as doors, hoods, deck-lids, trunk-lids and tailgates. It is used for 6xxx series aluminum alloys and high strength steel alloys as these applications require materials with high strength and good ductility to avoid cracks and fractures during the hemming process [18]. While other joining processes like clinching and self-pierce riveting are only locally spotted, hemming can be used to connect the joining parts along a large area and achieve sealing of the parts [21].

When performing hems, it is common to see three types of defects as it can be seen in figure 6. Creep and grow or roll-in and roll-out are the inward and outward shift of the hem edge, respectively, which leads to a change in the outer panel size. Recoil is the out-of-plane displacement of the outer sheet hem edge when performing the final hemming. Warp is an indentation formed in the outside of the outer sheet after the final hemming [17].

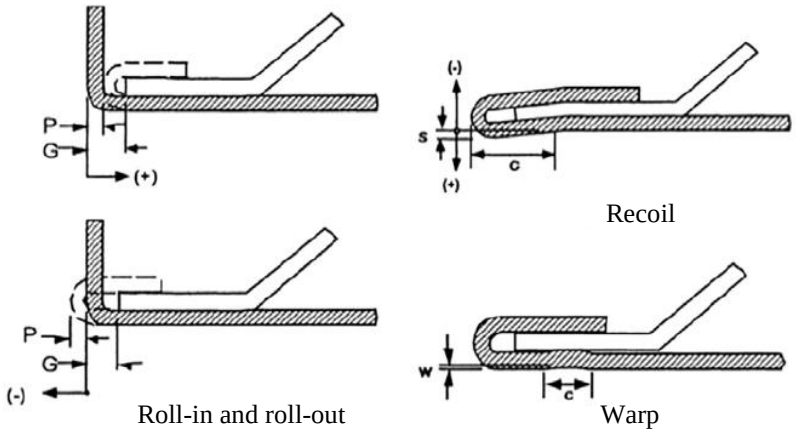

Figure 6 – Defects of the hemming process. Adapted from [18].

Furthermore, like any other sheet metal forming operation the occurrence of fractures or splits and wrinkles are also common in the hemming process, as shown in figure 17 [17].

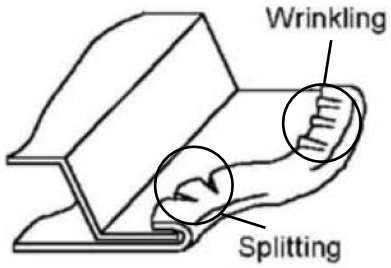

Figure 7 – Wrinkling and splitting defects in the hemming process. Adapted from [17].

Clinching is a relatively cheap and highly productive process where two or more sheets can be joined by forming without addition elements [22]. The conventional clinching process consists in the joining by plastic deformation of two or more sheets by means of a punch, normally with a round or square shape, and a die, which can be fixed or extensible. In this process, as shown in figure 8, the punch forces the sheets into the die in order to form a mechanical interlock between the sheets [23].

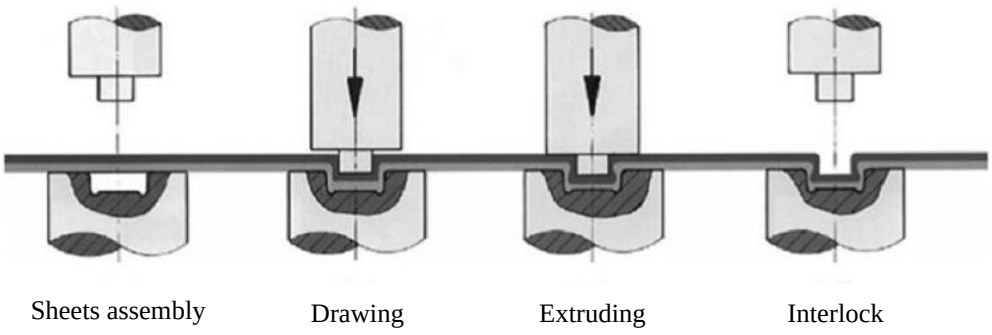

Figure 8 - Conventional clinching process using a fixed die. Adapted from [23].

In table 1, the advantages and disadvantages of the clinching process compared in general with other methods that join thin sheets, such as self-pierce riveting, adhesive bonding and spot welding are listed [24]:

Table 1 - Advantages and disadvantages of the clinching process [24].

Advantages	Disadvantages
It can join a wide variety of sheet materials; Cheap equipment; The process is fast and easy; The joints have good fatigue resistance; Lower carbon dioxide emissions and energy consumption.	It is required high forces; Sheets with high hardness and low ductility are difficult or not suitable to join.

Several variants of the clinching process were developed to overcome some limitations of the conventional clinching process. Hole clinching was developed to join high-strength or low-ductility materials to ductile materials. In this process, a pre-drilled sheet made of a high-strength or low-ductility material is used as the die-sided sheet, while a ductile material is used as the punch-sided sheet and is idented into the die cavity through the hole of the die-sided sheet, to form a mechanical interlock between the sheets. Lee et al. [3] used the hole clinching process to join AA6061-T4, as the ductile material, to DP780, 22MnB5 and CFRP, as the die-sided material.

Busse et al. [25] developed a new clinching process called shear-clinching, illustrated in figure 9, and similar to the hole clinching process to join materials with limited formability. The process uses a punch with two parts, consisting in an inner and an outer punch, in a such way that the die-sided sheet is shear-cut and the punch-sided sheet is extruded through the hole of the inner sheet. Contrary to the hole clinching process, neither the pre-drilled hole nor the positioning operations are necessary [26]. Hörhold et al. [2] joined AA6016-T4 with 22MnB5 by the shear clinching process and hole clinching process and tested the joints strength. While under shear load the shear clinched specimens had a strength almost as high as the hole clinching specimens, about 7% less, in the case of tensile load the shear clinched joints beard had about 19% less load and much lower displacements until break. The applicability of the shear clinching process for the joining of three sheets was studied by Wiesenmayer and Merklein [27]. It was possible to perform a mechanical interlock when using a ductile top layer, AA5182-O, with two high-strength materials as the middle and bottom layer (DP600).

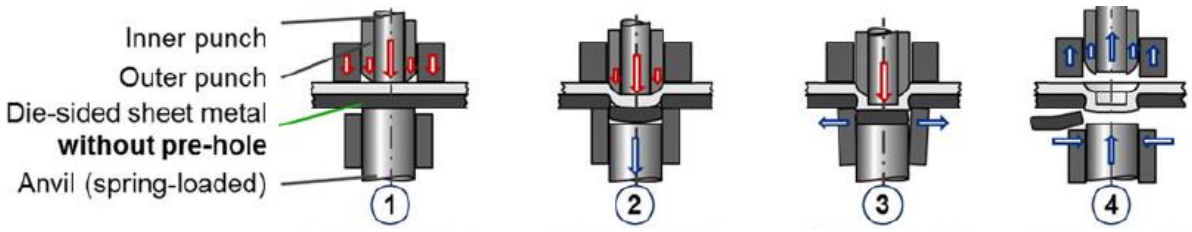

Figure 9 - Schematic illustration of the shear clinching process: 1 - Fixation and preloading, 2 – Drawing and shear-cutting, 3 – Compression and extrusion, 4 – Back stroke and eject. Adapted from [2].

The self-piercing riveting (SPR) process is another joining process where an auxiliary joining element is used. In this process two or more sheets are joined by driving a rivet that pierces the upper sheet and flares within the lower sheet to form a mechanical interlock [28]. In this process a pre-drilled hole it is not required unlike the conventional riveting, decreasing the processing time [29]. Figure 10 shows the four stages of the SPR process.

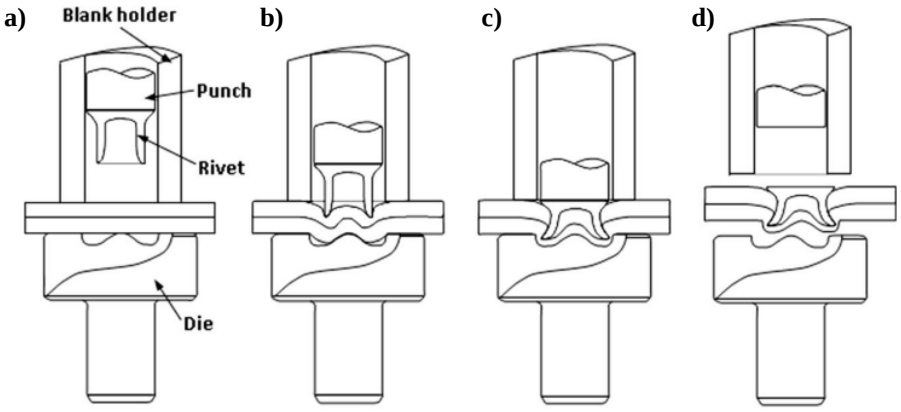

Figure 10 – Self-pierce riveting process illustration. (a) Clamping; (b) Piercing; (c) Flaring; (d) Releasing. Adapted from [28].

The process starts by lowering the blank holder and clamping the sheets on the die. The punch is then lowered to force the rivet into the sheet by either punching or pushing until it starts to flare and form a mechanical interlock. Finally the punch is retracted and the joined sheet are released from the die [28].

In table 2, some advantages and disadvantages between self-pierce riveting and other general joining processes are summarized:

Table 2 - Advantages and disadvantages of the self-pierce riveting process. [28]

Advantages	Disadvantages
Low emissions and noise pollution;	Rivets represent an additional cost;
Can join dissimilar materials;	High forces involved;
Short cycle time;	Not suitable for brittle materials.
Does not require pre-drilled holes;	
High static and fatigue joint strengths.	

The self-pierce riveting process is a very rigid and inflexible process as it has few controllable parameters to adapt to different conditions. The addition of a tumbling punch to the conventional self-pierce riveting process can create possibilities for a versatile joining process [30].

The geometry of the rivet can be varied to adapt the process for different purposes. Kato et al. [31] developed a short thin pipe rivet in a process called double-sided self-pierce riveting (DSSPR), depicted in figure 11. The pipe rivet, with chamfered ends, is placed between the sheets and with a single stroke the rivet pierces and holds the sheets together. Nonetheless, convention DSSPR process has limitation when joining dissimilar materials with very different strengths, as the rivet is less pierced in the sheet with higher strength resulting in an asymmetrical mechanical interlock. Alves et al. [32] studied the joining of AA5754-H111 and

PVC by the DSSPR process using rivets with different chamfered angles in each side and also by a two-stroke approach where the higher strength material is firstly pierced by the rivet and only then the PVC sheet is placed for the second stroke. In another study, Alves et al. [33] studied the feasibility of introducing a flat-bottom hole in the sheet with higher strength in which the rivet, with different chamfered angles, can be inserted. With this method, the positioning and alignment of the rivets was solved and also the joint strength considerably improved when compared with a conventional DSSPR joint.

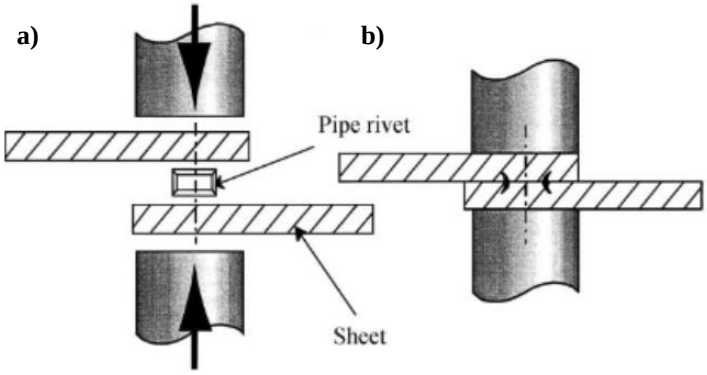

Figure 11 - Schematic illustration of the DSSPR process: (a) before joining and (b) after joining. Adapted from [31].

2.3 Joining magnesium and aluminum alloys

The growing need to join magnesium to aluminum alloys is related to the properties of the base metals. Individually, both metals are utilized extensively in the automotive and aerospace industries due to various advantages, respectively, including light weight, high specific strength and recyclability. Even so, some specific advantages may favor aluminum (such as higher strength or creep resistance) or magnesium (for higher damping capacity), and thus certain applications are in favor of one of the metals over the other. Joining technologies can provide the opportunity to employ the advantages of both metals simultaneously [6].

Welding is the most commonly joining process used on automotive assembly lines due advantages offered by dissimilar welding, such as cost reduction, higher energy efficiency, optimization of materials and the ability to ‘tailor’ the materials design to suit optimal properties in specific areas. Dissimilar welding is used to manufacture tailor-welded blanks which are then stamped for the construction of automotive body structures. However, a major drawback that impacts the progress of Al–Mg dissimilar welding is the formation of Al–Mg based brittle intermetallic compounds (IMCs) which are detrimental to the mechanical properties of the joints [6].

Friction stir welding (FSW) is a solid-state joining technique and the process consists of a non-consumable rotating tool with a specifically designed pin and shoulder passed through the line of joint of the two materials to be joined [34], the process can be visualized in figure 12. FSW is therefore a good candidate to attenuate the deleterious IMC effects through the solid-state welding technique by controlling the thermal history of the process [6].

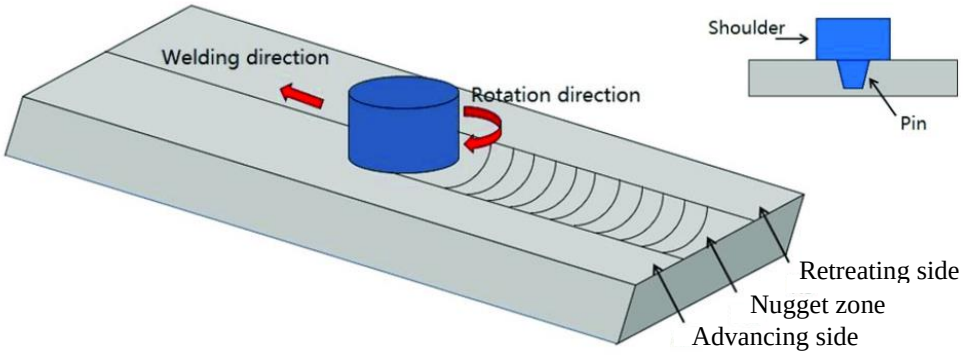

Figure 12 - Friction stir welding schematic illustration. Adapted from [35].

It is possible to utilize a wide variety of aluminium and magnesium alloys, although the great majority of the aluminium alloys used are from the 5000 and 6000 series and the AZ31 in the case of the magnesium. This is due to their adequate properties to be used in the industrial sectors such as the automotive industry. [6]

Park et al. [36] in 2002 successfully joined AA1050 and AZ31 with 6 mm thickness by FSW without defects near the weld center. Zettler et al [37] joined AA6040 and AZ31 with 2 mm thickness and achieved a joint strength of 80% of the lower strength base material as Al_2Mg_2 and $Al_{12}Mg_{17}$ IMCs were formed only in localized regions and not in the entire stir zone. Kwon et al. [38] and Shigematsu et al. [39] joined A5052P-O and AZ31B-O using different tool rotation speeds and tool transverse speeds, achieving joints strengths of 66% and 72%, respectively. In order to reduce the heat input and to control the formation of IMCs, Underwater Friction Stir Welding (UFSW) has a good potential for joining magnesium and aluminum alloys, as the welding is performed either in a water container or while water flows across the surface of the sample, controlling the heat input in the weld zone [40]. Zhao et al. [41] used UFSW to join AA6013 and AZ31 with 2.5 mm thickness, obtaining a joint strength of 152.3 MPa and a thin IMC layer. There has been however little research works on UFSW and it still requires further investigation [40].

In recent years a significant amount of research has been done in the area of hybrid mechanical and solid-state joining processes. Wang and Stevenson [42] proposed a friction stir blind riveting method (FSBR), where the sheets are joined by means of a rotating friction stir rivet that is driven in the sheets via a mandrel causing the materials to soften, then the mandrel withdraws and the rivet expands to form the joint, as shown in figure 13. White et al. [43] used FSBR to successfully join AA5005-H34 and AZ31B-O with 2 mm thickness and verified that the stacking order affected profoundly the joint, as the insertion force was dependent on the alloy in the top of the stack and the behavior under tensile shear loading was determined by the alloy at the bottom of the stack. Min et al. [44] studied the effect of the spindle speed and feed rate in the joining of AM60 (3.05 mm) with AA6022 (1.5 mm) and AA6082 (3.15 mm). A good FSBR joint was only obtained when the AM60 sheet was placed on top, and high spindle speeds and lower feed rates were also necessary to generate enough friction heat to improve the plasticity of the AM60 sheet. Although the FSBR process has a high potential over the conventional blind riveting process to accomplish a crack-free joining of magnesium alloys, the process automation and required equipment are more complex than the conventional process [8].

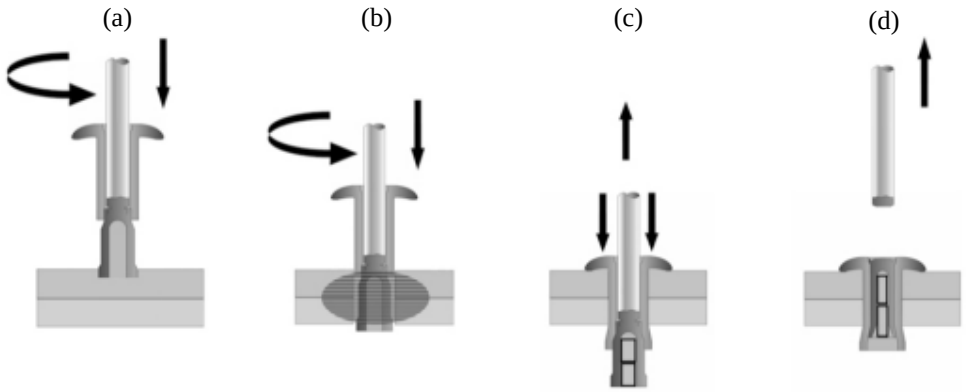

Figure 13 – Schematic illustration of the Friction Stir Blind Riveting (FSBR) process: (a) Plunging, (b) Stirring, (c) Upsetting and (d) Joint. Adapted from [43].

There are also multiple works on hybrid self-piercing riveting with a scope of not only reducing the riveting force but also to improve the plasticity of brittle materials such is the case of magnesium alloys. Hahn et al. [45] added a vibration mechanism to a conventional self-pierce riveting machine which heated the sheets with its vibration, reducing the riveting insertion force. Sun et al. [46] proposed a self-piercing riveting process assisted by ultrasonic energy to locally improve the ductility of the sheets. Drossel et al. [47] replaced the conventional SPR die by a new movable die concept which could control the damage in the lower sheet by superimposing the forming zone with compressive stresses. A dieless riveting process was proposed by Neugebauer et al. [48] where a pre-heated flat anvil is used as a counter tool instead of a contoured die (figure 14). A crack-free joint were performed between AZ31 (as the lower sheet) and AlMg3 (as the upper sheet) sheets with 0.8 and 1.45 mm thickness, respectively. Nevertheless, the feasibility of these hybrid-self pierce riveting processes relies on a heat assist source to improve the ductility of the magnesium alloys and in the controllability of the temperature of the sheets [8].

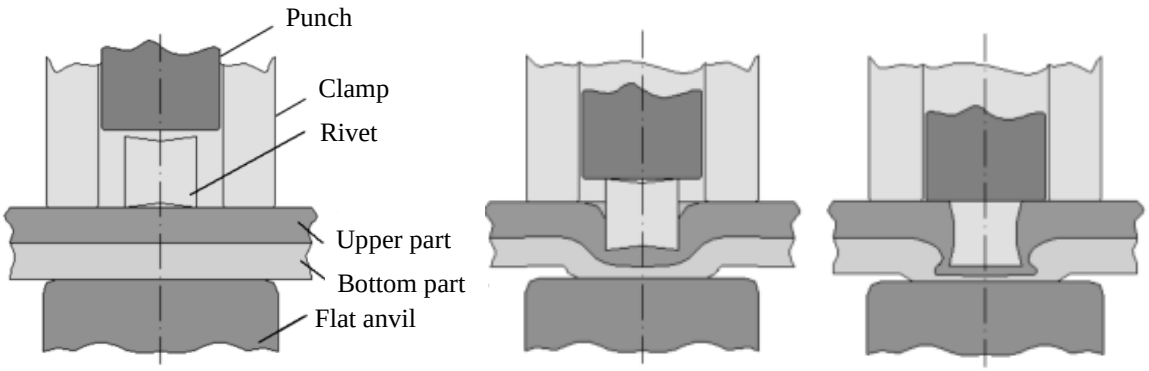

Figure 14 – Schematic illustration of dieless rivet clinching. Adapted from [48].

2.4 Ductile fracture

Materials can be described as ductile or brittle depending on the quantity of macroscale plastic deformation that precedes their fracture. While fracture in brittle materials occurs due to the rapid propagation of elastic stresses and it is not visible by permanent distortion, and so it cannot be visually anticipated, on the other side the fracture of ductile materials is preceded by visible plastic deformation [49]. In metal forming processes the ductility of the materials is a key aspect that allows them to be deformed to the desired form without fracture [49]. As damage and fracture impacts the quality of the final part, it is of great importance to know the mechanisms of damage evolution and ductile fracture in order to precisely predict failure in process design phase [50].

2.4.1 Damage evolution

In deformation-based processes the ductile fracture of the materials is mainly caused by voids, which can appear in the material after plastic deformation or can be already present before plastic deformation occurs due to the previous processing of the material [51]. In a process called Microvoid Coalescence (MVC) where the voids nucleate (formation of voids), grow and coalesce, fracture occur in the majority of metallic alloys [49].

The main mechanisms for the nucleation of the voids is at the interfaces of inclusion and/or second-phases particles caused by plastic deformation [49]. The debonding of these interfaces is considered the main factor for the initiation of the voids. Aluminum alloys contains a large volume fraction of intermetallic brittle phases dispersed in its matrix, such as iron based and magnesium-silicon intermetallic with distinct properties, leading to void nucleation when submitted to plastic deformation [50]. On the other side the inclusions have little strength in the interface bond with the matrix and also have distinctive mechanical properties. The debonding of these interfaces occurs in the directions of the major strain in the matrix [49] (figure 15).

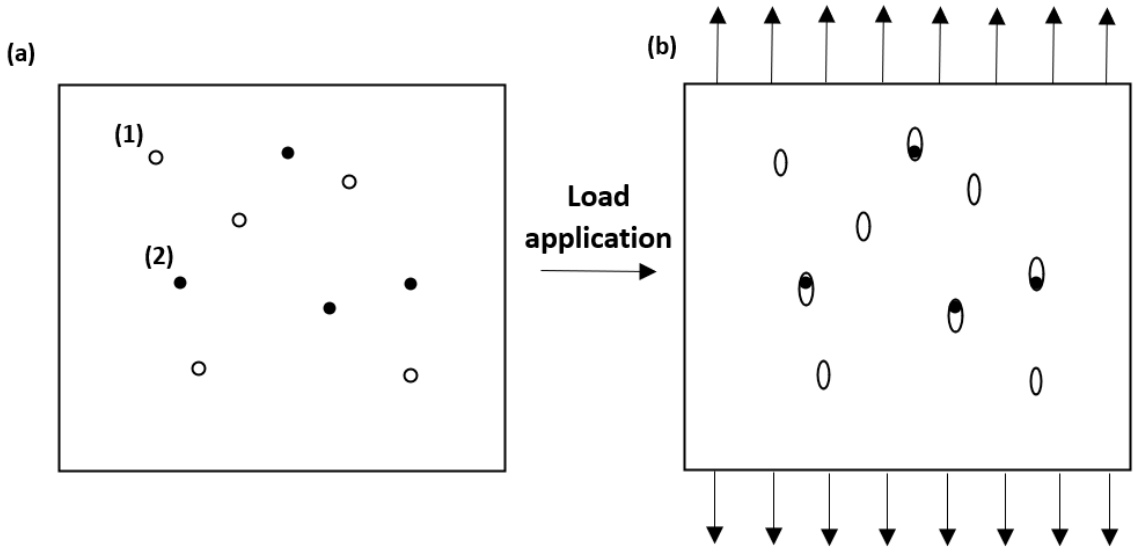

Figure 15 – Void nucleation. (a) Initial material; (b) Nucleation of the voids after application of a tensile load. (1) Initial porosity and (2) Inclusions.

As the voids are nucleated, the increase of the plastic deformation leads to the enlargement of the size of the voids in a phenomenon usually called void growth. The continuous growth of the voids leads to the link up (or coalescence) of adjacent voids (figure 16) because of the plastic strain in the intervoid matrix, leading to the final fracture surface [50].

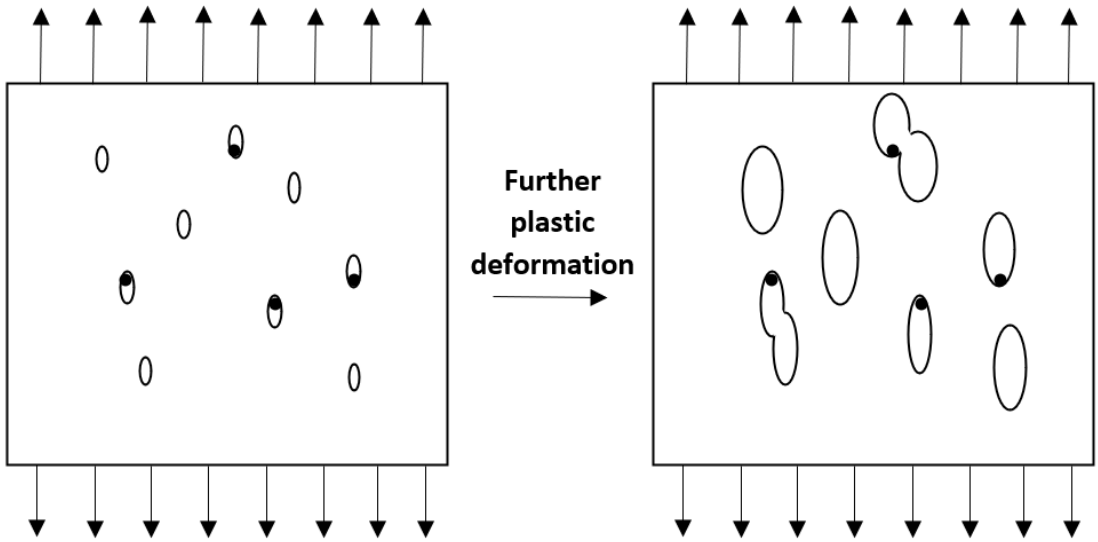

Figure 16 – Void growth and coalescence due to the further increase of the plastic deformation.

2.4.2 Ductile fracture modeling and prediction

In order to predict ductile damage evolution and the onset of fracture in metal forming processes, ductile fracture criterial (DFC) have been continually developed and improved [50]. The DFC can be classified as follows [51]:

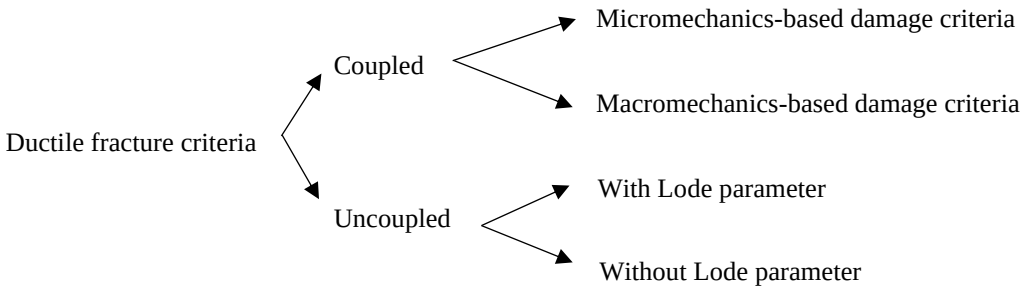

The difference between the coupled and uncoupled DFC is that the coupled considers the effect of the damage accumulation on the material yield surface. Despite the uncoupled DFC have limitations in the prediction of fracture in comparison with the coupled DFC, they are more widely used because they are simple to calibrate and to formulate. The damage accumulation is formulated with the general function in equation 2.1 [50].

$$\int_0^{\bar{\varepsilon}_f} f(\sigma, \bar{\varepsilon}^p)\, d\bar{\varepsilon}^p \geq C \tag{2.1}$$

In equation 2.1 the $\bar{\varepsilon}_f$ is the equivalent plastic strain to fracture, the σ is the stress tensor, the $\bar{\varepsilon}^p$ is the equivalent plastic strain and the C is the fracture threshold of the material. In the case of uncoupled DFC without considering the Lode parameter, they have a simple form and are more commonly used for specific processes with specific deformation paths [50]. On the other side, the uncoupled DFC that consider the Lode parameter have a better accuracy in the prediction of ductile fracture, as different stress states can not be distinguished solely by the stress triaxiality (η) [51]. Nonetheless, Their fracture locus is a 3D surface instead of a 2D and more tests should be performed to calibrate the parameters of the DFC [50].

2.4.3 Modified Mohr Coulomb fracture criterion

The Mohr-Coulomb fracture criterion has been widely used in rock and soil mechanics as it correctly takes into account the effect of hydrostatic pressure and the Lode angle parameter [52]. Bai et al. [52] Extended the Mohr-Coulomb criterion to the spherical coordinate system in a tridimensional space of equivalent plastic strain, normalized Lode angle parameter and stress triaxiality to describe ductile fracture of isotropic solids. This fracture criterion is called the Modified Mohr-Coulomb model (MMC) that can be seen as follows in equation 2.2.

$$\bar{\varepsilon}_p^f = \left\{ \frac{K}{C_2} \left[C_3 + \frac{\sqrt{3}}{2-\sqrt{3}} (1 - C_3) \left((\sec \frac{\bar{\theta}\pi}{6} - 1) \right) \right] \times \left[\sqrt{\frac{1+C_1^2}{3}} \cos \frac{\bar{\theta}\pi}{6} + C_1 \left(\eta + \frac{1}{3} \sin \frac{\bar{\theta}\pi}{6} \right) \right] \right\}^{-\frac{1}{n}} \quad (2.2)$$

The fracture envelope is affected by K and n which are the strength coefficient and the work hardening exponent, respectively, obtained by uniaxial tensile tests and utilizing an adequate strain hardening law. Furthermore, this criterion should be calibrated by performing at least three formability tests to obtain the material coefficients C_1, C_2 and C_3. [53].

In this phenomenological criterion, the damage evolution is described in terms of macroscopic variables in the form of equivalent plastic strain and stress state. The damage increment is defined by the increment of equivalent plastic strain utilizing an weighting function [53], which can be represented as follows in equation 2.3:

$$D = \int_0^{\bar{\varepsilon}_p} \frac{d\bar{\varepsilon}_p}{\bar{\varepsilon}_p^f(\eta, \bar{\theta})} \quad (2.3)$$

Where an increment of the equivalent plastic strain ($d\bar{\varepsilon}_p$) is divided by the equivalent plastic strain to fracture for the respective stress state ($\bar{\varepsilon}_p^f(\eta, \bar{\theta})$), contributing to the damage accumulation in the material in which fracture is predicted when the damage indicator (D) reaches unity.

The fracture envelope can be plotted as a surface in a 3D space of equivalent plastic strain ($\bar{\varepsilon}_p$), normalized Lode angle parameter ($\bar{\theta}$) and stress triaxiality (η). However, in sheet metal forming processes, plane stress condition can often be assumed and, in that condition, the stress triaxiality and the normalized Lode angle parameter are not independent parameters and can be uniquely correlated as seen in equation 2.4 and figure 17 [53].

$$\bar{\theta} = 1 - \frac{2}{\pi}\cos^{-1}\left[-\frac{27}{2}\eta\left(\eta^2 - \frac{1}{3}\right)\right] \tag{2.4}$$

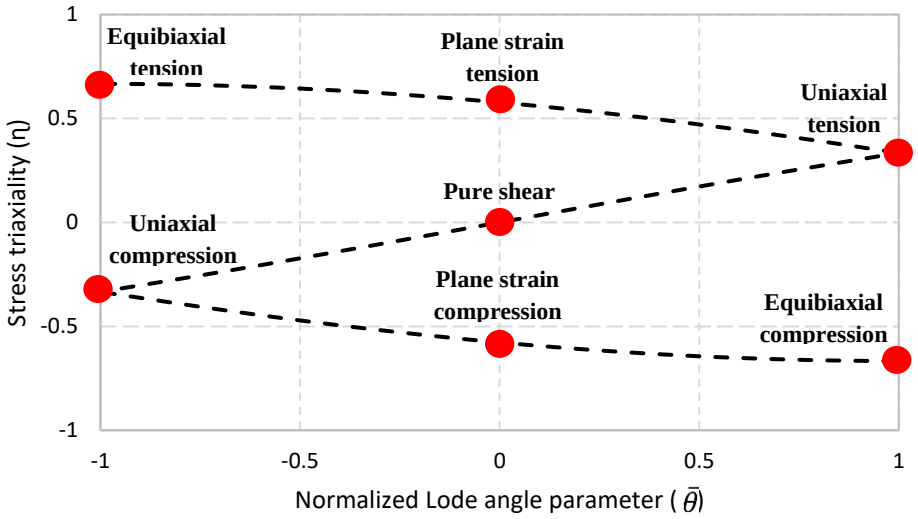

Figure 17 - The correlation between the stress triaxiality and the normalized Lode angle parameter under plane stress condition.

Therefore, by removing the normalized Lode angle parameter from equation 2.2 using the correlation in equation 2.4, the fracture envelope can now be plotted in a curve in a 2D space of equivalent plastic strain and stress triaxiality.

Under the assumption of proportional loading, the forming limit of materials can be expressed in the space of in-plane principal strains ($\varepsilon_1, \varepsilon_2$) which is called the fracture forming limit diagram (FFLD) [53].

Assuming plane stress condition and planar anisotropy:

$$\eta = \frac{1}{3}\frac{1+\beta}{\sqrt{1-\beta+\beta^2}} \tag{2.5}$$

$$\beta = \frac{\sigma_2}{\sigma_1} \tag{2.6}$$

$$\beta = \frac{\alpha\left(1+\frac{1}{r_0}\right)+1}{1+\frac{1}{r_{90}}+\alpha} \tag{2.7}$$

Where β is the ratio between the minor and major in-plane stresses, α is the ratio between minor and major in-plane strains and r_0 and r_{90} the Lankford coefficients along the rolling direction and perpendicular to the rolling direction, respectively.

According to Hill´s 1948 yield criterion, the equivalent plastic strain can be corelated with the strain ratio and the major in-plane strain and expressed as follows in equation 2.8 [53]:

$$\bar{\varepsilon}^p = \varepsilon_1\sqrt{\frac{(1+r_0)r_{90}}{1+r_0+r_{90}}\left(\frac{1+r_{90}}{r_{90}} + \frac{1+r_0}{r_0}\alpha^2 + 2\alpha\right)} \tag{2.8}$$

Finally, the major and minor in-plane strains ($\varepsilon_1, \varepsilon_2$) can be correlated by equation 2.9:

$$\varepsilon_2 = \alpha\varepsilon_1 \tag{2.9}$$

Xiao et al. [54] used the modified Mohr-Coulomb (MMC) model and the modified Johnson-Cook (J-C) model to study the flow and fracture of a ZK60 alloy for different loading states and strain rates. Results showed that the MMC model tracked the fracture behavior more accurately than the J-C model, with a maximum relative error of 10% for elemental fracture strain and 7.2% for elongation. Xiao et al. [55] investigated the accuracy of the MMC model and J-C model on the prediction of ballistic resistance of AA2024-T351 plates. The FE simulations using the MMC fracture criterion predicted the experimentally obtained ballistic limit with an error lower than 3%, while the J-C fracture criterion overpredicted it by 28.5%. Talebi-Ghadikolaee et al. [56] analyzed the fracture behavior of AA6061-T6 sheets during the U-bending and using the MMC ductile fracture criterion, obtaining an overall error of the predicted fracture displacement of about 2%. The MMC fracture criterion is able to predict with relatively good accuracy the fracture strain of different materials in a wide range of stress states, as it can be calibrated by several formability tests with different loading conditions and it takes into account the effect of the normalized Lode angle parameter. Due to these and the relative ease to calibrate, in this work the MMC fracture criterion will be used to design the hole hemming process.

2.5 Hole hemming process

The hole hemming process was newly developed by Kasaei MM and da Silva LF [4] with the objective of joining dissimilar material sheets with very different mechanical properties. A finite element analysis was made to study the feasibility of the process for joinning a dual phase steel, DP780, and an aluminum alloy, AA6061-T6. In the end the results showed that the hole hemming process has a high potential for joining dissimilar materials. The process is inspired in the conventional hemming process and a schematic illustration of the process can be seen in figure 18.

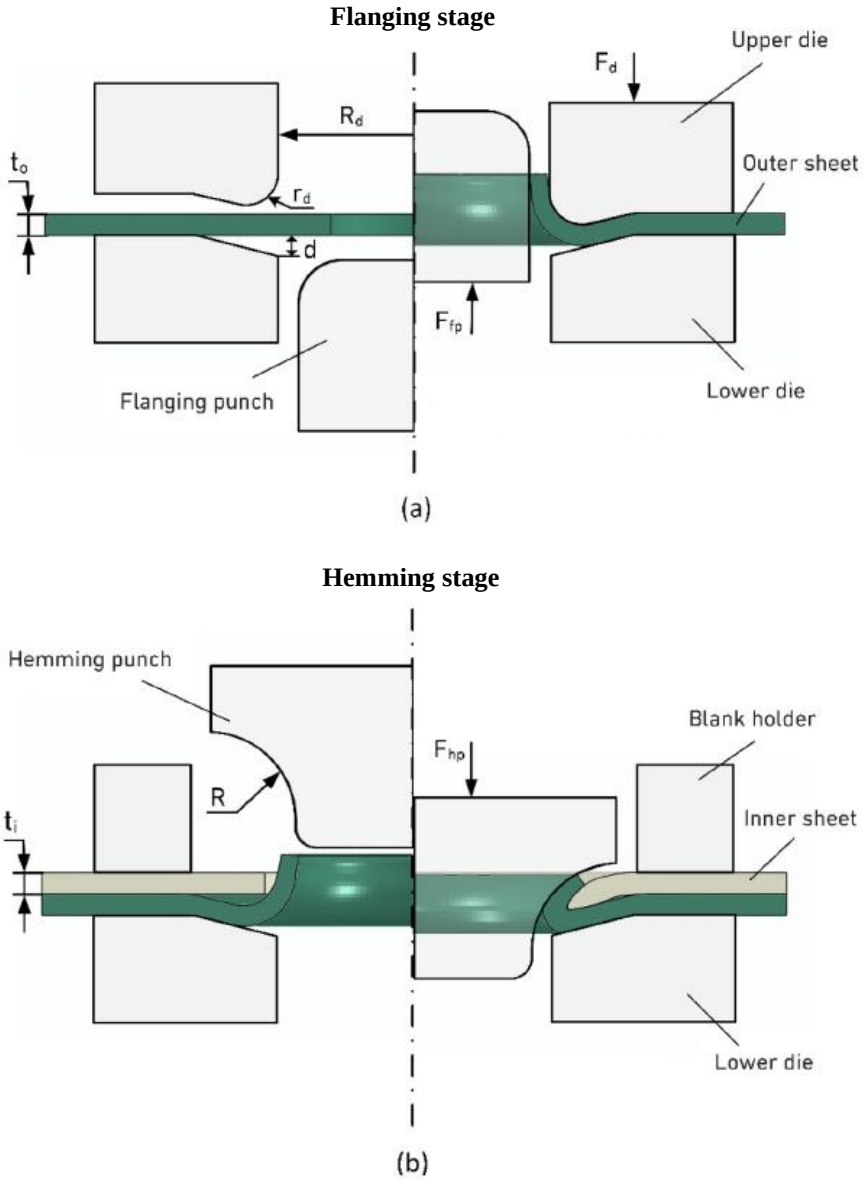

Figure 18 - Schematic ilustration of the Hole Hemming process: (a) Flanging stage and (b) Hemming stage.

The main difference between the hole hemming process and the conventional hemming process is the location of the mechanical interlock. In fact, in the hemming process the sheets are joined along their edges while in the hole hemming process the joint is performed through concentric pre-drilled holes which can be made anywhere in the sheets. This represents a significant advantage over the hemming process which has limited applications due to the restriction of the joint location in the sheet edges.

The hole hemming process is performed in two different stages, the flanging stage and the hemming stage. In the flanging stage, figure 18 (a), a flange is formed in the hole of the outer sheet by means of a punch, the flanging punch, and two dies, the lower and upper die. In a first phase of the stage, the outer sheet is correctly aligned and placed in the top of the lower die and then the upper die moves down to fix the outer sheet. After this, the flanging punch advances to bend the edge of the outer sheet in a 90° angle and form the flange. As it can be seen in figure, the dies create an indentation near the flange, which allows the hole edge of the inner sheet to be placed at the closest possible position to the flange during the hemming stage.

In the hemming stage, figure 18 (b), the inner sheet is placed and aligned on the top of the outer sheet and the upper die is replaced by a blank holder which fixes the sheets in the correct place. After this, the hemming punch advances and causes the flange to overlap the hole edge of the inner sheet, producing a tight mechanical interlock with low deformation in the inner sheet. Because of this, this process has a high potential of joining magnesium with aluminum alloys as long as the magnesium alloy is used as the inner sheet and the aluminum alloy is sufficiently ductile to be used as the outer sheet.

2.6 Design of the process

Like any other process, the hole hemming process has its own process parameters that affect the feasibility and quality of the joint. Figure 19 shows a schematic illustration of the hole hemming process with the respective process parameters.

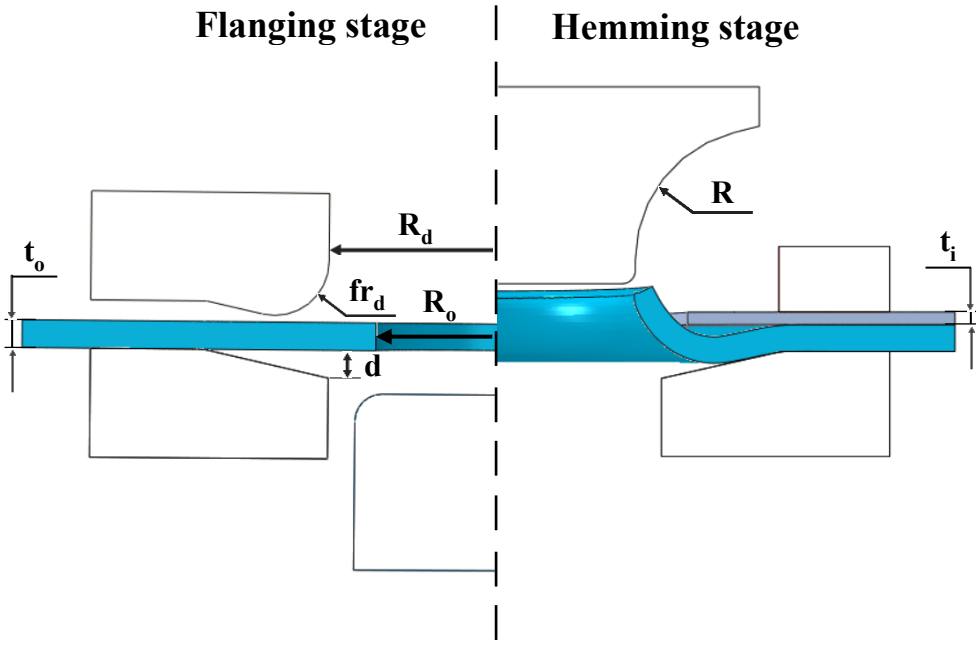

Figure 19 - Schematic illustration of the Hole Hemming process and process parameters.

In the first stage, the flanging stage, the hole radius of the outer sheet (R_o) and the radius of the dies (R_d) determine the length of the hole flange (F) through equation 2.10. The filet radius of the upper die (fr_d) determines the bend radius in the outer sheet and so its deformation, this value should be carefully chosen considering the formability and thickness of the sheet. The indentation depth (d) allows the hole edge of the inner sheet to be placed near the flange of the outer sheet and its value should be similar to the thickness of the outer sheet in order to not occur pultrusion in the top surface. The fillet radius of the hemming punch (R) controls the evolution of the deformation in the outer sheet during the hemming stage.

$$F = R_d - R_o \tag{2.10}$$

3 Experiments

The work was carried out in commercial aluminum alloy AA6082-T4 [57] and laboratory made ECO-magnesium alloy AZ31 [58]. ECO-AZ31 is made by a new processing technology in which Ca is added to molten Mg alloy. Although the aluminum exhibits a constant thickness of 2.05 mm, there is a significant variation in the thickness of the magnesium sheets perpendicular to the extrusion direction, having a smaller thickness in the middle and higher thickness in the edges.

In order to perform the finite element analysis of the hole hemming process, it is first necessary to characterize the materials. In this chapter, the plastic behavior and anisotropy of the aluminum and magnesium alloys will be studied by performing uniaxial tension tests in three directions (0°, 45° and 90° to the rolling direction, in case of the aluminum alloy, and to the extrusion direction, in case of the magnesium alloy). Moreover, formability tests will be performed to calibrate the ductile fracture criterion and obtain the fracture envelopes of the materials.

3.1 Material characterization

To obtain the mechanical properties, anisotropy and hardening behavior of the aluminum and magnesium alloy sheets, uniaxial tension tests were carried out in three different directions. Three specimens were tested for each direction. In figure 20 it is possible to see the dimensions of the uniaxial tension specimens.

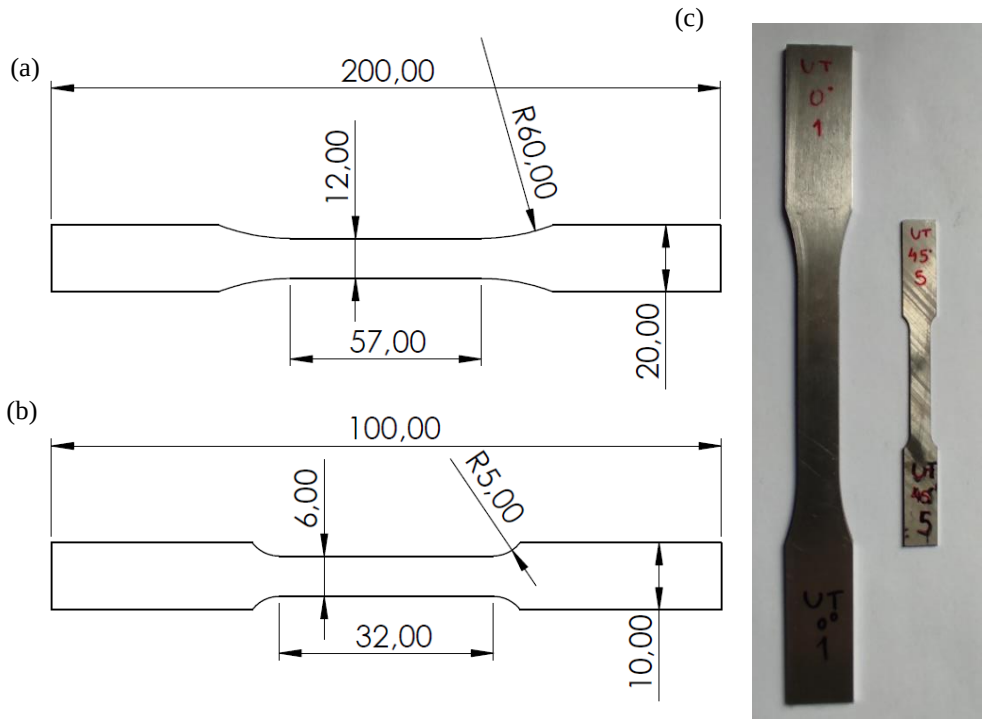

Figure 20 - Dimensions of the uniaxial tension specimens for (a) AA6082-T4 and (b) AZ31. (c) AA6082-T4 and AZ31 uniaxial tension specimens. Dimensions in mm.

The uniaxial tension tests were performed on a INSTRON 3367 machine (with a maximum capacity of 30 kN), as shown in figure 21, with a constant test speed of 3mm/min. To measure the displacement of the gauge section and the major and minor strains in function of the time, a camera (Canon EOS M5 equipped with a Canon EF-M 18-55 mm F/3.5-5.6 lens) was used to record the deformation of specimens during the test with a frame rate of 25 fps.

The resulting videos were analyzed by the Digital image correlation (DIC) software GOM correlate.

Figure 21 – AZ31 specimen during the uniaxial tension test in the INSTROM 3367 machine equipped with a digital camera for measuring strain and displacement.

In order to have an accurate capture of data by the DIC software, it is first necessary to create a stochastic speckle pattern on a surface of the specimens. This was done by uniformly spraying the specimens with white paint, then spraying it with black paint to make a stochastic pattern in the top of the white paint layer, as shown in figure 22.

Figure 22 – AZ31 uniaxial tension specimens painted with a stochastic pattern.

The thickness and the width of the specimens were measured by means of a micrometer with 0.01 mm resolution and a caliper with 0.05 mm resolution, respectively. The measured values are listed in table 3 and 4. As it can be seen, the thickness of the AA6082-T4 sheets are uniform, while in the case of the AZ31 sheets there is a significant thickness variation between different specimens.

Table 3 - Dimensions of the thickness and width in the AA6082-T4 uniaxial tension specimens. t - average thickness (mm) measured in three different points; w – average width (mm); A – cross section area (mm^2).

	0°			**45°**			**90°**		
	t	**w**	**A**	**t**	**w**	**A**	**t**	**w**	**A**
N1	2.04	12.1	24.68	2.05	12.1	24.81	2.05	12.1	24.81
N2	2.04	12.1	24.68	2.05	12.1	24.81	2.05	12.1	24.81
N3	2.04	12.1	24.68	2.05	12.1	24.81	2.05	12.1	24.81
N4	2.04	12.1	24.68	2.05	12.1	24.81	2.05	12.1	24.81

Table 4 – Dimensions of the thickness and width in the AZ31 uniaxial tension specimens. t - average thickness (mm) measured in three different points; w – average width (mm); A – cross section area (mm^2).

	0°			**45°**			**90°**		
	t	**w**	**A**	**t**	**w**	**A**	**t**	**w**	**A**
N1	1.20	6.2	7.461	0.79	6.15	4.845	0.82	6.40	5.28
N2	0.80	6.2	4.974	0.79	6.15	4.879	0.84	6.40	5.35
N3	0.80	6.2	4.939	0.82	6.15	5.043	0.82	6.25	5.10

For a good correlation between the data obtained from the machine and the data of the DIC software, the recording of the video was started at the same time as the test was started. After the occurrence of fracture, figure 23, the test and the video recording were stopped.

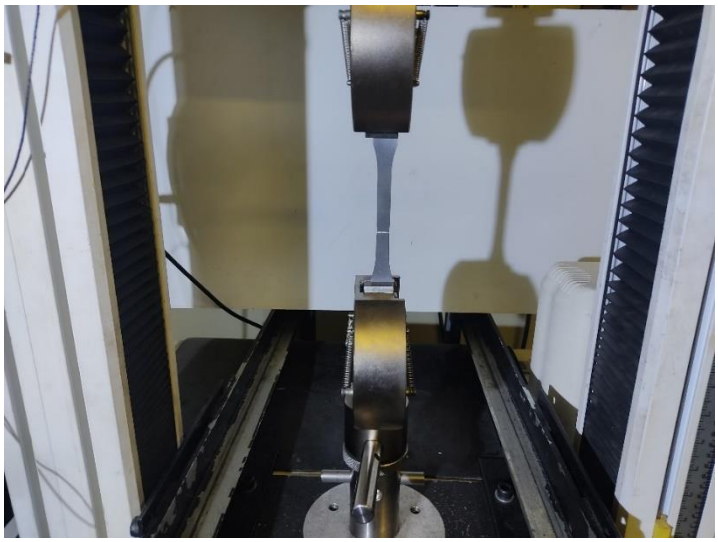

Figure 23 - A fractured AA6082-T4 uniaxial tension specimen after being tested.

In the DIC software each video was scaled using the width of the corresponding specimen, then the displacement of the gauge section and the major and minor strains at a point of the fracture zone were extracted according to figure 24.

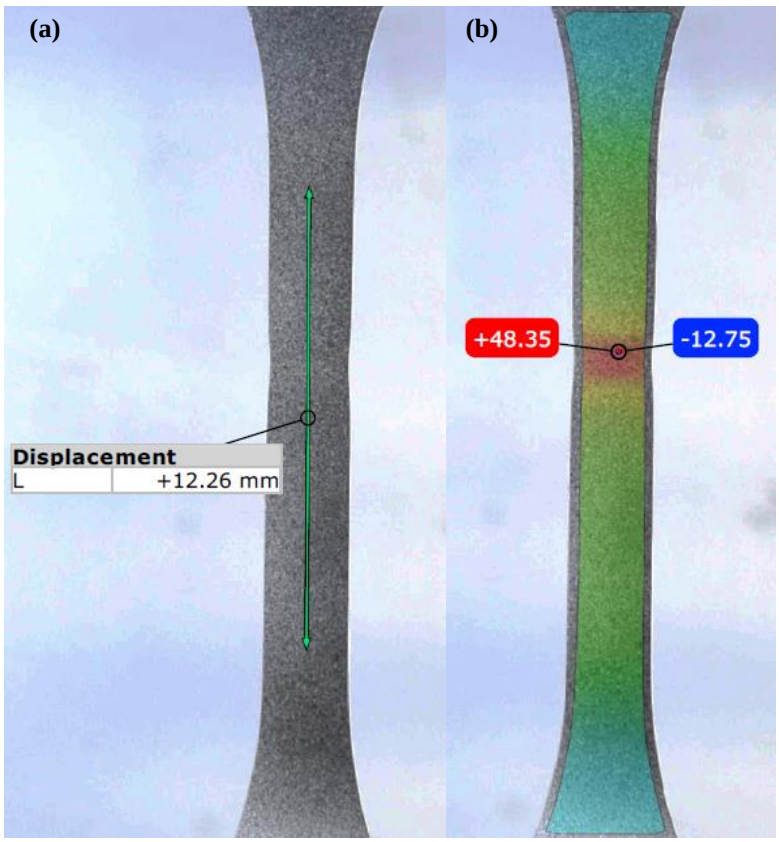

Figure 24 – Method of obtaining data in the GOM correlate DIC software: (a) displacement of the gauge section and (b) major and minor strains at a point of the fracture zone.

3.1.1 Mechanical properties

Figure 25 and 26 show the load-displacement curves obtained from the uniaxial tension tests of the AA6082-T4 and AZ31 specimens, respectively. It should be noted that the displacement was extracted from the machine.

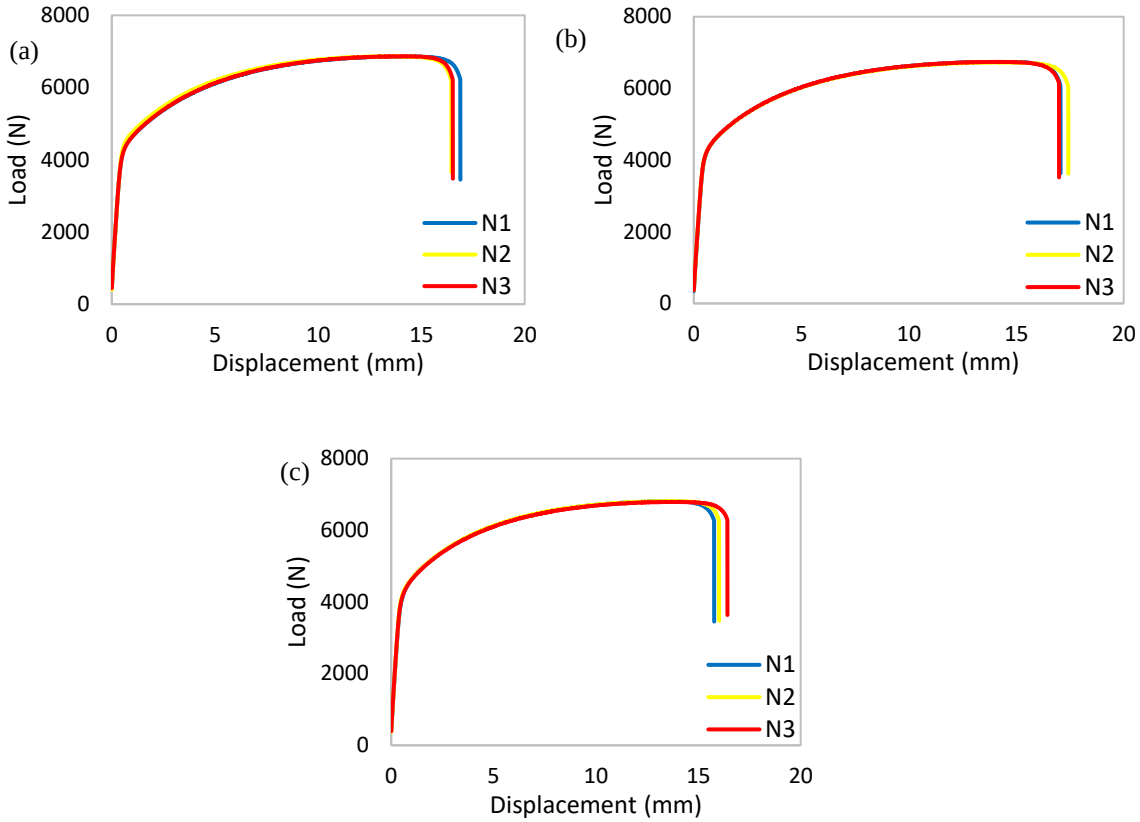

Figure 25 – Load-displacement curves for the AA6082-T4 uniaxial tension specimens in the (a) 0° (b) 45° and (c) 90° directions.

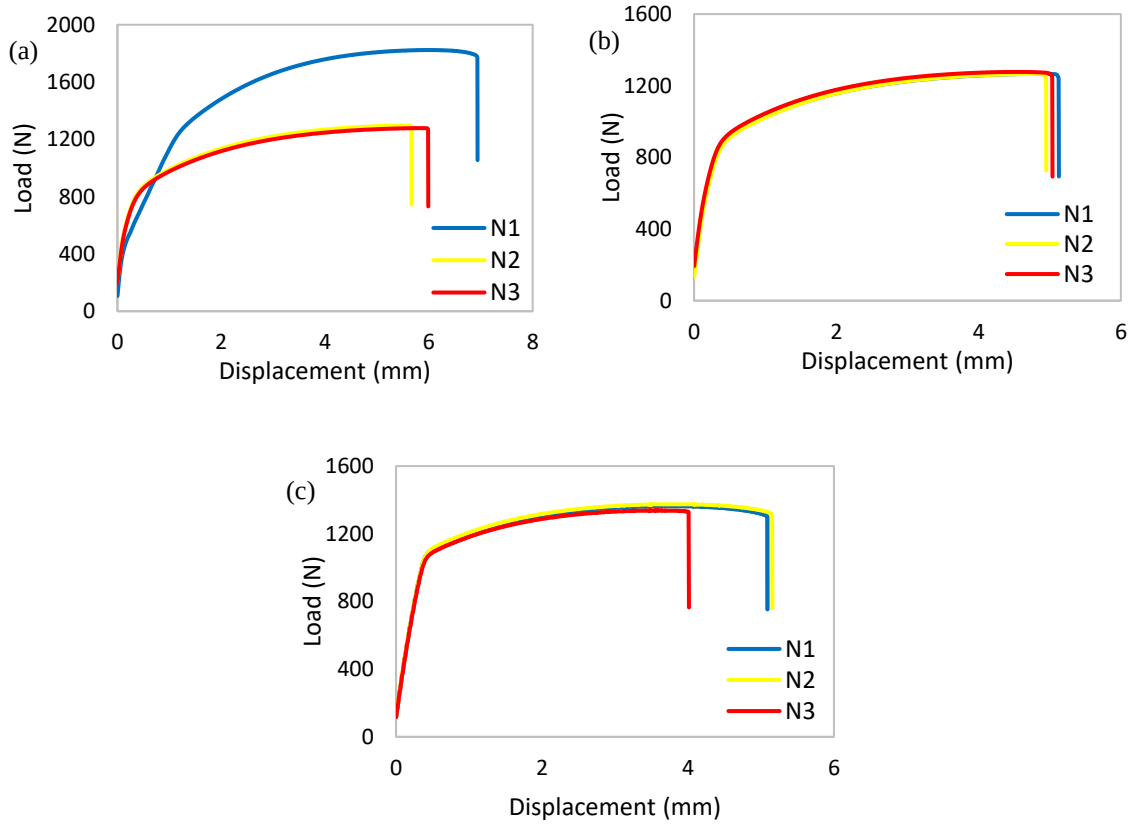

Figure 26 – Load-displacement curves for the AZ31 uniaxial tension specimens in the (a) 0° (b) 45° and (c) 90° directions.

Figure 25 shows that there is a good correlation between the load-displacement curves for different AA6082-T4 specimens.

In figure 26 (a), the significant difference observed in the load for the N1 specimen compared with N2 and N3 specimens is due to its much higher thickness, about 50% higher. Furthermore, in figure 26 (c), the fracture displacement in the N3 specimen is less than that in the other two specimens, because fracture occurred outside the gauge section. For this reason its results were not considered.

By correlating the displacement of the gauge length obtained from the GOM software and the load obtained from the machine, the engineering stress-strain curves were plotted which can be seen in figures 27 and 28. The average values for yield stress, ultimate tensile stress and elongation are summarized in table 5 and 6.

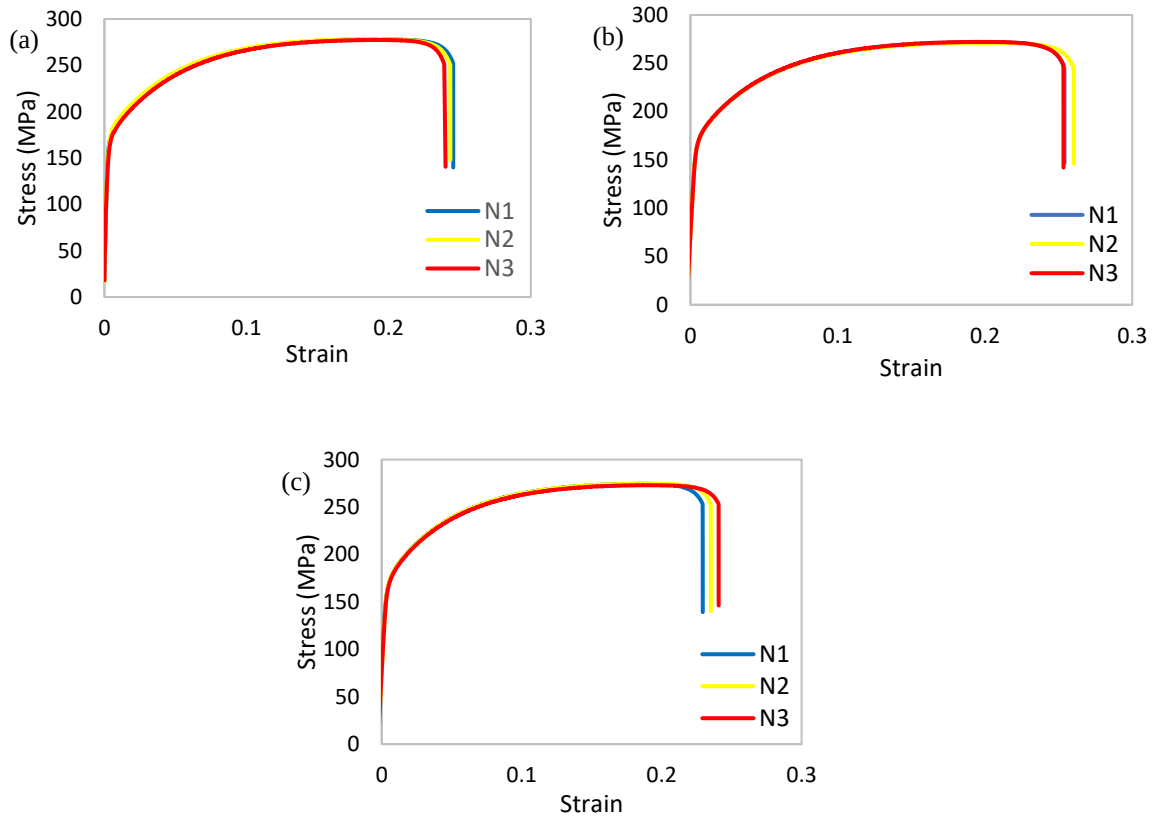

Figure 27 – Stress-strain curves for the AA6082-T4 uniaxial tension specimens in the (a) 0° (b) 45° and (c) 90° directions.

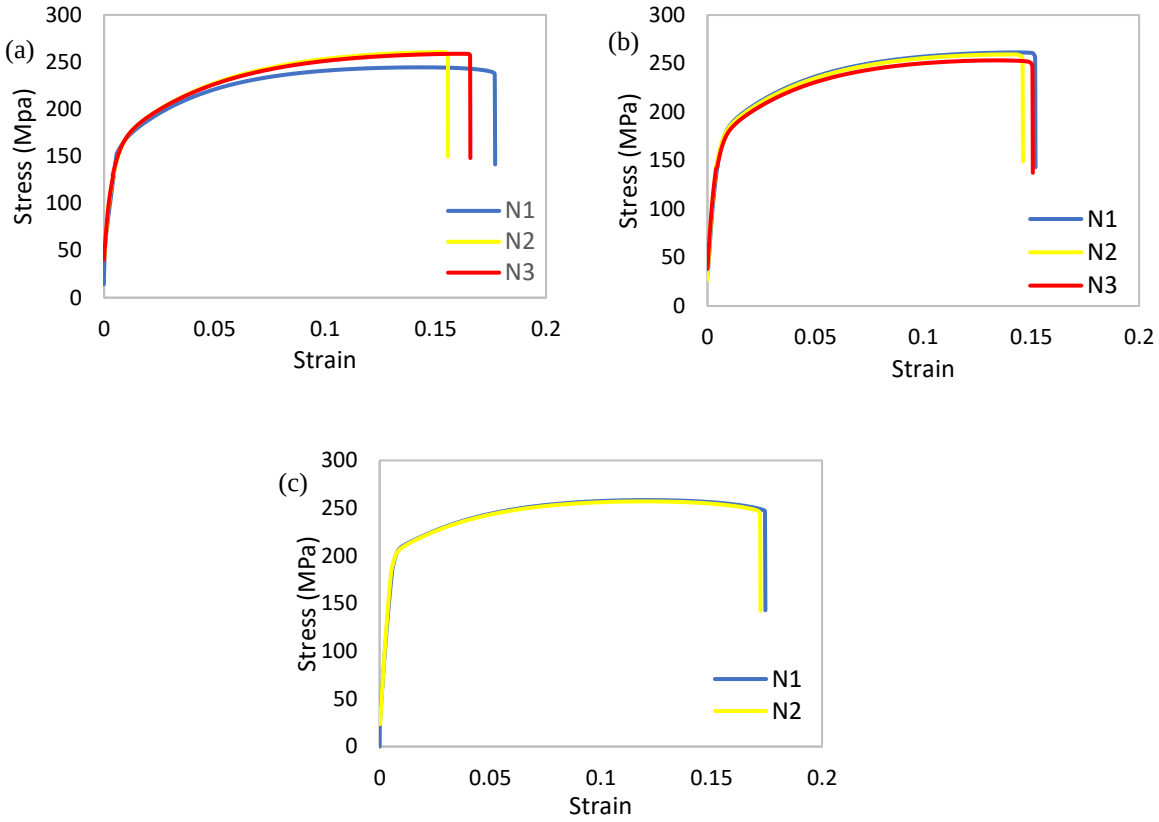

Figure 28 – Stress-strain curves for the AZ31 uniaxial tension specimens in the (a) 0° (b) 45° and (c) 90° directions.

Table 5 - Mechanical properties of the AA6082-T4.

	Average Yield Stress (MPa)	Average Ultimate Tensile Stress (MPa)	Average Elongation (%)
AA6082-T4 (0° Direction)	172	278	24.3
AA6082-T4 (45° Direction)	163	271	25.6
AA6082-T4 (90° Direction)	164	274	23.5

Table 6 - Mechanical properties of the AZ31.

	Average Yield Stress (MPa)	Average Ultimate Tensile Stress (MPa)	Average Elongation (%)
AZ31 (0° Direction)	142	260	16.1
AZ31 (45° Direction)	159	258	15.0
AZ31 (90° Direction)	193	257	17.3

Comparing the mechanical properties of the AA6082-T4 and the AZ31 reveals that the difference between their strengths is not as significant while the elongation of the AA6082-T4 is about 50% higher than the elongation of the AZ31. In addition, there is a significant difference between the yield stress in different directions for the AZ31, highlighting a strong anisotropic behavior of this material which will be further investigated in the next chapter.

3.1.2 Anisotropy

Sheet metals usually exhibit the anisotropy of mechanical properties depending on the loading direction. This anisotropic behavior is due to the characteristics of the manufacturing process and the materials crystallographic structure [59].

The anisotropy of the materials can be defined through the Lankford coefficients which are defined by equation 3.1:

$$r = \frac{\varepsilon_{22}}{\varepsilon_{33}} = \frac{ln\frac{w}{w_0}}{ln\frac{t}{t_0}} \tag{3.1}$$

where ε_{22} and ε_{33} are the strains in the width and thickness directions, respectively, w and w_0 are the initial and final width and t and t_0 are the initial and final thickness. Using the law of volume constancy, the strain through thickness (ε_{33}) can be obtained using the in-plane principal strains (ε_{11} and ε_{22}) as follows is equation 3.2:

$$\varepsilon_{33} = -(\varepsilon_{11} + \varepsilon_{22}) \tag{3.2}$$

In this work, the Lankford coefficients were calculated using the major and minor strains extracted from the GOM software between 10 to 15% elongation for the AA6082-T4 specimens and 5 to 10% elongation for the AZ31 specimens. The resulting Lankford coefficients are presented in table 7 and 8. r_0, r_{45} and r_{90} are the Lankford coefficients at 0, 45 and 90 degrees to the rolling or extrusion direction.

The anisotropy can be also analyzed by the normal anisotropy ($\bar{r}$) coefficient, which represents the average of the Lankford coefficients (equation 3.3), and by the planar anisotropy (Δr) coefficient, which measures the variation of the normal anisotropy (equation 3.4).

$$\bar{r} = \frac{r_0 + 2r_{45} + r_{90}}{4} \tag{3.3}$$

$$\Delta r = \frac{r_0 + r_{90} - 2r_{45}}{2} \tag{3.4}$$

Table 7 – Lankford coefficients and normal and planar anisotropy parameters of the AA6082-T4.

	r_0	r_{45}	r_{90}
N1	0.51	0.55	0.63
N2	0.51	0.54	0.63
N3	0.59	0.57	0.72
Average	0.54	0.55	0.66
Normal anisotropy, $\bar{r}$		**Planar anisotropy, Δr**	
0.58		0.047	

Table 8 - Lankford coefficients and normal and planar anisotropy parameters of the AZ31.

	r_0	r_{45}	r_{90}
N1	0.74	1.17	1.78
N2	0.62	1.29	1.75
N3	0.70	1.27	-
Average	0.68	1.24	1.77
Normal anisotropy, $\bar{r}$		**Planar anisotropy, Δr**	
1.24		-0.017	

Although both materials display little planar anisotropy, they are highly anisotropic, especially the AZ31 that is associated to its hexagonal close-packed (HCP) crystal structure. The anisotropic behavior of the AZ31 was also noticed during the uniaxial tension tests, so that fracture occurred before the onset of necking in the 0° direction, while necking happened in the 90° direction. In addition, the difference of the yield stress in the different directions (seen in table 6) is evidence for this highly anisotropic behavior.

3.1.3 Yield criterion

The Hill 1948 anisotropic Yield Criterion was used for both the materials, which is expressed according to equation 3.5:

$$\bar{\sigma}^2 = F(\sigma_{22} - \sigma_{33})^2 + G(\sigma_{33} - \sigma_{11})^2 + H(\sigma_{11} - \sigma_{22})^2 + 2L\sigma_{23}^2 + 2M\sigma_{31}^2 + 2\sigma_{12}^2 \quad (3.5)$$

where $\bar{\sigma}$ is the equivalent stress and F, G, H, L, M and N are the material constants. When plane stress condition is considered, only F, G, H and N are necessary to be determined as $\sigma_{31} = \sigma_{33} = \sigma_{31} = 0$. The material constants are determined with the anisotropic yield stress ratios R_{11}, R_{22}, R_{33} and R_{12} by the following equations 3.6 to 3.9:

$$F = \frac{1}{2}\left(\frac{1}{R_{22}^2} + \frac{1}{R_{33}^2} - \frac{1}{R_{11}^2}\right) \quad (3.6)$$

$$G = \frac{1}{2}\left(\frac{1}{R_{33}^2} + \frac{1}{R_{11}^2} - \frac{1}{R_{22}^2}\right) \quad (3.7)$$

$$H = \frac{1}{2}\left(\frac{1}{R_{11}^2} + \frac{1}{R_{22}^2} - \frac{1}{R_{33}^2}\right) \quad (3.8)$$

$$N = \frac{3}{2R_{12}^2} \quad (3.9)$$

The anisotropic yield stress ratios are defined by equations 3.10 to 3.13:

$$R_{11} = \frac{\sigma_{11}^y}{\sigma_0} \quad (3.10)$$

$$R_{22} = \frac{\sigma_{22}^y}{\sigma_0} \quad (3.11)$$

$$R_{33} = \frac{\sigma_{33}^y}{\sigma_0} \quad (3.12)$$

$$R_{12} = \sqrt{3}\frac{\sigma_{12}^y}{\sigma_0} \quad (3.13)$$

where σ_0 is an arbitrary reference yield stress and σ_{ij}^y is the yield stress value. If it is considered $\sigma_0 = \sigma_{11}^y$, then the anisotropic yield stress ratios can be expressed by equations 3.14 to 3.17:

$$R_{11} = 1 \quad (3.14)$$

$$R_{22} = \sqrt{\frac{r_{90}(r_0+1)}{r_0(r_{90}+1)}} \quad (3.15)$$

$$R_{33} = \sqrt{\frac{r_{90}(r_0+1)}{r_0+r_{90}}} \quad (3.16)$$

$$R_{12} = \sqrt{\frac{3r_{90}(r_0+1)}{(2r_{45}+1)(r_0+r_{90})}} \quad (3.17)$$

The Hill 1948 Yield criterion does not predict correctly the yield stress when $\frac{r_0}{r_{90}} < 1$ and $\frac{\sigma_0}{\sigma_{90}} > 1$ or vice-versa [60] which is the case of the AA6082-T4. Because of this and as the aluminum exhibits considerably normal anisotropy, the anisotropic yield stress ratios of the aluminum were calculated considering normal anisotropy. The values of the anisotropic yield stress ratios are listed in table 9. These values were used to calculate the material constants, shown in table 10, and consequently draw the yield locus of the materials, as shown in figure 29.

Table 9 - Hill 1948 anisotropic yield stress ratios.

Material	R_{11}	R_{22}	R_{33}	R_{12}	R_{13}	R_{23}
AA6082-T4	1	1	0.89	1.05	1	1
AZ31	1	1.25	1.10	1.02	1	1

Table 10 - Hill 1948 material constants.

Material	F	G	H	N
AA6082-T4	0.63	0.63	0.37	1.36
AZ31	0.23	0.59	0.41	1.44

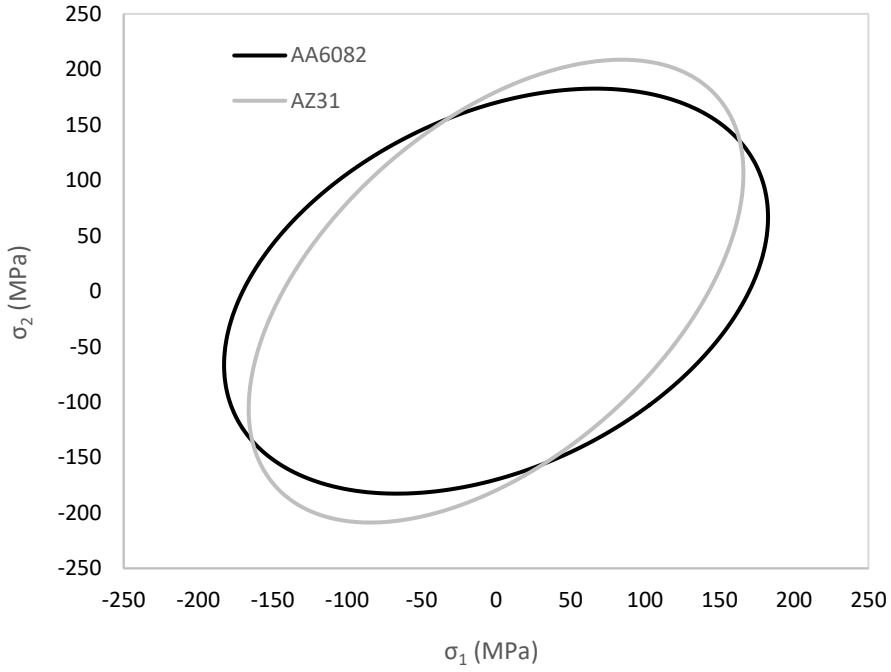

Figure 29 – Yield locus defined by the Hill 1948 criterion.

3.1.4 Hardening law

In an initial phase, the hardening behavior of the materials was described by means of the Hollomon hardening law, which is defined as follows in equation 3.18:

$$\sigma = K(\varepsilon)^n \tag{3.18}$$

The σ and ε are the true stress and true strain, respectively. K and n are the strength coefficient and the hardening exponent, respectively, which are necessary to be determined. To this end, the engineering stress-strain curve in 0° direction was converted to the true stress-true strain by means of the following equations 3.19 and 3.20:

$$\varepsilon = \ln(1 + \varepsilon_e) \tag{3.19}$$

$$\sigma = \sigma_e(1 + \varepsilon_e) \tag{3.20}$$

where ε_e and σ_e are the engineering strain and stress, respectively. The true stress-true strain curves are then plotted. These curves were approximated by the Hollomon hardening law, which resulting parameters can be seen in table 11.

Table 11 - Coefficients of the Hollomon hardening law for both materials.

Material	K	n
AA6082-T4	476	0.207
AZ31	455	0.214

To validate the hardening law, the finite element simulation of the uniaxial tension test was performed in Abaqus. The comparison between the experimental and numerical load-displacement results are shown in the figure 30.

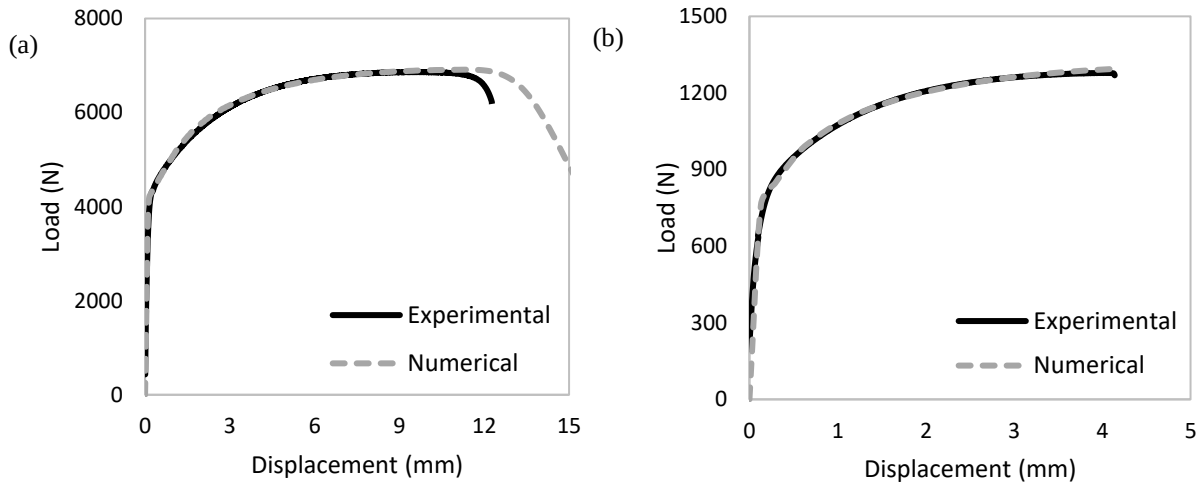

Figure 30 - Comparison of the experimental and numerical load-displacement curves using the Hollomon hardening law: (a) AA6082-T4 and (b) AZ31.

Despite there is a good correlation between the experimental and numerical curves, in the case of the AA6082-T4 the onset of necking is not accurately predicted by the model, which would constitute a problem in the calibration of the ductile fracture criterion and in the prediction of the fracture during the simulations of the hole hemming process. This is not a problem in the case of the AZ31, because fracture occurs before the onset of necking and the numerical results have a good correlation with the experimental results. As a result of this, a new hardening law was opted to use for the AA6082-T4.

In the new approach, a combination of the Swift and Voce hardening law was used that can be expressed as it follows in equation 3.21:

$$\sigma = \alpha\left[K\left(\varepsilon_0 + \varepsilon_p\right)^n\right] + (1-\alpha)[A + B(1 - e^{-c\varepsilon_p})] \tag{3.21}$$

where K and n are the strength coefficient and the hardening exponent of the Swift law, A, B and c are the parameters of the Voce law, ε_0 is the pre-strain and α is the weighting factor. The parameters of the Swift and Voce hardening laws were determined by fitting them to the true stress-true plastic strain curves. Then, the weighting factor was obtained through a reverse approach by performing the finite element simulations of the uniaxial tension test until there was a good correlation between the experimental and numerical results, similar to what is shown in figure 31. The fitting parameters are summarized in table 12.

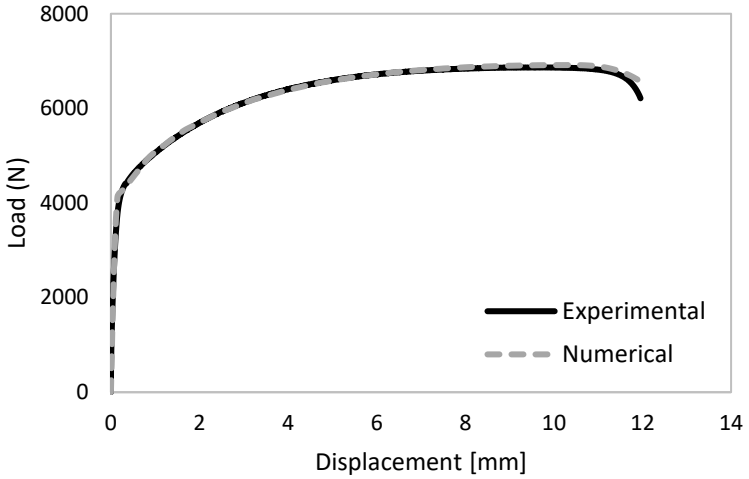

Figure 31 - Comparison of the experimental and numerical load/displacements curves using the combination of the Swift and Voce hardening law for the AA6082-T4

Table 12 – Parameters of the combination of the Swift and Voce Hardening law for the AA6082-T4.

α	K	ε_0	n	A	B	c
0.64	501.2	0.0077	0.2328	174.4	172.9	13.13

3.2 Formability tests

To calibrate the fracture criterion, three different formability tests including the shear tension, plane strain tension and notched tension tests were carried out, besides the uniaxial tension tests. These tests were chosen to cover different loading modes. The experimental specimens and the respective dimensions are shown in figure 32 and 33, respectively. The specimens were cut from the supplied sheets along the rolling or extrusion direction by a CNC milling machine.

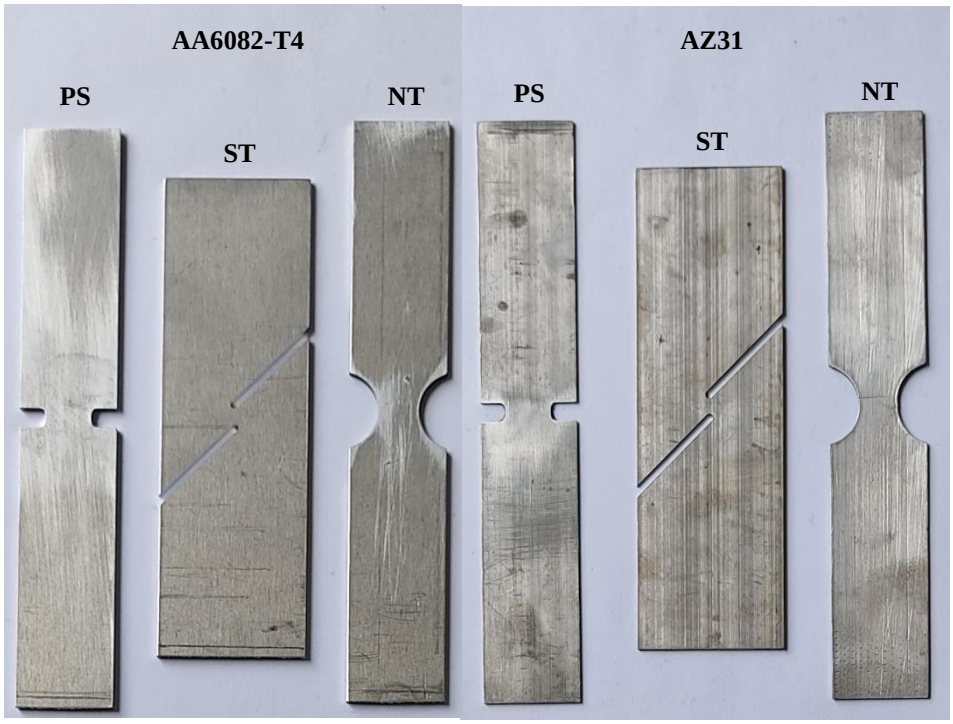

Figure 32 - Experimental formability test specimens: PS - Plane Strain tension specimen, ST - Shear Tension specimen and NT - Notched Tension specimen.

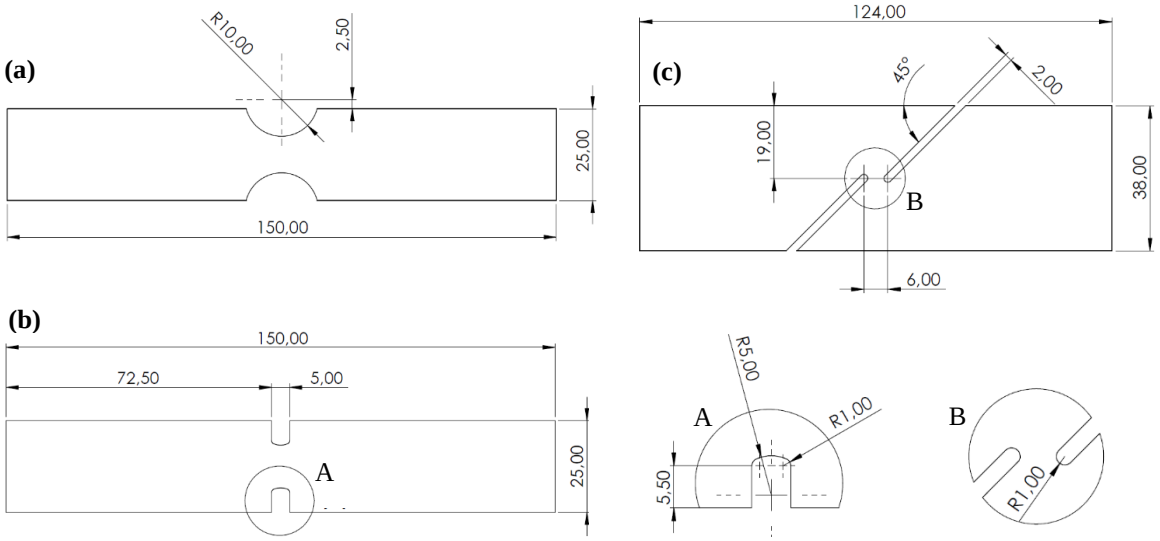

Figure 33 - Dimensions of the formability test specimens: (a) Notched Tension specimen, (b) Plane Strain tension specimen and (c) Shear Tension specimen. Dimensions in mm.

The formability test specimens were tested in the INSTRON 3367 with a constant test speed of 1 mm/min. Similar to the uniaxial tension specimens, the specimens were painted with a stochastic pattern, figure 34, to obtain the displacement and major and minor strains by the DIC software GOM Correlate.

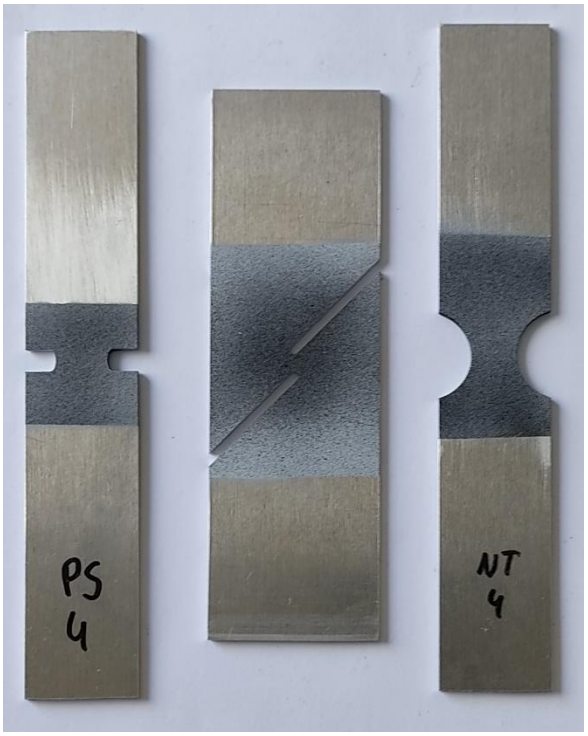

Figure 34 - AA6082-T4 calibration test specimens painted with a stochastic pattern.

For each calibration test, three different specimens were tested that the measured thickness of each one can be seen in table 13. The load/displacement curves of each test can be seen in figures 35 to 36. Similar to the uniaxial tension specimens, for the AA6082-T4 there is a good correlation of the load/displacement curves between different specimens, while the load/displacement curves of the AZ31 specimens present significant differences between different specimens due to the thickness variation.

Table 13 - Thickness of the calibration tests for both materials. Dimensions in mm.

	NT		**PS**		**ST**	
	AA6082-T4	**AZ31**	**AA6082-T4**	**AZ31**	**AA6082-T4**	**AZ31**
N1	2.05	0.99	2.05	0.80	0.84	2.05
N2	2.05	0.80	2.05	0.83	0.85	2.05
N3	2.05	0.84	2.08	1.01	0.80	2.05

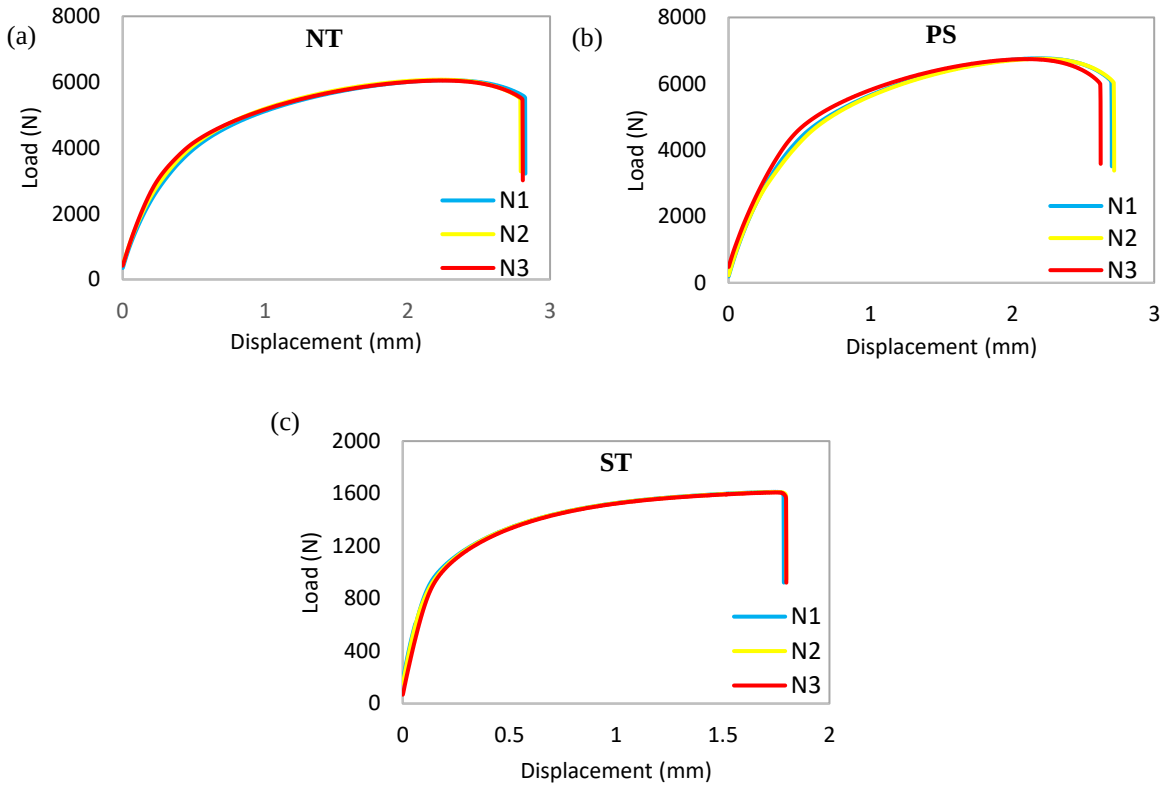

Figure 35 - Load/displacement curves of the AA6082-T4 calibration tests: (a) Notched Tension specimens, (b) Plane Strain tension specimens and (c) Shear Tension specimens.

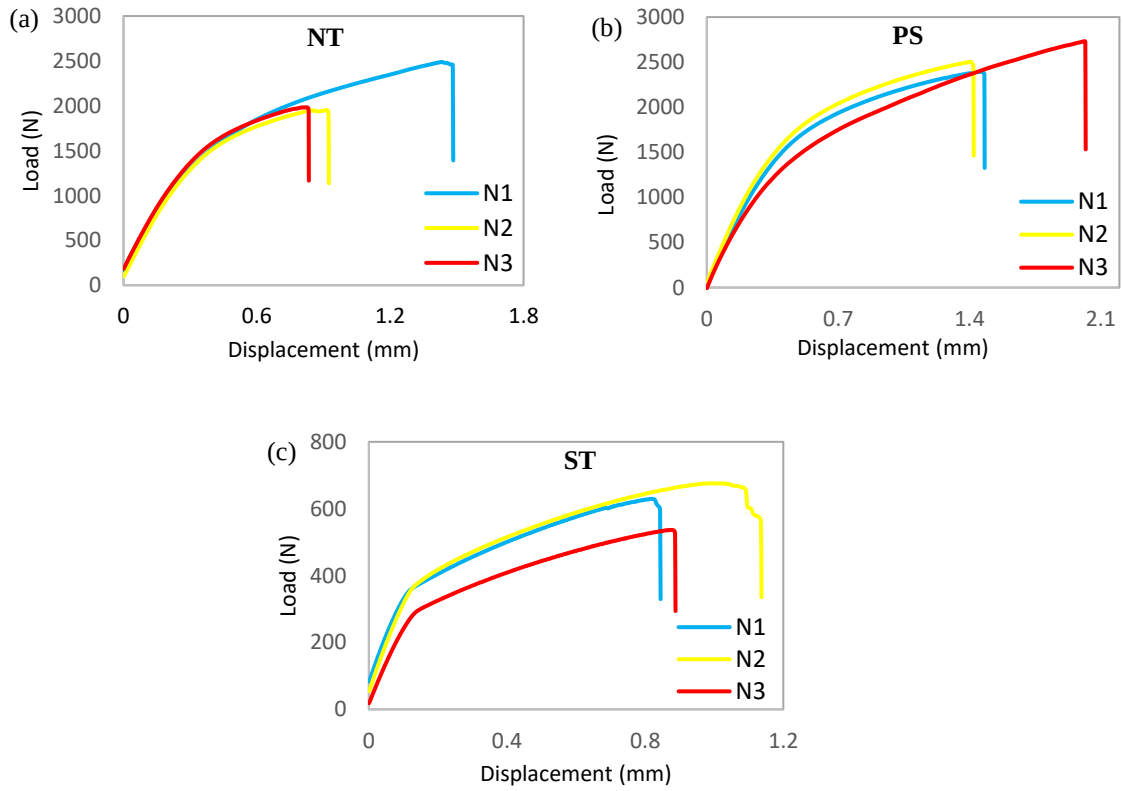

Figure 36 - Load/displacement curves of the AZ31 calibration tests: (a) Notched Tension specimens, (b) Plane Strain tension specimens and (c) Shear Tension specimens.

3.3 Hole hemming experiments

To perform the experimental tests of the hole hemming process, a hole hemming tool was developed inside the group. An illustration of the tool is shown in figure 37.

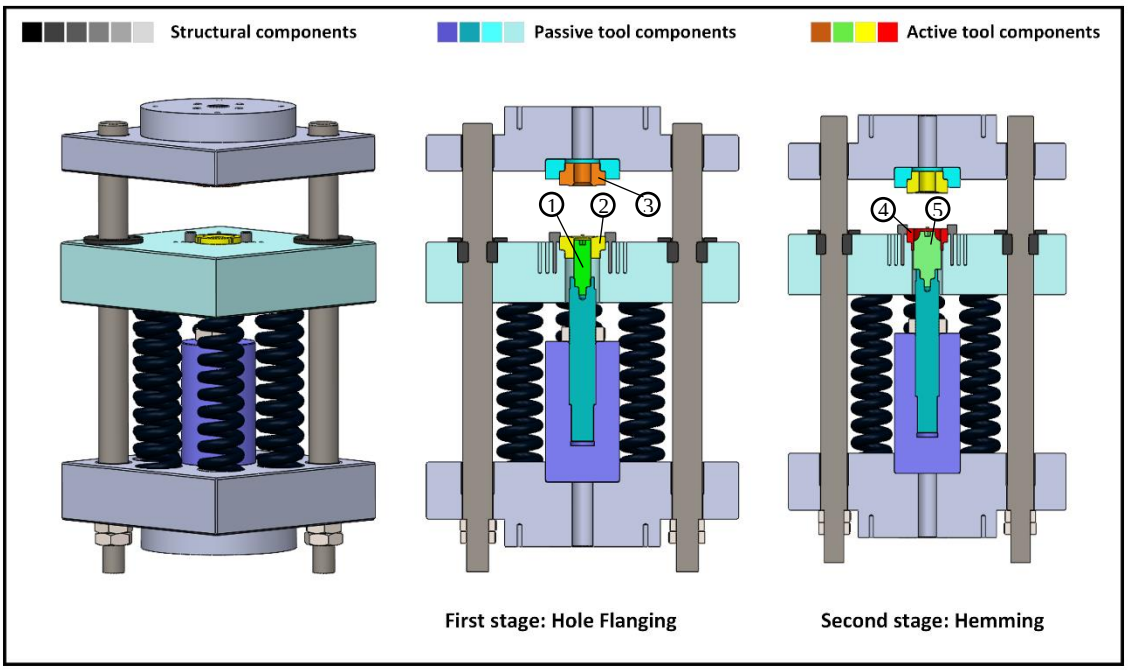

Figure 37 - Illustration of the hole hemming tool: 1 - Flanging punch, 2 - Bottom die, 3 - Upper die, 4 - Blank holder, 5 - Hemming punch.

The active tool components (components that come into direct contact with the sheets during the process) of the hole hemming tool are the flanging punch (no.1) the hemming punch (no.5), the upper die (no.3), the bottom die (no.2), and the blank holder (no.4). The passive tool components (components that surround the active tool components and support them directly or indirectly) of the hole hemming tool are the punch holder that fixes the different types of punches, the height adjuster that allows to change the height of the punches, the die holder and the middle plate that accommodate the different dies. The structural components (components that accommodate the passive tool components and are process independent) of the hole hemming tool are the upper drive plate, the lower plate, the guide pillars, the bushings, the alignment pins, the keys, the plates, the nuts, and the springs.

Figure 38 shows the experimental equipment. The experimental tests were performed in a servo hydraulic INSTROM 8801 with a maximum load capacity of 100 kN.

Figure 38 – Experimental equipment of the hole hemming process.

Figure 39 shows the experimental specimens used in the hole hemming process to study the joint (joint characterization specimens) and to test the loading capacity of the joint (single lap shear tests specimens).

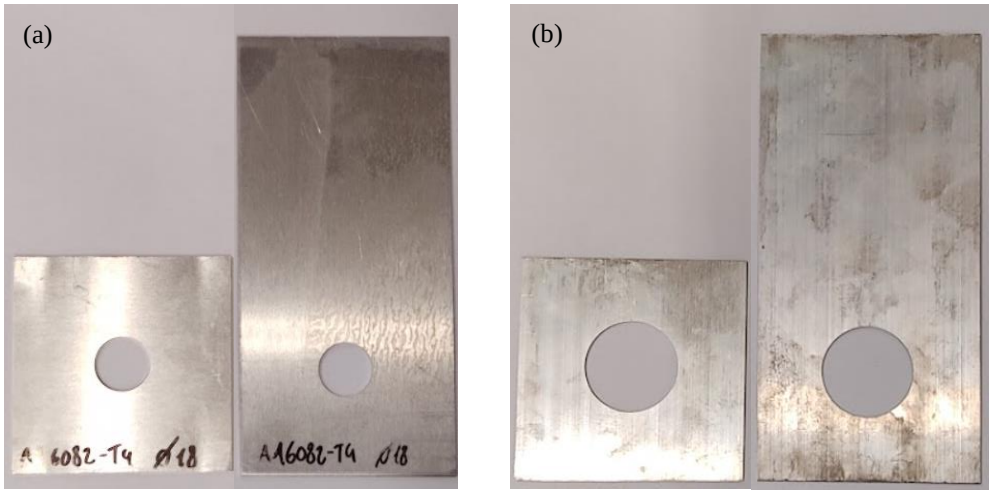

Figure 39 - Experimental hole hemming specimens: (a) On the left, AA6082-T4 joint characterization specimen, on the right, single lap shear test specimen and (b) on the left, AZ31 joint characterization specimen, on the right, single lap shear test specimen.

The process starts by inserting the correct active tool components. In the flanging stage, the bottom die is fixed to the middle plate (figure 40 (a) no.1), the flanging punch is fixed in the punch holder (figure 40 (a) no.2) and the upper die is fixed to the die holder (figure 40 (b) number no.3). Then, the outer sheet is introduced in the top of the bottom die and aligned with the alignment pins, as shown in figure 40 (c).

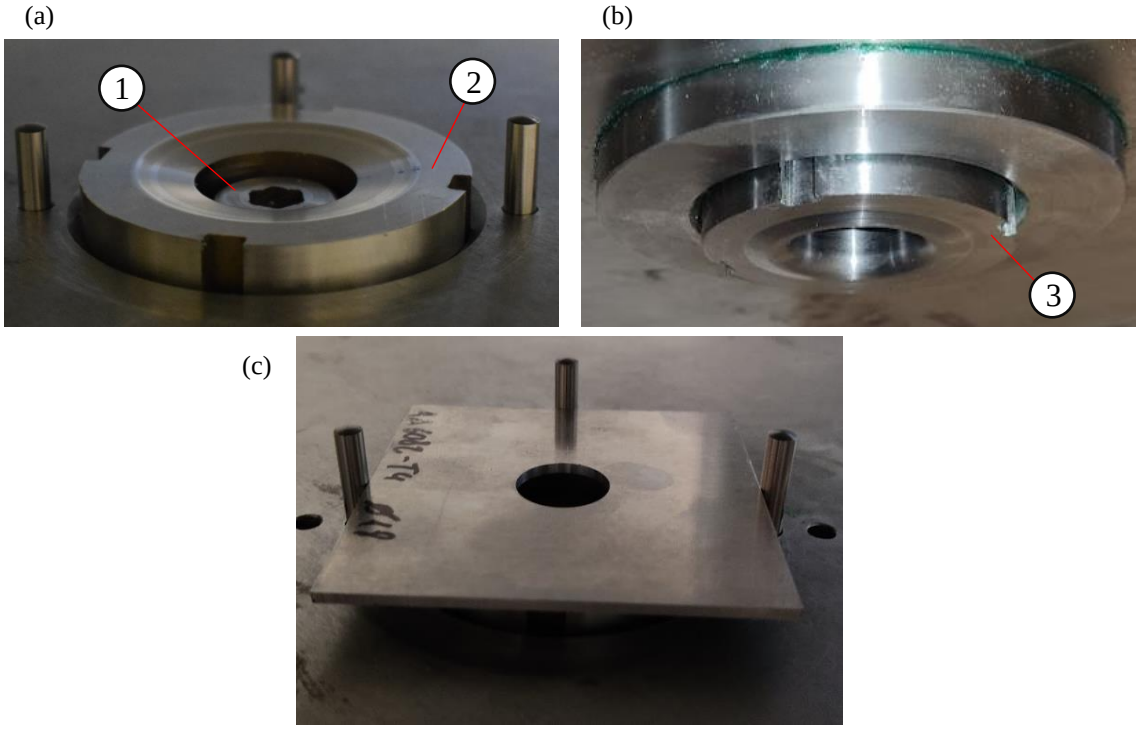

Figure 40 – Flanging stage components and positioning of the outer sheet: (a) 1 – Flanging punch and 2 – bottom die, (b) 3 – upper die and (c) positioning of the outer sheet in the top of the bottom die by means of alignment pins.

After the previous steps, it is applied displacement to the bottom and middle plate until the top die closes into the specimen and forms the indent. Then, the middle plate is fixed in position while the bottom plate continues the displacement, making the flanging punch to advance into the dies and forming a flange in the specimen, as shown in figure 41.

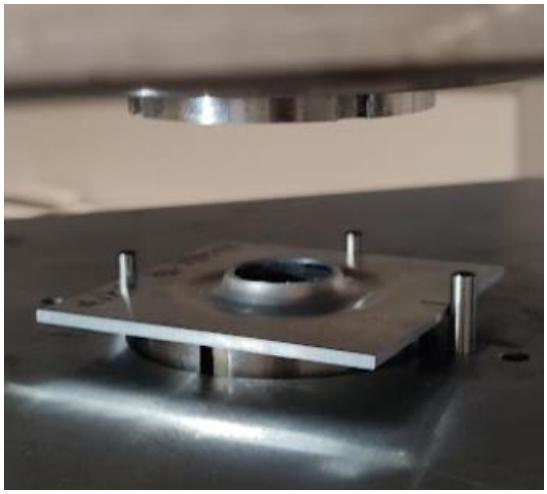

Figure 41 - Formed specimen after the flanging stage.

The process continues by changing the active tool components. In the hemming stage, the blank holder is fixed to the middle plate (figure 42 (a) no.1), the hemming punch is fixed in the punch holder (figure 42 (a) no.2) and the bottom die is taken from the middle plate to be fixed to the die holder (figure 42 (b) no.3). Then, the inner sheet (figure 42 (c) no.4) is assembled through its hole into the flange of the outer sheet (figure 42 (c) no.5) and both are introduced in the top of the blank holder, with the inner sheet facing down and aligned with the alignment pins, as shown in figure 42 (d).

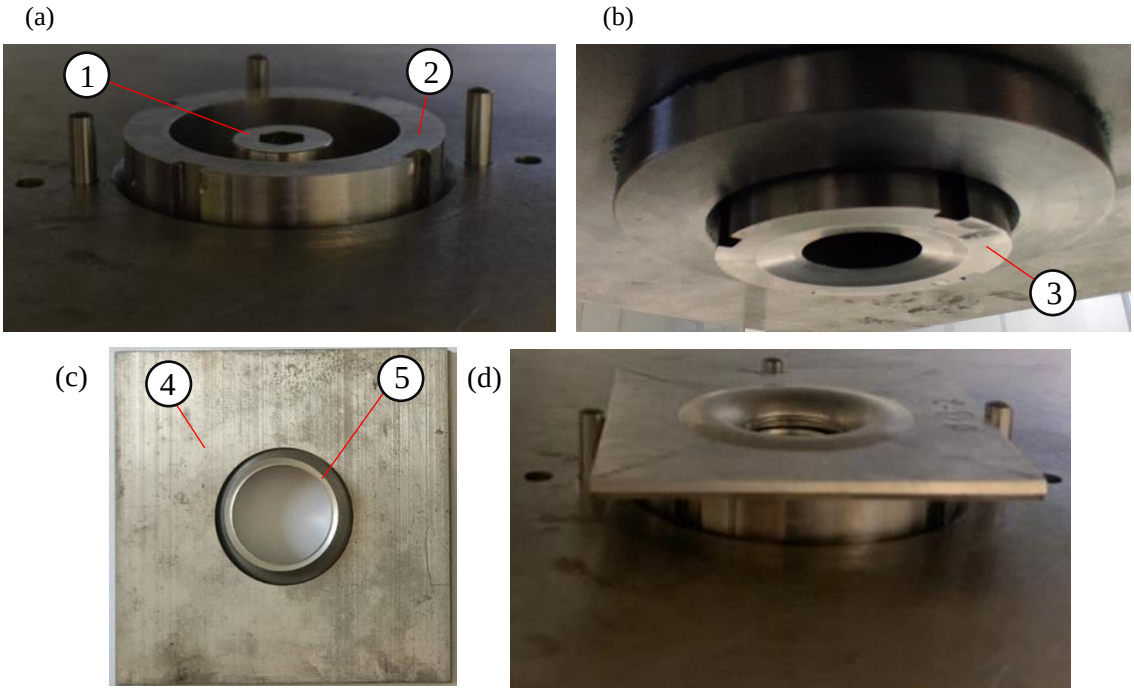

Figure 42 - Hemming stage components and positioning of the sheets: (a) 1 – Hemming punch and 2 – blank holder, (b) 3 – bottom die, (c) 4 – inner sheet and 5 – outer sheet and (d) positioning of the sheets in the top of the blank holder by means of alignment pins.

A displacement is then applied to the bottom and middle plate until the bottom die closes into the outer sheet. Then, the middle plate is fixed in position while the bottom plate continues the displacement, making the hemming punch to advance into the dies and forcing the flange of the outer sheet to overlap the hole edge of the inner sheet and compressing it and forming a tight mechanical interlock. The final joint is shown in figure 43.

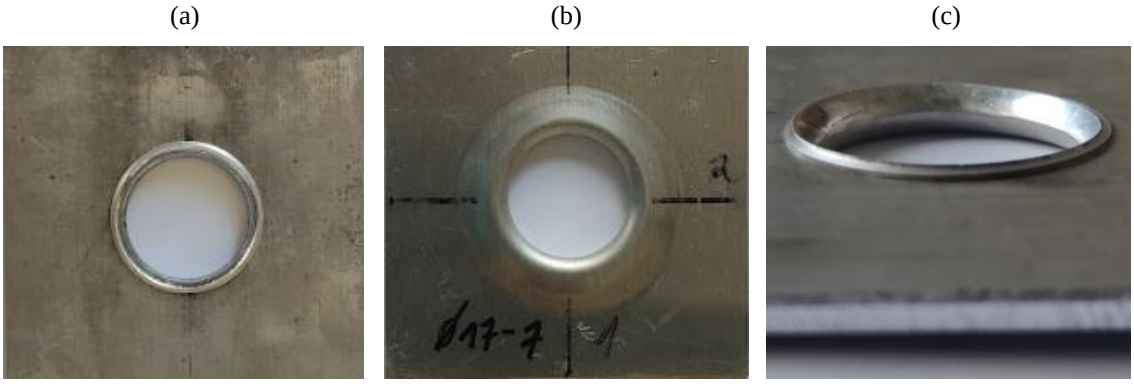

Figure 43 – Final joint: (a) top view, (b) bottom view and (c) lateral view.

3.4 Single lap shear test

The shear strength of the hole hemmed joints was evaluated by the performance of single lap shear tests. The inner and outer sheet specimens are machined to the size of 70 mm (width) x 150 mm (length). Before the hole hemming process, holes are drilled in the opposite extremity to the hemming hole for the fixation in the testing machine. During the hole hemming process, the specimens are aligned to obtain an overlapping section with 70 x 70 mm. The resulting single lap shear test specimen is shown in figure 44.

Figure 44 - Single lap shear test specimen.

The single lap shear tests were performed on a INSTRON 3367 machine (with a maximum capacity of 30 kN) with a constant test speed of 1 mm/min. To align the sheets in the loading direction, the fixation is done with an additional sheet in each end. Figure 45 shows a single lap shear specimen placed on the testing machine ready to test.

Figure 45 – Single lap shear test specimen fixed to the testing machine.

3.5 Work plan

Table 14 shows the work plan of the experimental hole hemming tests.

Table 14 - Hole hemming experimental work plan. Dimensions in mm.

Type	R_o	R_i
Joint characterization	9	14.5
Joint characterization	8.5	14.5
Joint characterization	8	14.5
Single lap shear test	9	14.5
Single lap shear test	8.5	14.5

The objective of these tests is to experimentally confirm the feasibility of the hole hemming process and also to study the effect of the flange length (F) by changing the hole radius of the outer sheet (R_o).

4 Finite element modeling

4.1 Calibration tests

In order to calibrate the ductile fracture criterion and the hardening law, the formability tests including shear, uniaxial tension, notched tension and plane strain tension tests, refer to section 3.2, were simulated using the commercial finite element code Abaqus.

The specimens were discretized by 3D solid elements C3D8R with a element size of 0.4 mm for the uniaxial tension, notched tension and plane strain tests and 0.25 mm for the shear tension test, which has the smaller critical area. However, the elements located outside the central critical area were created considerably larger. Due to the thickness of the sheets, 8 and 5 elements through thickness were considered for the AA6082-T4 and AZ31 specimens, respectively. The mechanical properties including the strain hardening and anisotropic behaviors were defined based on the results obtained in section 3. Isotropic hardening was assumed. A dynamic explicit solver with a time scaling approach was employed to improve the computational performance. It should be noted that the ratio of the kinetic energy to the internal energy was monitored to be negligible. Variables such as the stress triaxiality (η), normalized Lode angle parameter ($\bar{\theta}$) and damage indicator (D) were defined in the FE model by means of a user subroutine VUSDFLD. The FE models for the calibration tests with their mesh details and boundary conditions are shown in figure 46.

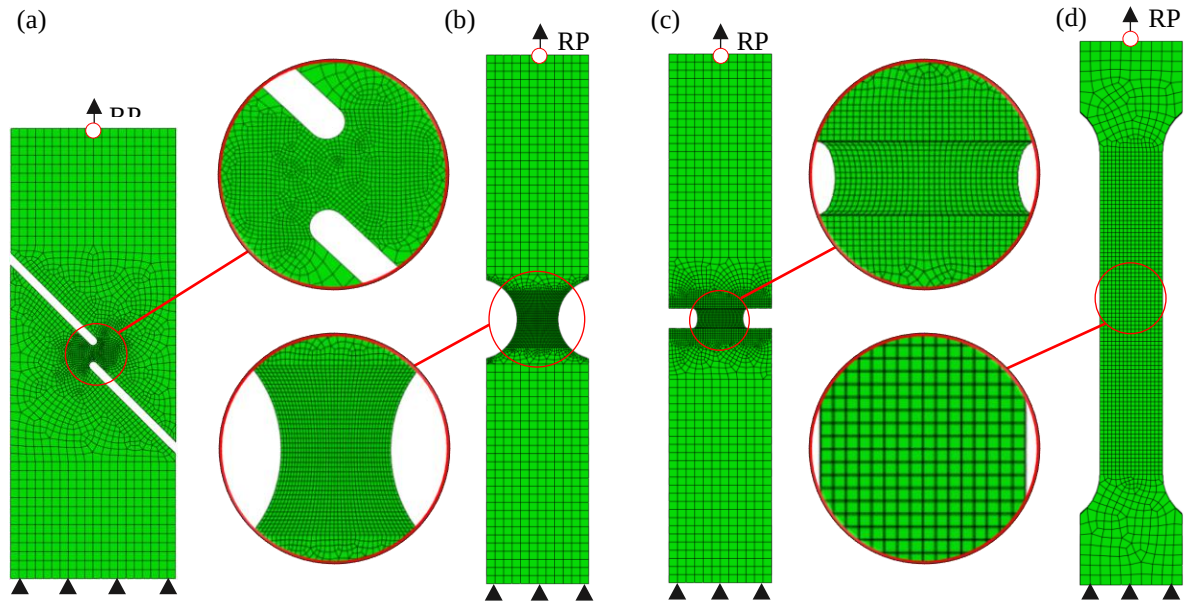

Figure 46 - FE models of the calibration tests with mesh details and boundary conditions: (a) Shear tension test, (b) Notched tension test, (c) Plane strain test, (d) Uniaxial tension test.

As seen in figure 47, one of the ends of the specimens were fixed while in the other end a displacement was applied to a reference point. In a first phase, before the calibration of the ductile fracture criterion, the history of stress state (figure 47 (a) and (b)) and equivalent plastic strain (figure 47 (c)) and also the force-displacement curves were obtained.

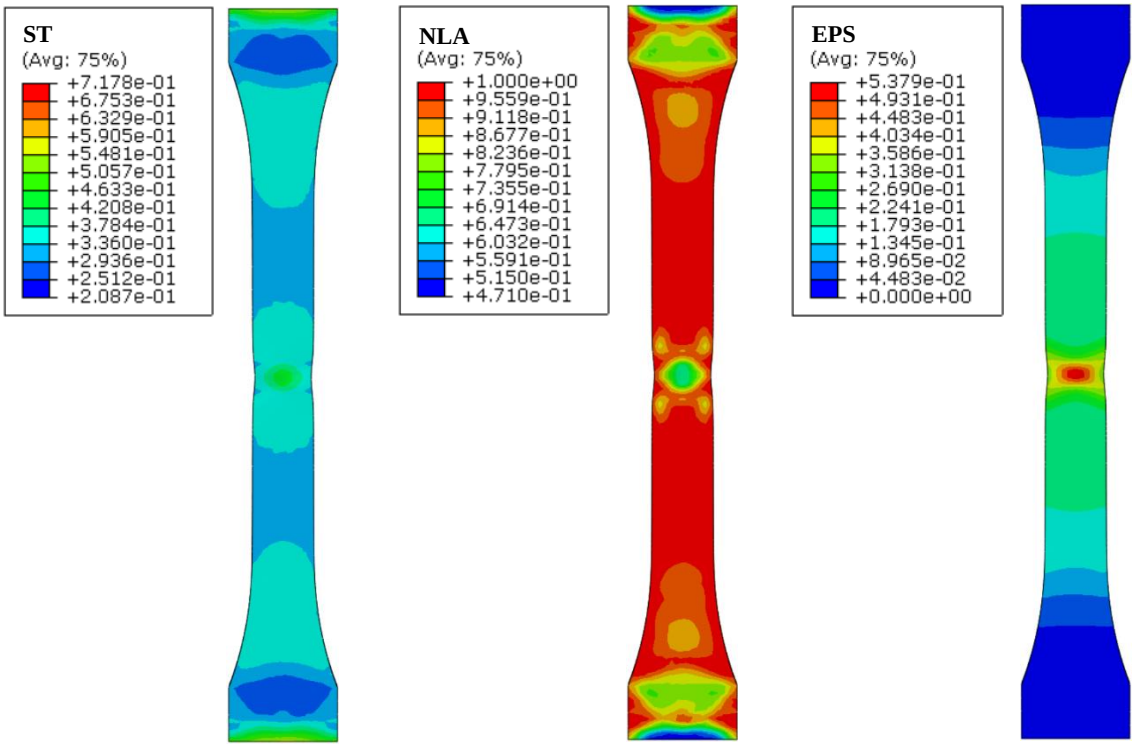

Figure 47 - Stress state and Equivalent plastic strain in a AA6082-T4 uniaxial tension FEM specimen before fracture: (a) Stress triaxiality, (b) Normalized Lode angle parameter and (c) Equivalent plastic strain.

After the calibration of the ductile fracture criterion and using a user subroutine VUSDFLD, the calibration tests were repeated and fracture was considered by activating element deletion when the value of damage in an element reached 1, as shown in figure 48. The fracture displacement is then extracted and compared with the experimental fracture displacement to evaluate the FE model accuracy.

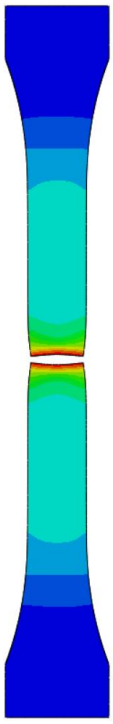

Figure 48 - AA6082-T4 uniaxial tension FEM specimen after fracture.

4.2 Hole hemming

The numerical simulations of the hole hemming process was also performed in the Abaqus software. Similar to the formability tests, the sheets were modeled using 3D solid elements C3D8R, considering 8 and 5 elements through thickness for the AA6082-T4 (the outer sheet) and AZ31 (the inner sheet), respectively. A smaller element size of 0.2 mm was applied in the hole sheet edges (figure 49) where the highest deformations are located. The mechanical properties of each material were defined using the material properties obtained in section 3. A dynamic explicit solver with a time scaling approach was used. The calibrated ductile fracture criteria for the AA6082-T4 and AZ31 sheets were separately defined in the user subroutine VUSDFLD to analyze the damage evolution and, finally, predict the fracture during the hole hemming process. The element deletion technique was activated to model the crack propagation when the damage indicator (D) reaches 1.

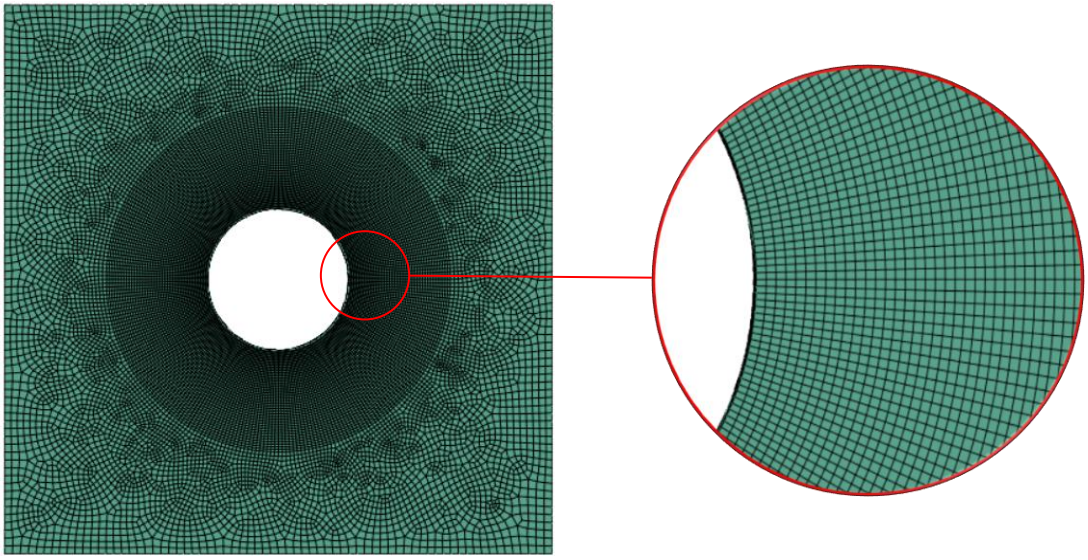

Figure 49 – Hole hemming FE model mesh details of a AA6082-T4 sheet.

The punches (flanging and hemming punch) and matrix (bottom and upper die and blank holder) were modeled as rigid bodies and the FEM apparatus can be seen in figure 50. The simulation is performed in three different steps by applying a displacement to the upper die, flanging punch and hemming punch, in that order. The frictional contact conditions between tools and sheets was defined by a penalty-based contact model using the Coulomb friction law for a friction coefficient of 0.08.

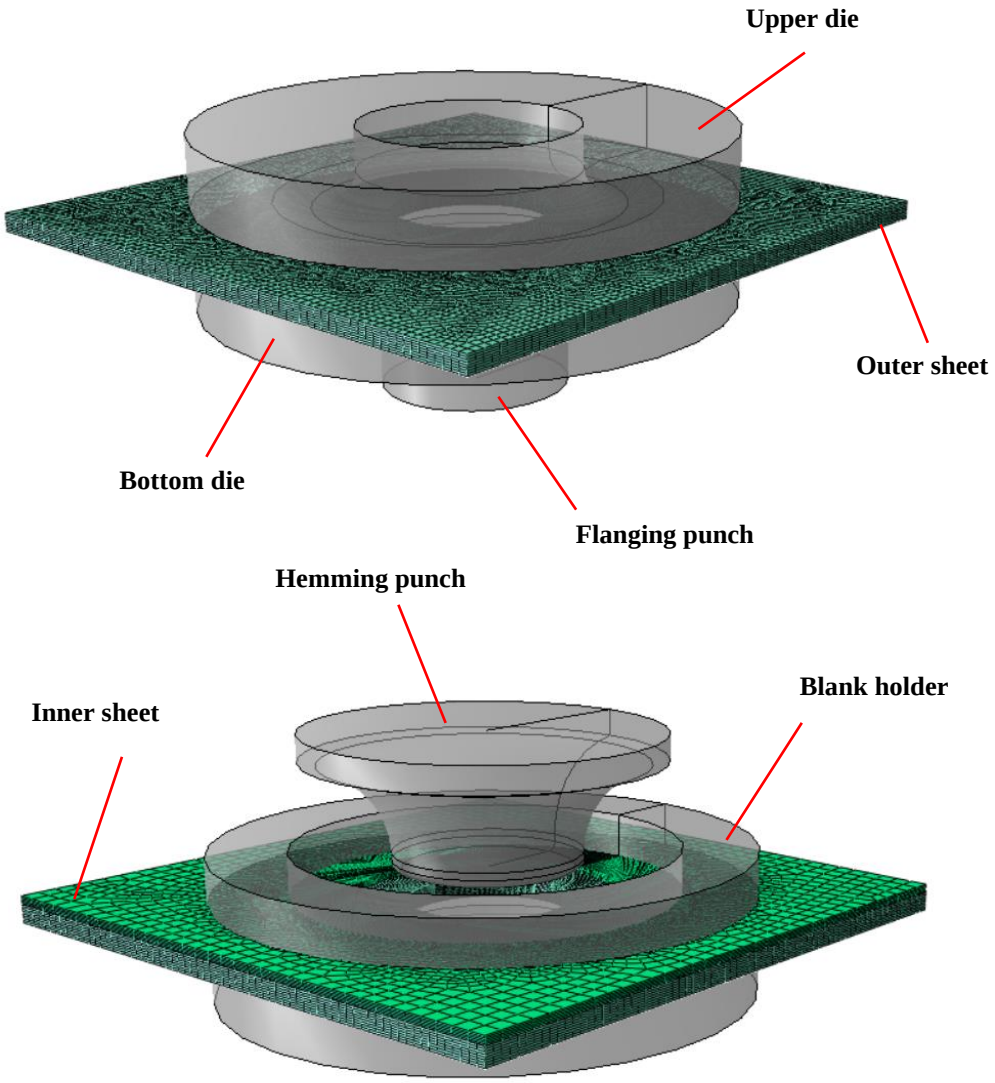

Figure 50 - FE modeling apparatus of the hole hemming process.

5.2.1 Destructive tests

The numerical simulations of the destructive tests (peel test, figure 51 (a), and single lap shear test, figure 52 (b)) are similar to the hole hemming simulation with three main differences. The first is that the geometries of the sheets were adjusted according to the test. The second is that 10 elements were considered through thickness for the inner sheet, which reason is stated in section 6.2.. Finally, a fourth step was added in the model which is the destructive test itself, where a displacement was applied in one of the ends of the inner sheet while the outer sheet was fixed.

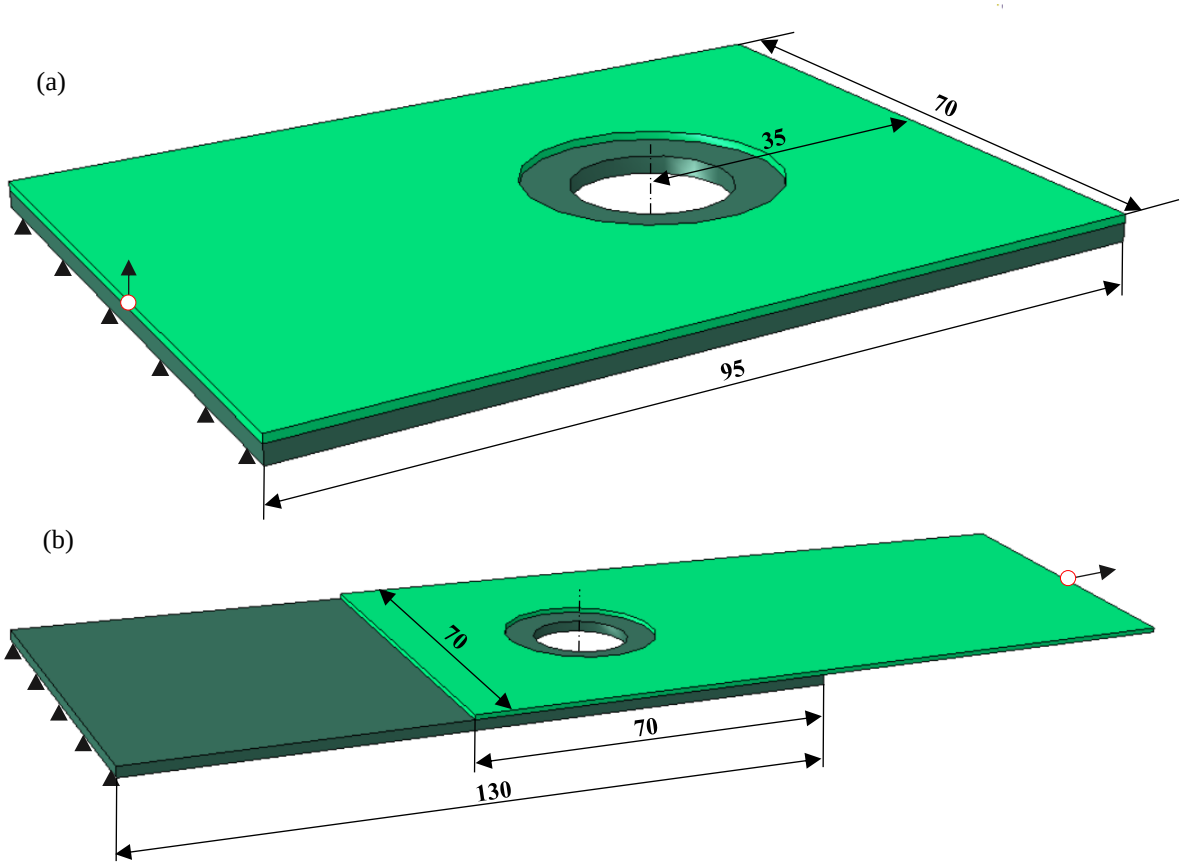

Figure 51 – Geometry and boundary conditions of the destructive test specimens FE models: (a) single lap shear test and (b) peel test.

4.3 Work plan

Table 15 shows the work plan used to study the impact of the process parameters in the feasibility and quality of the joint.

Two different levels are studied for the filet radius of the upper die (fr_d) and die radius (R_d). It should be noted that by changing the R_d and keeping the flange length (F) constant in fact it is being study the effect of the hole radius of the outer sheet (R_o). Concerning the flange length and fillet radius of the hemming punch (R) five and four different levels, respectively, are studied. In the case of the thickness of the inner sheet, it was considered a constant thickness of 0.95 mm which is the estimated thickness where the first contact with the outer sheet is made. The indention depth (d) was fixed to 2 mm to match the thickness of the outer sheet in order to not occur pultrusion in the top surface of the inner sheet. Furthermore, it was considered a 2 mm gap between the inner sheet and outer sheet flange to minimize the buckling of the inner sheet.

Table 15 - Work plan used to study the hole hemming process parameters.

Case	t_o (mm)	t_i (mm)	d (mm)	fr_d (mm)	F (mm)	R (mm)	R_d (mm)	R_o (mm)	R_i (mm)
1	2.05	0.95	2	3	3.5	8	10.5	7	12.5
2	2.05	0.95	2	4	3.5	8	10.5	7	12.5
3	2.05	0.95	2	4	3	8	10.5	7.5	12.5
4	2.05	0.95	2	4	3.25	8	10.5	7.25	12.5
5	2.05	0.95	2	4	3.75	8	10.5	6.75	12.5
6	2.05	0.95	2	4	4	8	10.5	6.5	12.5
7	2.05	0.95	2	4	3.5	4	10.5	7	12.5
8	2.05	0.95	2	4	3.5	6	10.5	7	12.5
9	2.05	0.95	2	4	3.5	10	10.5	7	12.5
10	2.05	0.95	2	4	3.5	8	12.5	9	14.5

5 Fracture modeling

5.1 Ductile fracture criterion

In order to design the hole hemming process, it is necessary to understand the fracture limits of the materials. In this work, the Modified Mohr Coulomb (MMC) fracture criterion, which is presented in section 2.4.3, was used to predict the fracture in the finite element analysis.

The MMC fracture envelope, equation 2.2, is not only dependent on the K (strength coefficient) and n (hardening exponent), which were determined in section 3.1.4., but also in the material coefficients C_1, C_2 and C_3. These material coefficients are obtained by fitting the fracture envelope in at least three calibration points that are obtained by formability tests with different loading paths. Figure 52 shows a typical MMC fracture envelope which consists of two branches, one from uniaxial compression to uniaxial tension and another from uniaxial tension to equibiaxial tension.

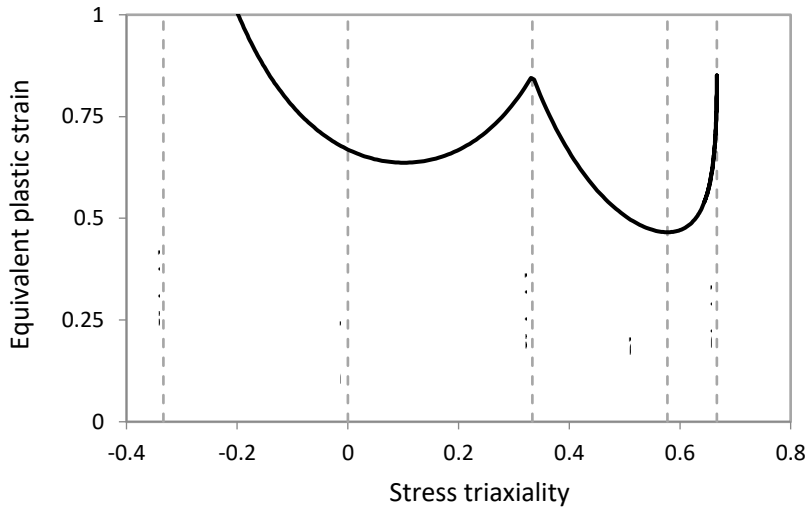

Figure 52 - Typical MMC fracture envelope expressed in a 2D space of Equivalent Plastic Strain and Stress Triaxiality.

5.2 Calibration method

An experimental and numerical hybrid approaches were used for the calibration of the MMC criterion. To acquire an accurate prediction of the fracture envelope, at least three distinct calibration points are required with loading paths near uniaxial tension, plane strain and pure shear. In this work, the calibration point with a loading path near uniaxial tension was obtained by testing the uniaxial tension specimens presented in section 3.1 (figure 20). The shear and plane strain specimens used are shown in section 3.2 (figure 32 and 33). Another specimen, the notched tension specimen, was also tested to more accurately estimate the fracture envelope between uniaxial tension and plane strain (figure 32 and 33). These tests were simulated in the commercial finite element software Abaqus, as described in section 4.1.

In the case of the AZ31, the results of the notched tension tests were not used in the calibration of the MMC criterion, due to the problem of the thickness variation in the AZ31 as explained in section 3. In fact, the results of the notched tension tests were not good as the grips of the machine only fixed a portion of the specimen where it had a higher thickness. Thus, the load was not evenly distributed along the specimen during the test, as seen in figure 53, and the deformation was concentrated at one side of the specimen. This effect was only observed in this calibration test.

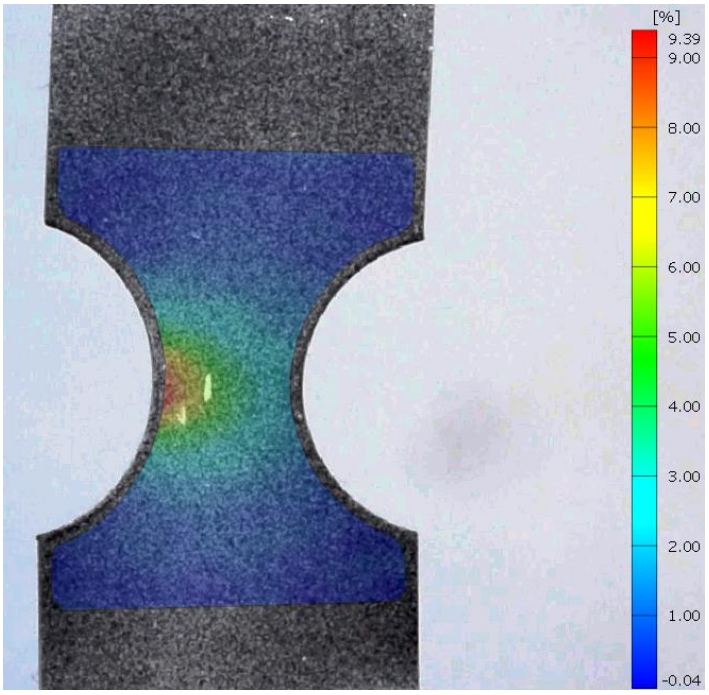

Figure 53 – Major strain of a AZ31 notched tension test specimen before fracture.

As seen in figures 25 and 26, while the load-displacement curves of the AA6082-T4 calibration tests are similar in the three trials, in the case of the AZ31 the curves vary due to the thickness variation. As the hole of the AZ31 sheet is made in the middle of the sheet to obtain a hole with a symmetric thickness distribution, the AZ31 specimen selected for each test to calibrate the fracture criterion were the ones which had a thickness similar to the thickness at the middle.

In order to apply the hybrid methods, it is first necessary to be sure about the accuracy of FE models. First it is necessary to confirm if there is a good correlation between the critical zone of the FE model and the experimental model, being considered critical the zone with the highest strain, as is shown in figure 54. Furthermore, figure 55 shows a comparison between the experimental and numerical load-displacement curves for the calibration tests. As seen, there is a good agreement between the curves, demonstrating the validity of the FE models.

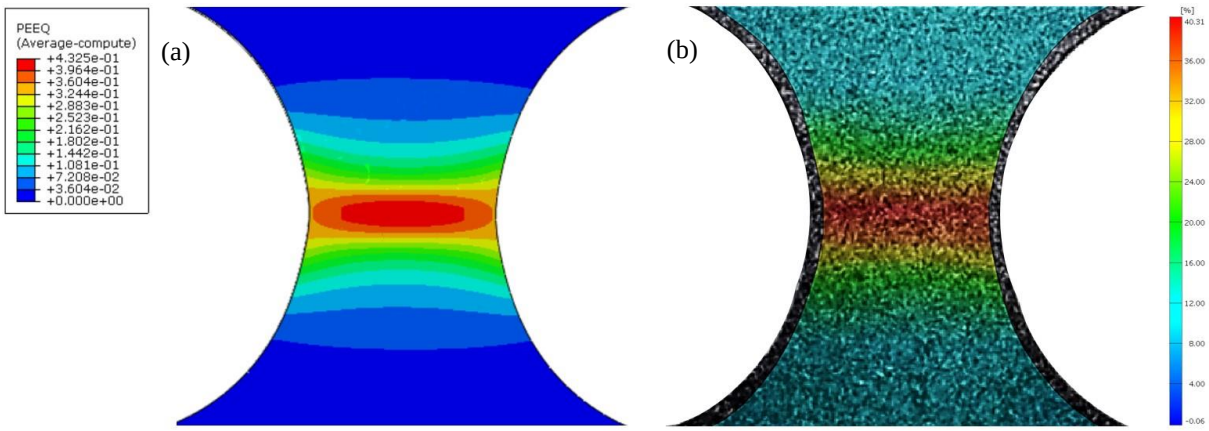

Figure 54 - Comparison between the strain contour of the FE model and the experimental test of a AA6082-T4 notched tension test: (a) FE model equivalent plastic strain countor and (b) DIC major strain countor.

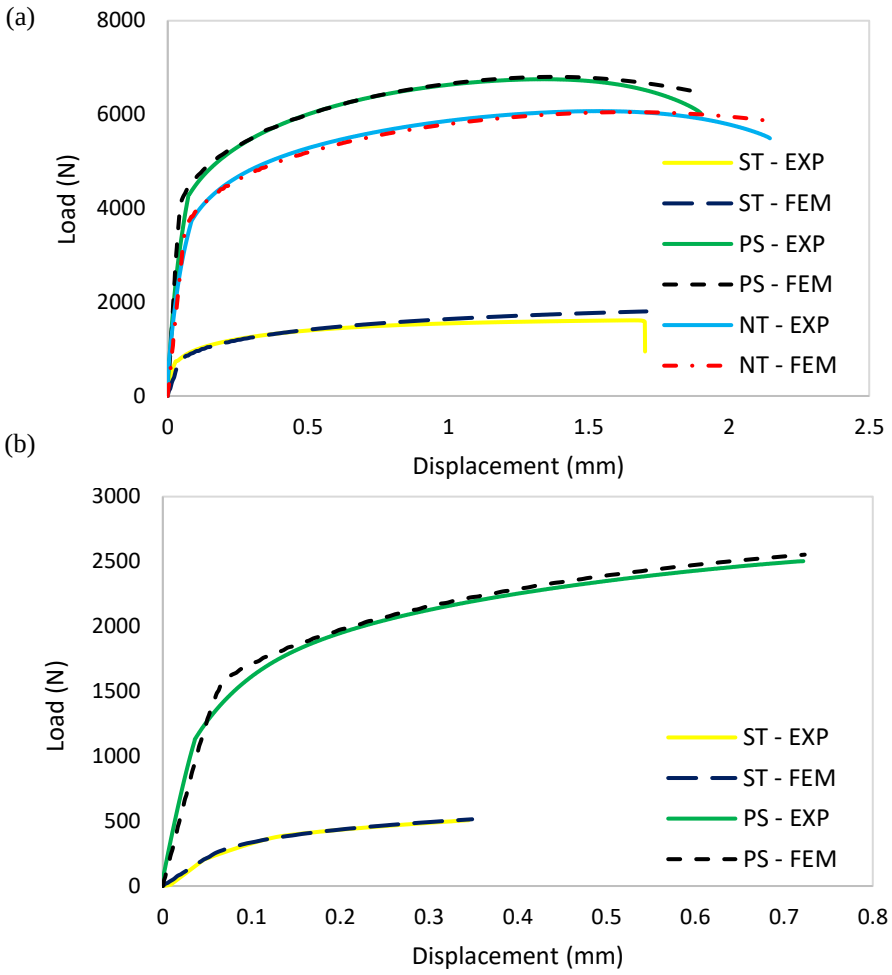

Figure 55 – Load-displacement curves comparison between the experimental and numerical results: (a) AA6082-T4 and (b) AZ31.

In the critical region, the stress triaxiality (η) and the normalized Lode angle parameter ($\bar{\theta}$) were obtained using the FE simulations. In addition, the equivalent plastic strain was extracted at the displacement when fracture occurs in the experimental tests. Figure 56 and 57 show the evolution of stress triaxiality (η) and normalized Lode angle parameter ($\bar{\theta}$) as function of the equivalent plastic strain.

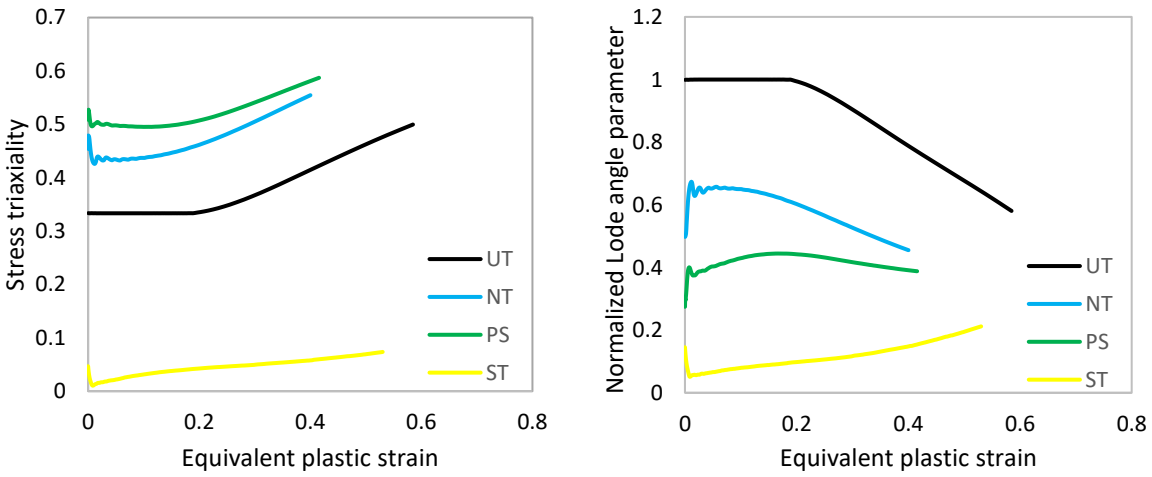

Figure 56 – Evolution of the Stress triaxiality (left) and Normalized Lode angle parameter (right) for the AA6082-T4.

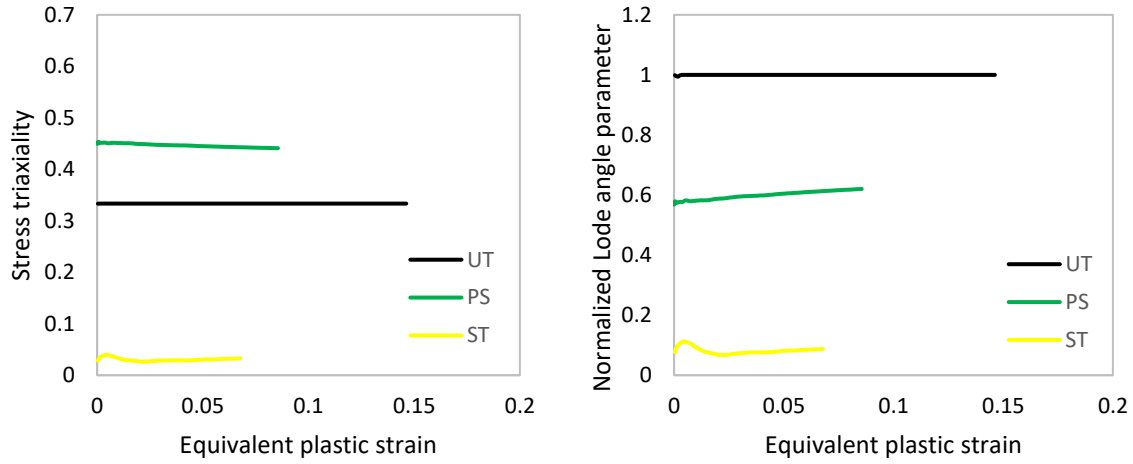

Figure 57 - Evolution of the stress triaxiality (left) and Normalized Lode angle parameter (right) for the AZ31.

There is a variation of the stress state along the tests especially in the AA6082-T4 as it undergoes higher deformations and it suffers necking before the occurrence of fracture. Because of this, it is necessary to obtain the average values of the stress triaxiality and normalized Lode angle parameter using equation 5.1 and 5.2.

$$\eta_{ave} = \frac{1}{\bar{\varepsilon}_p^f} \int_0^{\bar{\varepsilon}_p^f} \eta(\bar{\varepsilon}_p)\, d\bar{\varepsilon}^p \tag{5.1}$$

$$\bar{\theta}_{ave} = \frac{1}{\bar{\varepsilon}_p^f} \int_0^{\bar{\varepsilon}_p^f} \bar{\theta}(\bar{\varepsilon}_p)\, d\bar{\varepsilon}^p \tag{5.2}$$

The major and minor strains were obtained in the critical point from the DIC software, then the equivalent strain was calculated at the last measurement of the DIC system by eq 2.8.

In the case of the AA6082-T4, the fracture strains obtained by the FEM were higher than the equivalent strains measured by the DIC (figure 58 (a)). Since the DIC method is highly dependent in the quality of the video and the stochastic pattern during the deformation, the accuracy of its results can be compromised for high localized deformation. This was particularly observed in the shear tension test in which the deformation was so high and concentrated in a small so that the mesh defined in the DIC software disappeared before crack opening.

The AZ31 undergone significantly less deformation and, in most cases, fractured without necking, therefore the results of the DIC were similar to the results of the FEM at the onset of fracture (figure 58 (b)). However, in the shear tension test, the fracture equivalent strain obtained from the FE simulation was much higher than the one of the DIC and even about 70% higher than the fracture strain in the uniaxial tension, which is unacceptable. Due to the high quality of the DIC measurement of the AZ31, this difference may be related to the modeling of the material behavior in the shear state. Thus, the result of the DIC was used in this case.

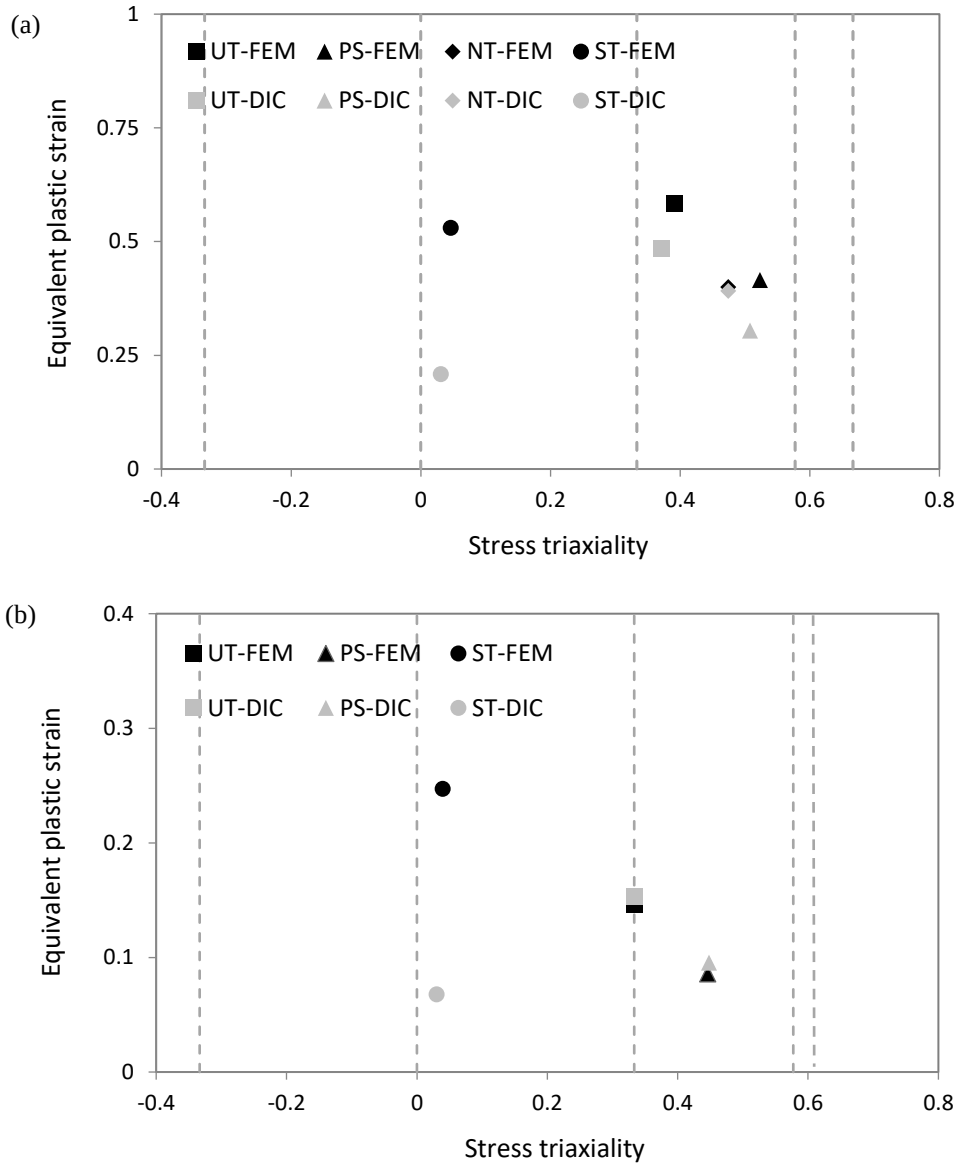

Figure 58 - Calibration points for both materials obtained by FEM and DIC: (a) AA6082-T4 and (b) AZ31.

Based on the given description, the resulting calibration points are listed in table 16 and 17. Moreover, the calibration points are shown in the space of the stress triaxiality (η) versus the normalized Lode angle parameter ($\bar{\theta}$) in figures 59. The results show that the calibration tests enable to reflect the desired stress states. All the points are also located on the theoretical curve obtained based on the assumption of plane stress condition, which confirms the existence of this condition in the test.

Table 16 - Calibration points for the AA6082-T4.

AA6082-T4	$\bar{\varepsilon}_f$	η_{ave}	$\bar{\theta}_{ave}$
UT	0.58	0.39	0.85
ST	0.53	0.046	0.12
PS	0.42	0.52	0.42
NT	0.40	0.47	0.58

Table 17 - Calibration points for the AZ31.

AA6082-T4	$\bar{\varepsilon}_f$	η_{ave}	$\bar{\theta}_{ave}$
UT	0.14	0.33	1
ST	0.068	0.030	0.081
PS	0.086	0.45	0.60

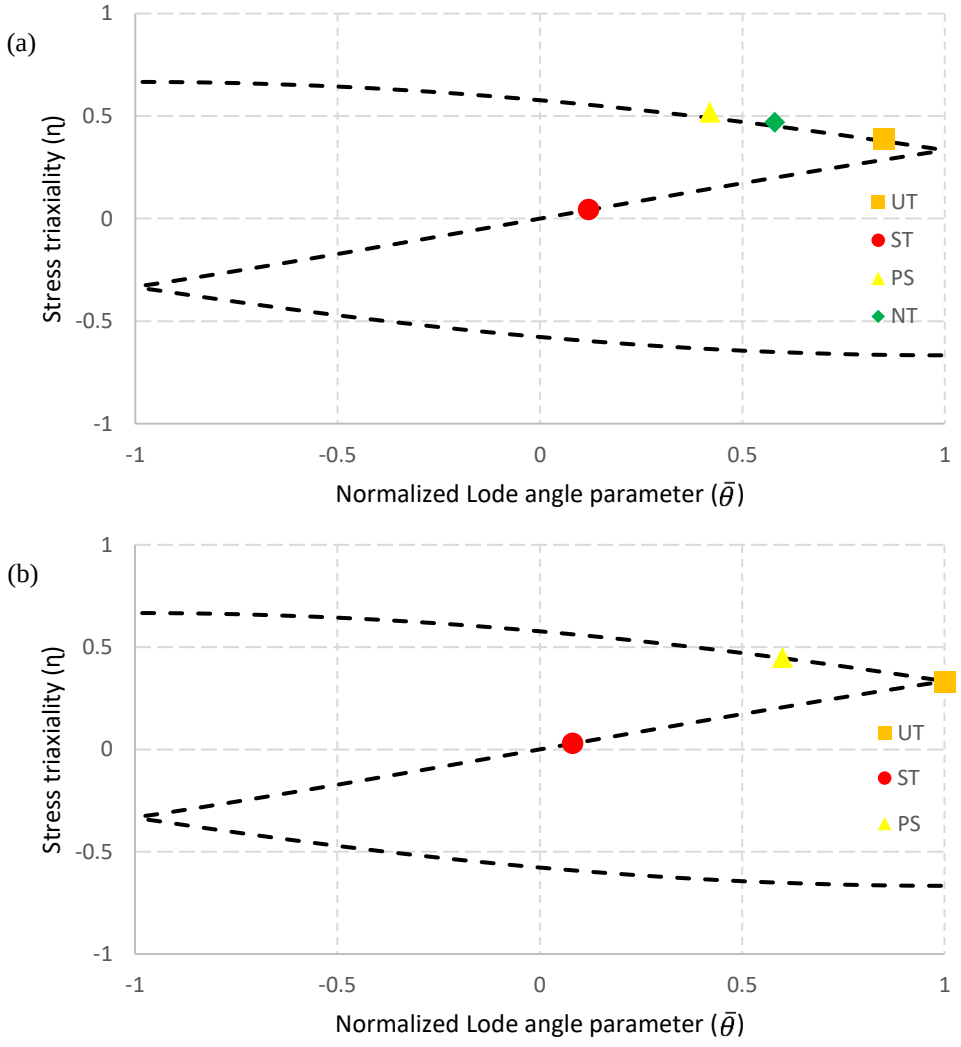

Figure 59 - Plane stress condition verification: (a) AA6082-T4 and (b) AZ31.

5.3 Fracture envelopes

For each material, the MMC fracture envelope, eq 2.2, was fitted to the calibration points in MATLAB. The resulting material constants are summarized in table 18. The 3D fracture envelopes for the AA6082-T4 and AZ31 sheets are shown in figure 60. Assuming the plane stress condition, the fracture envelopes are also plotted in the space of equivalent plastic strain and stress triaxiality along with the corresponding calibration points (figure 61). In both cases, the fracture envelope shows a good agreement with the calibration points.

Table 18 - MMC material constants.

Material	C1	C2	C3
AA 6082-T4	0.078	235	0.981
AZ31	0	150	1

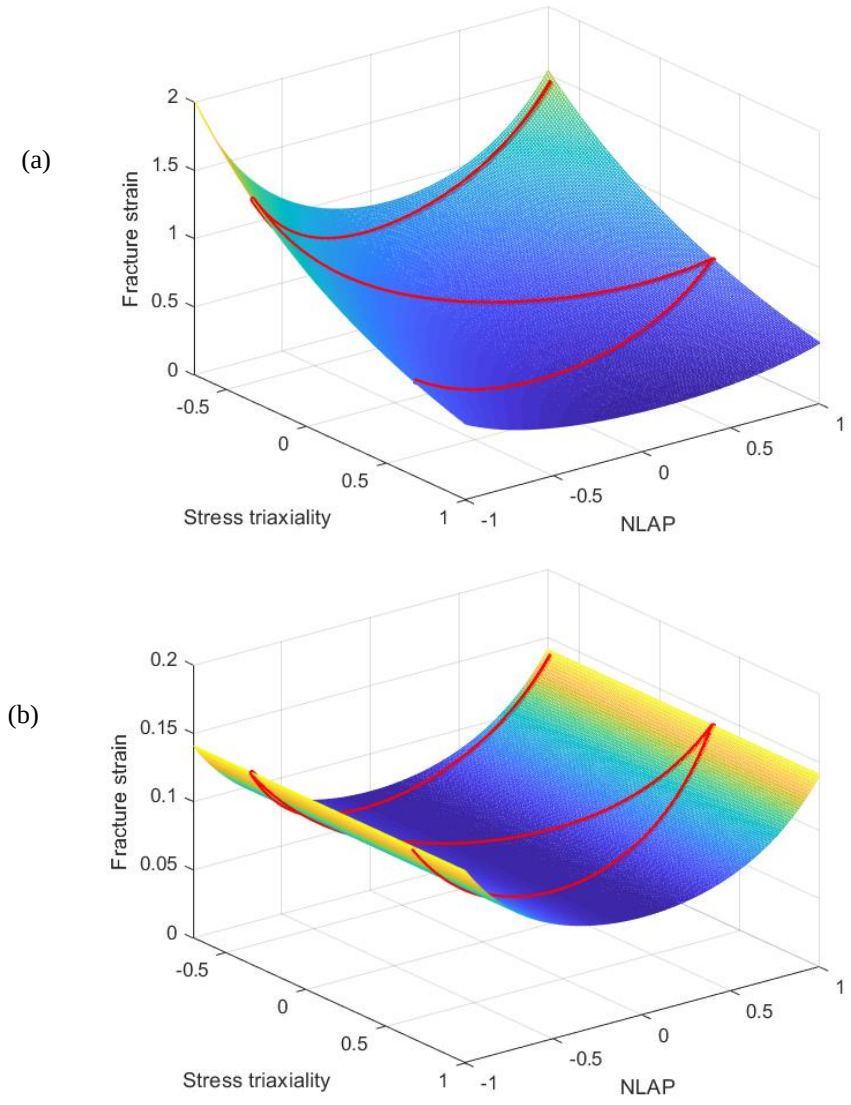

Figure 60 – 3D MMC fracture envelopes: (a) AA6082-T4 and (b) AZ31. The red line present in the surface shows the fracture strain for plane stress state.

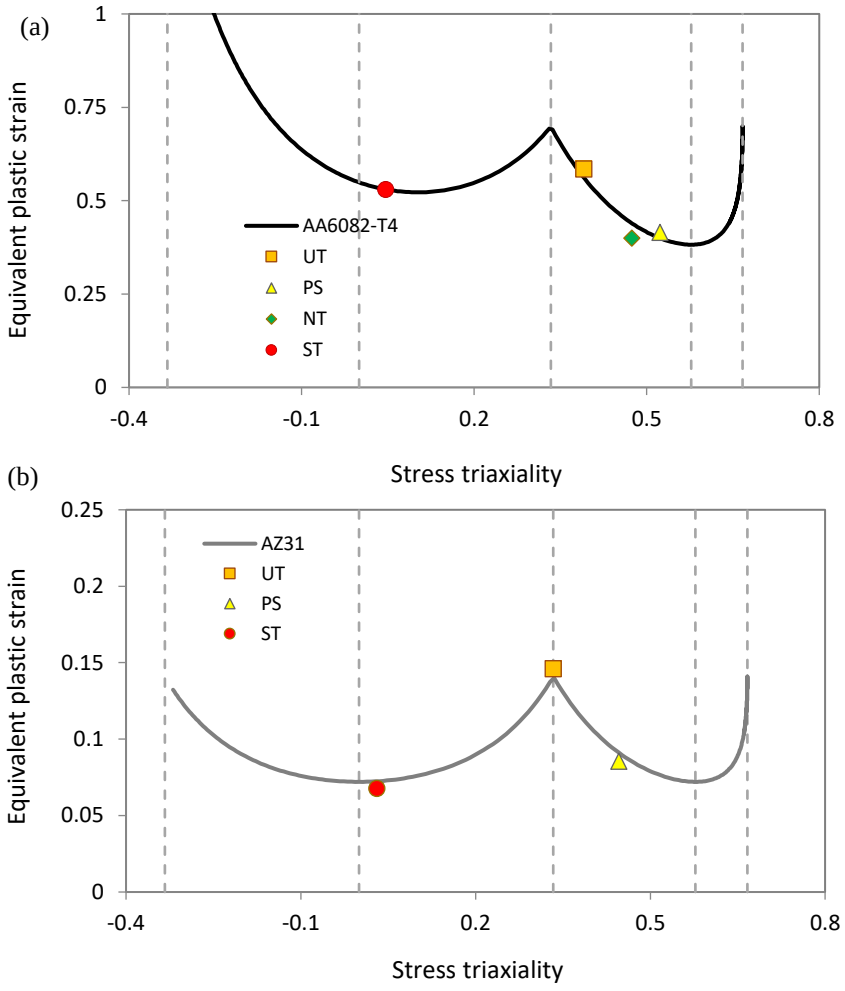

Figure 61 – MMC fracture envelopes with the respective calibration points: (a) AA6082-T4 and (b) AZ31.

The fracture envelopes of the AA6082-T4 and AZ31 sheets are compared in figure 62. As seen, there is a huge difference between the fracture envelopes, exhibiting significantly higher formability of the AA6082-T4 sheet in all the stress states and highlighting the difficulty of forming the AZ31 sheet at room temperature.

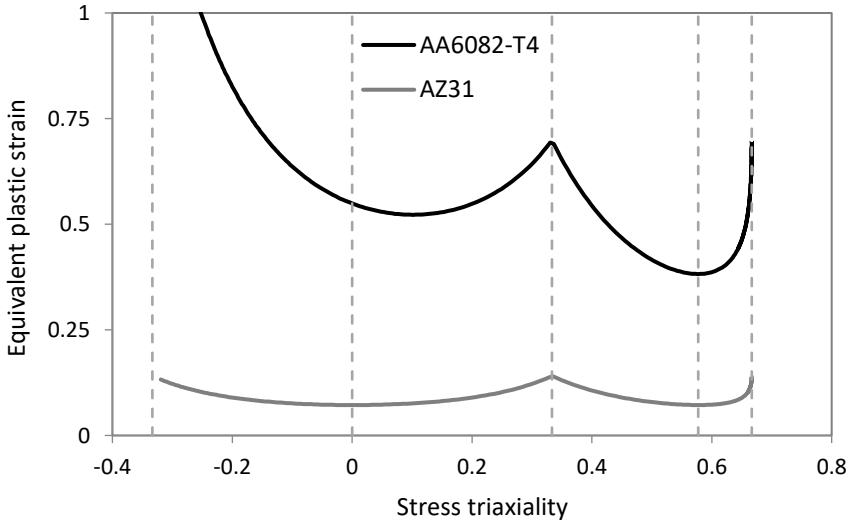

Figure 62 - Comparison of the AA6082-T4 and AZ31 fracture envelopes.

5.3.1 Evaluation of the fracture criterion

The finite element analyses of the formability tests were once again performed to evaluate the accuracy of the calibrated MMC criterion. The criterion was defined in ABAQUS by means of a VUSDFLD subroutine. In these simulations, when the damage indicator reached one, fracture was predicted. The fracture displacements are compared with the experimental fracture displacements for the AA6082-T4 and AZ31 sheets, in table 19 and 20, respectively.

Table 19 – Fracture displacement error prediction using the calibrated MMC for the AA6082-T4.

Fracture displacement	**Uniaxial tension test**	**Notched tension test**	**Plane strain tension test**	**Shear tension test**
Experimental (mm)	12.25	2.15	1.90	1.70
FE prediction (mm)	12.15	2.21	1.85	1.63
Relative error (%)	0.8	2.8	2.6	4.1

Table 20 - Fracture displacement error prediction using the calibrated MMC for the AZ31.

Fracture displacement	**Uniaxial tension test**	**Plane strain tension test**	**Shear tension test**
Experimental (mm)	4.14	0.73	0.53
FE prediction (mm)	3.95	0.78	0.32
Relative error (%)	4.6	6.8	39.6

6 Results and discussion

6.1 Deformation mechanics

The contours values of equivalent plastic strain and damage indicator of the outer sheet are shown in Figure 63. According to figure 63 (a), the maximum equivalent plastic strain in the end of the flanging stage is located in the hole edge that is in contact with the flanging punch, while, as seen in figure 63 (b), the maximum damage is located in the bend zone. The high value of strain in the hole edge is due to the intense local contact between the hole edge and flanging punch, while not reflecting in high values of damage due to the mainly compressive stresses involved. The zone with the highest damage depends on the combination of the process parameters, and for a different combination it may be located in the flange edge. In the hemming stage, figure 63 (c) and (d), the damage continues to increase in the flange edge and bend zone, and, in this case, fracture eventually occurs in the flange edge.

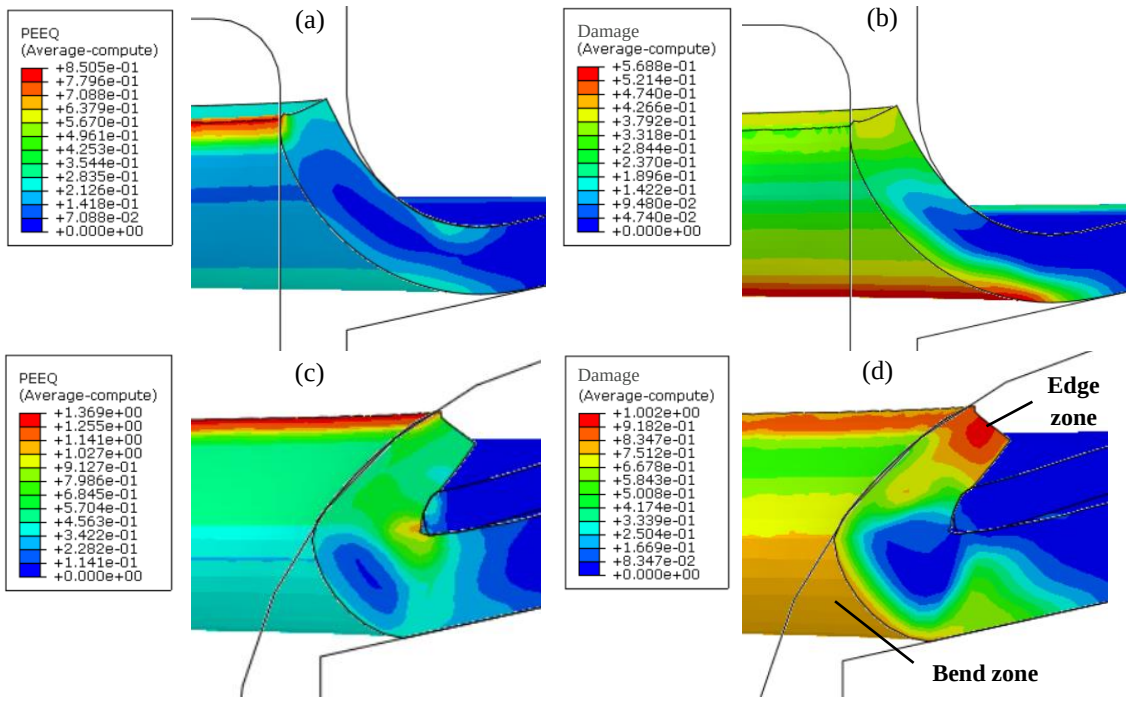

Figure 63 – Contour values of equivalent plastic strain and damage indicator in the outer sheet during the hole hemming process: (a) equivalent plastic strain at the end of the flanging stage, (b) damage value of the outer sheet at the end of the flanging stage, (c) equivalent plastic strain at the end of the hemming stage, (b) damage value of the outer sheet at the end of the hemming stage.

Figure 64 shows the loading path of the edge and bend zone in a two-dimensional space of stress triaxiality and equivalent plastic strain during the hole hemming process. The edge zone undergoes higher deformations than the bending zone. Nonetheless, the majority of the deformation path in the edge zone is located between pure shear and uniaxial tension, while the majority of the deformation path in the bending zone is located between uniaxial tension and plane strain due to the bending deformation, which have lower fracture strains.

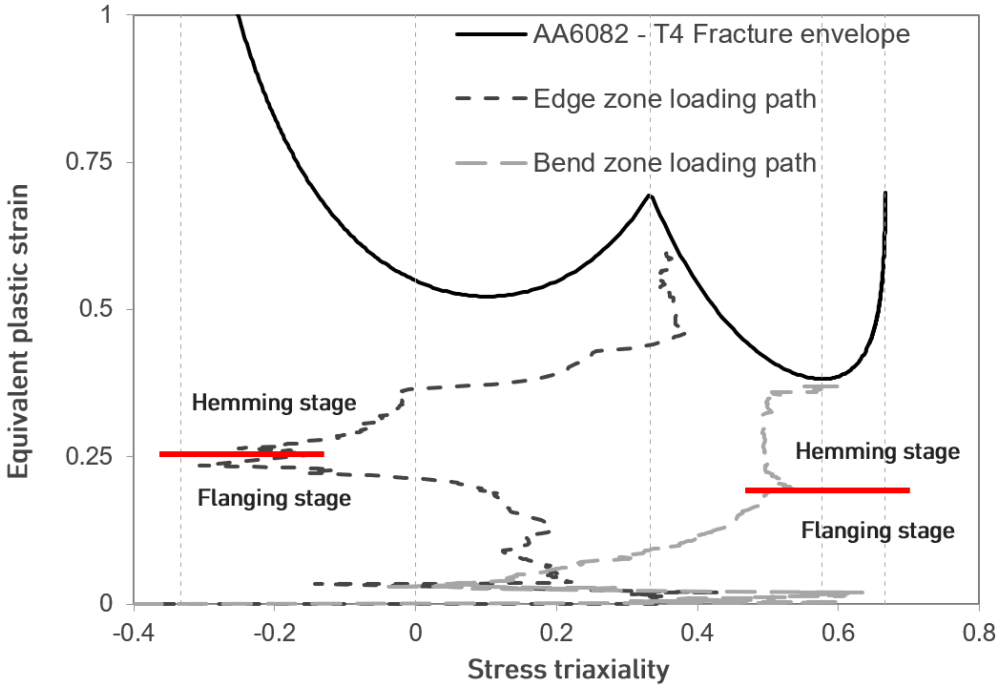

Figure 64 – Loading path of the critical regions on the outer sheet along the hole hemming process.

6.2 Influence of the process parameters

Figure 65 shows the effect of the fillet radius of the upper die (fr_d) in the damage of the outer sheet at the end of the flanging stage. The increase of the fr_d lead to the decrease of the damage in the bend zone due to the creation of a higher radius in the bend region, as it can be also confirmed by checking the evolution of damage versus the flanging punch displacement in figure 66 (a). Figure 66 (b) also shows that this parameter has no influence in the damage in the edge zone in the end of the flanging stage.

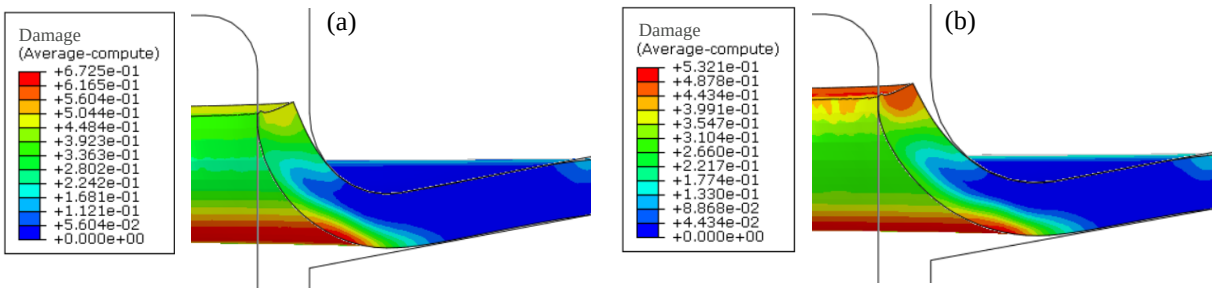

Figure 65 - Damage distribution in the outer sheet in the end of the flanging stage for different values of fillet radius of the upper die: (a) fr_d = 3 mm and (b) fr_d = 4 mm.

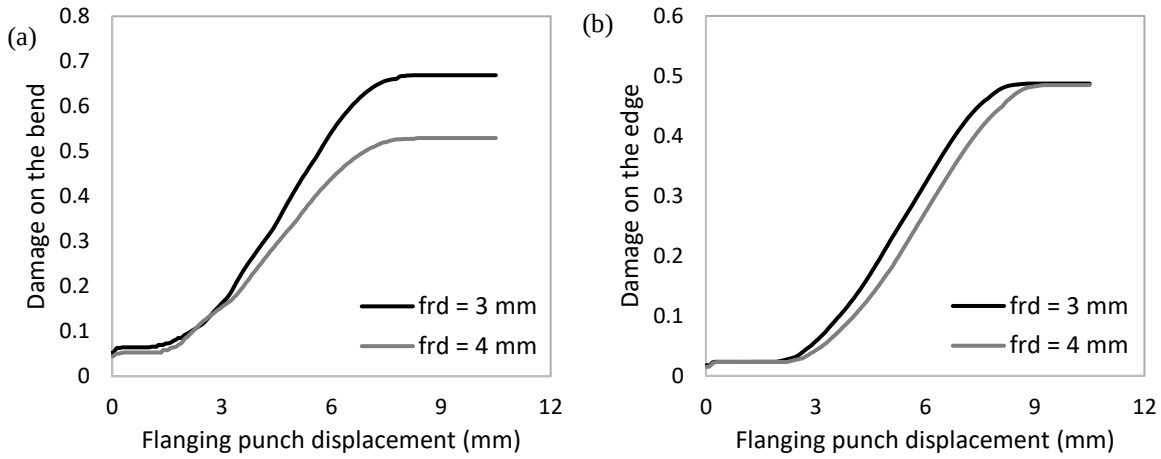

Figure 66 - Damage evolution in the critical zones during the flanging stage for different fr_d: (a) Bend zone and (b) edge zone.

Figure 67 shows the effect of the flange length (F) on the formed flange shape and damage in the outer sheet in the end of the flanging stage and figure 68 the damage evolution during the flanging stage. The higher the flange length, the higher is the damage in the edge in the end of the flanging stage, which is expected as the ratio between the final and initial hole radius increase and the flanging strain is a function and proportional to this ratio. Besides that, with the increase of the flange length the critical region with the highest damage in the end of the flanging stage shifts from the bend to the edge.

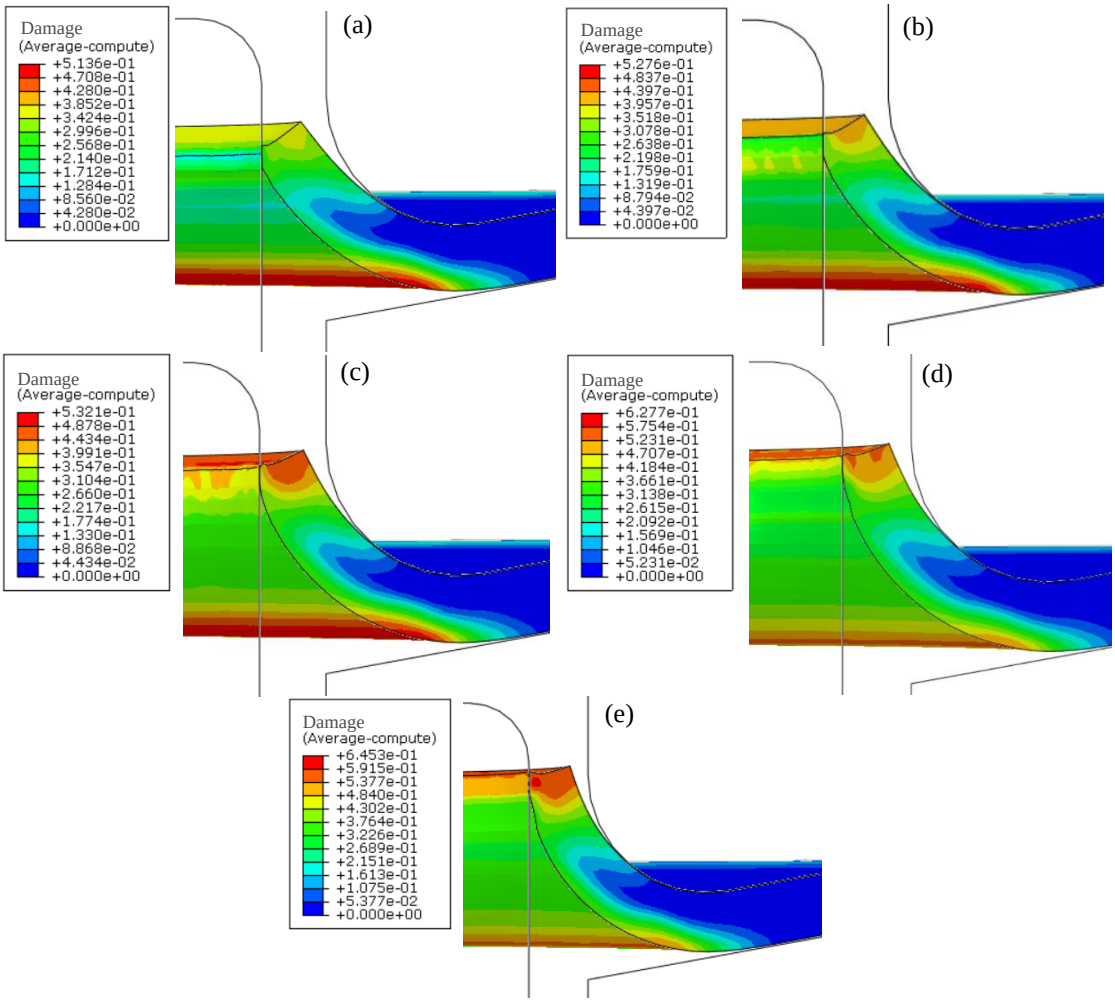

Figure 67 - Damage distribution in the outer sheet in the end of the flanging stage for different values of flange lengths: (a) F = 3 mm, (b) F = 3.25 mm, (c) F = 3.5 mm, (d) F = 3.75 mm and (e) F = 4 mm.

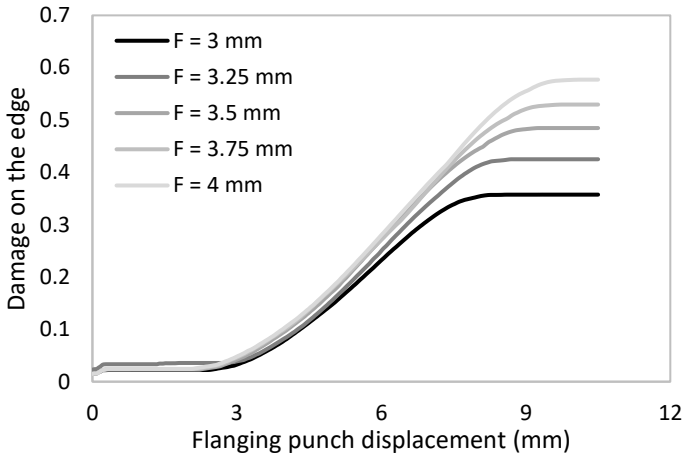

Figure 68 - Damage evolution in the edge zone during the flanging stage for different flange lengths (F).

The flange length is an important consideration in the process as it affects considerably the quality of the mechanical interlock between the two sheets. Although for a flange length of 3 mm the damage in the end of the flanging stage is much lower, figure 69 (a) shows that in the hemming stage no mechanical interlock is formed as the flange is too short and it is compressed before it overlaps the inner sheet to form a proper mechanical interlock. Nonetheless, for higher flanges (figure 69 (e)) fracture can occur in the outer sheet before a mechanical interlock is formed with both sheets. The value of this parameter should be carefully considered in order to obtain a proper mechanical interlock without the occurrence of fracture.

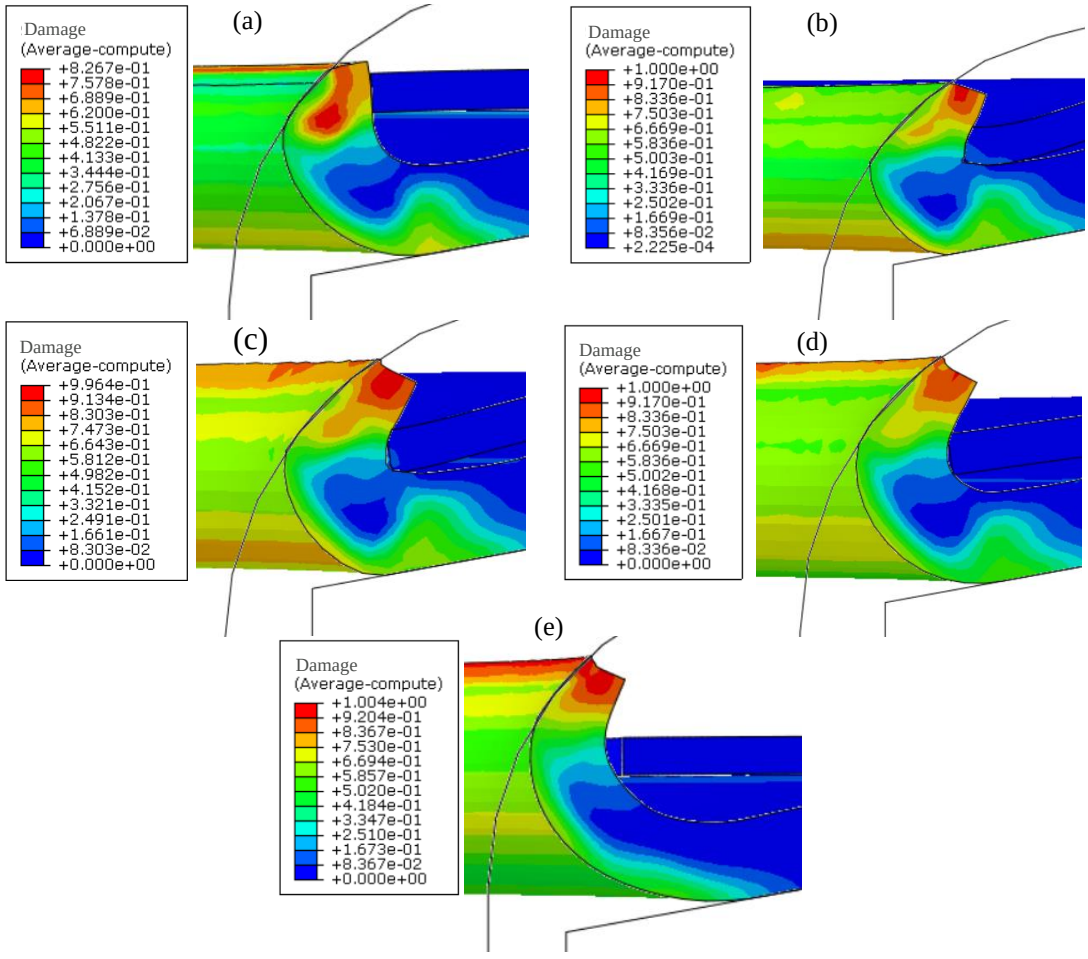

Figure 69 - Damage distribution in the outer sheet during the hemming stage for different values of flange lengths (F): (a) F = 3 mm, (b) F = 3.25 mm, (c) F = 3.5 mm, (d) F = 3.75 mm and (e) F = 4 mm.

The flange length also influences the required force in the flanging punch during the flanging stage, which is shown in figure 70. The higher the flange length the higher is the required force in the flanging punch as for higher flanges more material is being deformed. Along with the mechanical interlock quality and fracture considerations, this effect should also be taken into account in the designing of the hole hemming process.

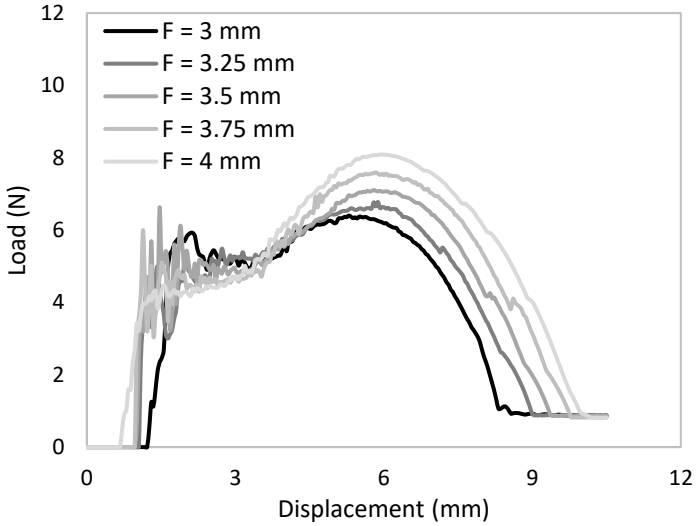

Figure 70 - Effect of the flange length on the required force in the flanging punch during the flanging stage.

Figure 71 shows the effect of the fillet radius of the hemming punch (R) in the damage of the outer sheet at the first contact with the inner sheet. The higher the fillet radius the higher will be the contact length between the outer and inner sheet and the better will be the quality of the resulting mechanical interlock. If the fillet radius is too low, no mechanical interlock is obtained as the flange is compressed by the hemming punch without overlapping first the inner sheet (figure 71 (a)).

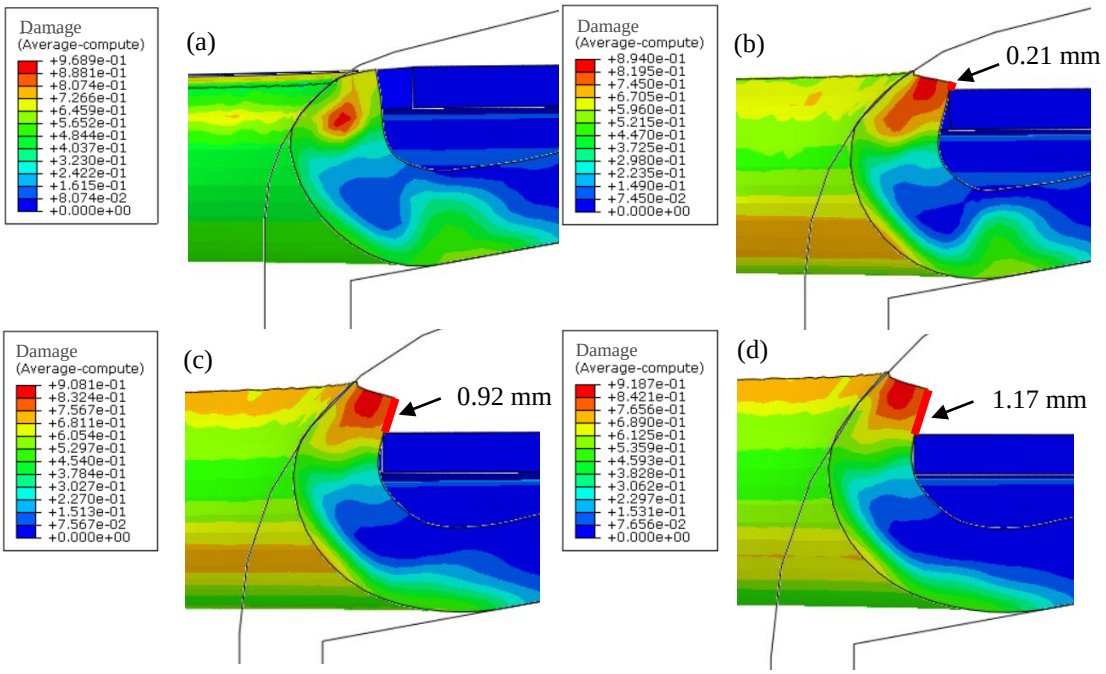

Figure 71 – Damage distribution in the outer sheet and contact length between the outer and inner during the hemming stage for different values of hemming punch fillet radius: (a) R = 4 mm, (b) R = 6 mm, (c) R = 8 mm and (d) R = 10 mm.

The graphic on figure 72 shows the damage evolution in the bend zone during the hemming stage. For higher fillet radius the flange of the outer sheet enters in contact with the hemming punch earlier than for lower fillet radius and so the damage growth also starts earlier. Furthermore, for higher fillet radius the first contact with the inner sheet and the mechanical interlock are made for lower hemming punch displacements and in the end the resulting damage in the bend zone is relatively the same.

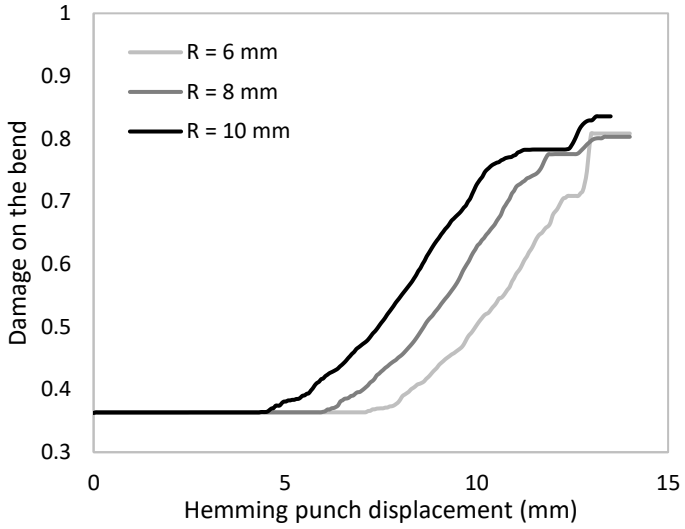

Figure 72 - Damage evolution in the bend zone during the hemming stage for different hemming punch fillet radius (R).

It was also investigated the effect of the fillet radius of the hemming punch on the required force in the hemming punch during the hemming stage, which is shown in figure 73. The higher the fillet radius the higher is the required force in the hemming punch as the hemming punch enters in contact with a higher surface area of the outer sheet flange. Furthermore, the forces involved in the hemming punch are much higher than the forces involved in the flanging punch and in the end of the stroke the forces increase exponentially, which is due to the compression of the materials while the mechanical interlock is being formed.

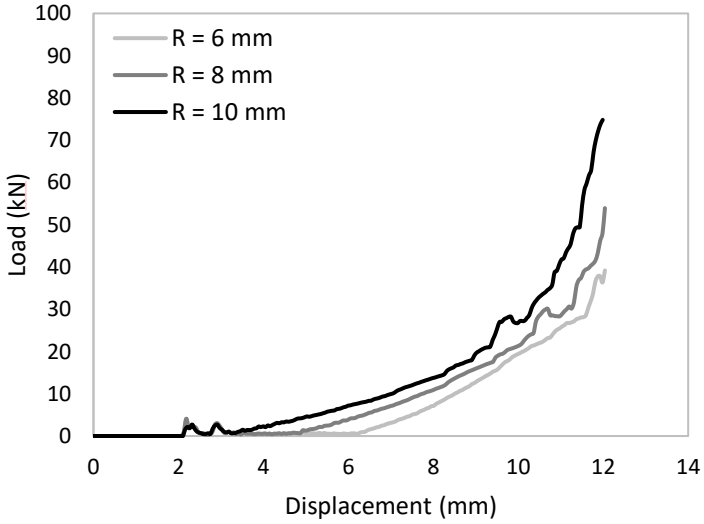

Figure 73 - Effect of the fillet radius of the hemming punch (R) on the required force in the hemming punch during the hemming stage.

Figure 74 (a) and (b) shows the damage in the outer sheet at the end of the flanging stage and figure 74 (c) and (b) the damage in the outer sheet for the same hemming punch displacement for different outer sheet hole radius (R_o) as the flange remains constant. By increasing the hole radius of the outer sheet there is a significant reduction of damage in the edge zone, which can also be seen in the damage evolution along the process in figure 75. In the case of the bend zone, figure 76 shows that there is an increase of the damage with the increase of the hole radius, but not as significant as the damage increase in the edge.

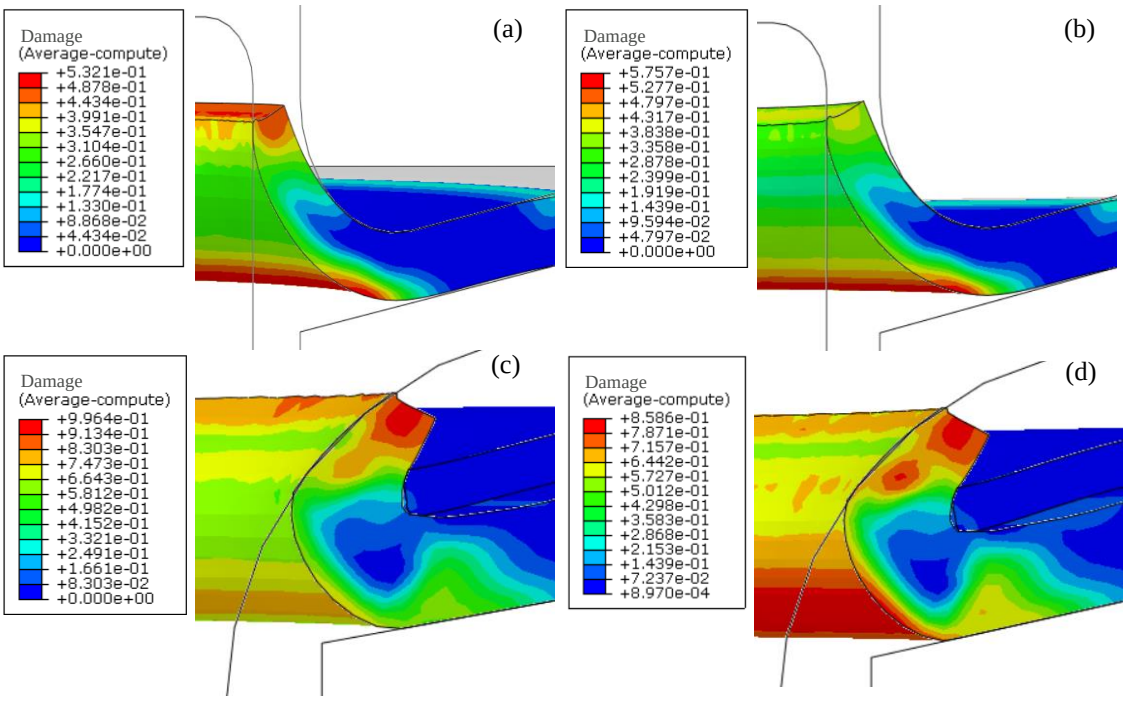

Figure 74 - Damage distribution in the outer sheet during the hole hemming process for different values of R_o. (a) and (b) damage distribution in the end of the flanging stage for R_o = 7 mm and R_o = 9 mm, respectively, (c) and (d) damage distribution in the middle of the hemming stage for R_o = 7 mm and R_o =

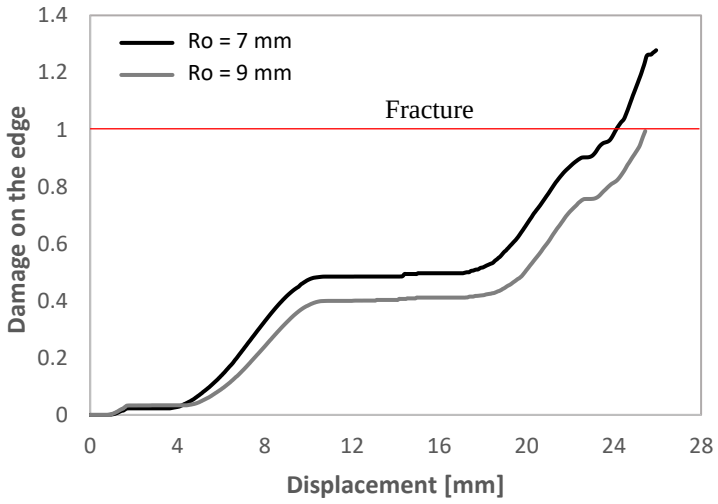

Figure 75 - Damage evolution in the edge zone during the hole hemming process for different outer sheet hole radius (R_o).

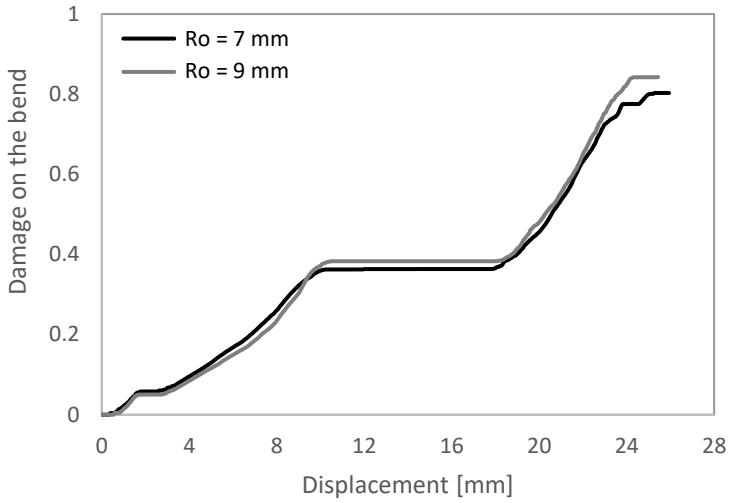

Figure 76 - Damage evolution in the bend zone during the hole hemming process for different outer sheet hole radius (R_o).

Concerning the inner sheet, during the process it undergoes low quantities of deformation. Even though, fracture in the inner sheet occurred in any of the previous cases (figure 77 (a) shows the damage in the inner sheet for the case 10, corresponding to the figure 74 (d)). Nonetheless, to save computational time in the previous simulation the number of elements and time period of the numerical model were kept to a minimum, which can negatively impact the results especially in the inner sheet which has much lower fracture strains. The case 10 was repeated but this time the 5 elements through thickness were changed to 10 elements. As shown in figure 77 (b), fracture no longer occurs in the edge, with the damage in that location being reduced about 75%, while fracture now occurs occasionally in the bottom side of the inner sheet. The contact interaction between the sheets is complex and sometimes the numerical model faces increments difficult to solve which may originate inaccurate results. With vision on this, the same case was repeated (again with 10 elements through thickness) using a three times higher time period (from 0.0005 to 0.0015) and the results are presented in figure 77 (c), showing that fracture no longer occurs in the inner sheet. As element deletion is activated in the numerical simulations of the destructive tests, 10 elements through thickness in the inner sheet are used on those simulations and also a much higher time period than the ones that were used to simulate the hole hemming process. It should be noted that when the elements through thickness of the outer sheet and the time period were increased, the results obtained for the outer sheet were the same.

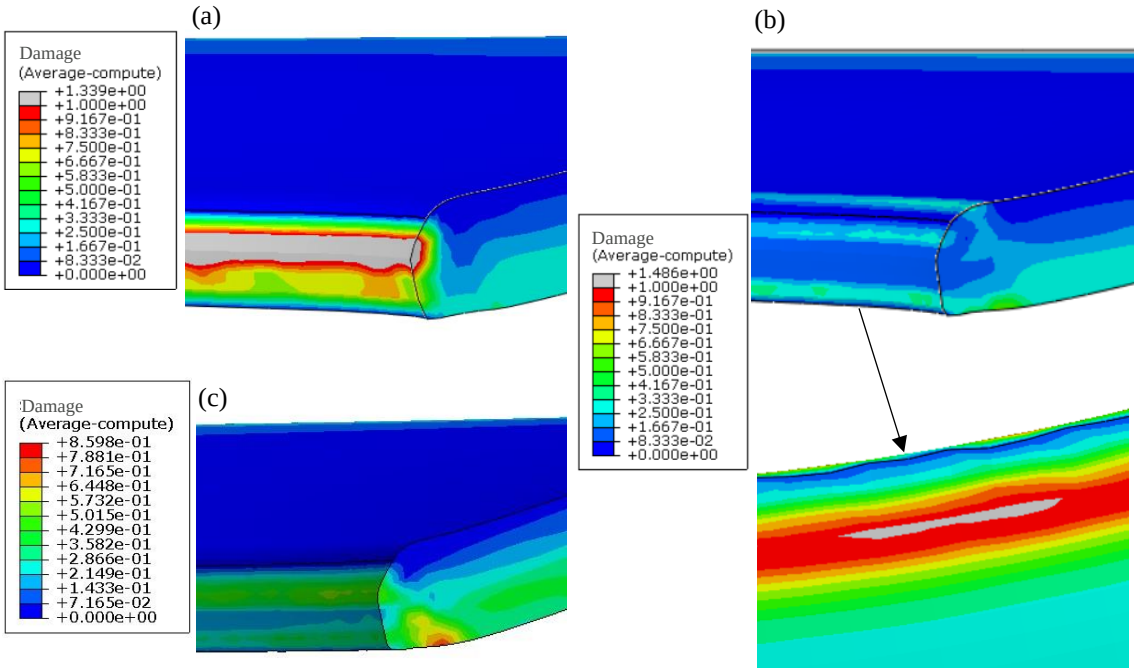

Figure 77 - Damage distribution in the inner sheet in the end of the hemming stage (a) using 5 elements through thickness and a time period of 0.0005, (b) using 10 elements through thickness and a time period of 0.0005 and (c) using 10 elements through thickness and a time period of 0.0015.

6.3 Process window

Figure 78 shows the process window for different F values. The contact between the inner and outer sheet occurred relatively at the same displacement for any value of F and the contact length increases with the increase of the flange length. Besides the contact length, the quantity of displacement between the contact and before fracture is also important, as the higher is the displacement the tighter will be the mechanical interlock. For these reasons, it was considered F = 3.5 mm the optimal parameter.

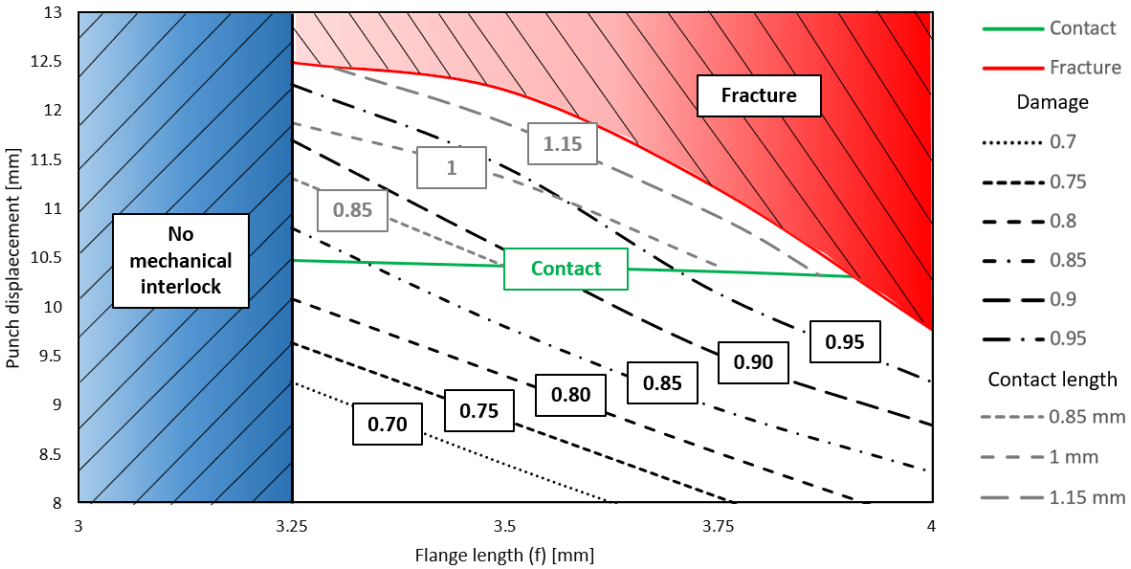

Figure 78 – Finite element process window for different values of flange length (F).

Figure 79 shows the process window for different R values and resumes the previous conclusions: Higher fillet radius leads to an earlier contact with the inner sheet and produces higher contact lengths, which produces higher quality joints. Furthermore, the contact, fracture and damage lines are relatively parallel between each other, therefore the damage evolution and the displacement between the contact and fracture are relatively the same.

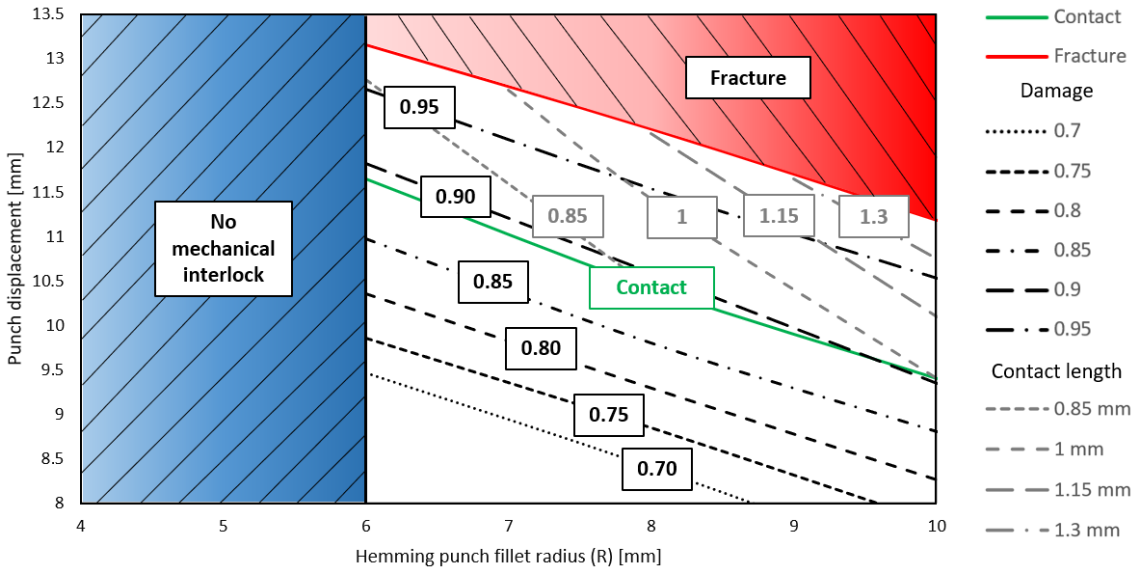

Figure 79 - Process window for different values of hemming punch filler radius (R).

Table 21 shows the optimal process parameters found for the hole hemming process.

Table 21 – Optimal process parameters for the hole hemming process.

fr_d (mm)	R (mm)	R_d (mm)	R_o (mm)	F (mm)
4	10	12.5	9	3.5

As for the same geometry of dies and punches it is possible to use different flange lengths, in the experimental hole hemming tests it was also performed tests for R_o = 8.5 mm (F = 4 mm) and R_o = 8 mm (F = 4.5 mm). Figure 80 shows and compares the FE damage contours results between these cases and figure 81 shows the respective process window. As shown, it is expected in the experimental tests to be possible to make a joint without cracks for the cases of F = 3.5 mm and F = 4 mm.

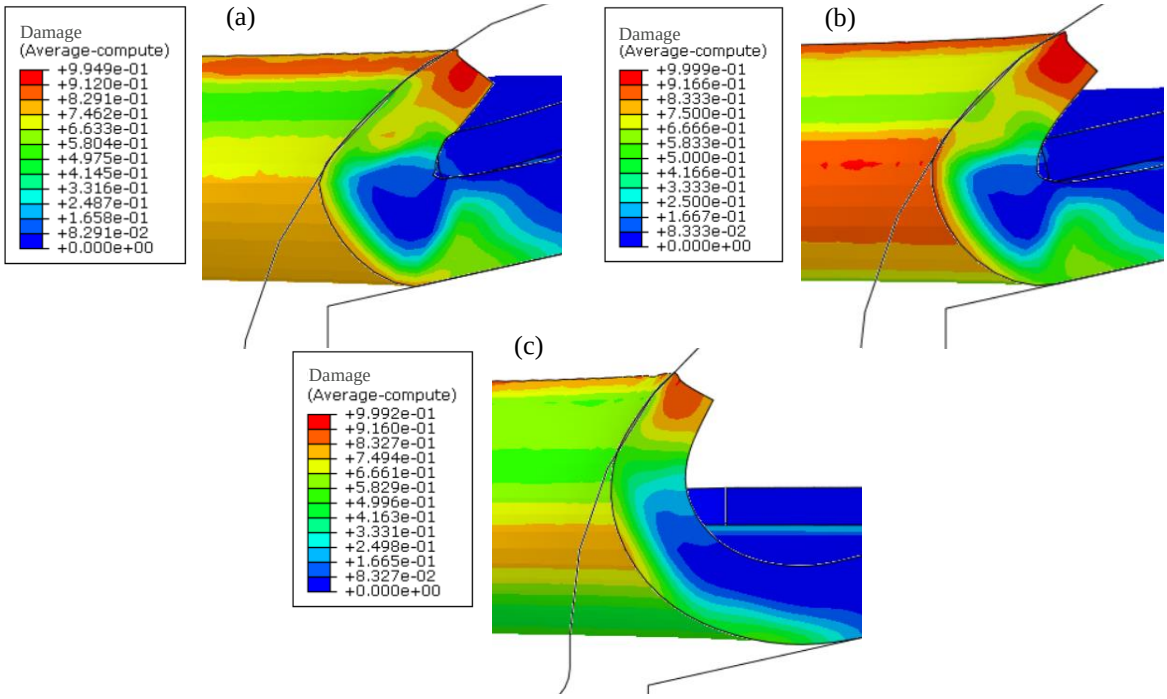

Figure 80 - Damage distribution in the outer sheet during the hemming stage for the experimental cases: (a) F = 3.5 mm, (b) F = 4 mm and (c) F = 4.5 mm.

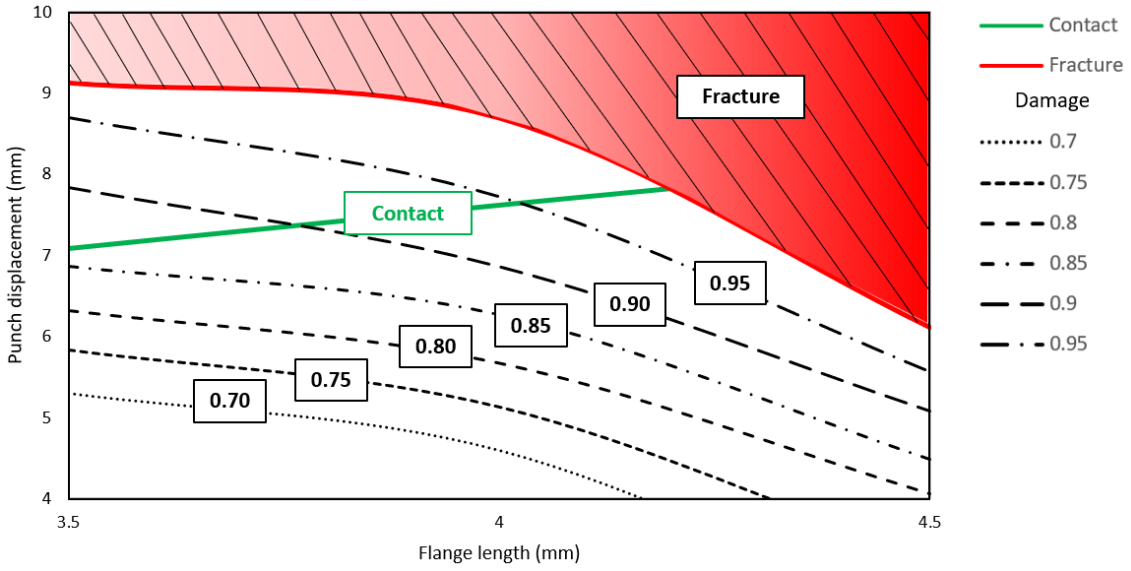

Figure 81 – Process window for the experimental cases.

6.4 Hole design

In the previous designs, the edge zone always exhibited high values of damage, limiting the process window. In order to decrease the damage in the edge zone, a new hole design for the outer sheet was developed based on the creation of four branches in the hole edge, as shown in figure 82. It was expected that the equivalent plastic strain created in the edge is significantly reduced using the new design.

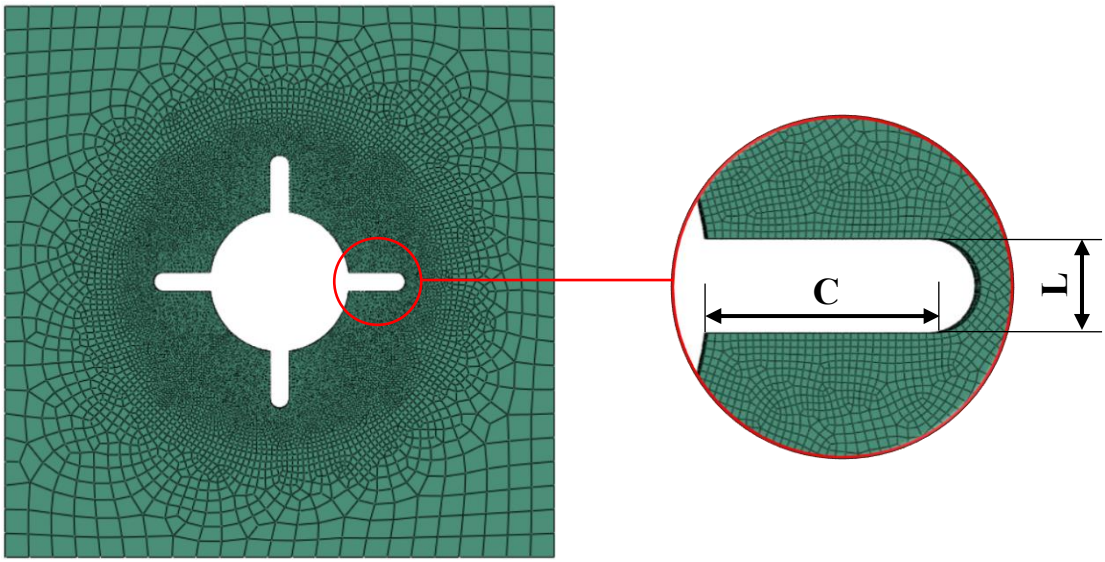

Figure 82 - New outer sheet hole design consisting in four branches.

Figure 83 shows the damage contours in the outer sheet at the moment of fracture using the case 10 process parameters and branches with C = 6 mm and L = 2.5 mm. Figure 84 shows that the damage in the edge was significantly reduced as intended. Nonetheless, this design creates in the branch a new critical region.

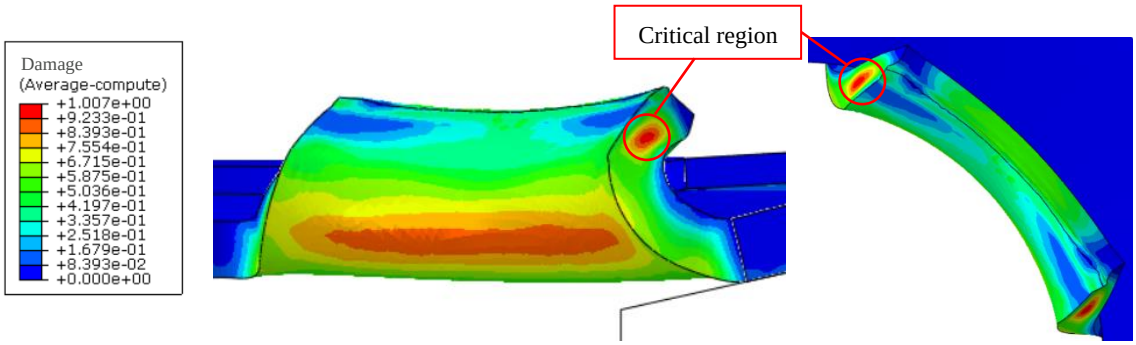

Figure 83 - Damage distribution in the outer sheet during the hole hemming process using hole branch design (C = 6 mm and L = 2.5 mm).

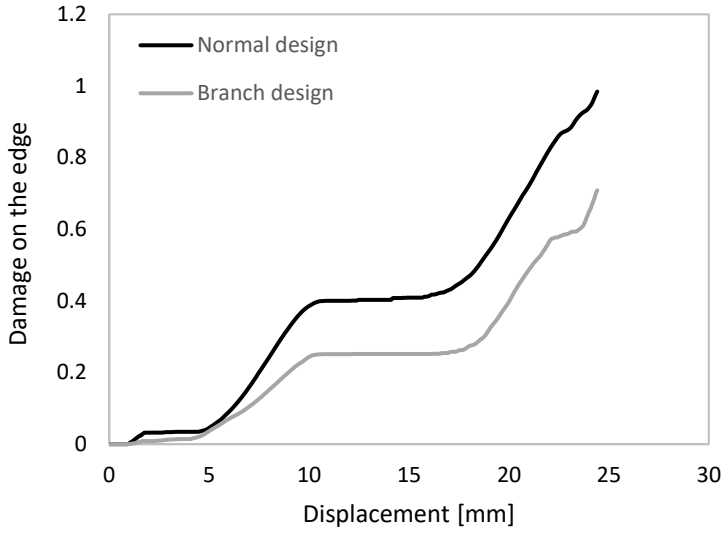

Figure 84 – Damage evolution in the edge zone during the hole hemming process for different hole designs.

The loading path of the branch region is shown in figure 85. During the flanging stage and before the contact with the inner sheet in the hemming stage the branch region undergoes low quantities of plastic deformations between pure shear and uniaxial tension stress states. Nonetheless, after contact with the inner sheet the deformation sharply increases and the loading path shifts to a stress state between pure shear and uniaxial compression.

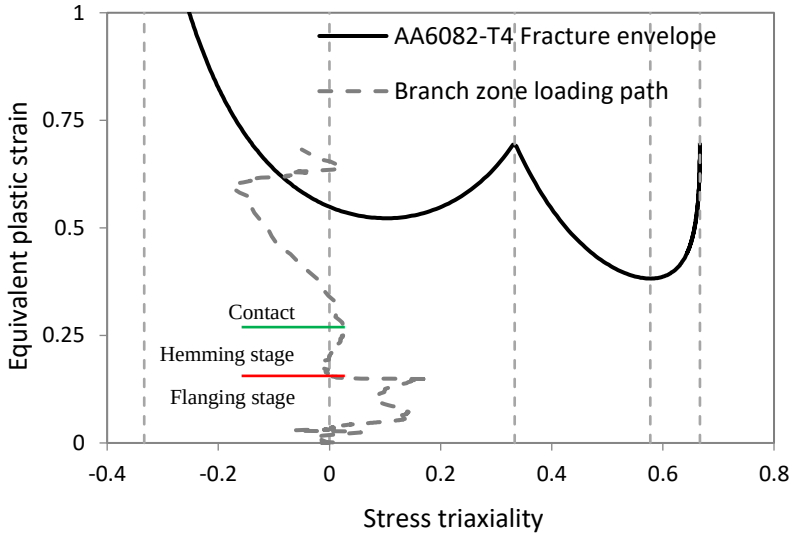

Figure 85 - Loading path of the branch zone critical region along the hole hemming process.

In spite of that, the results in the critical region may be overestimated by FE model and so it would be interesting in another work to investigate the possibility of this new design to be used in cases where the damage in the edge limits the process window.

6.5 Experimental hole hemmed joints

Figure 86 shows one of the resulting specimens for each studied diameter in the end of the flanging stage. For higher diameters the flange lengths are lower and, as predicted, no specimen exhibited fracture after this stage. Figure 87 shows a comparison between the experimental and numerical loading displacement curves during the flanging stage for each case and there is a good agreement between the curves.

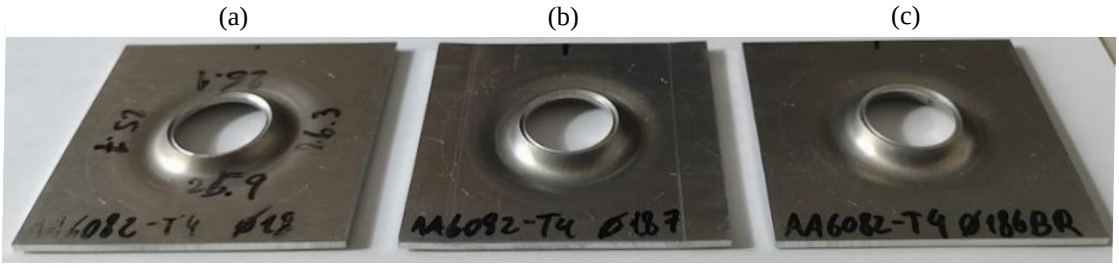

Figure 86 - Hole hemming specimens after the flanging stage: (a) F = 3.5 mm (Ro = 9 mm), (b) F = 4 mm (Ro = 8.5 mm) and (c) F = 4.5 mm (Ro = 8 mm)

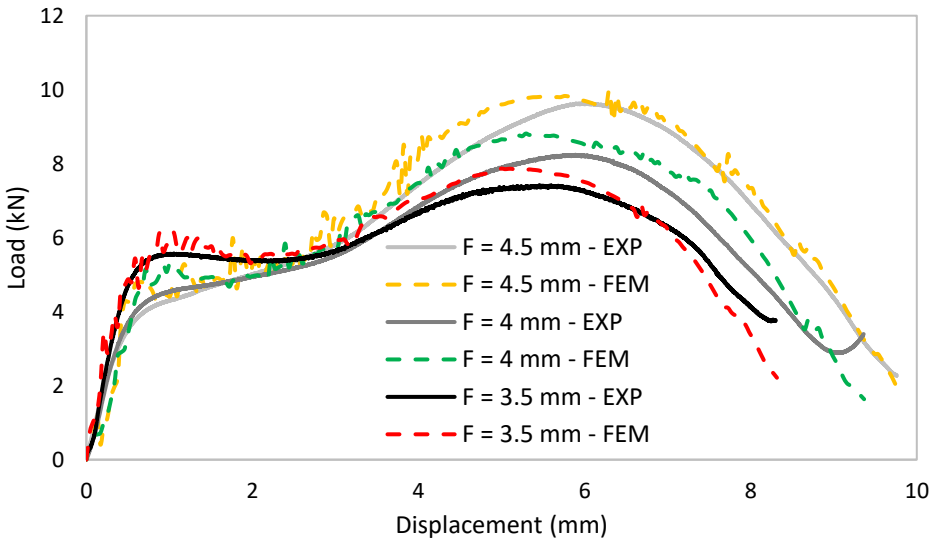

Figure 87 – Flanging stage load-displacement curves comparison between the experimental and numerical results.

Two of the hole hemmed joints after the hemming stage for the F = 4.5 mm case are shown in figure 88. As expected from the FE simulations, fracture occurred in the edge of the outer sheet. Nevertheless, it was possible to obtain tight mechanical interlocks. In figure 89 it is shown a comparison between the experimental and numerical load-displacement curves during the hemming stage for the F = 4.5 mm case. For lower displacements the experimental load is higher, which may be due to the friction between the outer sheet and the hemming punch. For higher displacements the load is less dependent on the friction and more dependent on the bending of the outer sheet and there is a better correlation between the curves.

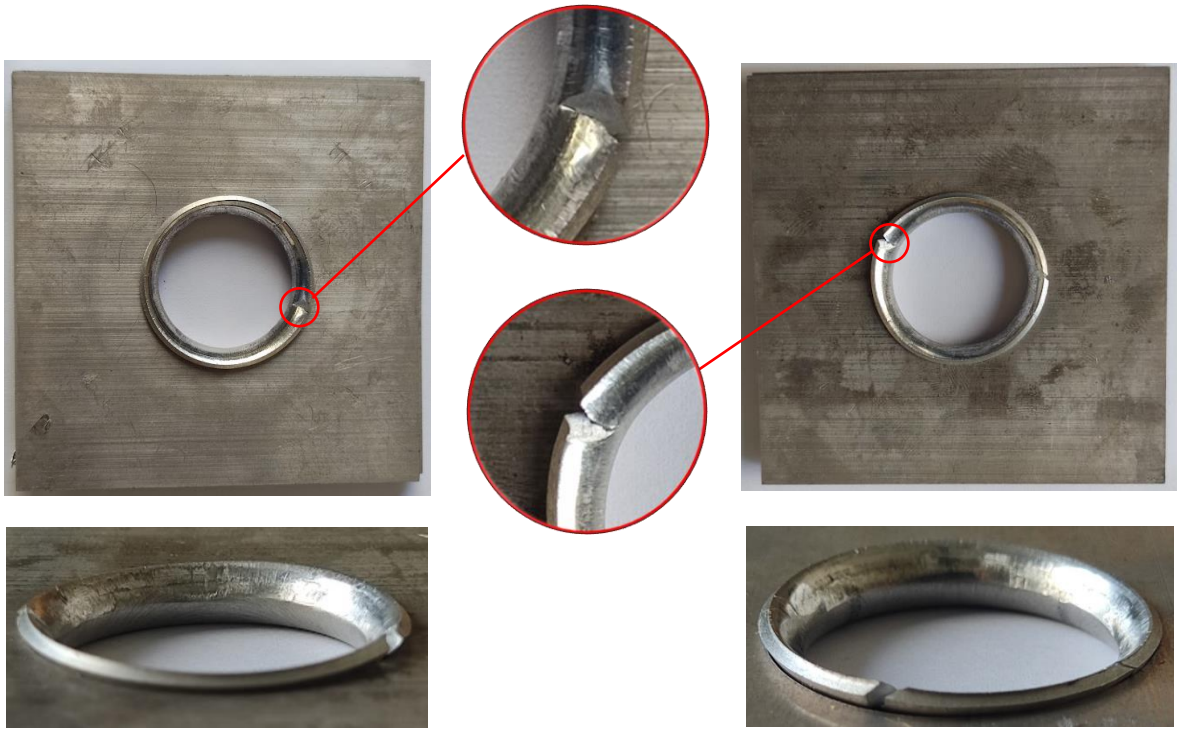

Figure 88 – Hole hemmed joints for the F = 4.5 mm case.

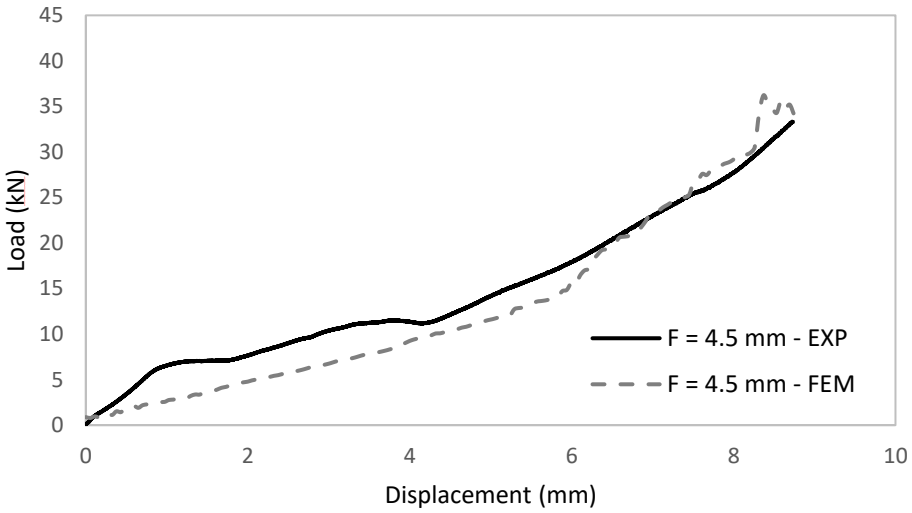

Figure 89 - Hemming stage load-displacement curves comparison between the experimental and numerical results for F = 4.5 mm.

Figure 90 shows two experimental hole hemmed joints for the F = 4 mm case, one without cracks (figure 90 (a)) and one with cracks (figure 90 (b)), and the respected hole hemmed joints obtained from the finite element analysis (figure 90 (c) and (d)). The difference between these two cases is the displacement of the hemming punch, as for higher displacements fracture will occur on the edge. As shown, the crack propagation in the FE model is similar to what was experimentally verified. Fracture initiates at the edge and progresses towards the middle section.

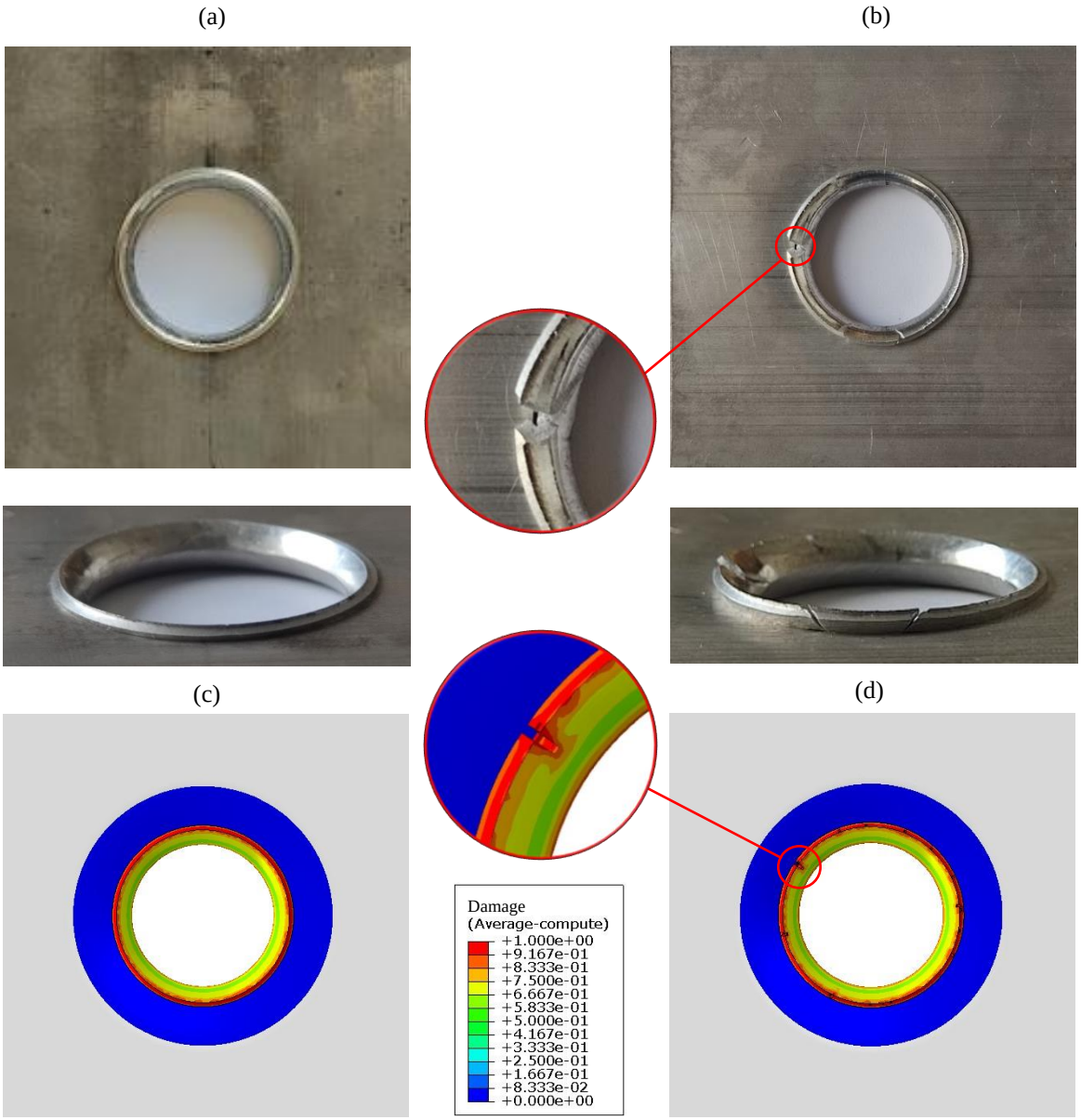

Figure 90 - Hole hemmed joints for the F = 4 mm case: Experimental (a) joint without cracks and (b) joint with cracks, and FE (c) joint without cracks and (d) joint with cracks.

Table 22 shows the fracture prediction error related to the critical displacement of the hemming punch, which is the displacement where fracture occurs in the finite element analysis, compared with the experimental data. Different displacements were tested to verify the accuracy of the MMC fracture criterion. It was possible to obtain a mechanical interlock in all the tests and fracture was predicted with a maximum error of 4.8%.

Figure 91 shows a comparison between the experimental and numerical load-displacement curves during the hemming stage and the same tendency of the previous case is verified.

Table 22 – FE model fracture prediction error.

Joint	Experimental hemming punch displacement (mm)	Visible cracks	FE predicted fracture displacement (mm)	Relative error (%)
1	8.01	No	8.69	-
2	8.06	No		-
3	8.27	Yes		4.8%
4	8.32	No		-
5	8.35	No		-
6	8.60	Yes		1.0%
7	8.66	Yes		0.3%
8	9.20	Yes		-

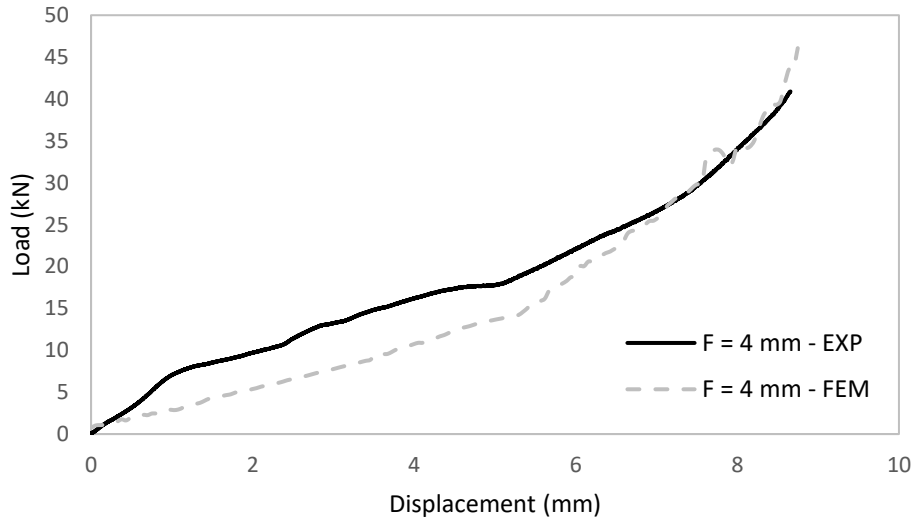

Figure 91 - Hemming stage load-displacement curves comparison between the experimental and numerical results for F = 4 mm.

For the case of F = 3.5 mm, it was difficult to obtain a mechanical interlock. Figure 92 (a) shows one of the failed joints where no mechanical interlock as the outer sheet did not overlap the inner sheet. Figure 92 (b) shows the flange of the outer sheet after the hemming stage. The flange in the end of the hemming stage is compressed and so it does not overlap the inner sheet to perform a mechanical interlock. This is due to the length of the flange in this case which is smaller than the other cases. It is more obvious in the experiments because of the problems related to the alignment between the inner sheet, outer sheet and hemming punch, which does not exist in the numerical model. Furthermore, the friction between the outer sheet and the hemming punch can have a significant impact in the joint, as for high frictions the flange is compressed against the hemming punch instead of sliding in it to overlap the inner sheet.

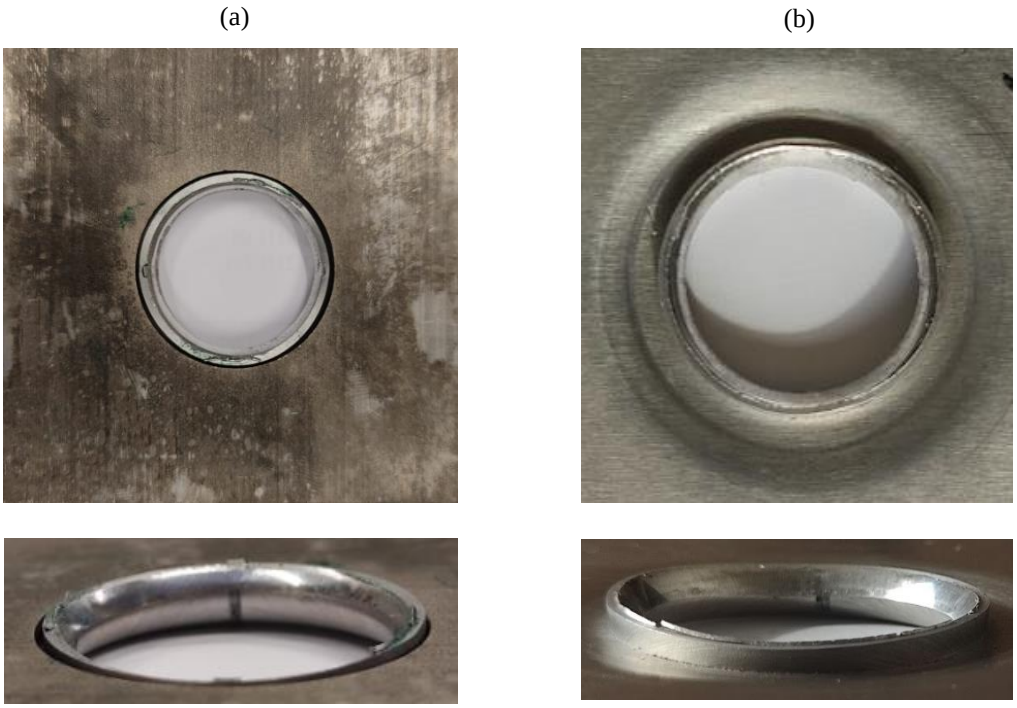

Figure 92 – First attempts for the F = 3.5 mm case: (a) failed joint and (b) compressed flange after the hemming stage.

Lubricant was then used to reduce the friction between the hemming punch and flange of the outer sheet. Figure 93 shows the only two joints where it was possible to obtain a mechanical interlock using different punch displacements. As shown, it was still not possible to obtain a mechanical interlock in all the perimeter of the inner sheet hole edge. In the case of figure 94 (b), where higher displacement was applied, there is the occurrence of fracture. Despite the lubricant helped to obtain a mechanical interlock, in the present case a flange of F = 3.5 mm. is not enough to create a good mechanical interlock without fracture. Figure 94 shows a comparison between the experimental and numerical load-displacement curves during the hemming stage and it can be made similar conclusions to the previous cases.

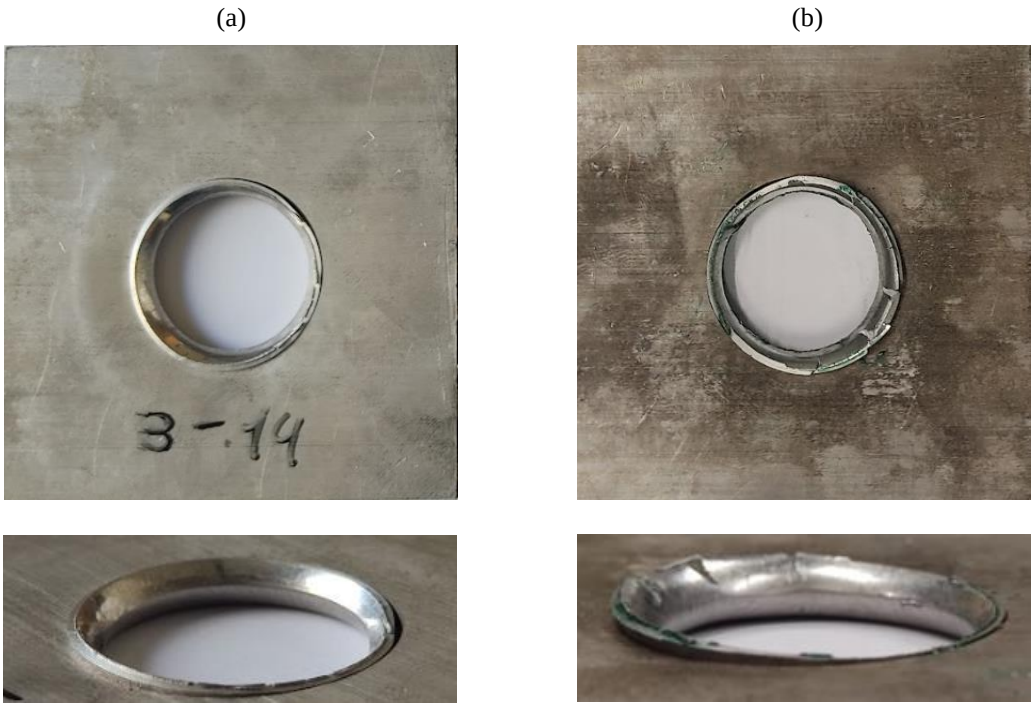

Figure 93 - Hole hemmed joints for the F = 3.5 mm case after applying lubricant: (a) lower displacement (b) higher displacement.

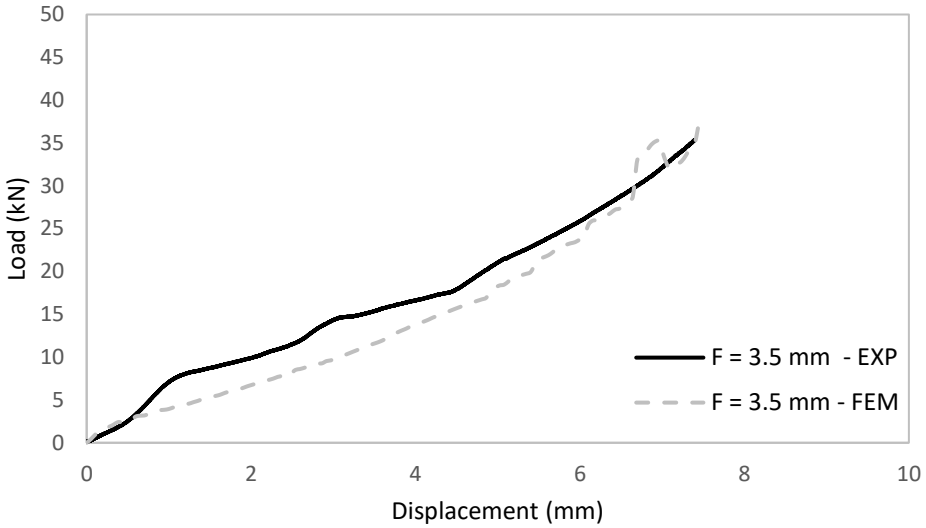

Figure 94 - Hemming stage load-displacement curves comparison between the experimental and numerical results for F = 3.5 mm.

6.6 Destructive tests

Figure 95 shows the joints that were used to perform the single lap shear tests for the F = 4 mm case. The joint no.1, figure 95 (a), has a small misalignment between the sheets, which can be due to machining problems and not aligning correctly the holes before the hemming stage. The joints no.2 and no.3, shown in figure 95 (b) and (c) respectively, do not present misalignment and fracture defects. The joint no.4, figure 95 (d), presents visible multiple cracks along the edge of the outer sheet flange.

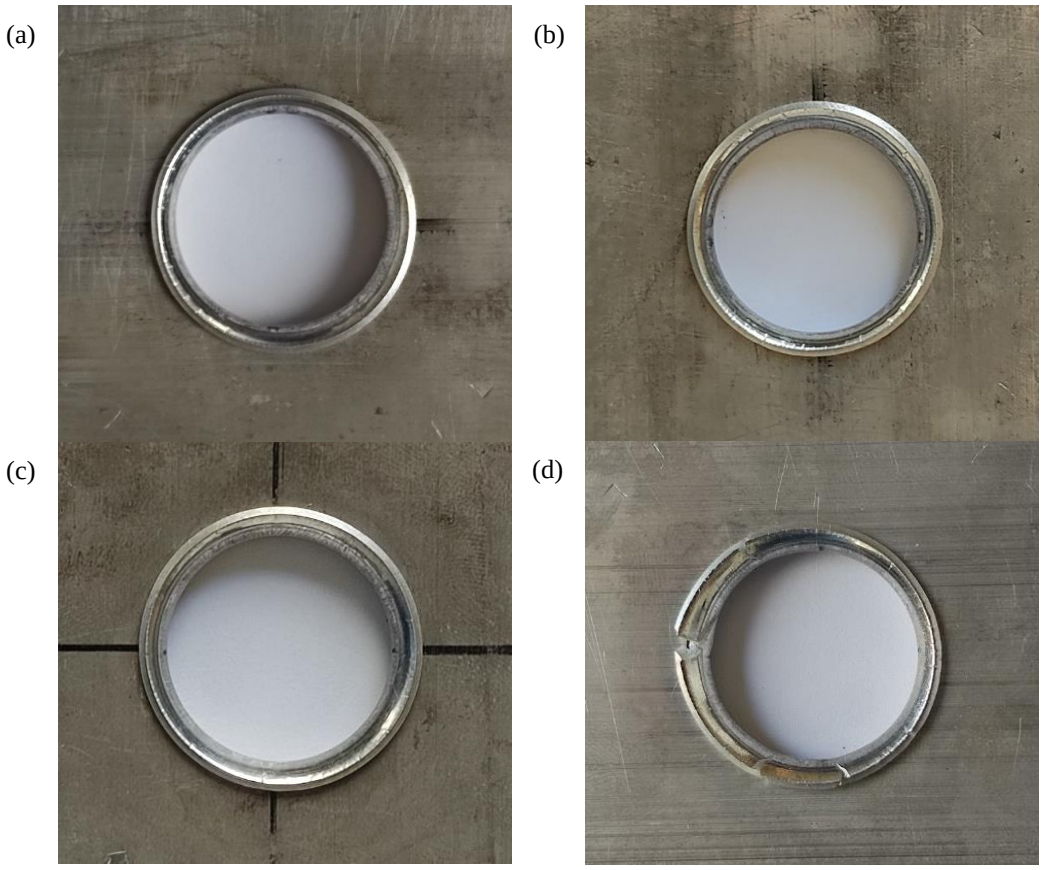

Figure 95 - Joints for the single lap shear tests: (a) joint no.1, (b) joint no.2, (c) joint no.3 and (d) joint no.4.

Figure 96 shows the respective experimental load-displacement curves of the performed single lap shear tests joints presented in figure 96. For the joint no.1, failure occurs for lower load and displacement when compared with the other tests. The joint no.1 was not well aligned, so the premature failure can be due to this. In the case of joint no.4, the load reached was about 2.5 kN and lower than the load of joint no.2 and no.3, which possible reason is stated later in this chapter. For the joints no.2 and no.3 in which the sheets were well aligned and no fracture was verified, a good correlation between their load-displacement curves was obtained. A maximum shear load of almost 2.9 kN was achieved and the fracture displacement of both tests was almost the same.

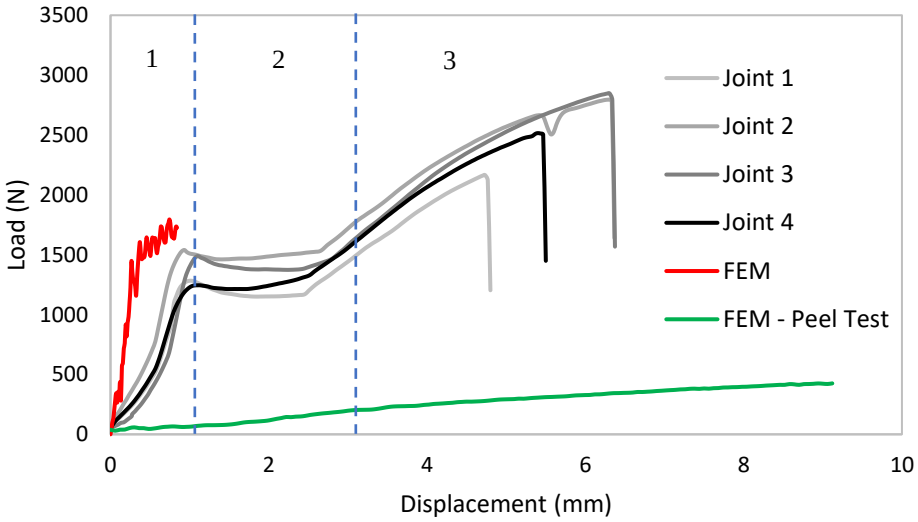

Figure 96 - Load-displacement curves of the experimental and numerical single lap shear tests for the F = 4 mm case and numerical load-displacement curve for the peel test.

During the single lap shear tests three different stages were distinguished. In the first stage (figure 96 1), the force increases sharply as the hole edge of the inner sheet is being compressed against the outer sheet flange, causing the inner sheet to slightly bend as shown in figure 97 and 98 (a). In the second stage (figure 96 2), the load slightly decreases and then stabilizes. This happens as the inner sheet starts to yield and the bending angle increases, as shown in figure 97 and 98 (b). This confirms that the joints are in hole bearing failure mode. In the third stage (figure 96 3), the load once again increases but with a lower rate when compared with the first stage. This happens as the bending of the inner sheet increases the contact area between the inner sheet and the outer sheet flange figure 97 and 98 (c), which lead to the verified increase of the load. Ultimately, fracture (figure 97 and 98 (d)) rapidly propagates in the inner sheet causing a load drop and the test to stop.

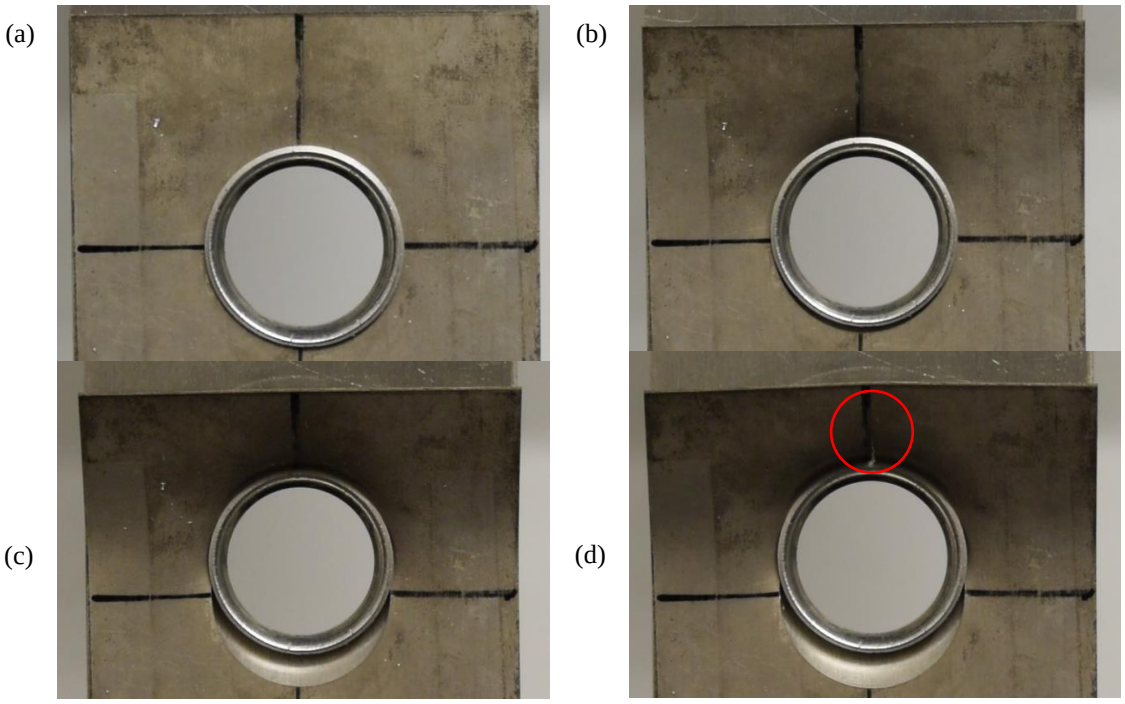

Figure 97 - Front view of the joint aspect during the single lap shear test: (a) end of stage 1, (b) end of stage 2, (c) during stage 3 and (d) end of the test.

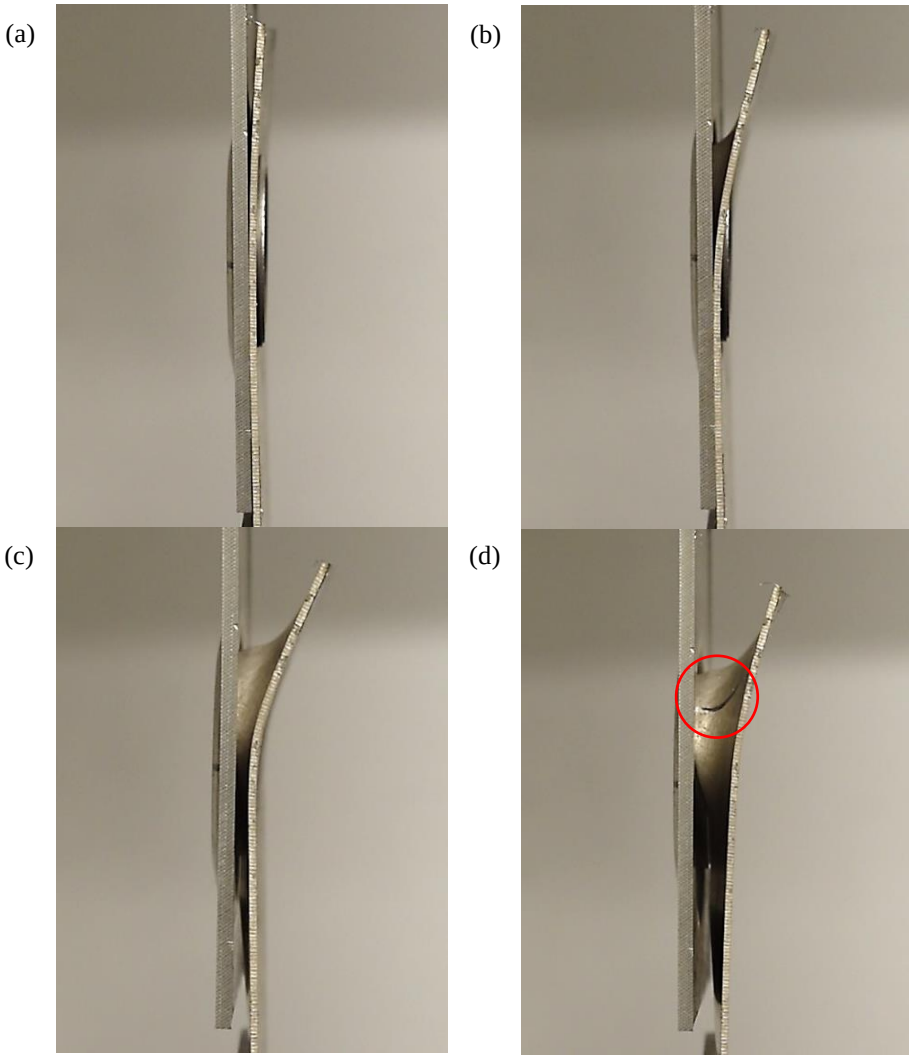

Figure 98 – Side view of the joint aspect during the single lap shear test: (a) end of stage 1, (b) end of stage 2, (c) during stage 3 and (d) end of the test.

The graphic in figure 96 also indicates the finite element predicted load-displacement curves of the single lap shear test and the peel test. As seen, in the finite element model the simulation stops with an error between the stage 1 and 2, failing to predict the majority of the test. It was atempted to increase the time period and refine the elements of the inner sheet but it ended with the same result. The complex contact interaction between two deformable bodies combined with element deletion and a sensitive fracture envelope for the inner sheet may lead to inacurate results. Because of this, in a future work the single lap shear test FE model should be improved. Furthermore, in the case of the peel test it was verified a maximum load of 425 N as the inner sheet was deformed and came out of the mechanical interlock with no deformation occuring in the outer sheet, as shown in figure 99.

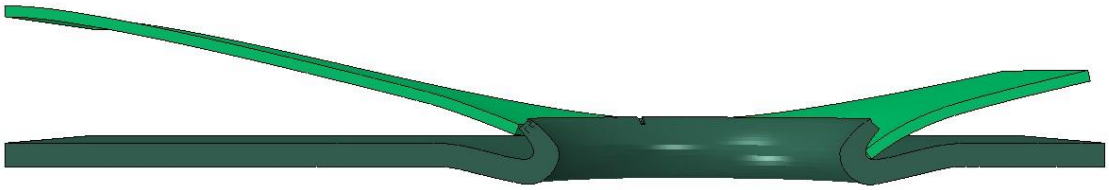

Figure 99 – Failure mode of the FEM peel test.

For the joint no.4, one of the cracks in the flange of the outer sheet may inderectly contributed to a premature failure of the joint. As shown in figure 100, the fracture in the inner sheet occured in a location that was in direct contact with a outer sheet flange crack. As the contact in that location is not good and the crack has a sharp edge, these factors may lead to premature failure of the joint.

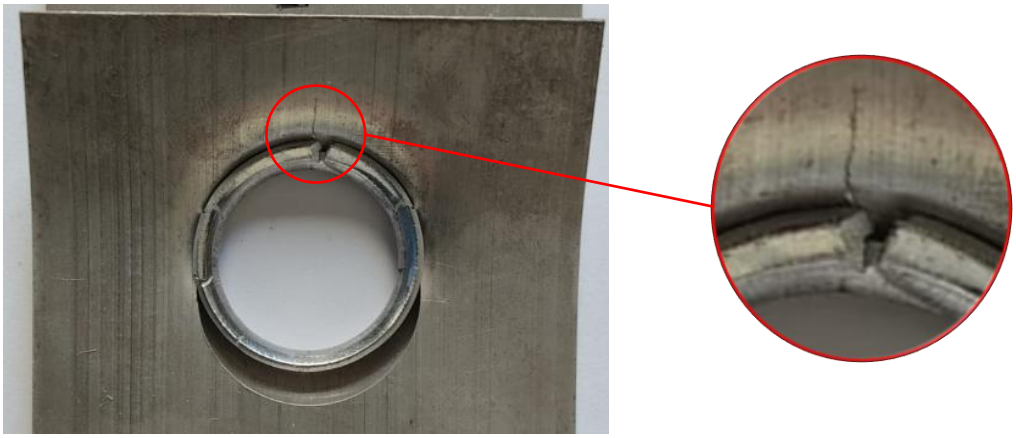

Figure 100 - Joint 4 after the performance of the single lap shear test.

In figure 101 (a) and (b) it is shown the aspect of the joint after the performance of the single lap shear test. The hole bearing mechanism is evident in the magnesium sheet. The magnesium sheet, figure 101 (c), is deformed while the aluminum sheet, figure 101 (d), is not, as the magnesium sheet not only have a sligtly lower strength but also because its thickness is more than two times lower than the aluminum sheet and the aluminum sheet also undergone strain hardening during the flanging and hemming stage. Because it has a slow failure mechanism, the hole bearing verified is preferable to other failure mechanisms such as net tension and shear-out which lead to unpredictable catastrophic failures. Furthermore, after the second stage the joint could withstand two times the force obtained in the end of the first stage, which increases the safety benefitions.

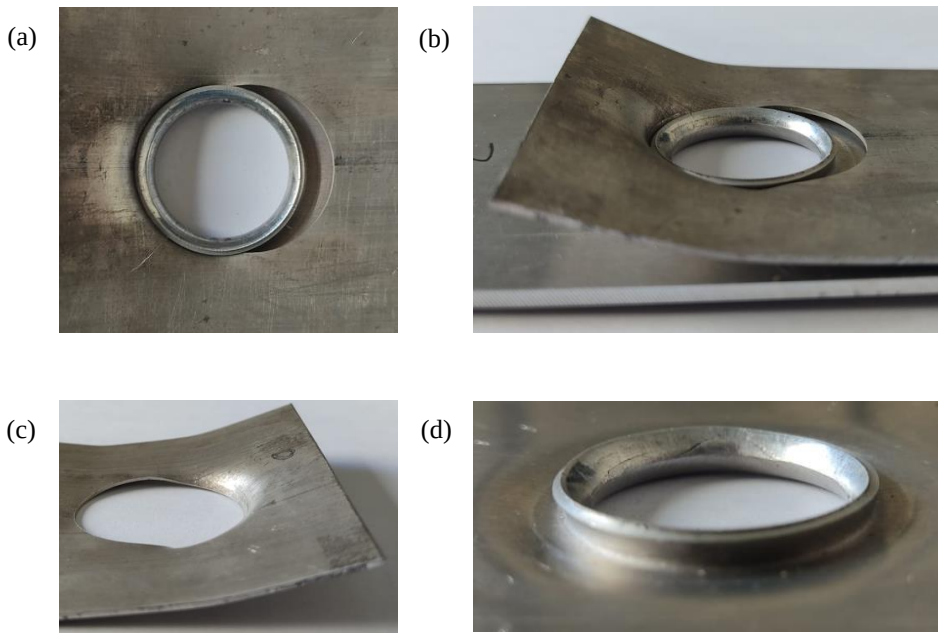

Figure 101 – Aspect of a hole hemmed joint and sheets after the single lap shear test: (a) front view and (b) side view of the hole hemmed joint, (c) magnesium sheet and (d) aluminum sheet.

6.6.1. Comparison of the hole-hemmed joints with other joints

The purpose of the hole hemming process is to join materials with very different mechanical properties, or in the present work materials with very different formability. It is difficult to find in the literature other joining processes by plastic deformation to join magnesium and aluminum alloys that do not involve heat input, which increases the complexity of the joint, and additional elements, which increases the weight of the joint. One case found was from Wen et al. [61], which joined AZ31 to AA6063 by flat hole clinching. Table 23 shows a comparison between the estimated strength of different joints between magnesium and aluminum alloys and the estimated variation of the mass. The strength is calculated based on the maximum load divided by the resisting area, which depends in the failure mode. The variation of mass is the ratio between the final mass of the joint and the initial mass of the volume that will be occupied by the joint.

Table 23 – Hole hemming process compared with other joining by forming processes.

Process	Aluminum alloy	Magnesium alloy	Failure mode	Mass variation (%)	Strength (MPa)
Hole hemming	AA6082-T4 t = 2.05 mm	AZ31 t = 0.85 mm	Hole Bearing	- 48.2	134 MPa
Flat hole clinching [61]	AA6063 t = 0.8 mm	AZ31 t = 1 mm	Shear failure	- 44.6	79 MPa
Rotating hammer riveting [62]	AA7055-T6 t = 2.6 mm	AZ31 t = 2.4 mm	Shear failure	+ 945	132 MPa
Friction self-pierce riveting [63]	AA6061-T6 t = 1 mm	AZ31 t = 2 mm	Hole Bearing	+ 630	151 MPa
Self-pierce riveting [63]	AA6061-T6 t = 1 mm	AZ31 t = 2 mm	Hole Bearing	+ 585	74 MPa

In the studied cases only the friction self-pierce riveting exhibits higher strength than the hole hemmed joint, which has an initial strength of about 71 MPa but it can reach a maximum strength of about 134 MPa. Nevertheless, the addition of the rivet increases substantially the weight of the joint. Furthermore, the hole hemmed joint was the process that presented the higher mass reduction. Furthermore, as it a slower failure mechanism, the hole bearing mechanism of the hole hemming process is also preferable to the shear failure mechanism of the flat hole clinching and rotating hammer riveting. Finally, the hole hemmed joints give a more clean and beautiful aspect of the joint, especially when compared with rivet-based joints.

There are however some drawbacks related to the hole hemmed joints. The necessity of drilling or punching holes is an additional step to the process that may create alignment problems. The joint also has a hole, unless a solution is found to seal the hole then it cannot be used in applications where sealing is mandatory.

The hole hemming process could successfully join materials with very different formability, obtaining a satisfactory joint strength without an additional element and heat input. Thus, the hole hemming process has a great potential to be applied to dissimilar material joining.

7 Conclusion

In this dissertation, a novel hole hemming process was developed to join magnesium and aluminum alloy sheets to follow up the trend in the automotive industry of manufacturing high performance vehicle structures with magnesium alloys.

The properties of the materials, AA6082-T4 and AZ31, were obtained through the performance of both numerical and experimental uniaxial tension tests, together with DIC analysis, and the hardening behavior was defined with an appropriate hardening law. The results showed that the magnesium alloy, compared with the aluminum alloy, had lower ductility and considerably high anisotropy. Furthermore, the fracture limits of the materials in different loading states were analyzed by conducting formability tests, i.e. uniaxial tension, plane strain tension, notched tension and shear tension tests. Then, the MMC ductile fracture criterion was calibrated using a hybrid experimental-numerical method. The resulting fracture envelopes indicated a great difference between the formability of these two materials. For the aluminum alloy the fracture criterion predicted satisfactorily the fracture displacement of all the tests with a maximum error of 4.1%, while for the magnesium alloy it exhibited slightly higher errors, except for the shear tension test.

A numerical model was created to study the feasibility of the process and the process parameters. The MMC was defined in the model by means of an appropriate subroutine to predict fracture and to identify the critical regions of the process, i.e. edge zone and bend zone, and their deformation mechanics. The results showed that the damage in the edge is affected by the ratio between the final and initial hole radius of the outer sheet, being possible to reduce the damage and thus avoid fracture in the edge either by increasing the initial outer sheet hole radius or by increasing the die radius (while maintaining the flange length). Nevertheless, the flange needs to be long enough to overlap the inner sheet and form a mechanical interlock. The damage in the bend zone could be reduced by increasing the fillet radius of the upper die and thus increasing the bending radius of the outer sheet flange. It was also found that the increasing of the fillet radius of the hemming punch leads to a higher overlap of the inner sheet by the outer sheet flange and results in a better mechanical interlock. However, the increase of the fillet radius of the hemming punch also causes a sharp increase to the required punch force. Process windows were defined for the main process parameters, the flange length and fillet radius of the hemming punch, and for the experimental hole hemming cases.

Experimental hole hemming tests were conducted for three different flange lengths. For the higher flange length of 4.5 mm, fracture in the edge was predicted in the numerical model and it was confirmed in all experimental tests. For the intermediate flange length of 4 mm, joints with tight mechanical interlocks were achieved while in some of them fracture happened at the edge. The fracture was predicted in function of the hemming punch displacement exhibiting a maximum error of 4.8%. For the smaller flange length of 3.5 mm, despite it was possible to obtain a good mechanical interlock in the numerical model, in the experimental tests the flange is too small as it is compressed before it overlaps the inner sheet to achieve a sound mechanical interlock.

The shear load of the joints for the flange length of 4 mm was experimentally tested by the performance of a single lap shear test. The hole bearing gradual failure mode was observed for a load of about 1.5 kN, while the increase of the displacement remarkably leads to an increase of the shear load to a maximum force of almost 2.9 kN.

8 Future works

It is often applied adhesives to conventional hemmed joints as it gives many benefits such as sealing, vibration isolation, anti-corrosion, dimensional accuracy and structural stability [64]. Therefore, it would be interesting to develop a hybrid adhesive-hole hemmed joint to study the effect of an adhesive on hole hemmed joints.

The branch design presented in chapter 6.4 is an interesting way to reduce the damage in materials with high concentrated damage in the edge region. In a future work this design could be put to practice to study its feasibility in reducing the damage in the edge region while not creating a new critical region inside the branch.

The friction between the hemming punch and the outer sheet is a very important consideration as it can completely change the aspect of the joint, load applied in the hemming punch and the damage along the sheets, and so it can be the difference between a good tight joint and a failed joint. The simulation of the process, the use of lubricants and surface treatment of the hemming punch in the future should take this into consideration.

At last, in this work it was not possible to experimentally perform destructive T peel tests as the space within the tool was limited. Furthermore, the alignment system should be rethought to easily obtain well aligned joints. Finally, more work is required for the finite element simulation of the shear test.

References

[[1] W. J. Joost, and P. E. Krajewski, “Towards magnesium alloys for high-volume automotive applications,” *Scripta Materialia,* vol. 128, pp. 107-112, 2017/02/01/, 2017.

[2] R. Hörhold, M. Müller, M. Merklein, and G. Meschut, “Mechanical properties of an innovative shear-clinching technology for ultra-high-strength steel and aluminium in lightweight car body structures,” *Welding in the World,* vol. 60, no. 3, pp. 613-620, 2016/05/01, 2016.

[3] C.-J. Lee, J.-M. Lee, H.-Y. Ryu, K.-H. Lee, B.-M. Kim, and D.-C. Ko, “Design of hole-clinching process for joining of dissimilar materials – Al6061-T4 alloy with DP780 steel, hot-pressed 22MnB5 steel, and carbon fiber reinforced plastic,” *Journal of Materials Processing Technology,* vol. 214, no. 10, pp. 2169-2178, 2014/10/01/, 2014.

[4] M. M. Kasaei, and L. F. da Silva, “Joining sheets made from dissimilar materials by hole hemming,” *Proceedings of the Institution of Mechanical Engineers, Part L: Journal of Materials: Design and Applications,* vol. 0, no. 0, pp. 14644207211072676, 2022.

[5] T. Lipman, and P. Maier, “Advanced materials supply considerations for electric vehicle applications,” *MRS Bulletin,* vol. 46, pp. 1-12, 02/14, 2022.

[6] L. H. Shah, N. H. Othman, and A. Gerlich, “Review of research progress on aluminium-magnesium dissimilar friction stir welding,” *Science and Technology of Welding and Joining,* vol. 23, no. 3, pp. 256-70, /, 2018.

[7] V. P. Singh, S. K. Patel, A. Ranjan, and B. Kuriachen, “Recent research progress in solid state friction-stir welding of aluminium–magnesium alloys: a critical review,” *Journal of Materials Research and Technology,* vol. 9, no. 3, pp. 6217-6256, 2020/05/01/, 2020.

[8] S. Han, Z. Li, Z. Wang, and Y. Li, “Review on joining processes of magnesium alloy sheets,” *The International Journal of Advanced Manufacturing Technology,* vol. 118, no. 9, pp. 2787-2803, 2022/02/01, 2022.

[9] E. Oberg, F. D. Jones, H. L. Horton, H. H. Ryffel, C. J. McCauley, and L. Brengelman, "7.4.5.2 Advanced Materials," *Machinery's Handbook (31st Edition)*: Industrial Press.

[10] B. Viswanadhapalli, and V. K. Bupesh Raja, "Application of Magnesium Alloys in Automotive Industry-A Review," *Emerging Trends in Computing and Expert Technology.* pp. 519-531.

[11] B. R. Powell, P. E. Krajewski, and A. A. Luo, "Chapter 4 - Magnesium alloys for lightweight powertrains and automotive structures," *Materials, Design and Manufacturing for Lightweight Vehicles (Second Edition)*, P. K. Mallick, ed., pp. 125-186: Woodhead Publishing, 2021.

[12] J. L. Dossett, "1.1.1 Space Lattices and Crystal Systems," *Practical Heat Treating - Basic Principles (2nd Edition)*: ASM International, 2020.

[13] F. C. Campbell, "1.2 Aluminum Alloys," *Lightweight Materials - Understanding the Basics*: ASM International, 2012.

[14] R. N. Lumley, "10.1.2 The Case for Aluminium," *Fundamentals of Aluminium Metallurgy - Recent Advances*: Elsevier, 2018.

[15] T. Altan, and A. E. Tekkaya, "6.4 Aluminum Alloys," *Sheet Metal Forming - Fundamentals*: ASM International, 2012.

[16] R. N. Lumley, "10.6 Application of aluminum alloys in automotive design and manufacture," *Fundamentals of Aluminium Metallurgy - Recent Advances*: Elsevier, 2018.

[17] T. Altan, and A. E. Tekkaya, "2.6 Hemming," *Sheet Metal Forming - Processes and Applications*: ASM International, 2012.

[18] Y. Dewang, and V. Sharma, "A study on sheet metal hemming process," *Materials Today: Proceedings*, vol. 27, pp. 2091-2095, 2020/01/01/, 2020.

[19] S. C. Tang, and J. Pan, "1.3 Flanging and Hemming," *Mechanics Modeling of Sheet Metal Forming*: SAE International, 2007.

[20] Z. Gu, G. Wang, and G. Yu, "Investigation on Fracture of a 6014-T4 Aluminum Alloy Sheet in the Flanging and Hemming Process Based on Numerical and Experimental Methods," *Metals*, vol. 10, no. 1, pp. 81, 2020.

[21] M. Salamati, M. Soltanpour, A. Fazli, and A. Zajkani, "Processing and tooling considerations in joining by forming technologies; part A—mechanical joining," *The International Journal of Advanced Manufacturing Technology*, vol. 101, no. 1, pp. 261-315, 2019/03/01, 2019.

[22] G. Buffa, L. Fratini, U. La Commare, D. Römisch, S. Wiesenmayer, S. Wituschek, and M. Merklein, "Joining by forming technologies: current solutions and future trends," *International Journal of Material Forming*, vol. 15, no. 3, pp. 27, 2022/03/30, 2022.

[23] H. Peng, C. Chen, H. Zhang, and X. Ran, "Recent development of improved clinching process," *The International Journal of Advanced Manufacturing Technology*, vol. 110, no. 11, pp. 3169-3199, 2020/10/01, 2020.

[24] H. Peng, C. Chen, X. Ren, and J. Wu, "Development of clinching process for various materials," *The International Journal of Advanced Manufacturing Technology*, vol. 119, no. 1, pp. 99-117, 2022/03/01, 2022.

[25] S. Busse, M. Merklein, K. Roll, M. Ruther, and M. Zürn, "Development of a mechanical joining process for automotive body-in-white production," *International Journal of Material Forming*, vol. 3, no. 1, pp. 1059-1062, 2010/04/01, 2010.

[26] G. Meschut, M. Merklein, A. Brosius, D. Drummer, L. Fratini, U. Füssel, M. Gude, W. Homberg, P. A. F. Martins, M. Bobbert, M. Lechner, R. Kupfer, B. Gröger, D. Han, J. Kalich, F. Kappe, T. Kleffel, D. Köhler, C. M. Kuball, J. Popp, D. Römisch, J. Troschitz, C. Wischer, S. Wituschek, and M. Wolf, "Review on mechanical joining by plastic deformation," *Journal of Advanced Joining Processes*, vol. 5, pp. 100113, 2022/06/01/, 2022.

[27] S. Wiesenmayer, and M. Merklein, "Potential of shear-clinching technology for joining of three sheets," *Journal of Advanced Joining Processes*, vol. 3, pp. 100043, 2021/06/01/, 2021.

[28] D. Li, A. Chrysanthou, I. Patel, and G. Williams, "Self-piercing riveting-a review," *The International Journal of Advanced Manufacturing Technology*, vol. 92, no. 5, pp. 1777-1824, 2017/09/01, 2017.

[29] K. Mori, T. Kato, Y. Abe, and Y. Ravshanbek, "Plastic Joining of Ultra High Strength Steel and Aluminium Alloy Sheets by Self Piercing Rivet," *CIRP Annals*, vol. 55, no. 1, pp. 283-286, 2006/01/01/, 2006.

[30] S. Wituschek, and M. Lechner, "Material characterisation methods for a tumbling self-piercing riveting process," *ESAFORM 2021*, 04/12, 2021.

[31] K. Kato, M. Okamoto, and T. Yasuhara, “Method of joining sheets by using new type rivets,” *Journal of Materials Processing Technology,* vol. 111, no. 1, pp. 198-203, 2001/04/25/, 2001.

[32] L. M. Alves, R. M. Afonso, P. T. Pereira, and P. A. F. Martins, “Double-sided self-pierce riveting of dissimilar materials,” *The International Journal of Advanced Manufacturing Technology,* vol. 115, no. 11, pp. 3679-3687, 2021/08/01, 2021.

[33] L. M. Alves, R. M. Afonso, P. T. Pereira, and P. A. F. Martins, “Double-sided self-pierce riveting with flat-bottom holes: a feasibility study,” *Production Engineering,* vol. 16, no. 2, pp. 401-409, 2022/04/01, 2022.

[34] O. Kayode, and E. Akinlabi, “An overview on joining of aluminium and magnesium alloys using friction stir welding (FSW) for automotive lightweight applications,” *Materials Research Express,* vol. 6, 07/15, 2019.

[35] Y. Li, F. Qin, C. Liu, and Z. Wu, “A Review: Effect of Friction Stir Welding on Microstructure and Mechanical Properties of Magnesium Alloys,” *Metals,* vol. 7, pp. 524, 11/25, 2017.

[36] S. H. C. Park, M. Masato, S. S. Yutaka, and K. Hiroyuki, "DISSIMILAR FRICTION-STIR WELDING OF ALALLOY 1050 AND MGALLOY AZ31." pp. 534-538.

[37] R. Zettler, A. A. Silva, S. Rodrigues, A. Blanco, and J. dos Santos, “Dissimilar Al to Mg Alloy Friction Stir Welds,” *Advanced Engineering Materials,* vol. 8, pp. 415-421, 05/11, 2006.

[38] Y. J. Kwon, I. Shigematsu, and N. Saito, “Dissimilar friction stir welding between magnesium and aluminum alloys,” *Materials Letters,* vol. 62, no. 23, pp. 3827-3829, 2008/08/31/, 2008.

[39] I. Shigematsu, Y.-J. Kwon, and N. Saito, “Dissimilar Friction Stir Welding for Tailor-Welded Blanks of Aluminum and Magnesium Alloys,” *MATERIALS TRANSACTIONS,* vol. 50, no. 1, pp. 197-203, 2009.

[40] M. A. Wahid, Z. A. Khan, and A. N. Siddiquee, “Review on underwater friction stir welding: A variant of friction stir welding with great potential of improving joint properties,” *Transactions of Nonferrous Metals Society of China,* vol. 28, no. 2, pp. 193-219, 2018/02/01/, 2018.

[41] Y. Zhao, Z. Lu, K. Yan, and L. Huang, “Microstructural characterizations and mechanical properties in underwater friction stir welding of aluminum and magnesium dissimilar alloys,” *Materials & Design,* vol. 65, pp. 675-681, 01/31, 2015.

[42] R. S. P.-C. Wang, *Friction stir rivet method of joining,* US7862271B2, 2011.

[43] G. White, S. Lathabai, V. Tyagi, and D. Ritchie, “Friction Stir Blind Riveting: A Novel Joining Process for Automotive Light Alloys,” *SAE International Journal of Materials and Manufacturing,* vol. 4, pp. 589-601, 01/04, 2011.

[44] J. Min, J. Li, B. E. Carlson, Y. Li, J. F. Quinn, J. Lin, and W. Wang, “Friction Stir Blind Riveting for Joining Dissimilar Cast Mg AM60 and Al Alloy Sheets,” *Journal of Manufacturing Science and Engineering,* vol. 137, no. 5, 2015.

[45] V. S. Ortwin Hahn, *Method and apparatus for joining metal sheets and the like,* US6199271B1, 2001.

[46] C. J. Sun X, Feng Z, Hu X, Davies RW, Huang H, *Ultrasonically Assisted Self-Piercing Riveting,* US20200101519A1, 2020.

[47] W.-G. Drossel, and M. Jäckel, “New Die Concept for Self-Pierce Riveting Materials with Limited Ductility,” *Key Engineering Materials,* vol. 611-612, pp. 1452 - 1459, 2014.

[48] R. Neugebauer, S. Dietrich, and C. Kraus, “Joining by Forming with a Flat Counter Tool - A New Way of Joining Magnesium Components,” *Materials Science Forum,* vol. 539-543, pp. 3949-3954, 2007.

[49] F. C. Campbell, "3. Ductile and Brittle Fracture," *Fatigue and Fracture - Understanding the Basics*: ASM International, 2012.

[50] H. Li, and M. Fu, "Chapter 3 - Damage Evolution and Ductile Fracture," *Deformation-Based Processing of Materials,* H. Li and M. Fu, eds., pp. 85-136: Elsevier, 2019.

[51] C. V. Nielsen, and P. A. F. Martins, "Chapter 2 - Formability*," *Metal Forming*, C. V. Nielsen and P. A. F. Martins, eds., pp. 7-107: Academic Press, 2021.

[52] Y. Bai, and T. Wierzbicki, “Application of extended Mohr–Coulomb criterion to ductile fracture,” *International Journal of Fracture,* vol. 161, no. 1, pp. 1, 2009/11/12, 2010.

[53] M. J. Mirnia, and M. Shamsari, “Numerical prediction of failure in single point incremental forming using a phenomenological ductile fracture criterion,” *Journal of Materials Processing Technology,* vol. 244, pp. 17-43, 2017/06/01/, 2017.

[54] Y. Xiao, Q. Tang, Y. Hu, J. Peng, and W. Luo, “Flow and fracture study for ZK60 alloy at dynamic strain rates and different loading states,” *Materials Science and Engineering: A,* vol. 724, pp. 208-219, 2018/05/02/, 2018.

[55] X. Xiao, H. Pan, Y. Bai, Y. Lou, and L. Chen, “Application of the modified Mohr–Coulomb fracture criterion in predicting the ballistic resistance of 2024-T351 aluminum alloy plates impacted by blunt projectiles,” *International Journal of Impact Engineering,* vol. 123, pp. 26-37, 2019/01/01/, 2019.

[56] H. Talebi-Ghadikolaee, H. Naeini, M. J. Mirnia, M. A. Mirzai, S. Alexandrov, and H. Gorji, “Experimental and numerical investigation of failure during bending of AA6061 aluminum alloy sheet using the modified Mohr-Coulomb fracture criterion,” *The International Journal of Advanced Manufacturing Technology,* vol. 105, 12/01, 2019.

[57] “NIE METAIS, Portugal.”

[58] Korea Institute of Industrial Technology.

[59] D. Banabic, *Sheet metal forming processes: constitutive modelling and numerical simulation*: Springer Science & Business Media, 2010.

[60] H. J. Bunge, K. Pöhlandt, A. Tekkaya, and D. Banabic, *Formability Of Metallic Materials*, 2000.

[61] T. Wen, Q. Huang, Q. Liu, W.-X. Ou, and S. Zhang, “Joining different metallic sheets without protrusion by flat hole clinching process,” *The International Journal of Advanced Manufacturing Technology,* vol. 85, no. 1, pp. 217-225, 2016/07/01, 2016.

[62] T. Wang, S. Whalen, X. Ma, J. Silverstein, H. Das, M. R. Pallaka, A. Ortiz, T. Roosendaal, P. Upadhyay, and K. S. Kappagantula, “Friction-based riveting technique for AZ31 magnesium alloy,” *Journal of Magnesium and Alloys,* vol. 10, no. 1, pp. 110-118, 2022/01/01/, 2022.

[63] Y. Li, Z. Wei, Y. Li, J. Wang, and X. Zhu, *Friction self-piercing riveting (F-SPR) of AA6061-T6 to AZ31B*, 2013.

[64] J. Li, W. Zhu, H. Sun, and G. Tang, “Multi-physics modeling and simulations on the curing process of one-component hemming adhesive under temperature cycle,” *Journal of Adhesion Science and Technology*, vol. 36, no. 5, pp. 507-530, 2022/03/04, 2022.

Appendices

Appendix A Paper

Joining magnesium and aluminum alloy sheets by a novel hole hemming process

J.A.C. Pereira[1], MM Kasaei[2], RJC Carbas[2], EAS Marques[2], LFM da Silva[1]

[1] Department of Mechanical Engineering, Faculty of Engineering, University of Porto, Porto, Portugal

[2] Institute of Science and Innovation in Mechanical and Industrial Engineering, Porto, Portugal.

Abstract

The use of magnesium alloys are a new trend in the automotive industry to manufacture high performance vehicle structures, being noteworthy for having the lowest density among all structural metals and others additional advantages. However, joining processes by plastic deformation of magnesium alloys are restricted by their low formability at room temperature. In this research work, a novel hole hemming process, newly developed by Kasaei and da Silva 2022, is employed for attaching magnesium AZ31 and aluminum AA6082-T4 alloy sheets in which only one of the sheets should be sufficiently ductile. First, the fracture limits of the materials are characterized under different loading states. Then, the hole hemming process for joining the mentioned material combination is studied by finite element analysis. The critical regions prone to fracture and their loading paths are studied. In addition, the influence of process parameters on the mechanical interlock is investigated to determine the process window. The performance of the designed process is thoroughly evaluated by conducting the hole hemming experiments with different process parameters and single-lap shear tests. Results show that the hole hemming process can appropriately join the magnesium and aluminum alloy sheets without the occurrence of fracture. Furthermore, the hole-hemmed joints resisted a maximum load of 2.9 kN with a gradual failure mechanism of hole bearing. Thus, the hole hemming is recommended for joining materials with very different formability.

Keywords: Deformation assisted joining, Lightweight structure, Hole hemming, Ductile fracture, Magnesium, Aluminum

1. Introduction

Nowadays, there is an urge in the automotive industry to reduce the weight of the automobiles in order to improve both the performance and fuel efficiency for environmental and economic reasons [1]. Nonetheless, concerns related to comfort and safety of the passengers is also a priority which leads to an increase in the weight of the automotive structure [2]. To accomplish this requirements, modern car manufactures produce lightweight automotive bodies with dissimilar materials in a design concept known as “multi-material design” [3], which consists in using different lightweight materials such as advanced high-strength steel (AHSS), aluminum alloys, magnesium alloys [4] and composites [5].

With a density of 1.74 $g.cm^{-3}$, magnesium is the lightest of all the structural metals, being 35% lighter than aluminium (2.7 $g.cm^{-3}$) and about four times lighter than steel (7.86 $g.cm^{-3}$). It has better noise and vibration characteristics than aluminium and great formability at high temperatures [6]. Magnesium has a specific strength similar to cast iron and similar or higher than many traditional automotive aluminum alloys and therefore it can enhance more mass reduction relatively to aluminium alloys. Moreover, it has a higher specific stiffness than

many polymeric materials and composites, leading to an improved mass reduction [7]. However, the accomplishment of the multi-material design depends on the feasibility of the processes used to join such dissimilar materials [8].

In fact, the weight of magnesium alloys in vehicles constitutes only a small percentage of the total weight due to challenges associated with manufacturing, processing, assembly, in-service performance and cost [9]. The majority of the manufacturing processes for converting metal sheets into automotive parts are employed at room temperature, including stamping, bending, hemming, flanging and trimming, which are difficult to be applied for magnesium alloys as magnesium has an hexagonal close packed crystal structure that has fewer slip systems compared with other structural metals such as iron and aluminum (which have a cubic crystal structure), making the deformation at room temperature difficult [7] and limiting the application of magnesium alloys in the automotive industry.

There is a growing need for joining magnesium to aluminium that is related to the properties of the base metals. Individually, aluminium alloys are extensively utilized in the automotive and aerospace industries due to various advantages, including light weight, high specific strength and recyclability. However, as described above, some specific advantages may favor magnesium. It is the joining technologies that can provide the opportunity to employ the advantages of both metals simultaneously [10].

Welding is the most commonly joining process used on an automotive assembly line. However, the joining of magnesium and aluminium alloys by conventional processes is difficult or impossible due to the formation of brittle intermetallic phases that deteriorates the mechanical properties of the joint [10]. Friction stir welding (FSW) is a process of choice when joining aluminum components [11] and is widely used in the automotive industry as it has the potential to join dissimilar materials efficiently due to low temperature generation. Nonetheless, solubility limitations between magnesium and aluminium in solid-solid phase still provokes the formation of brittle intermetallic phases [12]. Adhesive bonding also finds increasing applications in the automotive industry due to its multiple advantages over other processes, including the possibility of joining dissimilar materials with high flexibility [13]. However, in adhesive bonding, specially in lap joints, premature failure often happens due to uneven stress distribution along the bondline [14].

Joining processes by plastic deformation, such as clinching [15] and riveting [16], are rapidly growing do to several advantages over other processes including productivity, costs, application range and environmental friendliness [17]. Nevertheless, the application of these processes are limited by the low ductility at room temperature of magnesium alloys [18]. Wang et al. [19] developed a new joining method called friction stir blind riveting (FSBR) that uses a combination of friction stir riveting and blind riveting. Min et al. [20] used the FSBR process to successfully join magnesium and aluminum alloys. However, the FSBR process and rivet structure are complex and the process is not suitable for car body thin walled sheets [18]. Neugebauer R et al. [21] developed a heat assisted dieless clinching process for increasing the plasticity of the magnesium alloy sheets. By heating the flat anvil with temperatures above 220°C it was possible to join magnesium and aluminium sheets with crack-free joints. Nevertheless, contrary to the conventional clinching process, in the dieless clinching process the counter tool cannot be used to control the material flow and the addition of the assist heat source increases the cycle time of the process and the complexity and requirements for the equipment.

In order to overcome the limitations of the joining of low ductility materials by plastic deformation, Kasaei MM and da Silva LF [4] developed a new joining process based on the hemming process called “hole hemming”. Similar to the conventional hemming process, an outer sheet is folded over the inner sheet to achieve a tight interlock. Thus, the inner sheet is not deformed and only the outer sheet is necessary to be sufficiently ductile in this process. The

main difference between this process and the conventional hemming process is that the mechanical interlock is realized between concentric pre-drilled holes that can be made anywhere in the inner and outer sheet, unlike the conventional hemming process where the mechanical interlock is limited to the edges of the sheets. In this work the joining of DP780 steel as the outer sheet and AA6061-T6 aluminium as the inner sheet was investigated using finite element analysis. To predict the damage evolution and the critical regions of the sheets, the modified Mohr-Coulomb (MMC) fracture criterion was used. Different process parameters were tested and in the end the potential of the hole hemming process was proved to successfully join dissimilar materials. However, this work suffers from lack of experimental validation.

The purpose of this study is to employ the novel hole hemming process for joining AZ31 magnesium and AA6082-T4 aluminum alloy sheets in which only the aluminum alloy needs to be sufficiently ductile. In a first phase the fracture limits of the materials are characterized under different loading states. Then, a finite element analysis is made to determine the critical regions prone to fracture and their loading paths during the hole hemming process for joining the mentioned materials. In addition, the process window is determined by studying the influence of the process parameters on the mechanical interlock and on the joining force. The designed process joints are visually characterized and their performance are thoroughly evaluated by means of a single-lap shear test.

2. Hole hemming process

The hole hemming process is performed in two different stages, the flanging stage and the hemming stage. In the flanging stage, figure 1 (a), a flange is formed in the hole of the outer sheet by means of a punch, the flanging punch, and two dies, the lower and upper die. In a first phase of the stage, the outer sheet is correctly aligned and placed in the top of the lower die and then the upper die moves down to fix the outer sheet. After this, the flanging punch advances to bend the edge of the outer sheet in a 90° angle and form the flange. As it can be seen in figure, the dies create an indentation near the flange, which allows the hole edge of the inner sheet to be placed at the closest possible position to the flange during the hemming stage. The hole radius of the outer sheet (R_o), the die radius (R_d), the fillet radius of the upper die (fr_d) and the indent depth (d) should be carefully determined to obtain a sound joint. The nominal length of the flange (F) produced in this stage is obtained as follows:

$$F = R_d - R_o \tag{1}$$

In the hemming stage, figure 1 (b), the inner sheet is placed and aligned on the top of the outer sheet and the upper die is replaced by a blank holder which fixes the sheets in the correct place. After this, the hemming punch advances and causes the flange to overlap the hole edge of the inner sheet, producing a tight mechanical interlock with low deformation in the inner sheet. Because of this, this process has a high potential of joining magnesium with aluminum alloys as long as the magnesium alloy is used as the inner sheet and the aluminum alloy is sufficiently ductile to be used as the outer sheet. The fillet radius of the hemming punch (R) controls the evolution of the deformation in the outer sheet during the hemming stage.

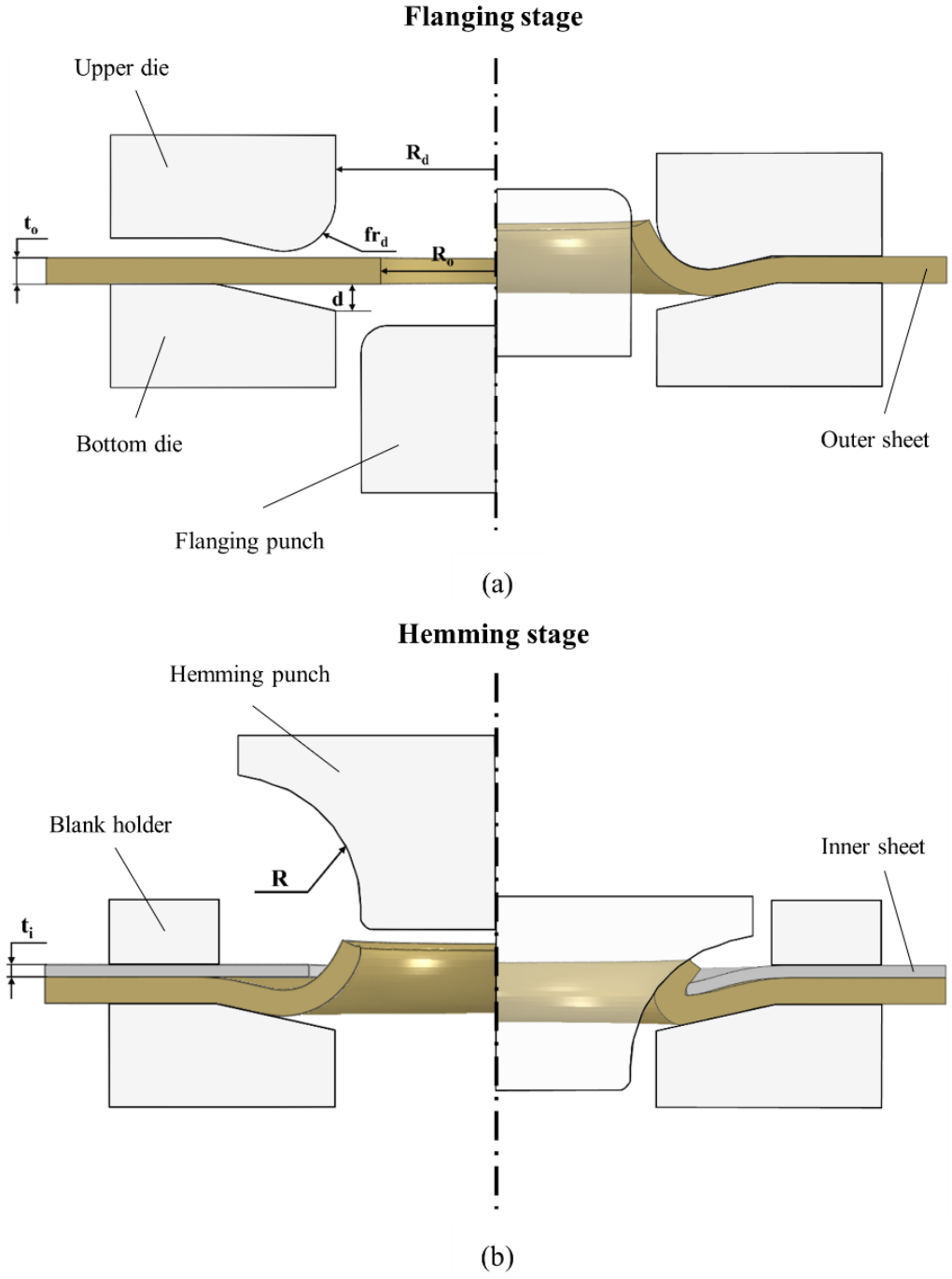

Figure 1 - Schematic representation of the hole hemming process: (a) flanging stage and (b) hemming stage.

3. Experimentation

3.1. Material characterization

The investigation was conducted using commercial AA6082-T4 and laboratory made ECO-AZ31 with 2 mm and 1 mm thickness, respectively. To obtain the mechanical properties and plasticity behavior, uniaxial tension tests, whose dimensions are shown in figure 2 (a), were carried out on the INSTRON 3367 machine, figure 2 (c), with a test speed of 3 mm/min. To study the anisotropic behavior of the materials, the specimens were cut in three different directions (0, 45 and 90°) to the rolling or extrusion direction. The displacement of the gauge

section and the major and minor strains were measured using the Digital image correlation (DIC) software GOM and the videos were recorded using the camara Canon EOS M5 equipped with a Canon EF-M 18-55 mm F/3.5-5.6 lens with a frame rate of 25 fps. For the effect the specimens were painted on the surface with a stochastic speckle pattern as shown in figure 2 (b).

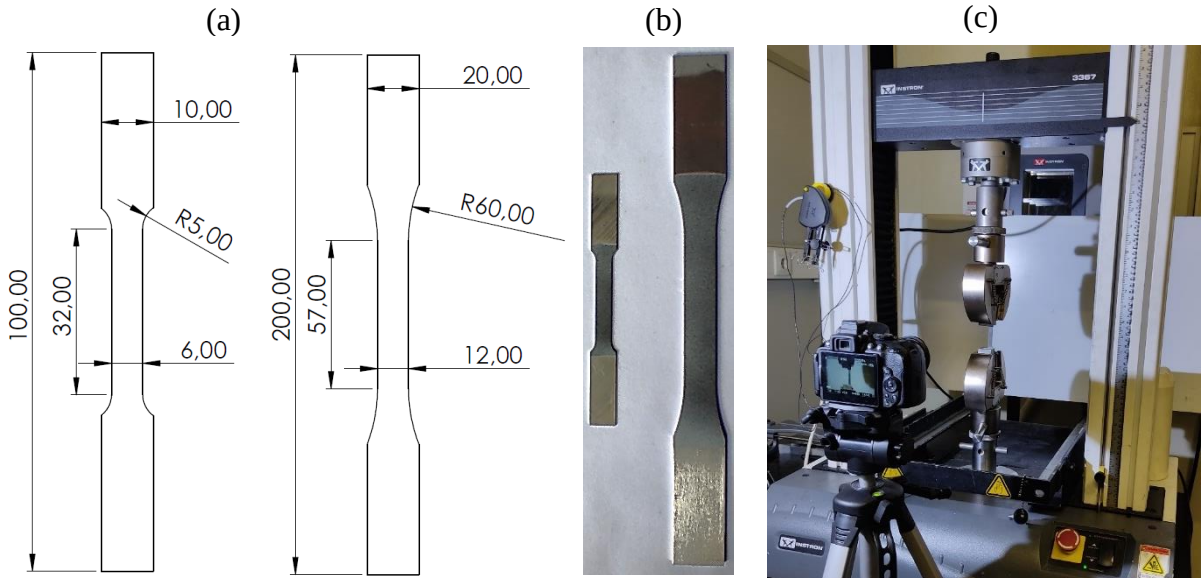

Figure 2 – Uniaxial tension specimens and the tensile testing machine: (a) Uniaxial tension specimens geometries and dimensions, (b) uniaxial tension specimens painted with a stochastic pattern and (c) INSTRON 3367 machine and digital camera.

The engineering stress-strain curves are shown in figure 3 (a), while there is not a significant difference between the yield and tensile strength, the AA6082-T4 exhibits about 50% higher elongation. The plasticity behavior of the AZ31 is described by the Hollomon hardening law as follows:

$$\sigma = K(\varepsilon)^n \tag{2}$$

where K and n are the strength coefficient and the hardening exponent, respectively. In the case of the AA6082-T4, to obtain a more accurate necking behavior, it is used a combination of the Swift and Voce hardening law as follows:

$$\sigma = \alpha\left[K\left(\varepsilon_0 + \varepsilon_p\right)^n\right] + (1-\alpha)[A + B(1 - e^{-c\varepsilon_p})] \tag{3}$$

where K and n are the strength coefficient and the hardening exponent of the Swift law, A, B and c are the parameters of the Voce law, ε_0 is the pre-strain and α is the weighting factor. The weighting factor was obtained through a reverse approach by performing the finite element simulations of the uniaxial tension test until there was a good correlation between the experimental and numerical results. The hardening laws parameters are listed in table 1 and the predicted load-displacement curves are compared with the experimental results in figure 3 (b).

Table 1 – Parameters of the materials hardening law.

Material	K	n	α	ε_0	A	B	c
AA6082-T4	501	0.233	0.64	0.0077	174	173	13.1
AZ31	455	0.214	-	-	-	-	-

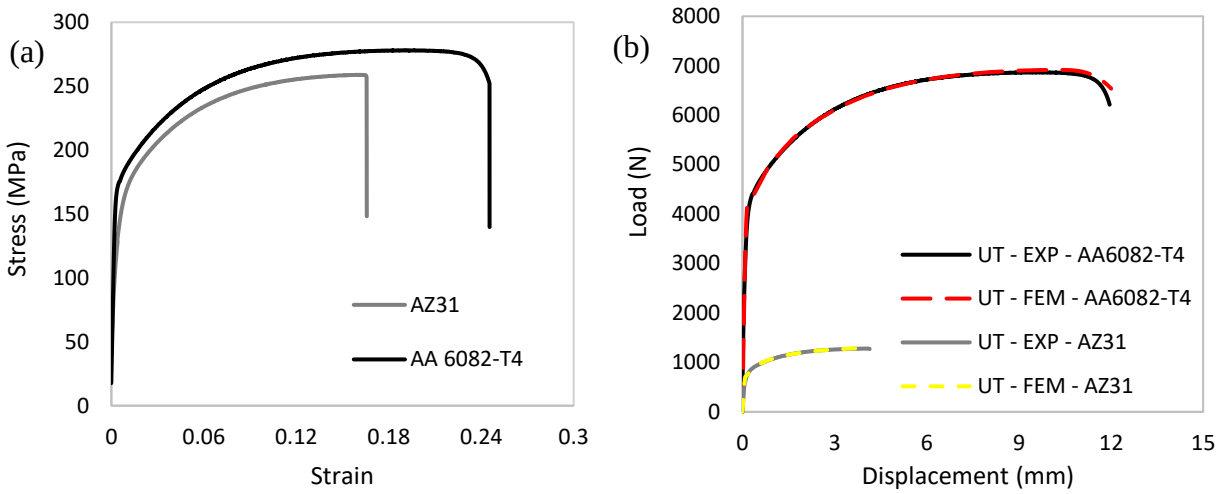

Figure 3 – (a) Materials stress-strain curves and (b) comparison of the materials experimental and numerical load-displacement curves.

The anisotropy of the materials is defined by the r values, which were calculated using the major and minor strains extracted from the GOM software between 10 to 15% elongation for the AA6082-T4 and 5 to 10% elongation for the AZ31 specimens. The strain through thickness was obtained using the law of volume constancy. The Hill 1948 anisotropic Yield criterion is used to define the onset of plastic deformation. The parameters of the Hill 1948 Yield criterion are calculated using normal anisotropy, in the case of the AA6082-T4, and r-based anisotropy, in the case of the AZ31. The r values and the Hill 1948 anisotropic yield stress ratios are shown in table 2. The AA6082-T4 exhibits relatively normal anisotropy, while the AZ31 is highly anisotropic.

Table 2 – Materials r values and Hill 1948 anisotropic yield stress ratios.

Material	Lankford coefficient, r			Normal anisotropy, $\bar{r}$	Hill 1948 anisotropic yield stress ratios					
	0˚	45˚	90˚		R11	R22	R33	R12	R13	R23
AA6082-T4	0.54	0.55	0.66	0.58	1	1	1.05	1.05	1	1
AZ31	0.68	1.24	1.77	1.23	1	1.25	1.10	1.02	1	1

3.2. Formability tests

To calibrate the fracture criterion, three different formability tests including the shear tension, plane strain tension and notched tension (only for the AA6082-T4) tests were carried out, besides the uniaxial tension tests. These tests were chosen to cover different loading modes. The experimental specimens and the respective dimensions are shown in figure 4. The specimens were cut from the supplied sheets along the rolling or extrusion direction by a CNC milling machine. The formability test specimens were tested in the INSTRON 3367 with a constant test speed of 1 mm/min. Similar to the uniaxial tension specimens, the specimens were painted with a stochastic pattern to obtain the displacement and major and minor strains by the DIC software GOM Correlate.

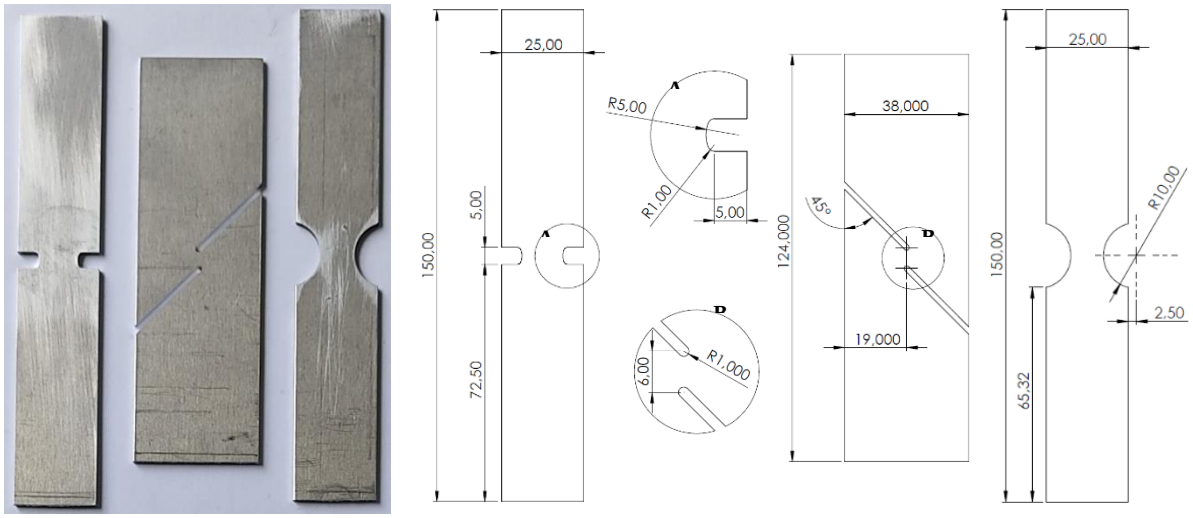

Figure 4 - Formability test specimens: From left to right, plane strain tension, shear tension and notched tension specimens.

3.3. Hole hemming experiments

The experimental hole hemming tests were performed in a tool projected by the group that was mounted in a servo hydraulic INSTROM 8801 with a maximum load capacity of 100 kN, as shown in figure 5 (a). The process starts by inserting the correct tool components. In the flanging stage (figure 5 (b) and (c)), the bottom die (no.8) is fixed to the middle plate (no.2), the flanging punch (no.9) is fixed in the punch holder (no.5) and the upper die (no.6) is fixed to the die holder (no.4). Then, the outer sheet is introduced in the top of the bottom die and aligned with the alignment pins (no.7). It is then applied displacement to the bottom (no.3) and middle plate until the top die closes into the specimen and forms the indent. Then, the middle plate is fixed in position while the bottom plate continues the displacement, making the flanging punch to advance into the dies and forming a flange in the specimen. In the hemming stage (figure 5 (d) and (e)), it is necessary to change the tools. The blank holder (no.10) is fixed to the middle plate, the hemming punch (no.11) is fixed in the punch holder and the bottom die is taken from the middle plate to be fixed to the die holder. Then, the inner sheet (no.13) is assembled through its hole into the flange of the outer sheet (no.12) and both are introduced in the top of the blank holder, with the inner sheet facing down and aligned with the alignment pins. A displacement is then applied to the bottom and middle plate until the bottom die closes into the outer sheet. Then, the middle plate is fixed in position while the bottom plate continues the displacement, making the hemming punch to advance into the dies and forcing the flange of the outer sheet to overlap the hole edge of the inner sheet, compressing it and forming a tight mechanical interlock.

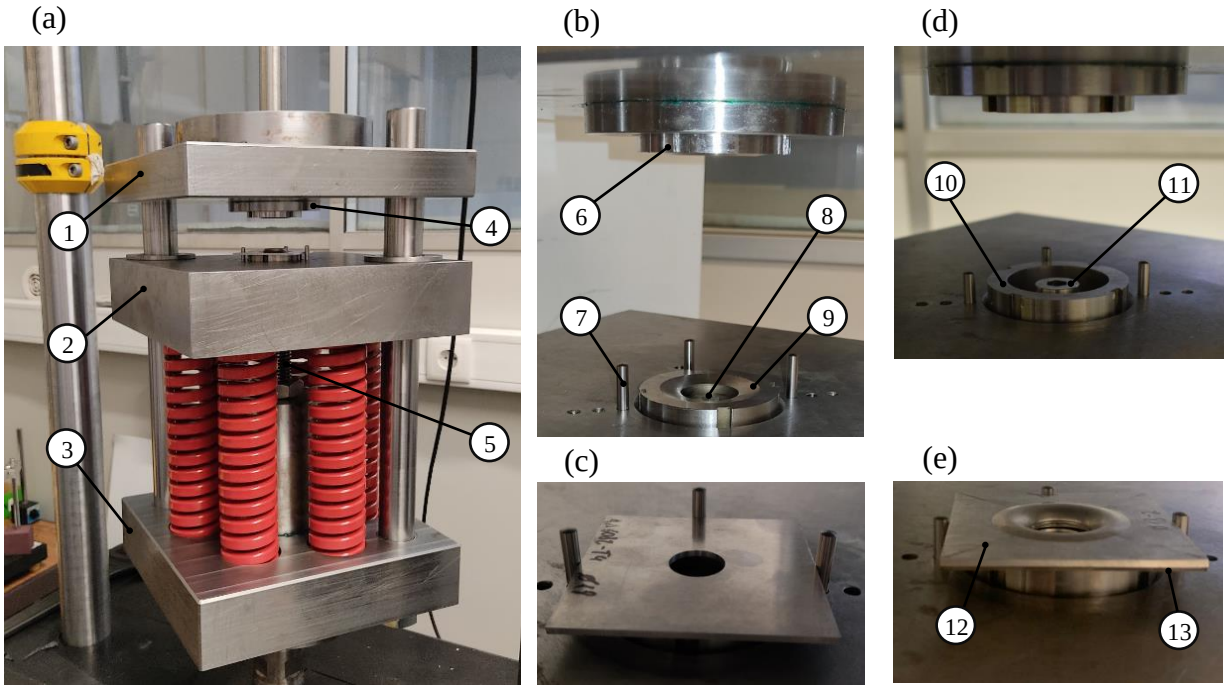

Figure 5 – Hole hemming experimental tests: (a) Hole hemming tool, (b) flanging stage tool components, (c) positioning of the outer sheet for the flanging stage, (d) hemming stage tool components and (e) positioning of the sheets for the hemming stage. 1 – upper plate, 2 – middle plate, 3 – bottom plate, 4 – die holder, 5 – punch holder, 6 – upper die, 7 – alignment pins, 8 – flanging punch, 9 – bottom die, 10 – blank holder, 11 – hemming punch, 12 – outer sheet and 13 – inner sheet.

Figure 6 shows the experimental specimens used in the hole hemming process to study the joint (joint characterization specimens, JC) and to test the loading capacity of the joint (single lap shear tests specimens, SLST). Table 3 contains the work plan for the experimental hole hemming tests. The objective of these tests is to experimentally confirm the feasibility of the hole hemming process and also to study the effect of the flange length (F) by changing the hole radius of the outer sheet (R_o).

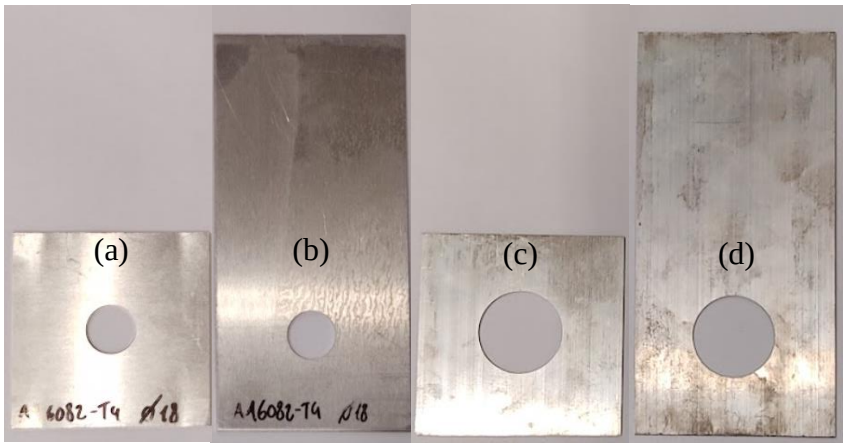

Figure 6 – Experimental specimens used in the hole hemming tests: AA6082-T4 (a) joint characterization and (b) single lap shear test specimens, and AZ31 (c) joint characterization and (d) single lap shear test specimens.

Table 3 - Hole hemming experimental work plan.

Type	R_o	R_i
Joint characterization	9	14.5
Joint characterization	8.5	14.5
Joint characterization	8	14.5
Single lap shear test	8.5	14.5

3.4. Single lap shear tests

The shear strength of the hole hemmed joints was evaluated by the performance of single lap shear tests. The inner and outer sheet specimens are machined to the size of 70 mm (width) x 150 mm (length). Before the hole hemming process, holes are drilled in the opposite extremity to the hemming hole for the fixation in the testing machine. During the hole hemming process, the specimens are aligned to obtain an overlapping section with 70 x 70 mm. The resulting single lap shear test specimen is shown in figure 7. The tests are performed on a INSTRON 3367 machine with a constant test speed of 1 mm/min and the fixation is done with an additional sheet in each end to align the sheets in the correct loading direction.

Figure 7 - Single lap shear test specimen.

4. Finite element modeling

4.1. Calibration tests

The formability specimens were described as 3D solid elements C3D8R with a element size of 0.4 mm for the uniaxial tension, notched tension and plane strain tests and 0.25 mm for the shear tension test, which has the smaller critical area. However, the elements located outside the central critical area were created considerably larger. Due to the thickness of the sheets, 8 and 5 elements through thickness were considered for the AA6082-T4 and AZ31 specimens, respectively. Isotropic hardening was assumed. A dynamic explicit solver with a time scaling approach was employed to improve the computational performance. It should be noted that the ratio of the kinetic energy to the internal energy was monitored to be negligible. Variables such as the stress triaxiality (η), normalized Lode angle parameter ($\bar{\theta}$) and damage indicator (D) were defined in the FE model by means of a user subroutine VUSDFLD. The FE models for the calibration tests with their mesh details and boundary conditions are shown in figure 8.

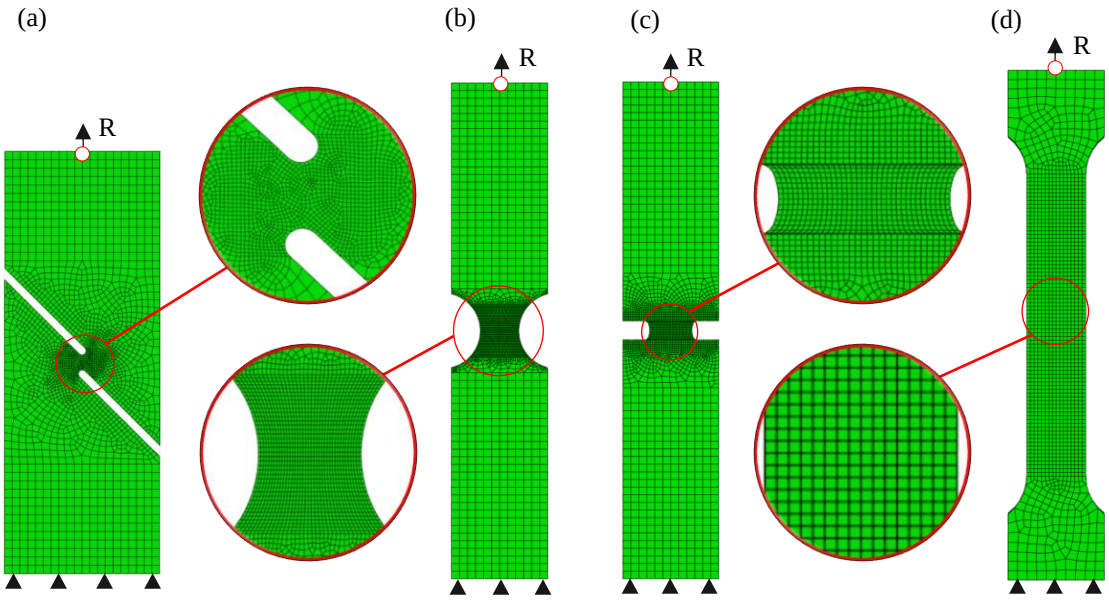

Figure 8 - FE models of the calibration tests with mesh details and boundary conditions: (a) Shear tension test, (b) Notched tension test, (c) Plane strain test, (d) Uniaxial tension test.

4.2. Hole hemming

The numerical simulations of the hole hemming process was also performed in the Abaqus software. Similar to the formability tests, the sheets were modeled using 3D solid elements C3D8R, considering 8 and 5 elements through thickness for the AA6082-T4 (the outer sheet) and AZ31 (the inner sheet), respectively. A smaller element size of 0.2 mm was applied in the hole sheet edges where the highest deformations are located. A dynamic explicit solver with a time scaling approach was used. The calibrated ductile fracture criteria for the AA6082-T4 and AZ31 sheets were separately defined in the user subroutine VUSDFLD to analyze the damage evolution and, finally, predict the fracture during the hole hemming process. The punches (flanging and hemming punch) and matrix (bottom and upper die and blank holder) were modeled as rigid bodies x. The simulation is performed in three different steps by applying a displacement to the upper die, flanging punch and hemming punch, in that order. The frictional contact conditions between tools and sheets was defined by a penalty-based contact model using the Coulomb friction law for a friction coefficient of 0.08. The FEM apparatus of the hemming stage as well as mesh details can be seen in figure 9.

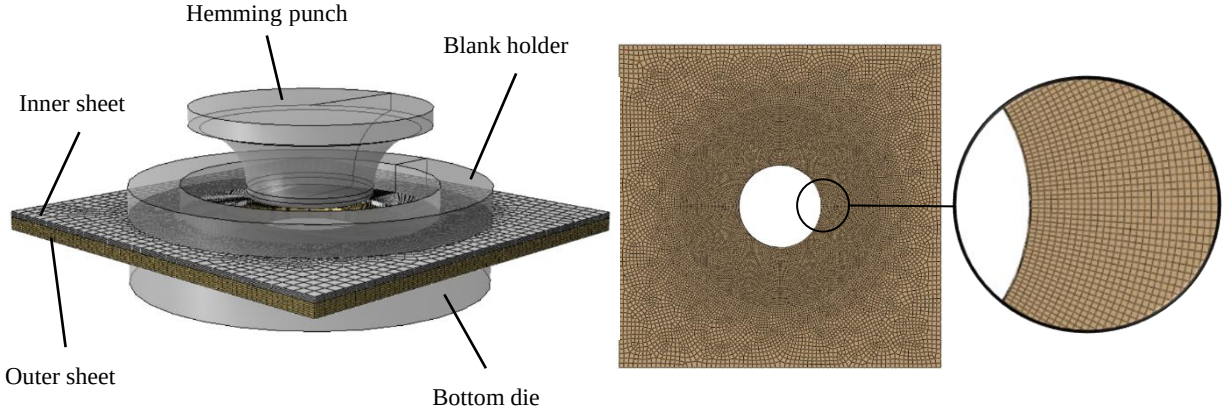

Figure 9 – FE modeling apparatus for the hemming stage and mesh details of the outer sheet.

Table 4 shows the work plan used to study the impact of the main process parameters in the feasibility and quality of the joint. The flange length (F) and fillet radius of the hemming punch (R) are the main process parameters with five and four different levels are studied, respectively.

Table 4 – Finite element studied process parameters.

Parameter	Value (mm)				
t_o	2				
t_i	1				
R_d	10.5				
R_o	$R_d - F$				
R_i	12.5				
d	2				
fr_d	4				
F	3	3.25	3.5	3.75	4
R	4	6	8	10	

5. Fracture modeling

5.1. Ductile fracture criterion

The onset of fracture in metal forming process can be numerically predicted by various ductile fracture models, which accuracy and complexity are dependent on the calibration tests required [22]. Bai and Wierzbicki [23] developed a fracture envelope by extending the Mohr-Coulomb criterion to the spherical coordinate system in a tridimensional space of equivalent plastic strain, normalized Lode angle parameter and stress triaxiality to describe ductile fracture of isotropic solids. This fracture criterion is called the Modified Mohr-Coulomb (MMC) model and it can be expressed as follows:

$$\bar{\varepsilon}_p^f = \left\{ \frac{K}{C_2} \left[C_3 + \frac{\sqrt{3}}{2-\sqrt{3}} (1 - C_3) \left(\sec \frac{\bar{\theta}\pi}{6} - 1 \right) \right] \left[\sqrt{\frac{1+{C_1}^2}{3}} \cos \frac{\bar{\theta}\pi}{6} + C_1 \left(\eta + \frac{1}{3} \sin \frac{\bar{\theta}\pi}{6} \right) \right] \right\}^{-\frac{1}{n}} \quad (4)$$

where K and n which are the strength coefficient and the work hardening exponent, respectively, of the material hardening law. Furthermore, this criterion should be calibrated by performing at least three formability tests to obtain the material coefficients C_1, C_2 and C_3. The MMC fracture envelope is only valid under proportional loading, therefore under different loading conditions it is implemented a damage accumulation law which can be represented as follows:

$$D = \int_0^{\bar{\varepsilon}_p} \frac{d\bar{\varepsilon}_p}{\bar{\varepsilon}_p^f(\eta, \bar{\theta})} \quad (5)$$

where an increment of the equivalent plastic strain ($d\bar{\varepsilon}_p$) is divided by the equivalent plastic strain to fracture for the respective stress state ($\bar{\varepsilon}_p^f(\eta, \bar{\theta})$), contributing to the damage accumulation in the material in which fracture is predicted when the damage indicator (D) reaches unity. The MMC fracture envelope is a surface in a 3D space of equivalent plastic strain ($\bar{\varepsilon}_p$), normalized Lode angle parameter ($\bar{\theta}$) and stress triaxiality (η). However, in sheet metal forming processes plane stress condition can be often assumed, and in that condition the stress triaxiality and the normalized Lode angle parameter are not independent parameters and can be uniquely correlated as follows:

$$\bar{\theta} = 1 - \frac{2}{\pi}\cos^{-1}\left[-\frac{27}{2}\eta\left(\eta^2 - \frac{1}{3}\right)\right] \tag{6}$$

5.2. Calibration method

An experimental and numerical hybrid approach is used for the calibration of the MMC criterion. The fracture displacement is experimentally obtained with the DIC software, while in the FE model it is obtained the fracture strain, stress triaxiality and normalized Lode angle parameter in the critical element until the experimental fracture displacement. The element with the highest equivalent plastic strain at the moment of fracture is most likely the critical element, therefore it is considered as the critical element. In the DIC it is also verified if the location of the critical element in the FE model matches the zone where the highest strain is located, as shown in figure 10.

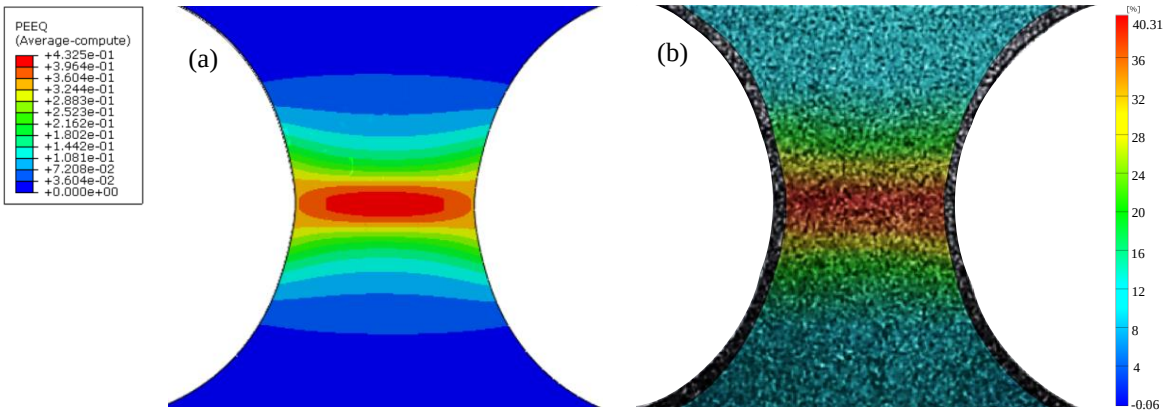

Figure 10 - Comparison between the strain contour of the FE model and the experimental test of a AA6082-T4 notched tension test: (a) FE model equivalent plastic strain countor and (b) DIC major strain countor.

The accuracy of the FE models is crucial for the applicability of the hybrid method. Figure 11 shows a comparison between the experimental and numerical load-displacement curves of the calibration tests. As seen, there is a good agreement between the curves, demonstrating the validity of the FE models.

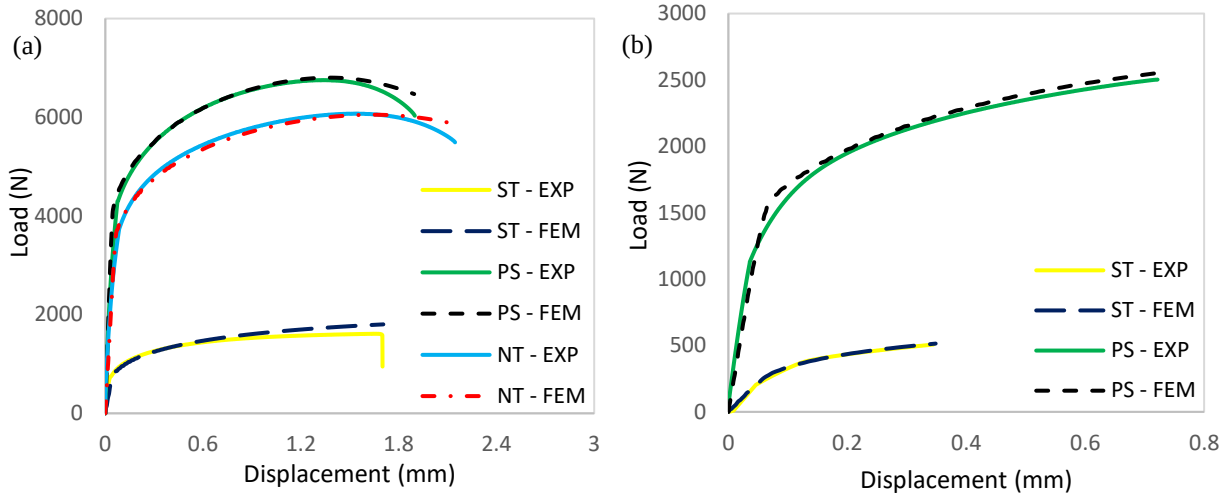

Figure 11 - Load-displacement curves comparison between the experimental and numerical results: (a) AA6082-T4 and (b) AZ31.

Figures 12 and 13 show the evolution of stress triaxiality (η) and normalized Lode angle parameter ($\bar{\theta}$) as function of the equivalent plastic strain in the critical element. As seen, there is a variation of the stress state along the formability tests especially in the AA6082-T4 as it undergoes higher deformations and it suffers necking before the occurrence of fracture. Therefore, it is necessary to obtain the average values of the stress triaxiality and normalized Lode angle parameter as follows:

$$\eta_{ave} = \frac{1}{\bar{\varepsilon}_p^f} \int_0^{\bar{\varepsilon}_p^f} \eta(\bar{\varepsilon}_p)\, d\bar{\varepsilon}^p \tag{7}$$

$$\bar{\theta}_{ave} = \frac{1}{\bar{\varepsilon}_p^f} \int_0^{\bar{\varepsilon}_p^f} \bar{\theta}(\bar{\varepsilon}_p)\, d\bar{\varepsilon}^p \tag{8}$$

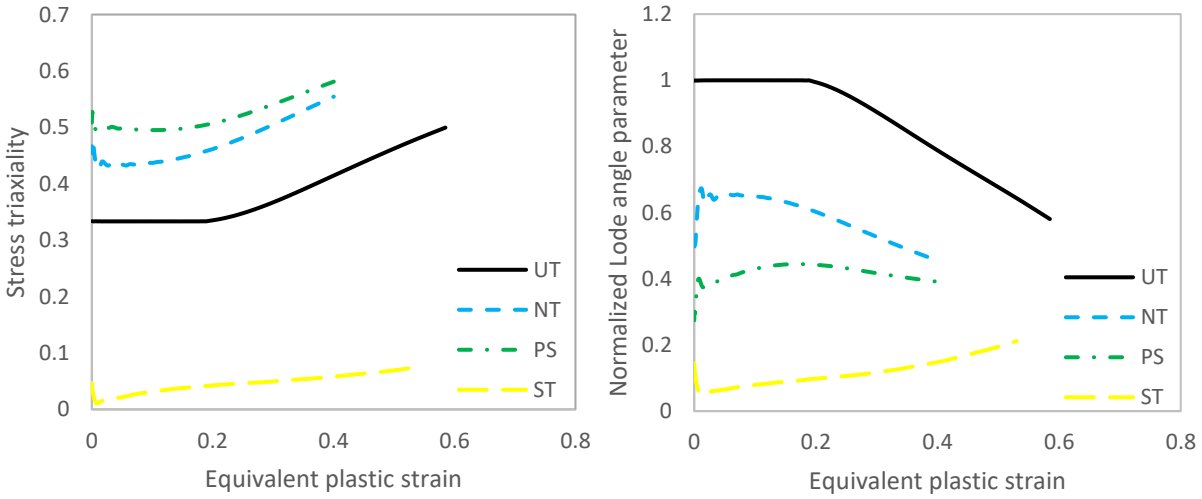

Figure 12 - Evolution of the Stress triaxiality (left) and Normalized Lode angle parameter (right) for the AA6082-T4.

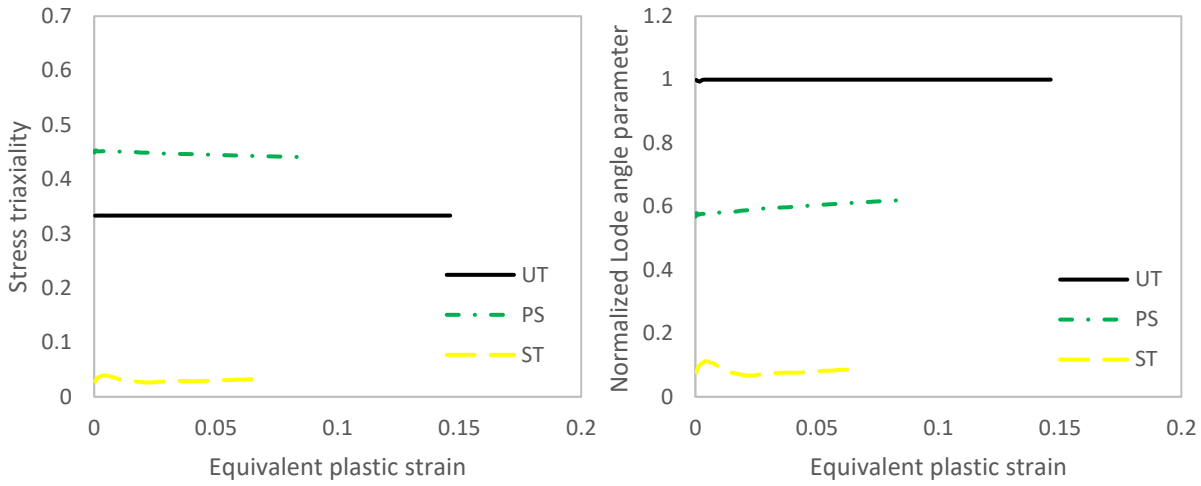

Figure 13 - Evolution of the Stress triaxiality (left) and Normalized Lode angle parameter (right) for the AZ31

In table 5 the resulting calibration points are listed. For each material, the MMC fracture envelope, equation 4, was fitted to the calibration points in MATLAB, obtaining the 3D and 2D, under assumption of plane stress condition, fracture envelopes shown in figure 14 and 15 and the material constants listed in table 6. The results show that the AA6082-T4 exhibits a much higher formability in all the stress states and highlight the difficulty of forming the AZ31 sheet at room temperature.

Table 5 – Materials calibration points.

Formability test	AA6082-T4			AZ31		
	$\bar{\varepsilon}_f$	η_{ave}	$\bar{\theta}_{ave}$	$\bar{\varepsilon}_f$	η_{ave}	$\bar{\theta}_{ave}$
UT	0.58	0.39	0.85	0.14	0.33	1
ST	0.53	0.046	0.12	0.068	0.030	0.081
PS	0.42	0.52	0.42	0.086	0.45	0.60
NT	0.40	0.47	0.58	-	-	-

Table 6 - Materials constants

Material	C_1	C_2	C_3
AA6082-T4	0.078	235 MPa	0.981
AZ31	0	150 MPa	1

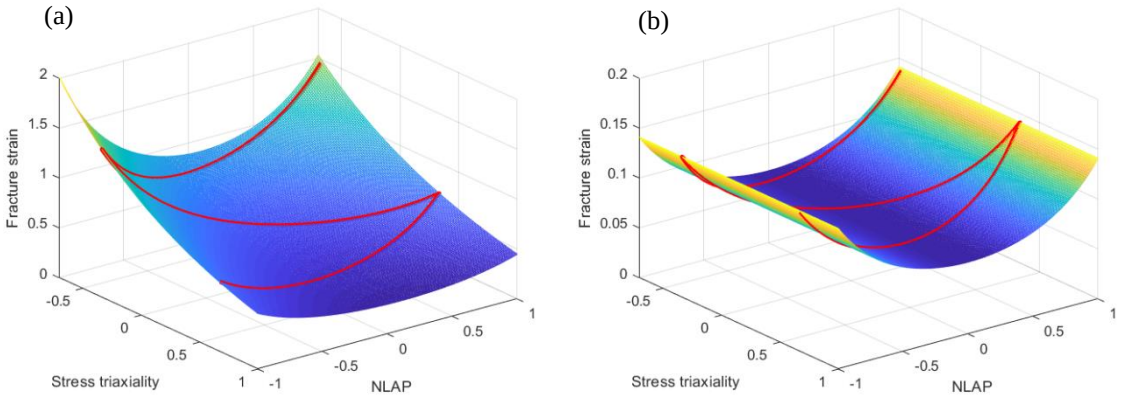

Figure 14 - 3D MMC fracture envelopes: (a) AA6082-T4 and (b) AZ31. The red line present in the surface shows the fracture strain for plane stress state.

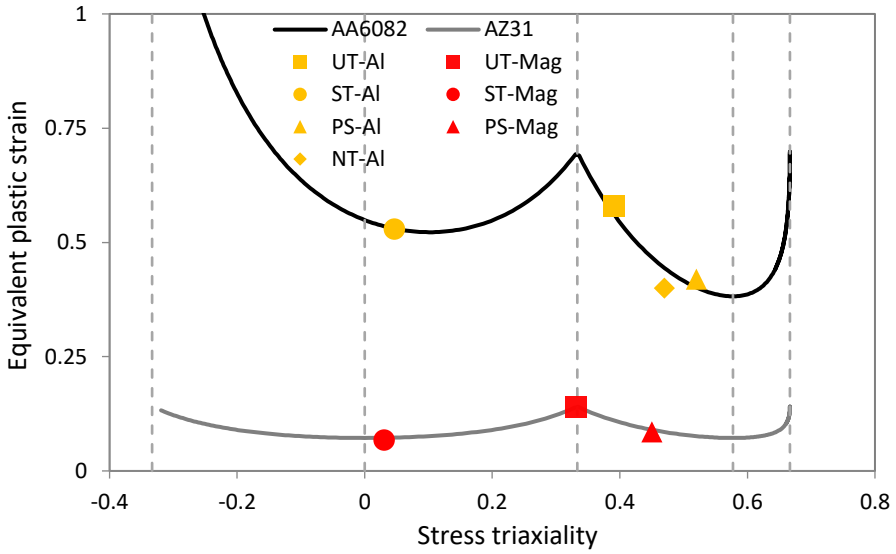

Figure 15 – Materials fracture envelopes and calibration points.

6. Results and discussion

6.1. Deformation mechanics

The contours values of equivalent plastic strain and damage indicator of the outer sheet are shown in Figure 16. According to figure 16 (a), the maximum equivalent plastic strain in the end of the flanging stage is located in the hole edge that is in contact with the flanging punch, while, as seen in figure 16 (b), the maximum damage is located in the bend zone. The high value of strain in the hole edge is due to the intense local contact between the hole edge and flanging punch, while not reflecting in high values of damage due to the mainly compressive stresses involved. The zone with the highest damage depends on the combination of the process parameters, and for a different combination it may be located in the flange edge. In the hemming stage, figure 16 (c) and (d), the damage continues to increase in the flange edge and bend zone, and, in this case, fracture eventually occurs in the flange edge. As shown in table 4, the indention depth (d) was fixed to 2 mm to match the thickness of the outer sheet in order to not occur pultrusion in the top surface of the inner sheet. Moreover, it is used 4 mm for the fillet radius of the upper die (fr_d) to control the deformation and damage in the bend area. Furthermore, it was considered a 2 mm gap between the inner sheet and outer sheet flange to minimize the buckling of the inner sheet.

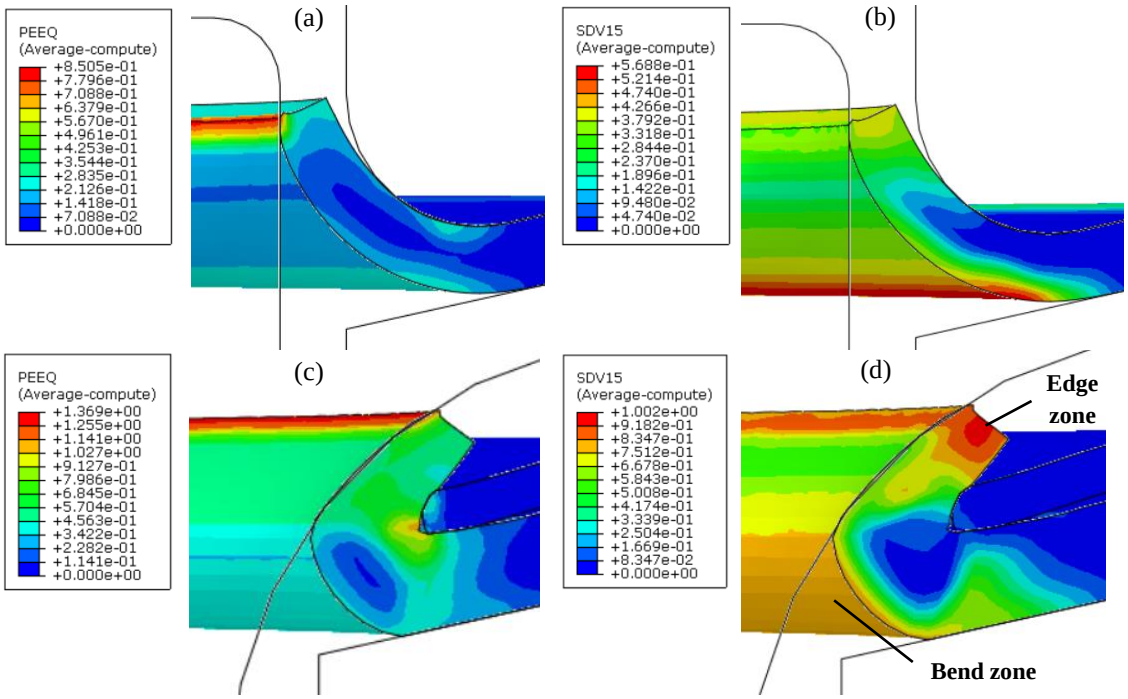

Figure 16 - Contour values of equivalent plastic strain and damage indicator in the outer sheet during the hole hemming process: (a) equivalent plastic strain at the end of the flanging stage, (b) damage value of the outer sheet at the end of the flanging stage, (c) equivalent plastic strain at the end of the hemming stage, (b) damage value of the outer sheet at the end of the hemming stage.

Figure 17 shows the loading path of the edge and bend zone in a two-dimensional space of stress triaxiality and equivalent plastic strain along the hole hemming process. The edge zone undergoes higher deformations than the bending zone. Nonetheless, the majority of the deformation path in the edge zone is located between pure shear and uniaxial tension, while the majority of the deformation path in the bending zone is located between uniaxial tension and plane strain due to the bending deformation, which have lower fracture strains.

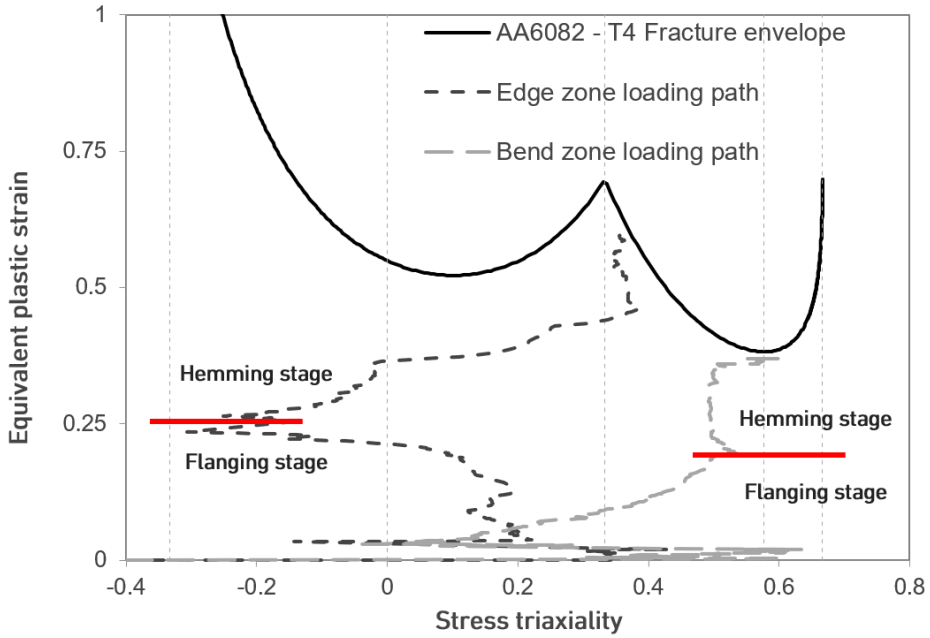

Figure 17 - Loading path of the critical regions on the outer sheet along the hole hemming process.

6.2. Influence of the process parameters

The damage evolution in the edge during the flanging stage for different values of flange length (F) is shown in figure 18 (a) and figure 18 (b) shows the influence of the flange length in the required force for the flanging punch during the flanging stage. Furthermore, figure 19 shows the effect of the flange length in damage contour and aspect of the joint at the moment of fracture.

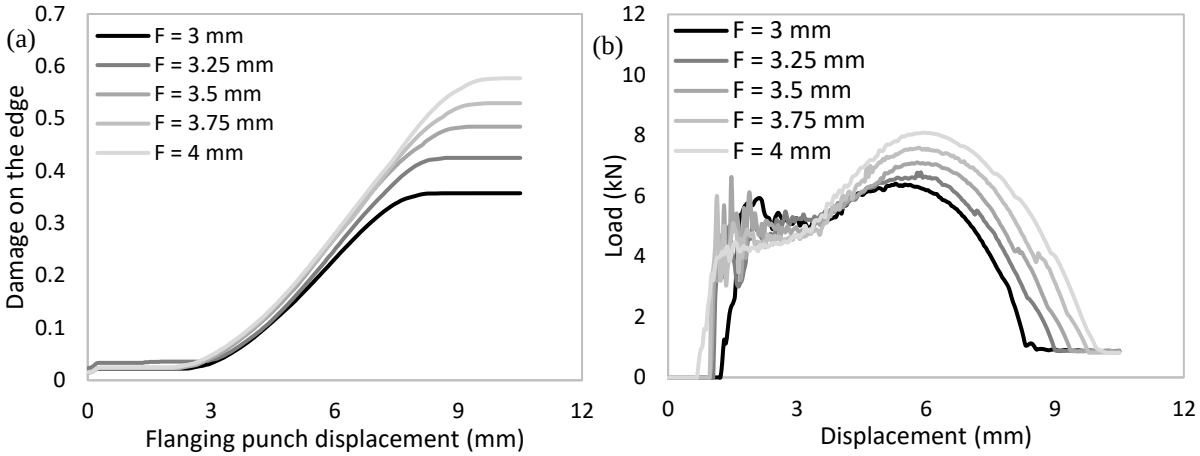

Figure 18 – Effect of the flange length (F): (a) in the damage evolution on the edge during the flanging stage and (b) on the required force in the flanging punch during the flanging stage.

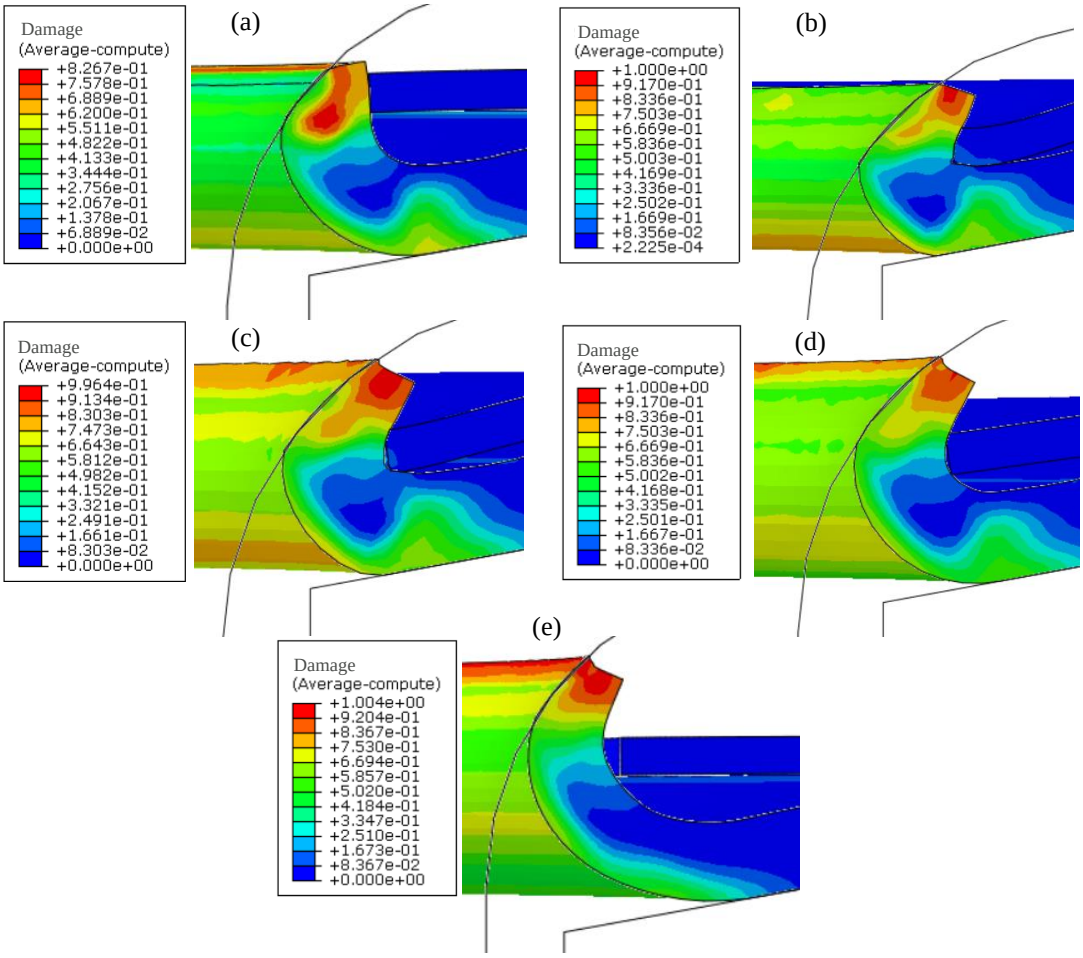

Figure 19 - Damage distribution in the outer sheet during the hemming stage for different values of flange lengths (F): (a) F = 3 mm, (b) F = 3.25 mm, (c) F = 3.5 mm, (d) F = 3.75 mm and (e) F = 4 mm.

The higher the flange length, the higher is the damage in the edge in the end of the flanging stage, which is expected as the ratio between the final and initial hole radius increase and the flanging strain is a function and proportional to this ratio, and the higher is the required force for the flanging punch, as more material is being deformed. The flange length is an important consideration in the process as it affects considerably the quality of the mechanical interlock between the two sheets. Although for a flange length of 3 mm the damage in the end of the flanging stage is much lower, figure 19 (a) shows that in the hemming stage no mechanical interlock is formed as the flange is too short and it is compressed before it overlaps the inner sheet to form a proper mechanical interlock. Nonetheless, for higher flanges (figure 19 (d)) fracture can occur in the outer sheet before a mechanical interlock is formed with both sheets. Along with the effect on the load of the flanging punch, the value of the flange length should be carefully considered in order to obtain a proper mechanical interlock without the occurrence of fracture.

Figure 20 shows the effect of the fillet radius of the hemming punch (R) in damage contour of the outer sheet and aspect of the joint at the first contact with the inner sheet. The higher the fillet radius the higher will be the contact length between the outer and inner sheet and the better will be the quality of the resulting mechanical interlock. If the fillet radius is too low, no mechanical interlock is obtained as the flange is compressed by the hemming punch without overlapping first the inner sheet (figure 20 (a)).

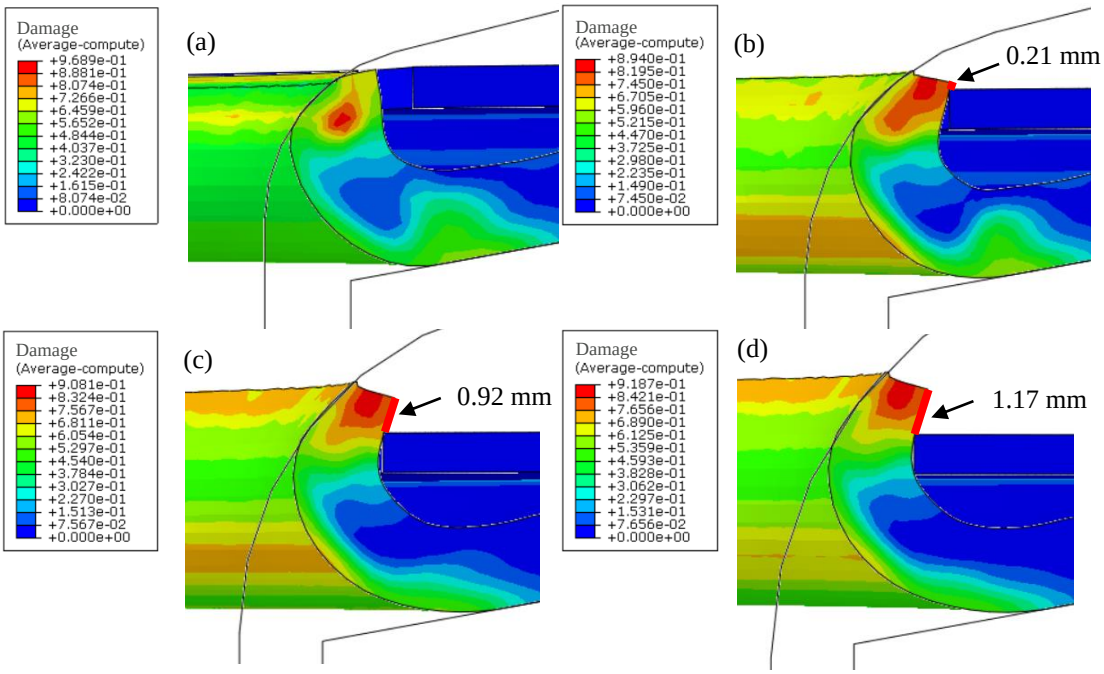

Figure 20 - Damage distribution in the outer sheet and contact length between the outer and inner during the hemming stage for different values of hemming punch fillet radius: (a) R = 4 mm, (b) R = 6 mm, (c) R = 8 mm and (d) R = 10 mm.

Figure 21 (a) shows the damage evolution in the bend zone during the hemming stage and figure 21 (b) shows the influence of the fillet radius of the hemming punch in the required force for the hemming punch during the hemming stage. For higher fillet radius the flange of the outer sheet enters in contact with the hemming punch earlier than for lower fillet radius and so the damage growth also starts earlier. Furthermore, for higher fillet radius the first contact with the inner sheet and the mechanical interlock are made for lower hemming punch displacements and in the end the resulting damage in the bend zone is relatively the same. Furthermore, the higher is the fillet radius the higher is the required force in the hemming punch, as the surface area of the outer sheet flange that is in contact with the hemming punch is higher.

The forces involved in the hemming punch increase exponentially in the end of the stoke and are considerably higher than the ones involved in the flanging punch, which is due to the compression of the materials while the mechanical interlock is being formed.

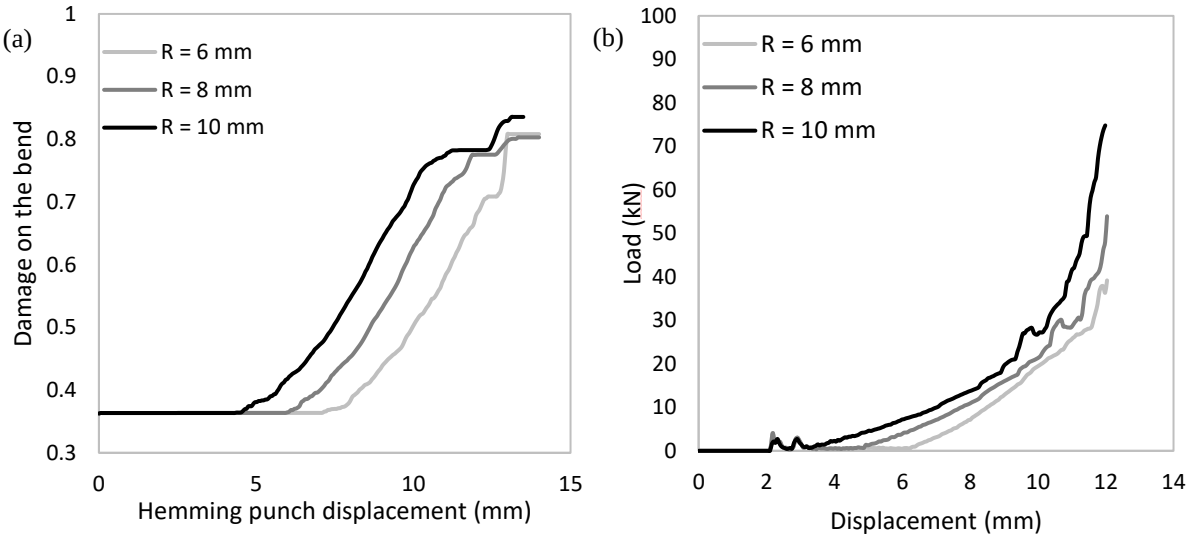

Figure 21 - Effect of the fillet radius of the hemming punch (R): (a) in the damage evolution on the bend during the hemming stage and (b) on the required force in the hemming punch during the flanging stage.

6.3. Process window

Figure 22 shows the process window for different F values. The contact between the inner and outer sheet occurred relatively at the same displacement for any value of F and the contact length increases with the increase of the flange length. Besides the contact length, the quantity of displacement between the contact and before fracture is also important, as the higher is the displacement the tighter will be the mechanical interlock.

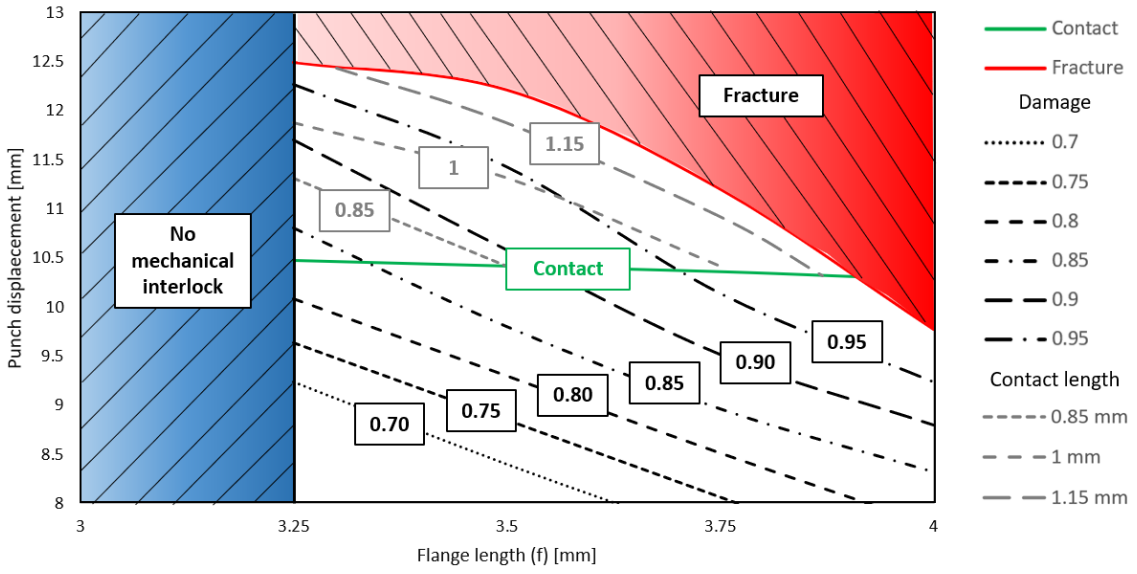

Figure 22 - Finite element process window for different values of flange length (F).

Figure 23 shows the process window for different R values and resumes the previous conclusions: Higher fillet radius leads to an earlier contact with the inner sheet and produces higher contact lengths, which produces better quality joints. Furthermore, the contact, fracture

and damage lines are relatively parallel between each other, therefore the damage evolution and the displacement between the contact and fracture are relatively the same.

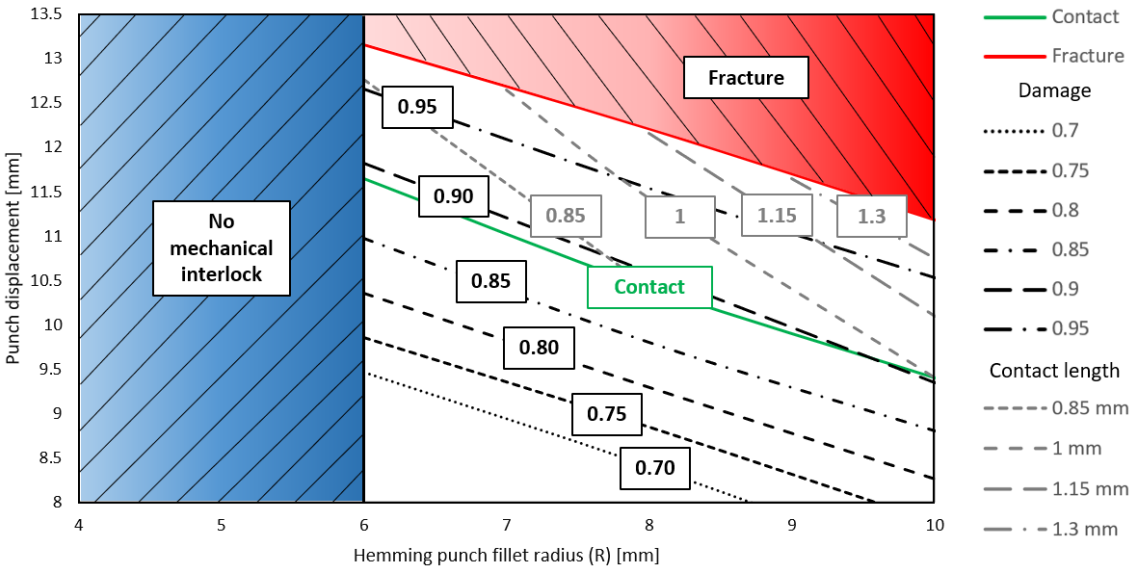

Figure 23 - Process window for different values of hemming punch filler radius (R).

In the present case the critical region of the process that limits the process window is the edge zone. In order to increase process window for the experimental tests, a die radius of 12.5 mm was preferred to the 10.5 mm studied above. By increasing the hole radius of the outer sheet and maintaining the flange length, it will allow to reduce the damage located in the edge. The process parameters used in the experimental tests are shown in table 7 and the FEM process window for the experimental tests is shown in figure 24. As it can be seen, it is expected that in the experimental tests it will be possible to obtain a joint without fractures for the cases of F = 3.5 mm and F = 4 mm. In the case of F = 4.5 mm it will not be possible to obtain a joint without fractures as fracture is predicted before the contact between the sheets.

Table 7 – Experimental process parameters.

Parameter	Value (mm)		
R_d	12.5		
R_o	$R_d - F$		
R_i	14.5		
d	2		
fr_d	4		
F	3.5	4	4.5
R	4		

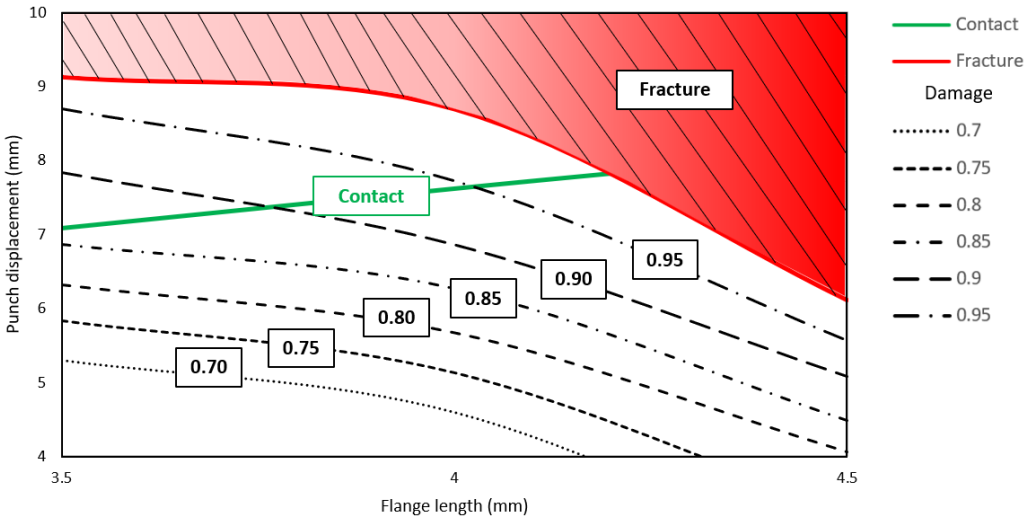

Figure 24 – Process window for the experimental hole hemming tests.

6.4. Hole hemming experimental tests

Figure 25 shows one of the resulting specimens for each studied flange length in the end of the flanging stage. For higher diameters the flange lengths are lower and, as predicted, no specimen exhibited fracture after this stage. Figure 26 shows a comparison between the experimental and numerical loading displacement curves during the flanging stage for each case and there is a good agreement between the curves.

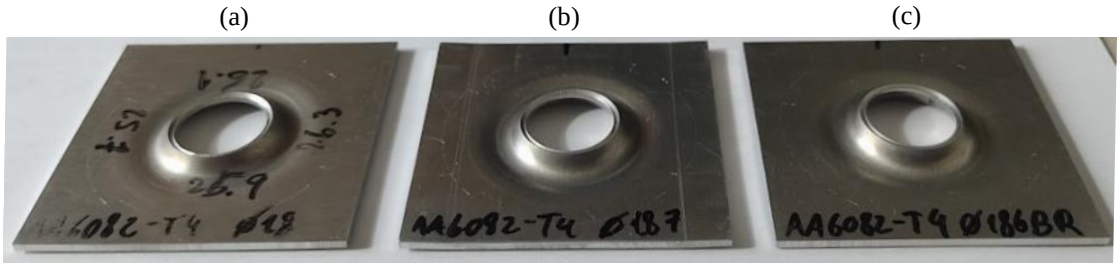

Figure 25 - Hole hemming specimens after the flanging stage: (a) F = 3.5 mm (Ro = 9 mm), (b) F = 4 mm (Ro = 8.5 mm) and (c) F = 4.5 mm (Ro = 8 mm).

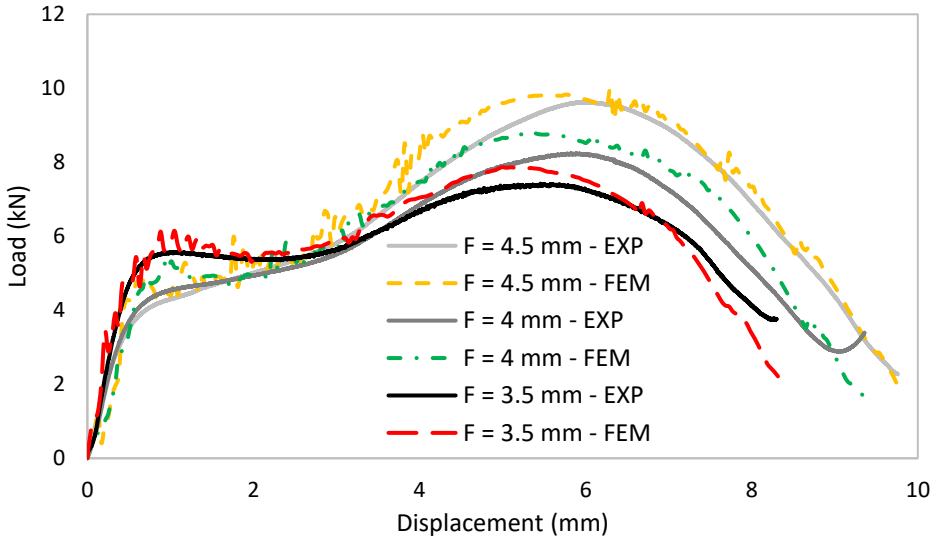

Figure 26 - Flanging stage load-displacement curves comparison between the experimental and numerical results.

Figure 27 shows one of the resulting joints for each studied flange length in the end of the hemming stage and one finite element analysis joint where fracture occurs.

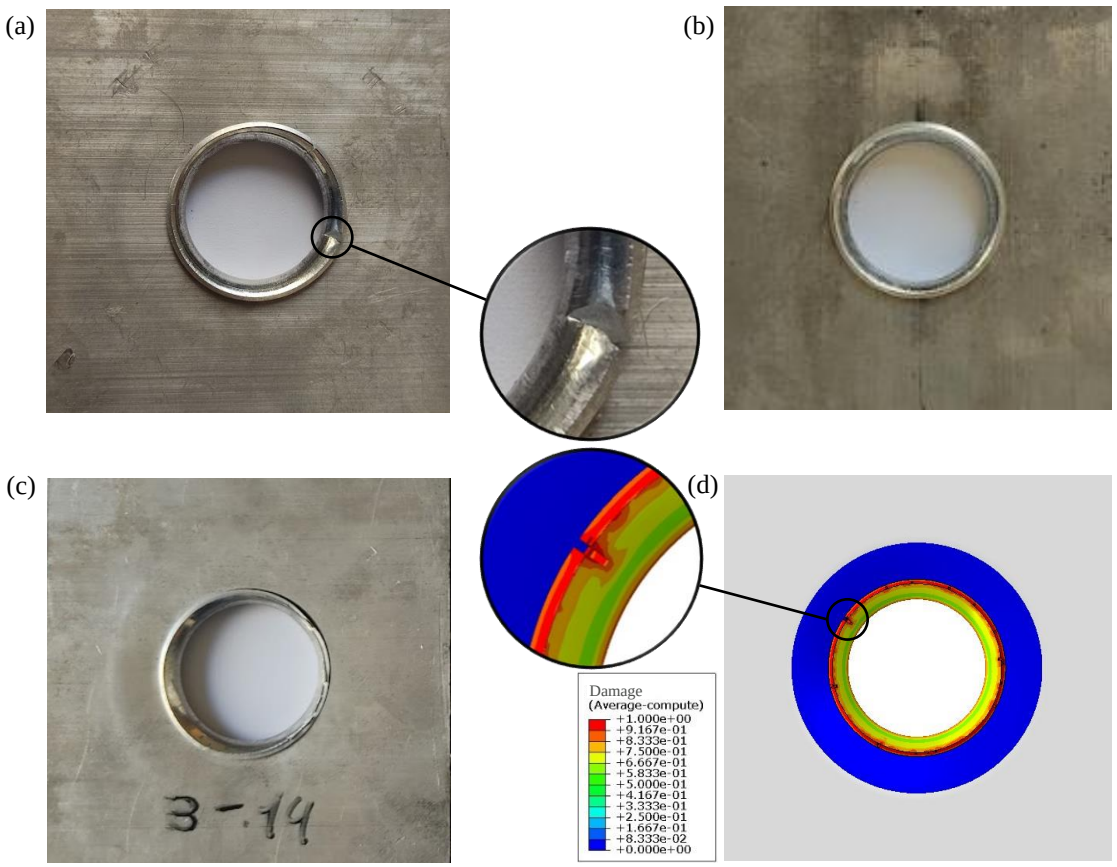

Figure 27 - Hole hemmed joints after the hemming stage: (a) F = 4.5 mm (Ro = 8 mm), (b) F = 4 mm (Ro = 8.5 mm) and (c) F = 3.5 mm (Ro = 9 mm).

Figure 27 (a) shows a hole hemmed joint for the F = 4.5 mm case and there are visible cracks on the edge of the flange of the outer sheet. Different hemming punch displacement were tried but cracks occurred for all the F = 4.5 mm case, as it was expected. Furthermore, figure 27 (d) shows a FEM joint where fracture occurred. As shown, the crack propagation in the FE model is similar to what was experimentally verified. Fracture initiates at the edge and progresses towards the middle section.

For the case of F = 4 mm, depending on the hemming punch displacement (different displacements were tested to verify the accuracy of the MMC fracture criterion) there are joints where cracks are visible (similar to figure 27 (a)) and joints with no visible cracks (figure 27 (b) shows one of them). The difference between a joint with and without cracks is the displacement of the hemming punch, as for higher displacements fracture will occur on the edge. Table 8 shows the fracture prediction error related to the displacement of the hemming punch compared with the critical FE model critical displacement, which is the displacement where fracture is predicted in the FE model. It was possible to obtain a mechanical interlock in all the tests and fracture was predicted with a maximum error of 4.8%.

For the case of F = 3.5 mm, it was difficult to obtain a mechanical interlock. As the flange length is smaller than the previous cases, the problems related to the alignment between the inner sheet, outer sheet and hemming punch, which do not exist in the numerical model, are more obvious. Furthermore, the friction between the outer sheet and the hemming punch can have a significant impact in the joint, as for high frictions the flange is more compressed and for the case of F = 3.5 mm it does not overlap the inner sheet. To reduce the friction between

the hemming punch and outer sheet it was used lubricant, nonetheless it was still not possible to obtain a proper mechanical interlock, as is shown in figure 27 (c).

Table 8 - *FE model fracture prediction error.*

Joint	Experimental hemming punch displacement (mm)	Visible cracks	FE predicted fracture displacement (mm)	Relative error (%)
1	8.01	No	8.69	-
2	8.06	No		-
3	8.27	Yes		4.8%
4	8.32	No		-
5	8.35	No		-
6	8.60	Yes		1.0%
7	8.66	Yes		0.3%
8	9.20	Yes		-

In figure 28 it is shown a comparison between the experimental and numerical load-displacement curves during the hemming stage for each case. For lower displacements the experimental load is higher, which may be due to the friction between the outer sheet and the hemming punch. For higher displacements the load is less dependent on the friction and more dependent on the bending of the outer sheet and there is a better correlation between the curves.

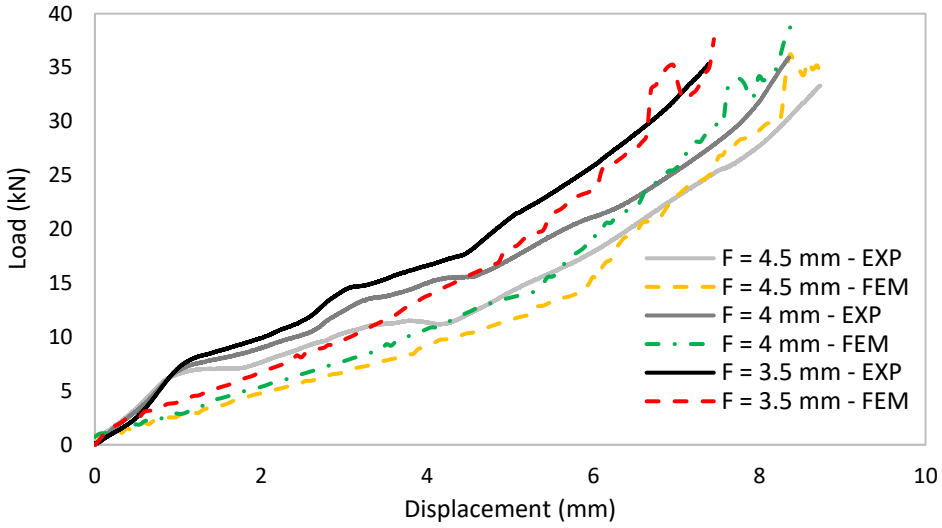

Figure 28 - Hemming stage load-displacement curves comparison between the experimental and numerical results.

6.5. Joint strength

Figure 29 shows the joints that were used to perform the single lap shear tests for the F = 4 mm case. The joint no.1, figure 30 (a), has a small misalignment between the sheets, which can be due to machining problems and not aligning correctly the holes before the hemming stage. The joints no.2 and no.3, shown in figure 29 (b) and (c) respectively, do not present misalignment and fracture defects. The joint no.4, shown in figure 29 (d), presents visible multiple fractures along the edge of the outer sheet flange.

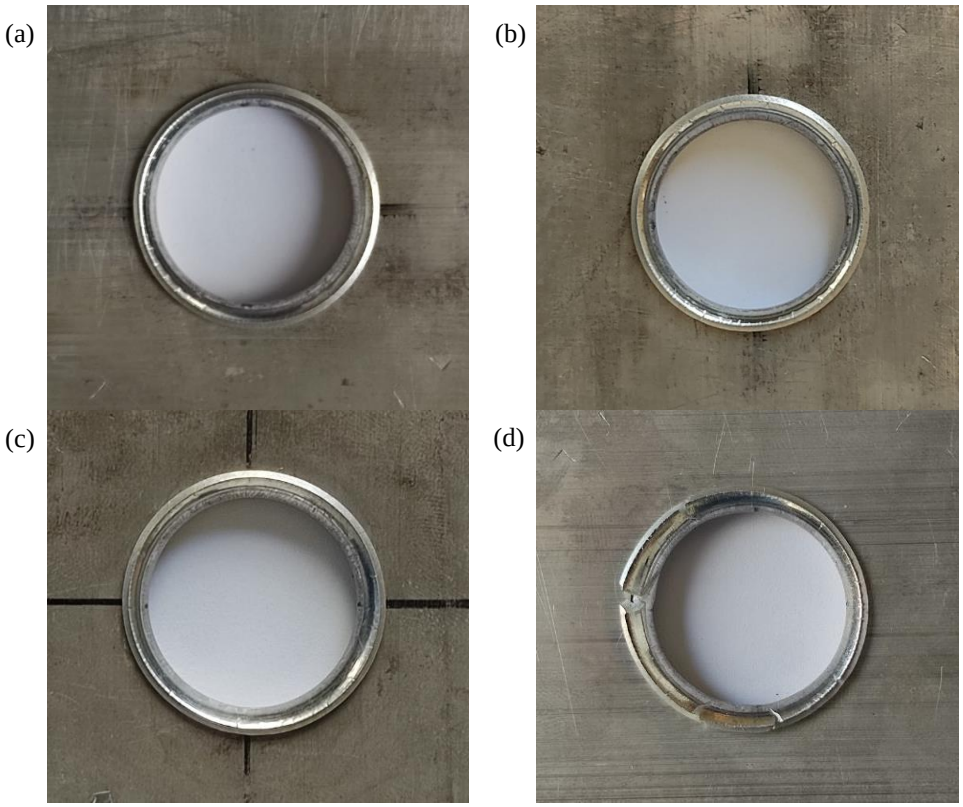

Figure 29 - Joints for the single lap shear tests: (a) joint 1, (b) joint 2, (c) joint 3 and (d) joint 4.

Figure 30 shows the respective experimental load-displacement curves of the performed single lap shear tests joints presented in figure 29. For the joint no.1, failure occurs for lower load and displacement when compared with the other tests. The joint no.1 was not well aligned, so the premature failure can be due to this. In the case of joint no.4, the load reached was about 2.5 kN and lower than the load of joint no.2 and no.3. The joint no.4 presented cracks in the outer sheet, which do not provide a good contact and also have sharp edges. These factors may lead to premature failure of the joint. For the joints no.2 and no.3 in which the sheets were well aligned and no fracture was verified, a good correlation between their load-displacement curves was obtained. A maximum shear load of almost 2.9 kN was achieved and the fracture displacement of both tests was almost the same.

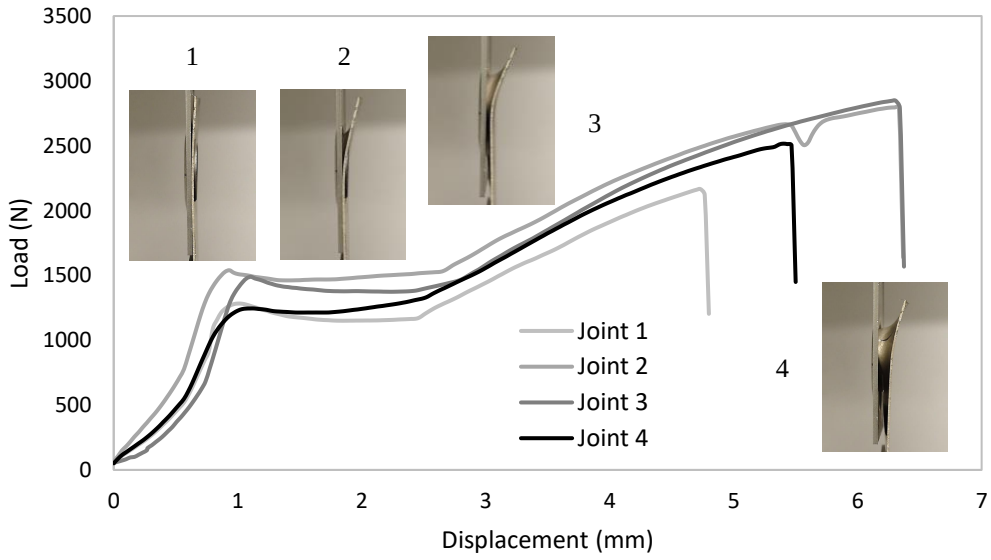

Figure 30 - Load-displacement curves of the experimental single lap shear tests for the F = 4 mm case.

During the single lap shear tests three different stages were distinguished. In the first stage (figure 30 no.1), the force increases sharply as the hole edge of the inner sheet is being compressed against the outer sheet flange, causing the inner sheet to slightly bend. In the second stage (figure 30 no.2), the load slightly decreases and then stabilizes. This happens as the inner sheet starts to yield and the bending angle increases. This confirms that the joints are in hole bearing failure mode. In the third stage (figure 30 no.3), the load once again increases but with a lower rate when compared with the first stage. This happens as the bending of the inner sheet increases the contact area between the inner sheet and the outer sheet flange, which lead to the verified increase of the load. Ultimately, fracture rapidly propagates in the inner sheet causing a load drop and the test to stop (figure 30 no.4).

In figure 31 (a) and (b) it is shown the aspect of the joint after the performance of the single lap shear test. The hole bearing mechanism is evident in the magnesium sheet. The magnesium sheet, figure 31 (c), is deformed while the aluminum sheet, figure 31 (d), is not, as the magnesium sheet not only have a sligtly lower strength but also because its thickness is more than two times lower than the aluminum sheet and the aluminum sheet also undergone strain hardening during the flanging and hemming stage. Because it has a slow failure mechanism, the hole bearing verified is preferable to other failure mechanisms such as net tension and shear-out which lead to unpredictable catastrophic failures. Furthermore, after the second stage the joint could withstand two times the force obtained in the end of the first stage, which increases the safety benefitions.

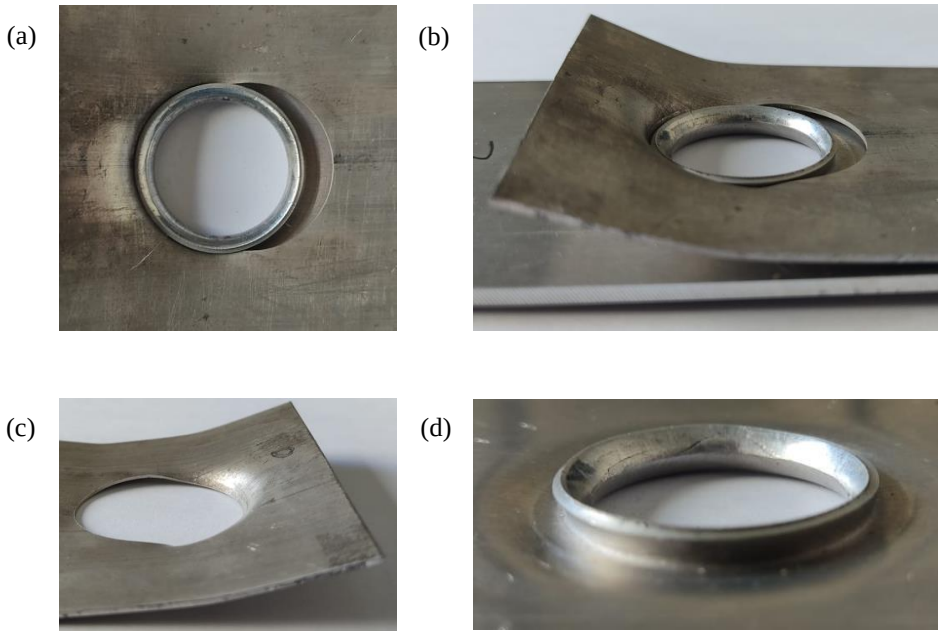

Figure 31 - Aspect of a hole hemmed joint and sheets after the single lap shear test: (a) front view and (b) side view of the hole hemmed joint, (c) magnesium sheet and (d) aluminum sheet.

7. Conclusions

In this paper, a novel hole hemming process was developed to join magnesium and aluminum alloy sheets to follow up the trend in the automotive industry of manufacturing high performance vehicle structures with magnesium alloys.

The materials, AA6082-T4 and AZ31, were characterized by the performance of uniaxial tension tests and the fracture limits under different loading states were analyzed by conducting formability tests. Results showed that the magnesium alloy, compared with the aluminum alloy, has considerably higher anisotropy and lower formability.

A numerical model was created to study the feasibility of the process and the main process parameters. The MMC fracture criterion was defined in the model by means of an appropriate subroutine to predict fracture and to identify the critical regions of the process, i.e. edge zone and bend zone, and their deformation mechanics. The results showed that the damage in the edge is affected by the ratio between the final and initial hole radius of the outer sheet, being possible to reduce the damage and thus avoid fracture in the edge either by increasing the initial outer sheet hole radius or by increasing the die radius (while maintaining the flange length). Nevertheless, the flange needs to be long enough to overlap the inner sheet and form a mechanical interlock. Furthermore, increasing the fillet radius of the hemming punch leads to a higher overlap of the inner sheet by the outer sheet flange and results in a better mechanical interlock. However, the increase of the fillet radius of the hemming punch also causes a sharp increase to the required punch force. Process windows were defined for the main process parameters, the flange length and fillet radius of the hemming punch, and for the experimental hole hemming cases.

Experimental hole hemming tests were conducted for three different flange lengths. For the flange of 4 mm, joints with tight mechanical interlocks were achieved while in some of them fracture happened at the edge. For the higher flange length of 4.5 mm, fracture in the edge was predicted in the numerical model and it was confirmed in all experimental tests. For the intermediate flange length of 4 mm, joints with tight mechanical interlocks were achieved while in some of them fracture happened at the edge. The fracture was predicted in function of the hemming punch displacement exhibiting a maximum error of 4.8%. For the smaller flange length of 3.5 mm, despite it was possible to obtain a good mechanical interlock in the numerical model, in the experimental tests the flange is too small as it is compressed before it overlaps the inner sheet to achieve a sound mechanical interlock.

The shear load of the joints for the flange length of 4 mm was experimentally tested by the performance of a single lap shear test. The hole bearing gradual failure mode was observed for a load of about 1.5 kN, while the increase of the displacement remarkably leads to an increase of the shear load to a maximum force of almost 2.9 kN.

References

[1] W. J. Joost, and P. E. Krajewski, “Towards magnesium alloys for high-volume automotive applications,” *Scripta Materialia,* vol. 128, pp. 107-112, 2017/02/01/, 2017.

[2] R. Hörhold, M. Müller, M. Merklein, and G. Meschut, “Mechanical properties of an innovative shear-clinching technology for ultra-high-strength steel and aluminium in lightweight car body structures,” *Welding in the World,* vol. 60, no. 3, pp. 613-620, 2016/05/01, 2016.

[3] C.-J. Lee, J.-M. Lee, H.-Y. Ryu, K.-H. Lee, B.-M. Kim, and D.-C. Ko, “Design of hole-clinching process for joining of dissimilar materials – Al6061-T4 alloy with DP780 steel, hot-pressed 22MnB5 steel, and carbon fiber reinforced plastic,” *Journal of Materials Processing Technology,* vol. 214, no. 10, pp. 2169-2178, 2014/10/01/, 2014.

[4] M. M. Kasaei, and L. F. da Silva, “Joining sheets made from dissimilar materials by hole hemming,” *Proceedings of the Institution of Mechanical Engineers, Part L: Journal of Materials: Design and Applications,* vol. 0, no. 0, pp. 14644207211072676, 2022.

[5] S. Vlase, V. Gheorghe, M. Marin, and A. Öchsner, “Study of structures made of composite materials used in automotive industry,” *Proceedings of the Institution of Mechanical Engineers, Part L: Journal of Materials: Design and Applications,* vol. 235, no. 11, pp. 2574-2587, 2021/12/01, 2021.

[6] B. Viswanadhapalli, and V. K. Bupesh Raja, "Application of Magnesium Alloys in Automotive Industry-A Review," *Emerging Trends in Computing and Expert Technology*. pp. 519-531.

[7] B. R. Powell, P. E. Krajewski, and A. A. Luo, "Chapter 4 - Magnesium alloys for lightweight powertrains and automotive structures," *Materials, Design and Manufacturing for Lightweight Vehicles (Second Edition)*, P. K. Mallick, ed., pp. 125-186: Woodhead Publishing, 2021.

[8] G. Meschut, M. Merklein, A. Brosius, D. Drummer, L. Fratini, U. Füssel, M. Gude, W. Homberg, P. A. F. Martins, M. Bobbert, M. Lechner, R. Kupfer, B. Gröger, D. Han, J. Kalich, F. Kappe, T. Kleffel, D. Köhler, C. M. Kuball, J. Popp, D. Römisch, J. Troschitz, C. Wischer, S. Wituschek, and M. Wolf, "Review on mechanical joining by plastic deformation," *Journal of Advanced Joining Processes*, vol. 5, pp. 100113, 2022/06/01/, 2022.

[9] T. Lipman, and P. Maier, "Advanced materials supply considerations for electric vehicle applications," *MRS Bulletin*, vol. 46, pp. 1-12, 02/14, 2022.

[10] L. H. Shah, N. H. Othman, and A. Gerlich, "Review of research progress on aluminium-magnesium dissimilar friction stir welding," *Science and Technology of Welding and Joining*, vol. 23, no. 3, pp. 256-70, /, 2018.

[11] D. Jacquin, and G. Guillemot, "A review of microstructural changes occurring during FSW in aluminium alloys and their modelling," *Journal of Materials Processing Technology*, vol. 288, pp. 116706, 2021/02/01/, 2021.

[12] V. P. Singh, S. K. Patel, A. Ranjan, and B. Kuriachen, "Recent research progress in solid state friction-stir welding of aluminium–magnesium alloys: a critical review," *Journal of Materials Research and Technology*, vol. 9, no. 3, pp. 6217-6256, 2020/05/01/, 2020.

[13] R. J. C. Carbas, M. A. Dantas, E. A. S. Marques, and L. F. M. da Silva, "Effect of the adhesive thickness on butt adhesive joints under torsional loads," *Journal of Advanced Joining Processes*, vol. 3, pp. 100061, 2021/06/01/, 2021.

[14] M. Q. dos Reis, E. A. S. Marques, R. J. C. Carbas, and L. F. M. da Silva, "Functionally graded adherends in adhesive joints: An overview," *Journal of Advanced Joining Processes*, vol. 2, pp. 100033, 2020/07/01/, 2020.

[15] H. Peng, C. Chen, H. Zhang, and X. Ran, "Recent development of improved clinching process," *The International Journal of Advanced Manufacturing Technology*, vol. 110, no. 11, pp. 3169-3199, 2020/10/01, 2020.

[16] J. Wu, C. Chen, Y. Ouyang, D. Qin, and H. Li, "Recent development of the novel riveting processes," *The International Journal of Advanced Manufacturing Technology*, vol. 117, no. 1, pp. 19-47, 2021/11/01, 2021.

[17] L. M. Alves, R. M. Afonso, and P. A. F. Martins, "Mechanical joining of sheets to tubes by squeeze-grooving," *Proceedings of the Institution of Mechanical Engineers, Part L: Journal of Materials: Design and Applications*, vol. 234, no. 1, pp. 120-129, 2020/01/01, 2019.

[18] S. Han, Z. Li, Z. Wang, and Y. Li, "Review on joining processes of magnesium alloy sheets," *The International Journal of Advanced Manufacturing Technology*, vol. 118, no. 9, pp. 2787-2803, 2022/02/01, 2022.

[19] P. Wang, and R. Stevenson, *Friction stir rivet method of joining*, US7862271B2, 2011.

[20] J. Min, J. Li, B. E. Carlson, Y. Li, J. F. Quinn, J. Lin, and W. Wang, "Friction Stir Blind Riveting for Joining Dissimilar Cast Mg AM60 and Al Alloy Sheets," *Journal of Manufacturing Science and Engineering,* vol. 137, no. 5, 2015.

[21] R. Neugebauer, S. Dietrich, and C. Kraus, "Dieless Clinching and Dieless Rivet-Clinching of Magnesium," *Key Engineering Materials,* vol. 344, pp. 693-698, 2007.

[22] M. J. Mirnia, and M. Vahdani, "Calibration of ductile fracture criterion from shear to equibiaxial tension using hydraulic bulge test," *Journal of Materials Processing Technology,* vol. 280, pp. 116589, 2020/06/01/, 2020.

[23] Y. Bai, and T. Wierzbicki, "Application of extended Mohr–Coulomb criterion to ductile fracture," *International Journal of Fracture,* vol. 161, no. 1, pp. 1, 2009/11/12, 2010.